THE DEVELOPMENT OF TITANIUM NITRIDE STRENGTHENED CREEP RESISTANT FERRITIC STEELS

JOHN A PUGH

THESIS SUBMITTED FOR THE DEGREE OF

DOCTOR OF PHILOSOPHY

IN THE UNIVERSITY OF STRATHCLYDE

METALLURGY & ENGINEERING MATERIALS GROUP

DEPARTMENT OF MECHANICAL ENGINEERING

UNIVERSITY OF STRATHCLYDE

GLASGOW, SCOTLAND

JUNE 2000

To Gail, Kieran and Rachel.

"Prescribing a strengthening method for a material

is like prescribing a treatment for a disease."

M F Ashby (1973)

To continue this medical analogy the work presented in this thesis

has shown that

"You can attack one symptom but cause

adverse side effects."

Abstract

Economic and environmental considerations have resulted in a worldwide drive to increase the cycle efficiency of fossil fired power plant. Boiler designs able to achieve significant efficiency increases already exist; the limiting factor is the performance of materials. As a result, much effort is currently being focussed on the development of enhanced materials to increase their operating temperature and/or pressure. The requirement that such materials should possess good thermal fatigue performance in addition to good creep performance dictates the selection of ferritic and martensitic steels for many components. Thus, most of the development effort in this field is currently focussed on martensitic steels that can operate beyond the current maximum plant design of 290 barg/580°C up to 335barg/630°C or even beyond.

The most advanced conventional ferritic steels such as E911, P92, P122 and NF12 are 9-12% Cr martensitic steels and gain their creep strength from the tempered martensite structure and the precipitated carbides and nitrides. Their long term creep performance is ultimately limited by the rate at which these precipitates coarsen or otherwise transform over time at elevated temperature.

This research work presents the development of an alternative alloy which aims to increase the high temperature long term creep performance by replacing the relatively low stability carbides and nitrides present in conventional ferritic steels with a thermodynamically more stable dispersion of titanium nitride particles.

To overcome the solubility limitation on precipitating a significant level of fine titanium nitride and to remove the dimensional constraints of gas phase nitriding, the

innovative technique being developed here is one of solid state nitriding using a nitride donor.

The microstructure and properties of the titanium nitride strengthened steels have been assessed at each stage of the alloy development using a range of optical and electron microscope examination techniques and hardness, tensile and creep mechanical assessment techniques. The results have shown that the processing route plays an important role in the development of the titanium nitride particles and these in turn play an important role in the development of the grain structure.

The initial evaluation of the creep rupture properties found them to be very poor, below that of the base material. This was due to two factors; relatively coarse titanium nitride particles and very fine grain size (due to the titanium nitride particles pinning) which resulted in extensive grain boundary sliding.

This research, therefore, investigates the development of the entire processing route, including the development of powder metallurgy and spray forming procedures with the aim of achieving a homogeneous dispersion of fine titanium nitride particles to resist dislocation creep and the development of a coarse interlocking grain structure to resist grain boundary sliding.

The achievements in the creep properties are presented in comparison with conventional ferritic creep resistant steels and advanced ferritic steels such as PM2000.

The properties achieved are discussed, not only in relation to the beneficial aspects such as creep strength and the effect this has on boiler cycle efficiency, but also in relation to deleterious effects that are a consequence of reduced creep ductility.

Finally, possible mechanisms to improve the properties as well as methods of reducing the production costs are assessed with a view to achieving the overall objective of developing a commercially viable material.

Preface

This thesis describes original work that has not been submitted for a degree at any other university.

This work was initiated by the BRITE EuRAM organised Project BRE2.CT93.0570 entitled "A Novel TiN Strengthened Creep Resistant Ferritic Steel for Advanced Power Plant". In addition to Mitsui Babcock Technology Centre, the partners were, AEA Technology plc, Osprey Metals Ltd., Babcock and Wilcox Española, Special Melted Products Ltd., Projectos Engenharia e Tecnologia/ISQ, and Research Centre Jülich GmbH. The work contained within this thesis is the authors contribution to this project and subsequent research work unless otherwise acknowledged.

The copyright of this thesis belongs to the author under the terms of the United Kingdom Copyright Acts as qualified by the University of Strathclyde Regulation 3.49.

Due acknowledgement must always be made of the use of any material contained in, or derived from this thesis. Some of the results from this thesis have been presented at the following events:

1) Pugh, J A, A Novel TiN Strengthened Creep Resistant Ferritic Steel for Advanced Power Plant. BRITE EuRAM Workshop on the Status of European Research Projects, VTT Technical Research Centre of Finland, Espoo, October (1995), p.55.

2)   Pugh, J A, TiN Steels! The Institute of Materials Young Persons Lecture Competition.
Winner of the Scottish Heat, March (1996).
Third place in the National Final, May (1996).

3)   Pugh, J A, A Material For The Next Millennium. Poster presentation of this research work was exhibited at the Duke of Edinburgh Awards Lunch at the Institute of Materials, November (1996).

4)   Pugh, J A, Creep Resistant Titanium Nitride Strengthened Steels for Advanced Power Applications. Materials for Advanced Power Engineering 1998. Proceedings of the 6th Liège Conference Part 1, (1998), p471.

Acknowledgements

Table of Contents

Nomenclature and Abbreviations

τ	Shear stress
δ	Crack opening displacement
λ	Interparticle spacing
ρ	Density
β	Geometrical constant
ε	Strain
$\dot{\varepsilon}$	Strain rate
$\dot{\varepsilon}_{gbs}$	Strain rate due to grain boundary sliding
$\dot{\varepsilon}_{disl}$	Strain rate due to dislocation creep
$\dot{\varepsilon}_{diff}$	Strain rate due to diffusion creep
ε_f^*	Rupture strain
σ	Stress
σ	Surface energy
σ_0	Threshold Stress
σ_h	Hoop stress
σ_y	Yield stress
σ_T	Local triaxial stress
ΔG	Free energy change
b	Burgers vector
η	Efficiency
C	Concentration
C^*	Power required to CCG
d	Grain diameter
D	Lattice diffusion coefficient
D_{BG}	Grain boundary diffusion coefficient

E	Youngs modulus
G	Shear modulus
K	Boltzmans constant
L	Grain length
M	Solubility
n	Creep exponent
N_A	Number of particles per unit area
P	Load
Q	Activation energy
r_o	Particle radius
r_{crit}	Critical particle radius
R	Universal gas constant
R'	Average radius of spherical domain
t	Time
t_p	Precipitation incubation time
t_r	Recrystallisation incubation time
t_{rup}	Time to rupture
T	Temperature
T_H	High temperature limit
T_L	Low temperature limit
T_m	Melting point
F_v	Volume fraction
v	Velocity
V	Particle molar volume
X	Distance

AEAT	Atomic Energy Authority, Technology
BCC	Body Centred Cubic
BCT	Body Centred Tetragonal
CCG	Creep Crack Growth
EDAX	Energy Dispersive Analysis of X-rays
FCC	Face Centred Cubic
GAR	Grain Aspect Ratio
HIP	Hot Isostatic Pressing
HRSG	Heat Recovery Steam Generator
IPS	Inter-Particle Spacing
MA	Mechanical Alloying
ODS	Oxide Dispersion Strengthening
PF	Pulverised Fuel
SEM	Scanning Electron Microscope
SR	Secondary Recrystallisation
SMP	Special Melted Products Ltd.
TEM	Transmission Electron Microscope
TMP	Thermo-Mechanical Processing
USC	Ultra-supercritical
VIM	Vacuum Induction Melting

Chapter 1

Power plant and the need for creep resistant ferritic materials

1.1   POWER PLANT REQUIREMENTS

The drive for ever increasing efficiency of coal fired power plant has always been present, however, in recent years it has been given greater impetus by the environmental concerns over polluting emissions of SO_x, NO_x and CO_2. Increased efficiency is therefore not only beneficial from an economic perspective in that it delivers lower electrical energy unit costs, but, it is also beneficial from an environmental perspective as the amount of harmful emissions per megawatt generated are in direct correlation with the efficiency of the power plant.

Coal fired power plant have historically been the principal method for generating heat and power.   Today coal still generates the largest percentage (40%) of electrical power world-wide. Of this 40% the majority is generated in pulverised fuel (PF) plant. Figure 1.1 illustrates the main components of a PF coal fired power plant and the process steps in generating electricity.   The World Energy Council Report "Energy for Tomorrows World" (1993) stated that for the next twenty to thirty years there will be a continued heavy reliance (amounting to approximately 90% of the total electrical energy generated worldwide) on coal, oil and natural gas. However, the reserves of oil and natural gas are unlikely to be sufficient to satisfy fully the increased power demands, and by the middle of the 21st century coal may be the

1

Figure 1.1 Schematic Diagram of a Coal - Fired Power Station.
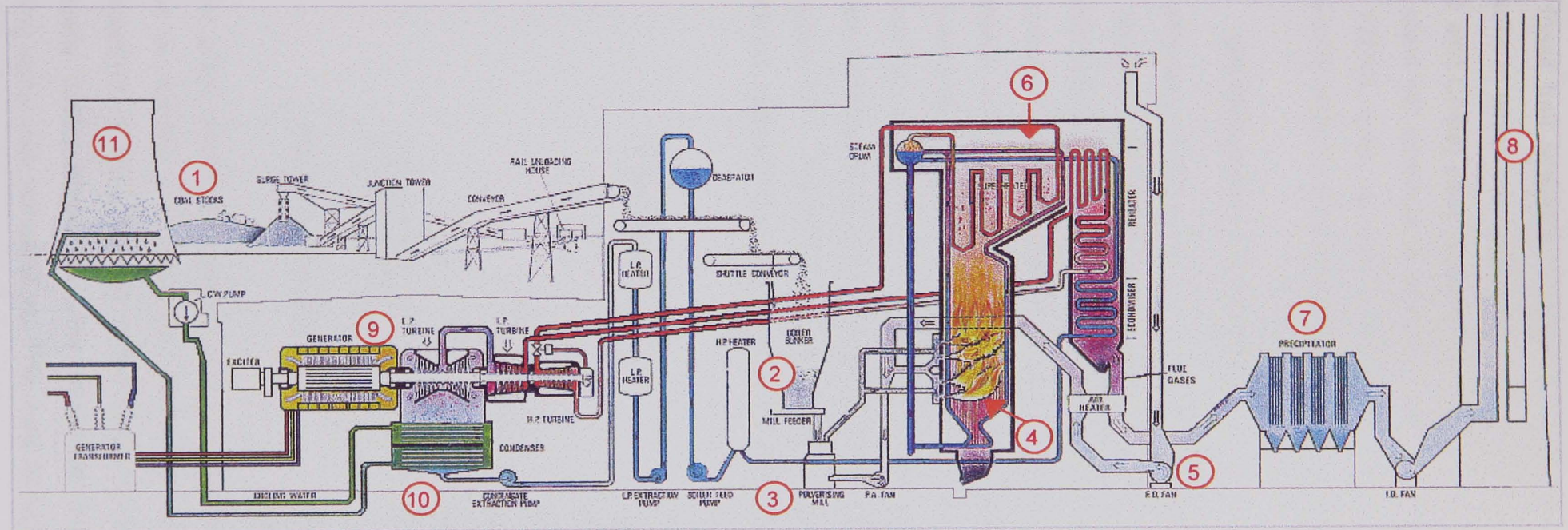
- Coal is taken from the stockpile (1) and conveyed to the bunkers (2).

- The coal is fed to the mill (3), pulverised and fed to the burners (4).

- Air for combustion is supplied from the forced draught fan (5).

- Hot combustion gases heat water and generate steam in the boiler (6).

- The cooled gases are cleaned in the electrostatic precipitators (7) and are exhausted from the chimney (8).

- The steam from the boiler drives the turbine generators (9) which generate electricity.

- The spent steam is condensed (10) and returned to the boiler.

- Cooling water for the condenser is provided via the cooling towers (11).

only fossil fuel available in substantial quantities. In the immediate future the countries in which the largest increases in electricity generation capacity will occur (India and China) have large indigenous deposits of coal, so the demand for coal fired plant will continue to expand. Thus, although higher efficiency power plant (e.g. HRSG) exist, as coal is the majority fuel today and in the future, the major world-wide effort is being expended on coal power plant technology.

1.2   INCREASING EFFICIENCY

The efficiency of boiler plant is controlled by the Second Law of thermodynamics. The Second Law is an expression of the fact that some heat must always be rejected during the cycle, and therefore the cycle efficiency is always less than unity. The definition given by Planck, reviewed by Rogers & Mayhew(1980), is that it is impossible to construct a system, which will operate in a cycle, extract heat from a reservoir and do an equivalent amount of work on the surroundings. Thus, the Second Law implies that if a system is to undergo a cycle and produce work, it must operate between at least two reservoirs of different temperatures. This is illustrated in Figure 1.2. The efficiency of a power plant is therefore proportional to the difference between the steam temperature exiting the boiler and the condenser temperature. Optimising the cold end of the cycle is limited as it is largely governed by the power station location i.e. sea water cooling reduces the temperature more than a land bound wet cooling tower, therefore, the sea water cooling gives a higher efficiency for a set upper temperature. In addition the lower the sea water temperature the higher the cycle efficiency thus
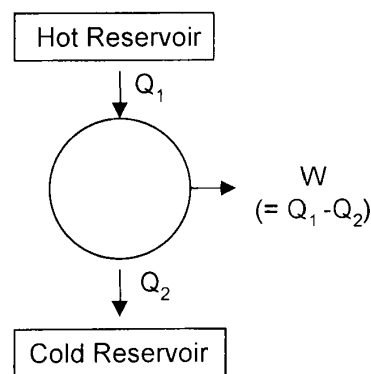
Figure 1.2 Heat Engine

power plant utilising sea water cooling in northern Europe are more efficient than those in Southern Europe for the same upper temperature. However, the optimisation of the cold end of the cycle is very close to its limit as in modern seawater cooled power plant the condenser temperature is only 8-9 K above the cooling water inlet temperature. The route to further increases in efficiency lies with increasing the upper temperature limit.

3

The historical trend in pulverised fuel steam cycle efficiency and the planned future is shown in Figure 1.3. Up to the break in 1990 the increases in efficiency were achieved by optimising the Rankine (1908) Cycle by means of increasing the
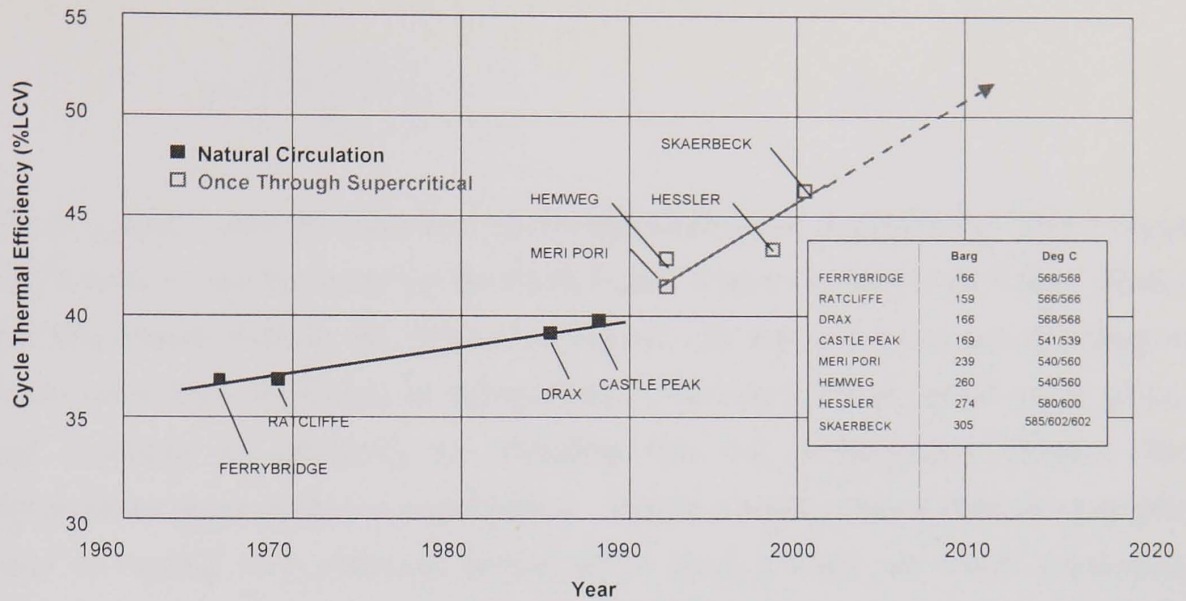
Figure 1.3 Efficiency variation with year of manufacture

temperature and pressure. A simple Rankine thermal cycle is shown in Figure 1.4. The Rankine Cycle works by pressurising the feed water by the feed pumps to boiler pressure before entering the boiler (adiabatic compression with internal losses due to compression). The water is then heated at constant pressure within the economiser (B-C in the diagram) followed by evaporation in the waterwalls (C-D) at constant pressure and temperature to form saturated steam (isothermal heat admission). After separation from any water, the steam is superheated (D-E) before leaving the boiler (E-F) and expanding in the turbine to give off work (adiabatic expansion with internal losses during expansion). Finally heat is removed from the cycle in the condenser at a constant low

Figure 1.4 Subcritical Rankine Cycle

temperature (isothermal heat transmission with phase shift). The efficiency of the cycle is defined as the work output from the cycle divided by the heat added to the cycle. The idealised efficiencies of a power cycle η is given by

$$\eta = \left(\frac{T_H - T_L}{T_H} \right) \tag{1.1}$$

where T_H and T_L are the high and low temperature limits respectively. The increase in efficiency in moving from Castle Peak Power Station to Meri Pori Power Station, Hemweg Power Station etc (shown in Figure 1.3) was achieved by changing the steam cycle from subcritical to supercritical. The supercritical steam cycle gives a step increase in efficiency by avoiding the low temperature isobaric heat transmission process during evaporation. This is possible due to the fact that when water is heated at a pressure above 221.2 barg it does not have a saturation temperature, nor does it produce a two phase mixture of water and steam as shown in Figure 1.5. Instead the fluid undergoes a transition where its physical properties (density and viscosity) change from that of water to that of steam. This can be understood by comparing the processes at a molecular level. During boiling at subcritical pressure individual molecules break out of the dense liquid clusters and as the physical surroundings permit, form a separate vapour phase. At supercritical pressure as heat is added to the liquid, the dense liquid clusters gradually divide into smaller clusters and the spacing of the molecules gradually increase. Although no evaporation takes place in the supercritical steam cycle there is still a phase shift from steam to water in the condenser. An example of an advanced supercritical cycle is shown in Figure 1.6.
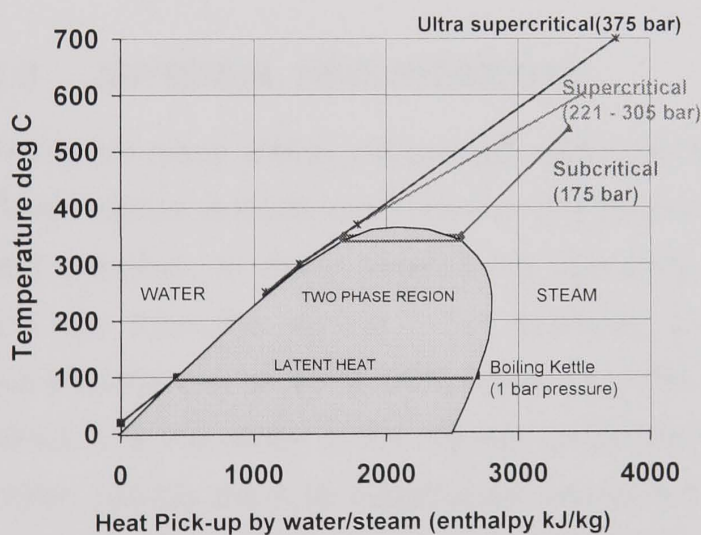
Figure 1.5 Water/steam enthalpy diagram

As can be observed from Figures 1.3, 1.4 and 1.6 the efficiency of the power plant can be increased by increasing the temperature and pressure. To optimise the hot end of the cycle, i.e. increase the average heat addition, heat should be added to the cycle at the highest possible temperature. Thus for advanced steam turbine plant, the current effort and that for the next decade will be to define the highest live steam temperatures which are achievable for the long term. The efficiency of a power plant is therefore only limited by the properties of the materials available for construction of the highest temperature and pressure components.
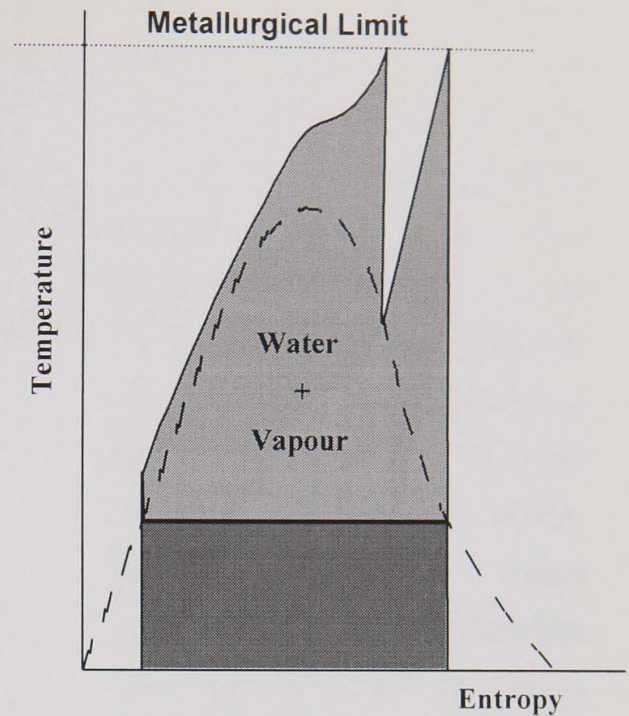
Figure 1.6 Supercritical Rankine Cycle with Reheat

1.3   MATERIAL REQUIREMENTS

There are many critical components within the steam power plant, however, as the steam turbine is totally dependant on the boiler to obtain the increase in temperature and pressure, in many aspects the operating conditions of the boiler are more arduous than the turbine. For example, the metal temperature of the final superheater can be some 50°C higher than the inlet temperature at the turbine. In effect, it is the ability of the highest temperature and pressure components of the boiler, namely the final superheater tubing and associated headers and pipework (shown in Figure 1.7) to cope with these severe conditions that govern the boiler operating conditions therefore the efficiency of the thermal cycle.

For components operating at 600°C plus and high pressures, creep is a critical factor and the power plant is designed to operate for a finite life (for example 250,000 hours, i.e. nearly 30 years). Although austenitic steels offer good creep and corrosion properties, their thermal properties are relatively poor with low thermal conductivity coupled with a high coefficient of expansion. During thermal cycling high temperature differentials can develop within thick section components such as
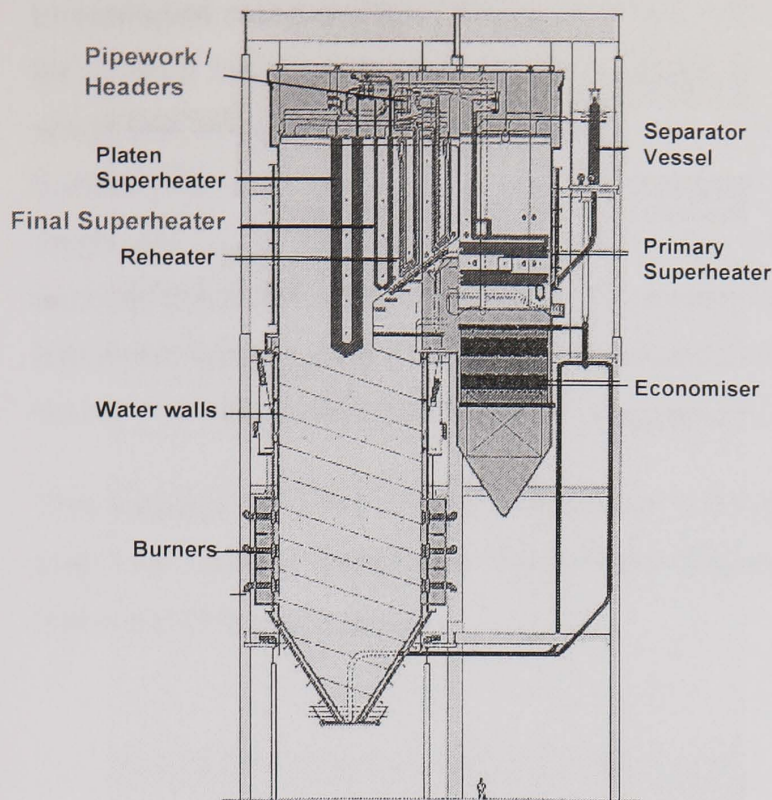
Figure 1.7 Supercritical "Boiler"

headers (as shown in Figure 1.8) leading to high reversible stresses (Figure 1.9) that can lead to thermal fatigue damage. It was the use of austenitic stainless steels for thick components that led to the failure of early supercritical plants such as Eddystone, Staubli et al (1998). To avoid unacceptable thermal stresses, austenitic thick walled components such as headers and pipework would require to be heated to operating temperature over an extended period, which would be uneconomical for plant operators meeting real time electricity demand. Thus, for flexible power plant, able to achieve two or three daily shifts which is a necessity for operators in todays highly competitive electricity supply market, there is a requirement for the extensive use of ferritic steels.
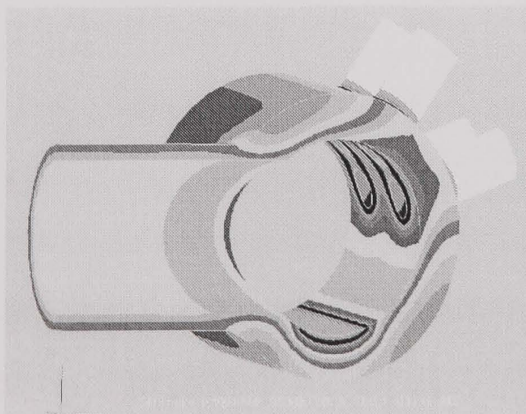
Figure 1.8 Temperature Distribution Part-Way Through Shutdown
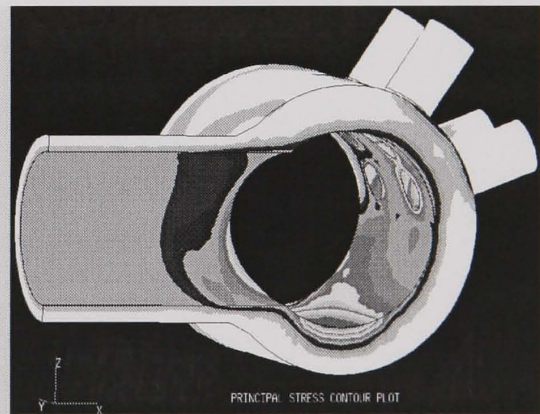
Figure 1.9 Stress Distribution during Thermal Transient

Designs exist for higher temperature ferritic plant, which will result in large increases in plant efficiencies. These higher efficiency stations are known as ultrasupercritical plant (USC), but to construct these plants requires the development of high

temperature creep resistant ferritic materials. World-wide, the current effort and that for at least the next decade, will be to define the highest live steam temperatures which are achievable for the long term use of ferritic / martensitic steels. Within Europe, the two main projects aimed at advancing the limits of ferritic / martensitic steels are COST 522 (1998) and Thermie 700 (1998). Due to physical constraints such as the instability of conventionally utilised carbides and nitrides 100 to 150°C below the austenite transformation temperature, the target temperature for 100,000 hours, 100 MPa operation for ferritic / martensitic steels in both projects is 650°C.

This thesis describes the work undertaken to develop a novel creep resistant ferritic steel that has the potential for higher temperature operation than any of the ferritic materials being developed.

Chapter 2

Development of ferritic / martensitic creep resistant steels

In developing alloys for service at elevated temperatures, the aim is to produce a material which can not only withstand the initial service conditions, but is capable of withstanding the service conditions throughout the whole of the expected design life. The determining factor in selecting a material for long term operation at high temperature is the creep strength.

2.1 CREEP

When assessing the resistance of materials to deformation and failure over long times under load at high temperatures, particular attention must be given to creep. Creep is defined, as time dependant strain occurring under a stress that is lower than the tensile yield point, Powell (1986). Creep is strongly dependent on the temperature, stress and the microstructure. Above 0.4 T_m (the absolute melting temperature), a typical creep curve shows three stages (Figure 2.1): in stage I, the strain rate decreases until a steady state is reached. The steady state rate is the minimum creep rate and corresponds to stage II or the secondary creep regime. This is followed by the tertiary stage, during which constantly increasing strain rate eventually leads to rupture. The high temperature strength of materials and their

deformation behaviour at elevated temperature are affected by four main deformation mechanisms.
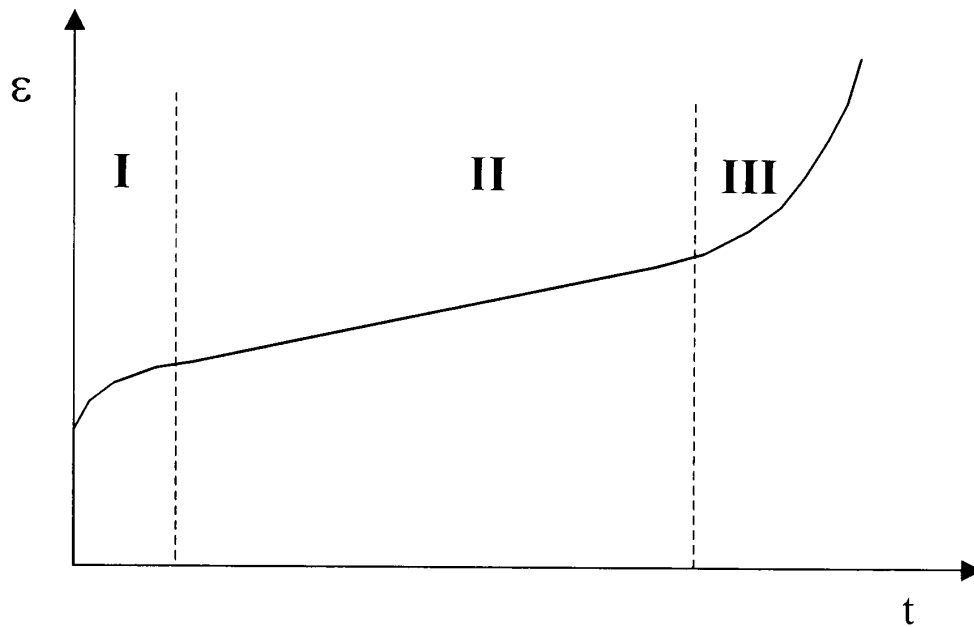
Figure 2.1 Typical creep curve above 0.4T$_m$ showing the three phases

2.2   CREEP DEFORMATION MECHANISMS

The four main deformation processes can be recognised as:

I.   The glide of dislocations.   Lowest temperature deformation mechanism involves dislocations moving along slip planes.   The dislocation motion is limited by precipitates in materials such as titanium nitride strengthened steels.

II.   The climb of dislocations.   Above around 400°C dislocations in iron based alloys can climb as well as glide.   Thus, if the glide of a dislocation is held up by a particle, climb may release it allowing it to glide to the next set of obstacles where the process is repeated.   The glide step in the motion is responsible for almost all the strain, but the climb step limits the rate of the entire mechanism.   The rate controlling process is the diffusive motion of single atoms or vacancies to or from the climbing dislocation.   Above approximately 450°C lattice diffusion is the dominant mode of mass transport, therefore the climb rate and thus the creep rate is controlled by the self-diffusion of iron.

III.   The sliding of grain boundaries. During secondary creep, it is possible for the grains to slide past each other along their boundaries.

IV.   The diffusion of vacancies. This involves stress induced diffusional flux of matter through or around the surfaces of grains. This category includes Nabarro Herring and Coble Creep.

These high temperature deformation processes govern the creep behaviour of the material. The strain that accumulates in a creeping material is dependent on the stress, temperature and the duration.

2.3   DEFORMATION MECHANISM MAPS

Different mechanisms may predominate for creep deformation at different combinations of stress and temperature; Ashby (1973) has represented these different regimes in terms of deformation maps. These maps represent the predominant creep deformation mechanism at different combinations of normalised shear stress (τ/G) and homologous temperature (T/Tm) for a given grain size. The extent of the fields in which a particular creep mechanism dominates varies from material to material and for a given material is strongly influenced by microstructure. The Ashby maps are being used here to identify the dominant deformation mechanism present under boiler operational conditions and thus prescribe an appropriate strengthening mechanism to counter the deformation and thus increase the creep strength. There are, however, few deformation mechanism maps for the high strength ferritic alloys. Shown in Figure 2.2a & b are examples of deformation maps for pure iron and Cr-Mo-V steel.
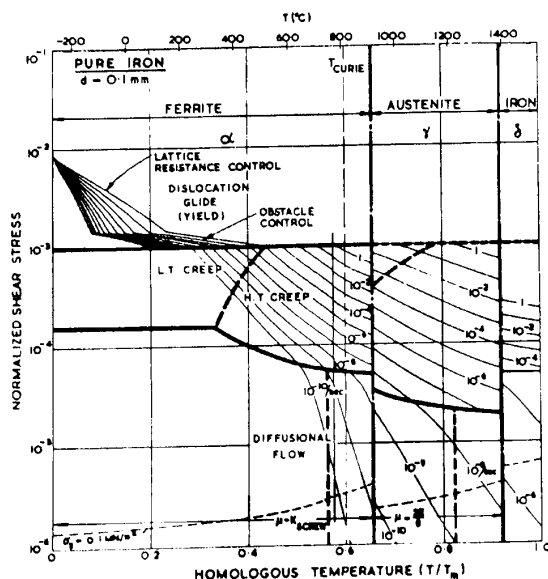
Figure 2.2a Ashby Map for Iron   Figure 2.2b Ashby Map for C-M-V
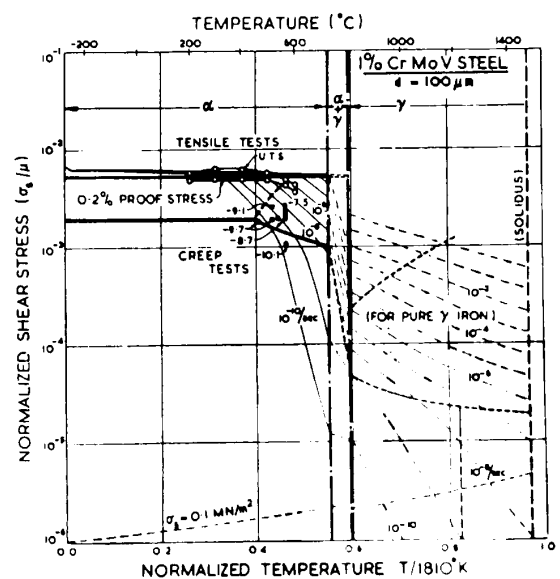
11

The limitation of the maps is that it can only describe the material in one condition, which in this case is its virgin state. The map does not take account of general microstructural degradation changes (particle coarsening, grain growth) that occur during creep.

From the available information, it is apparent that the creep resistant ferritic steels used for boiler components operate mainly in the Power Law Creep regime. However, at the highest temperature and lowest stresses, diffusional flow may influence the creep performance.

2.4 POWER LAW CREEP SUPPRESSION

At a microscopic level, power law creep is the uniform strain produced by dislocations that move between barriers by glide with short climb excursions to bypass the barriers. It is suppressed metallurgically by introducing more obstacles that have to be bypassed. These obstacles can be solid solutions, grain boundaries, precipitates etc. Ashby (1973) classified the various obstacles according to their bypassing activation energy. This revealed that isolated solute atoms were the weakest and most precipitates and dispersions were the greatest.

To obtain good creep properties in ferritic alloys, the primary requirement is to maintain the dislocation density by hindering dislocation movement. This can be achieved by a suitable dispersion of particles within the grains of the matrix. The particles should be hard; i.e. they do not shear as dislocations pile up against them. The presence of alloying elements in solid solution also improves the creep resistance as the solute elements increase the frictional forces on the dislocations as they pass through the matrix. The greater the lattice distortion, the greater the frictional forces and thus dislocation impediment. There are limits to applying this argument for improving the creep resistance, as the greater the lattice distortion produced by the solute, the lower will be its solubility in the solvent. Recently, in martensitic steels, tungsten has been shown to exert a strong effect on solid solution creep strengthening, Hald (1995).

2.5   STRUCTURAL STABILITY AND CREEP

From the above, essentially the presence of the precipitates or solid solution elements provides the barrier to dislocation movement. Consequently, the aim is to produce the most stable precipitate, or immovable clusters of atoms as possible.

For a given size (e.g. 20nm) and spacing, each of the different precipitates, or atom clusters has, more or less, the same ability to impede dislocation. It is widely recognised that some are better or worse than others, simply because they are used at different temperatures. What is actually being observed is the ability of the precipitates to maintain their edge to edge spacing, i.e. resistance to Ostwald ripening, which gets more rapid as the temperature increases.

The result of coarsening of precipitates and also the increased ease that dislocations can get around obstacles as the temperature is increased, results in a fall off in strength as the temperature is increased, as shown in Figure 2.3 for mean 100,000 rupture lives as given by PD6525(1990). The chemical composition ranges of the alloys presented and their initial heat treatment condition are given in Table 2.1. Also given in Figure 2.3 are the precipitate(s) for each material, which it has been determined decisively affects the creep properties at elevated temperature. As can be observed, it is the nitride precipitates, or more specifically the vanadium nitride precipitates that currently impart the most advanced range of martensitic steels with their high creep strength.
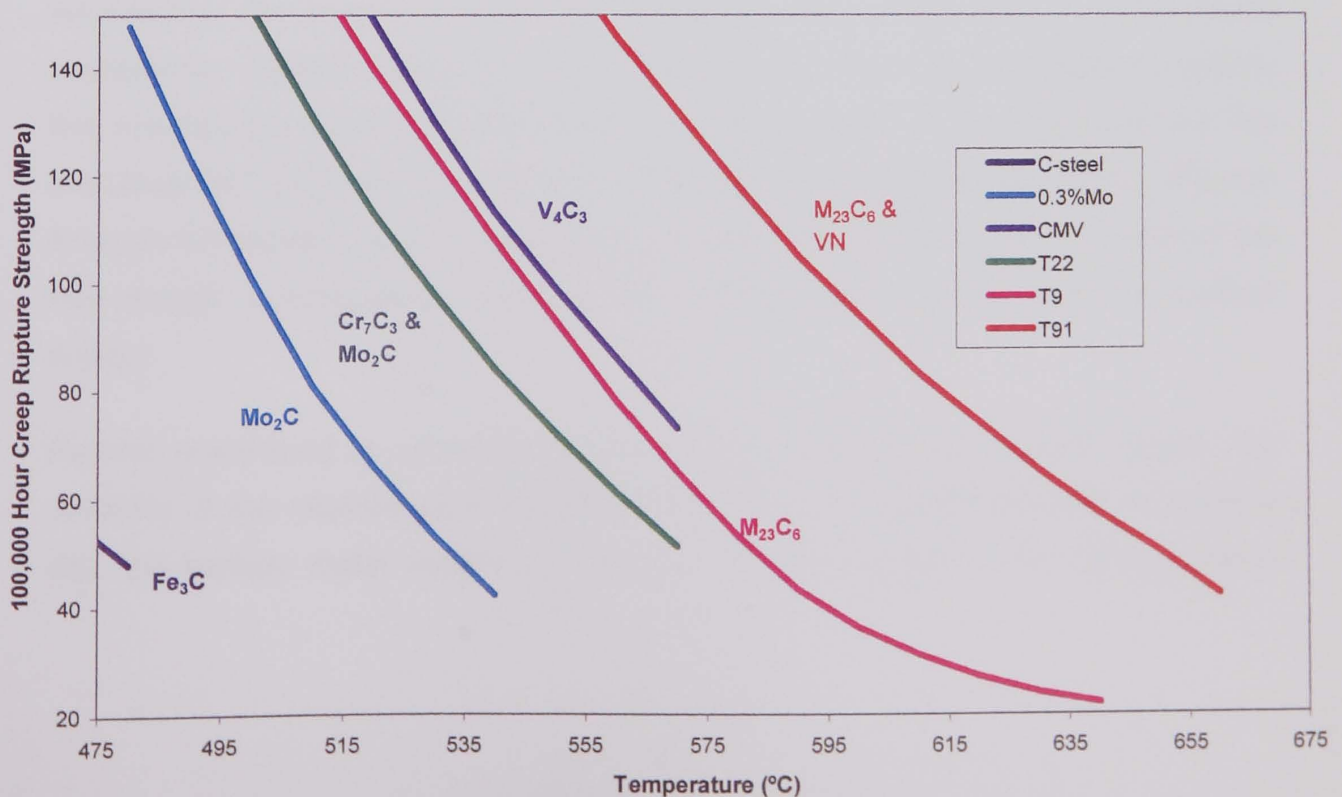
Figure 2.3 100,000 hour Creep rupture strength V. Temperature

13

Material	C Steel		0.3 Mo		CMV		T22		T9		T91	
Wt%	Min	Max	Min	Max	Min	Max	Min	Max	Min	Max	Min	Max
C		0.25		0.20	0.10	0.18		0.18		0.15	0.08	0.12
Si		0.35	0.10	0.40	0.15	0.40		0.50	0.25	1.00	0.20	0.50
Mn	0.40	1.40	0.40	0.80	0.40	0.70		0.80	0.30	0.60	0.30	0.60
P		0.045		0.040		0.040		0.040		0.030		0.020
S					0.30	0.60	2.00	2.50	8.00	10.00	8.00	9.50
Cr			0.25	0.35	0.50	0.70	0.90	1.20	0.90	1.10	0.85	1.05
Mo								0.30				0.40
Ni											0.030	0.070
Nb											0.06	0.10
V					0.22	0.28					0.18	0.25
Al				0.012		0.020		0.020		0.020		0.03
Cu								0.30				
Sn								0.030				
Norm(^{0}C)			880	960	930	990	900	980	850	950	1040	1090
Temper			600	650	640	720	630	720			730	790

Table 2.1 Composition ranges and standard heat treatments of the common boiler materials

2.5.1 Precipitate Stability (Ostwald Ripening)

Although at long service times various microstructural degradation effects take place such as the reduction in dislocation density and the growth of the sub grain boundaries, the primary change, which triggers many of the others, is precipitate coarsening. Ostwald ripening is the mechanism by which the precipitates coarsen, this involves the growth of large particles at the expense of the small particles that are taken into solution. The solute from the small particle is transferred by diffusion through the solvent, where it re-deposits on the large particle. By this method the free energy is reduced by reducing the surface area and therefore the surface energy.

Particle coarsening is controlled by the diffusion rate (D), the particle size(r), the solubility of the relevant atom species in the matrix in equilibrium with the particle (M), the particle molar volume (V) and the surface energy of the particle matrix

interface (σ). The relationship between these factors is described by the Wagner (1961) equation:

$$r^3 - r_o^3 = \frac{8\sigma D[M]V}{9RT} \cdot t$$

(2.1)

The most important factor is M, the solubility of the relevant atom species in the matrix in equilibrium with the particle, because this controls the flux of solute from the dissolving particles to the growing particles during particle coarsening. The lower the solubility, the more resistant will the particle be to coarsening.

In the absence of well founded solubility data the enthalpy of formation can be used as a guide to the stability and thus to the solubility of various carbides and nitrides. (The stability increases as the enthalpy of formation decreases.) Data from Honeycombe (1981) is given in Table 2.2:

PHASE	APPROX. ENTHALPY OF FORMATION (KJmol^{-1})
Fe$_3$C (M$_3$C)	-10
Cr$_7$C$_3$ (M$_7$C$_3$)	-20
Cr$_{23}$C$_6$ (M$_{23}$C$_6$)	-25
Mo$_2$C (M$_2$X)	-30
W$_2$C (M$_2$X)	-35
Cr$_2$N (M$_2$X)	-40
VC (MX)	-55
NbC (MX)	-70
TiC (MX)	-95
NbN (MX)	-110
VN (MX)	-125
TiN (MX)	-170

Table 2.2 Approximate enthalpy of formation data, after Honeycombe (1981)

These values are approximate as other elements in a phase can alter the stability and solubility. From the above, increased resistance to particle coarsening will be shown by carbides and nitrides containing Cr, Mo, W, Nb, V and Ti. Table 2.2 explains much of the development in ferritic / martensitic steels because the above

order, up to vanadium nitride more or less defines the chronological sequence in which alloying elements have been introduced to the steels to increase their high temperature strength by increasing the particle stability.

The objective of this research work is to investigate the possibilities of commercially producing an alloy using the precipitate most resistant to particle coarsening namely titanium nitride.

2.6   VANADIUM NITRIDE VERSUS TITANIUM NITRIDE

In order to determine the benefit gained in moving to titanium nitride strengthening a direct comparison between the vanadium nitride and titanium nitride has been performed.   Titanium nitride and vanadium nitride are both isomorphic having a rocksalt structure (B1 NaCl Fm3m) and similar lattice parameters (0.4233nm and 0.4118nm for titanium nitride and vanadium nitride respectively) according to Smithells (1998).

From the review by Gladman (1997), the temperature dependence of the solubility products for vanadium nitride in the austenite phase and titanium nitride in the liquid and austenite phase is shown in Figure 2.4. In both cases the solubility levels were determined by Narita (1975). Other determinations of the relevant solubility are available, but, whilst the values do vary, in all cases there is a significant decrease in the solubility of the titanium nitride with respect to the vanadium nitride.
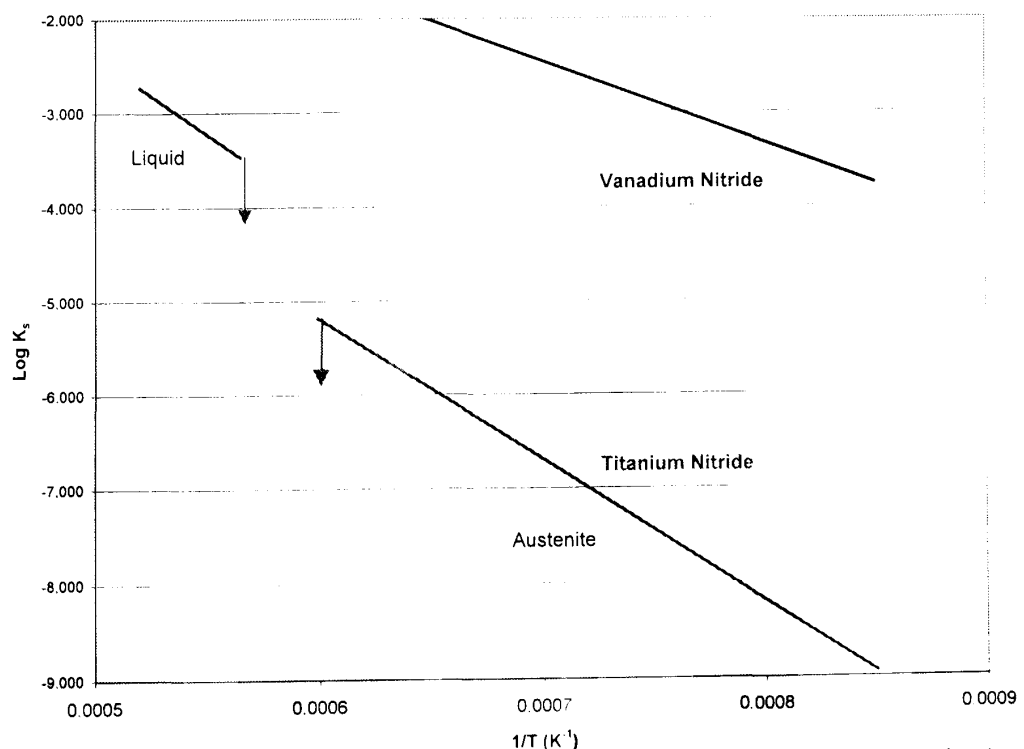
Figure 2.4 Temperature dependence of the solubility products of vanadium nitride and titanium nitride

16

The gap in the data for the solubility of titanium nitride between the liquid and austenite represents the δ-ferrite range for which there is no data available. The solubility relationships for the liquid and austenite phases developed by Narita (1975) are given in Table 2.3.

Logarithm of Solubility Product		
	Liquid	Austenite
VN	-	$-\dfrac{8700}{T} + 3.63$
TiN	$-\dfrac{16586}{T} + 5.90$	$-\dfrac{15020}{T} + 3.82$

Table 2.3 Solubility relationships for vanadium nitride and titanium nitride derived by Narita (1975)

Using the solubility relationships for the austenitic phase, particle coarsening curves were calculated by means of Equation 2.1 and the data presented in Table 2.4 for titanium nitride and vanadium nitride.

	VN	TiN	Reference
Molecular Mass	65	62	Smithells
Lattice Parameter (nm)	0.4118	0.4233	"
Molecules/Unit Cell	4	4	"
Density (Mgm^{-3})	6.18	5.42	
Molar Volume m^3	10.52×10^{-6}	11.44×10^{-6}	
Solubility at 900°C	1.63×10^{-4}	1.04×10^{-9}	Narita
	V	Ti	
Diffusion			
A (m^{2}s^{-1})	2.5×10^{-5}	1.5×10^{-5}	Smithells
Q (KJmol^{-1})	264.2	251.2	"
At 900°C	4.29×10^{-17}	9.76×10^{-17}	
Surface Energy			
σ (Jm^{-2})	0.8	0.8	Gladman

Table 2.4 : Data for calculation of particle coarsening rates in the austenite phase

The comparison of the particle coarsening rates of vanadium and titanium nitrides is shown in Figure 2.5. As can be observed vanadium nitride shows a much more rapid rate of coarsening than is shown with titanium nitride. The origin of this difference in the coarsening characteristic can clearly be found in Table 2.5 where, although the diffusion coefficient D is greater for titanium nitride than for vanadium nitride and thus would contribute to a more rapid titanium nitride coarsening rate, this is not the controlling factor. As described above, the major factor controlling the relative coarsening rates of the two nitrides is the solute concentration M. The soluble titanium is approximately 100,000 times less than vanadium resulting in the coarsening rate of the titanium nitride particles being significantly less than the most stable precipitate utilised as a strengthening mechanism in advanced conventional ferritic/martensitic steels.
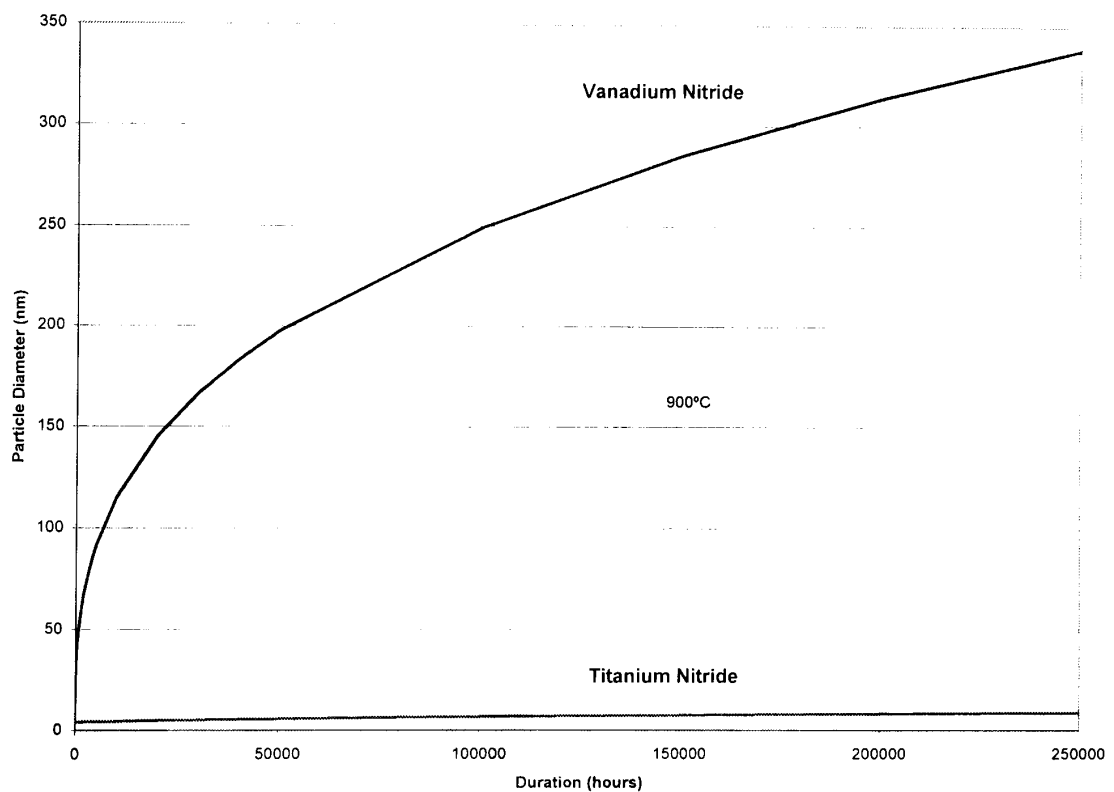
Figure 2.5 Comparison of the calculated particle coarsening rates of vanadium and titanium nitrides at 900°C

Although there are no solubility data available for titanium nitride or vanadium nitride in a ferritic matrix, an indication of their solubility can be obtained by comparing the solubility data of vanadium nitride and titanium nitride with niobium nitride, niobium carbide, titanium carbide and vanadium carbide for which there is data available for solubility in ferrite. The comparison is shown in Figure 2.6.
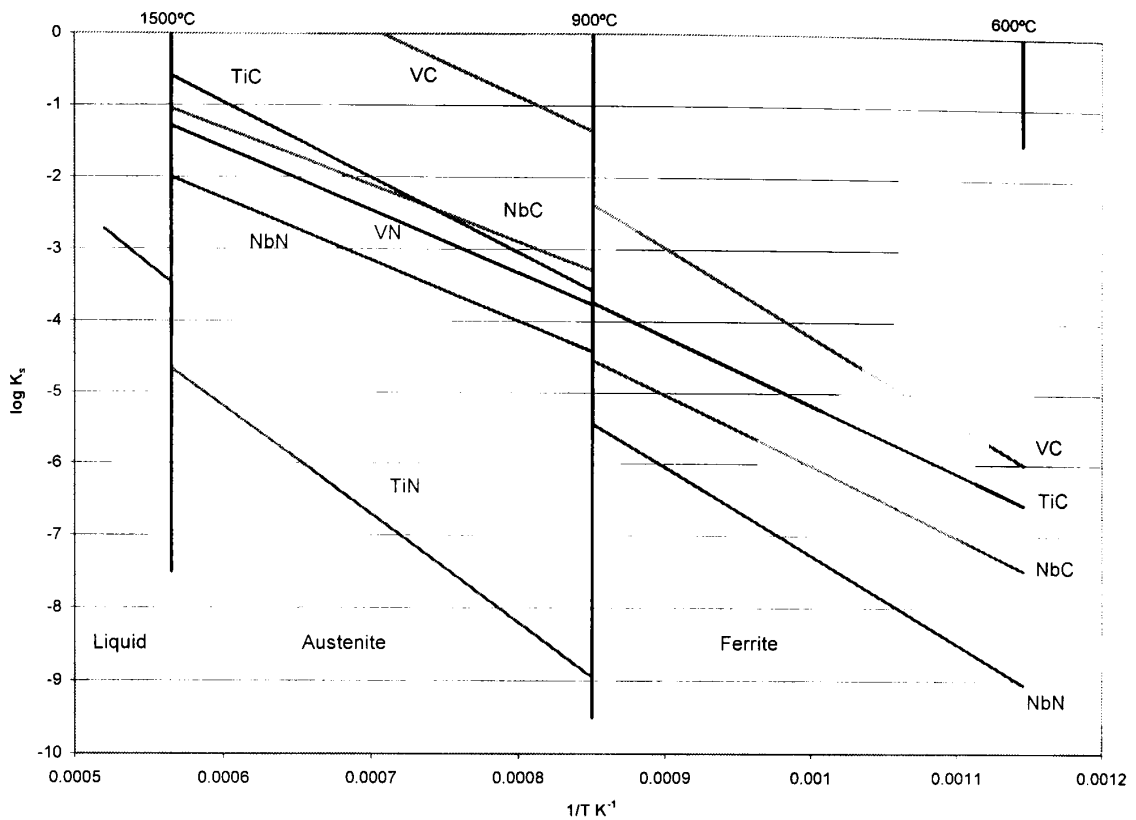
Figure 2.6 Comparison of microalloy solubilities after Gladman (1997)

Although there is more "free" space in the BCC lattice than the FCC lattice, the larger number of possible interstitial positions results in the space per interstitial being less. Thus, in all cases there is a step decrease in the solubility upon the transformation from austenite to ferrite. The data suggest that the solubilities of these compounds are around an order of magnitude less in ferrite than the corresponding solubilities in austenite at the same temperature. The exception to this is titanium carbide where the decrease is less.

Applying this factor to the data in Table 2.3 and utilising the ferritic diffusion rates could give an estimate of the relative coarsening rates of the two nitrides in the ferritic matrix. This would again show the titanium nitride precipitates to be significantly more stable than the vanadium nitride precipitates.

Although titanium nitride precipitates have the greatest stability of the compounds discussed and, therefore, have potentially the greatest increase in long term high temperature creep behaviour, in fact, titanium nitride does not play a major role in high strength ferritic steel. This is due to the same properties that give the titanium nitride its high stability, namely its thermodynamic stability and low solubility. The very low solubility actually limits the amount of titanium nitride precipitates that can

contribute to the strength of the alloy. For example a low nitrogen steel containing 0.018wt% nitrogen and 0.037wt% titanium, if it is assumed that the liquid solidified directly as austenite then using the Narita (1975) data, the proportions of titanium nitride precipitated in the liquid, during solidification and in the solid state is shown in Figure 2.7. The titanium nitride precipitated in the liquid state is given by A-B, B-C is the precipitation that occurs during solidification and C-D is the solid state precipitation. This figure demonstrates that for this composition any titanium level above 0.024wt% will result in precipitation of titanium nitride in the liquid at $1500^{\circ}C$. The significance of this is that precipitation of titanium nitride in the liquid state results in titanium nitride cuboids with edge lengths of up to 5μm (Figure 2.8). Precipitates of this magnitude do not contribute to the strength of the alloy by inhibiting dislocation movement. Moreover, due to the titanium nitride thermodynamic stability these coarse precipitates cannot re-precipitate as in conventional normalising and tempering operations and are thus regarded as redundant titanium nitride. The titanium nitride particles precipitated during solidification are smaller; however, the smallest particles required to strengthen the alloy are precipitated in the solid state. For this composition any titanium above 0.003wt% is not contributing effectively to precipitate strengthening.

The temperature dependence of the solubility is greatest at the stoichiometric ratio, however, even then any titanium above 0.009wt% will not result in precipitation in the solid. Hence, for conventional steelmaking practices, strength improvements from titanium is limited to microalloy additions, thus, with the conventional production route it is not possible to significantly strengthen a material principally by titanium nitride precipitates.

2.7 OBJECTIVE OF STUDY

The objectives of the research work described in this thesis are:

- to develop the processing route necessary to obtain a creep resistant ferritic steel strengthened primarily by titanium nitride precipitates,

- to determine its mechanical properties and

- to assess its suitability for advanced steam power plant components such as tubes, pipes and headers.
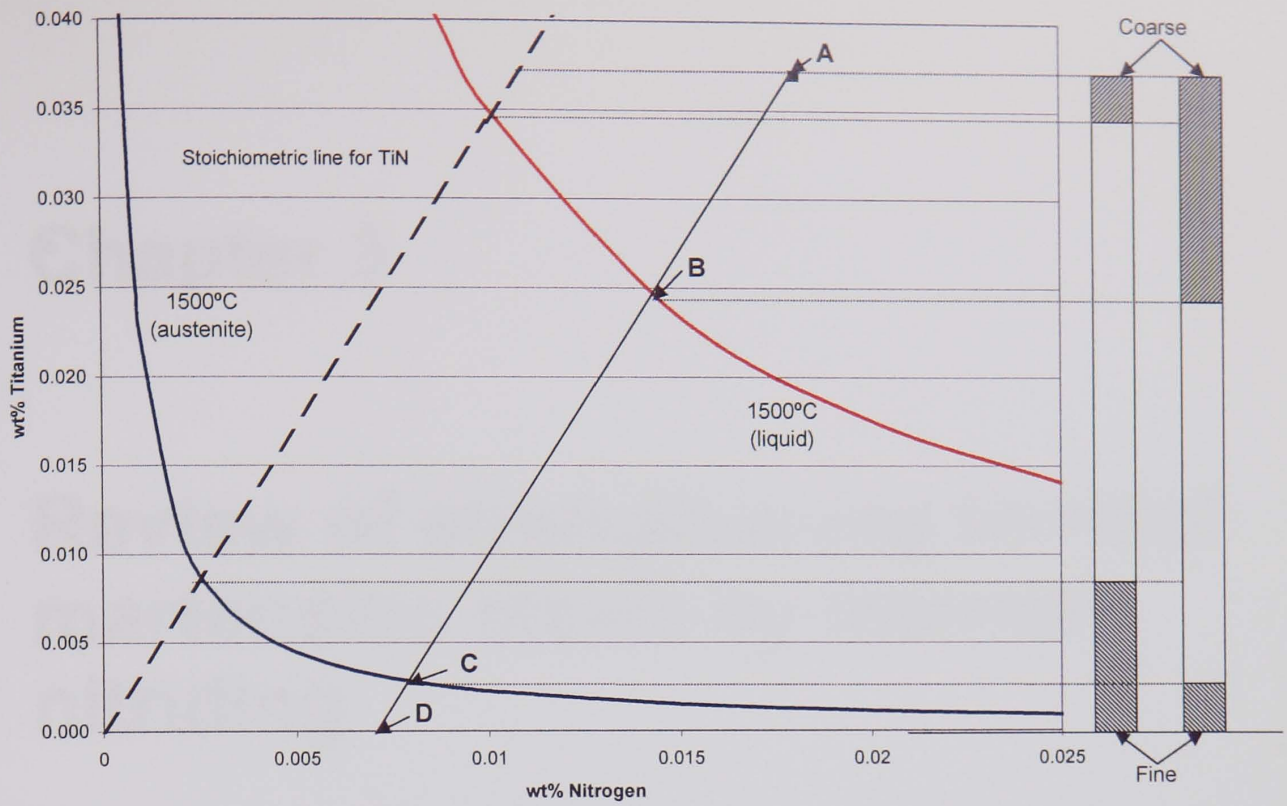
Figure 2.7 Solubility diagram for titanium nitride showing the effects of titanium and nitrogen contents on precipitation size.
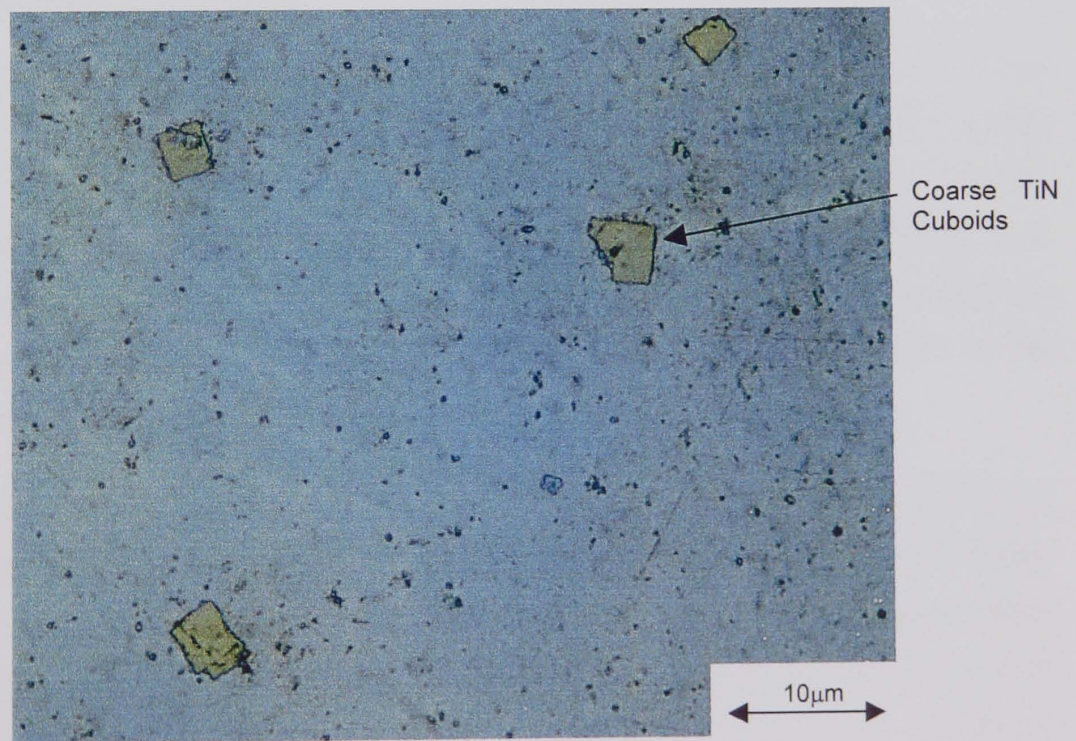
Figure 2.8 Coarse titanium nitride particles resulting from precipitation in the liquid state

Chapter 3

Review of strengthening ferritic/ martensitic steels by internal nitriding

3.1   INTERNAL NITRIDING

In order to overcome the fine precipitate limits and thus the strengthening limits imposed by the very low solubility of titanium nitride, the process of internal nitriding was utilised.   The strengthening of metal alloys through the formation of titanium nitride or other stable nitride precipitates by a process of internal nitriding is a derivation of the process of internal oxidation.   Internal oxidation is the process by which oxygen diffuses into an alloy and causes sub surface precipitation of the oxides of one or more alloying elements.

The basic theory of internal oxidation has been substantially reviewed by Birks and Meier (1983).   The present section is limited to an overview of the main concepts before specific aspects applicable to titanium nitride dispersion strengthened alloys and donor technology is explored in more detail.   The overview is given in terms of the process of internal oxidation, however the basic principles apply equally to internal nitriding.

Birks and Meier have summarised the necessary conditions for internal oxidation as:

I.   The soluble metal oxide must have a more negative free energy of formation than the parent metal oxide.

II. The solubility and diffusivity of oxygen in the base metal must be sufficient to ensure that the activity of oxygen at the reaction front is sufficient for the solute metal oxide for form there.

III. There is a maximum solute concentration for which internal oxidation will occur. If the solute concentration exceeds this value, external oxidation occurs, i.e. the solute metal oxide forms at the parent metal surface rather than internally.

IV. Dissolution of oxygen into the alloy must not be prevented by any surface layer.

3.2   GAS NITRIDING OF FERRITIC/ MARTENSITIC STEELS

This section reviews the work previously undertaken to produce stronger ferritic and martensitic steels through precipitation hardening by internal nitriding from a gas. Work has been undertaken concerning the development of a more creep resisting ferritic steel, particularly for fast reactor cladding using precipitation strengthening from nitrides (principally titanium nitride) by gas nitriding. A variety of alloy compositions and nitriding and degassing treatments have been applied and a correspondingly wide variety of microstructures, including a diversity of precipitate distributions, morphologies and chemistries have been observed.

In comparison to the extent of work expended on austenitic steels by using this strengthening mechanism, there is relatively little information available on nitriding ferritic stainless steels containing strong nitride formers. Notable work has, however, been conducted by Kindlimann (1984), Rickerby & Hendry (1986), Laing (1989), and Wilson (1989a&b). The various findings are described and discussed, and the microstructures and properties correlated with the compositional and processing variables.

3.2.1. Nitriding Treatment

Nitriding treatments applied to the ferritic steels essentially fall into two categories:

(a) Nitriding at elevated temperatures in a nitrogen/hydrogen mixture, typically 1000-1050°C.

(b) Nitriding at intermediate temperature in ammonia. Temperatures are generally relatively low (typically 550°C) although substantially higher temperatures (up to 980°C) were used by Kindlimann (1984).

3.2.1.1 Ammonia Nitriding versus Nitrogen Nitriding

A metal surface exposed to nitrogen gas will dissolve nitrogen into interstitial solid solution according to the reaction

$$\tfrac{1}{2}N_2(g) = \underline{N} \tag{3.1}$$

Where $\underline{N}$ represents interstitial nitrogen. At equilibrium the activity of nitrogen in solution will be given by

$$a_N = k'pN_2^{\frac{1}{2}} \tag{3.2}$$

where k' is a temperature dependant equilibrium constant. For molecular nitrogen, this equilibrium constant is relatively small and it is only at elevated temperatures (e.g. >1000°C), that significant nitriding will occur, Lai (1990). Dissolution of nitrogen by direct dissociation of ammonia onto a steel surface, however, is much greater. The equilibrium constant k" for the reaction

$$NH_3(g) = \frac{3}{2}H_2(g) + \underline{N} \tag{3.3}$$

$$a_N = k'' \frac{pNH_3}{pH_2^{3/2}} \tag{3.4}$$

is much greater at a given temperature than k', Jack (1973). Thus, much higher pressures of molecular nitrogen are required to give the same activity of nitrogen in solution as that achieved in an ammonia-containing mixture at atmospheric pressure. However, ammonia will dissociate into molecular nitrogen and hydrogen (away from the metal surface) at elevated temperatures so its application is limited

to relatively low temperatures (up to 600°C typically). When the dissociation occurs, it is not the dissociation pressure of the ammonia but the pressure of the molecular nitrogen in the gas that applies.

To maximise the absorption of atomic nitrogen at the metal surface, it is necessary to ensure a good supply of uncracked ammonia using high flow rates as well as a low nitriding temperature, Lai (1990). Higher nitriding temperatures require higher gas flow rates as ammonia dissociation can also occur on furnace furniture Kindlimann (1984). Kindlimann has performed ammonia nitriding of ferritic steels at temperatures up to about 1000°C (1800°F), employing high gas flow rates.

In ammonia nitriding, mixtures of ammonia/hydrogen mixtures are generally used as a means to control the nitrogen activity. When using molecular nitrogen for nitriding, mixtures containing a small amount of hydrogen are generally employed to ensure that the atmosphere is reducing, thus preventing oxidation of the metal surface. Kindlimann notes that a non-oxidising gas mixture is necessary because oxygen tends to interfere with the absorption of nitrogen into the surface.

3.2.2 Nitrogen Nitriding at Elevated Temperatures

Wilson (1989a) nitrided titanium containing variants of the 12%Cr ferritic/martensitic steels FV448 and FI (compositions given in Table 3.1) in a 95%N_2:5%H_2 gas mixture at temperatures in the range 1100-1150°C. The samples were degassed in pure hydrogen at the same temperatures. The titanium nitride dispersions formed were found to be coarse (several microns) and consequently did not contribute a significant strength increment to the steels.

Desig-nation	C	Si	Cr	Mo	Ni	Nb	Mn	Ti	V	References
FV448:Ti	0.09	0.49	10.83	0.60	0.64	0.37	0.81	0.89	0.32	Wilson (1989a)
FI: Ti	0.014	0.36	12.46	0.02	0.02	-	0.69	1.41	0.03	Wilson (1989a)
6137	0.005	0.41	9.10	0.60	2.51	-	0.77	1.96	-	Laing (1989)
6138	0.018	0.43	9.10	0.57	1.02	-	0.77	1.45	-	Laing (1989)
Alloy 3	0.012	0.57	11.25	-	0.13	-	0.58	1.78	-	Kindlimann (1984)
Alloy 5	0.013	0.3	17.8	2.11	0.04	-	0.48	1.21	-	Kindlimann (1984)

Table 3.1 : Compositions of alloys studied by gas-phase nitriding

The morphologies of the titanium nitride precipitates were different in the two steels. In FV448, they were predominantly cruciform, with some rod or plate like particles also present. The nitrided FI steel exhibited acicular titanium nitride precipitates, several microns in length, aligned along specific matrix crystal directions in a Widmanstätten pattern. There was evidence of "banding" in the distribution of the titanium nitride precipitates in FV448 and, to a lesser extent, in FI. The origin of this was not determined.

Wilson found similar matrix structures in the two steels. The core and inner nitrided regions were ferritic while the near surface nitrided regions were martensitic. It was deduced that the steels were ferritic at the nitriding temperatures prior to nitriding and that the titanium nitride precipitates nucleated in ferrite. The presence of martensite, however, indicated a transformation to austenite. Wilson postulated that the increasing nitrogen concentration towards the sample surface away from the nitriding front reached a level sufficient to stabilise the austenite phase (Figure 3.1). Thus, a secondary front at which the matrix transformed from ferrite to austenite, followed the primary front.
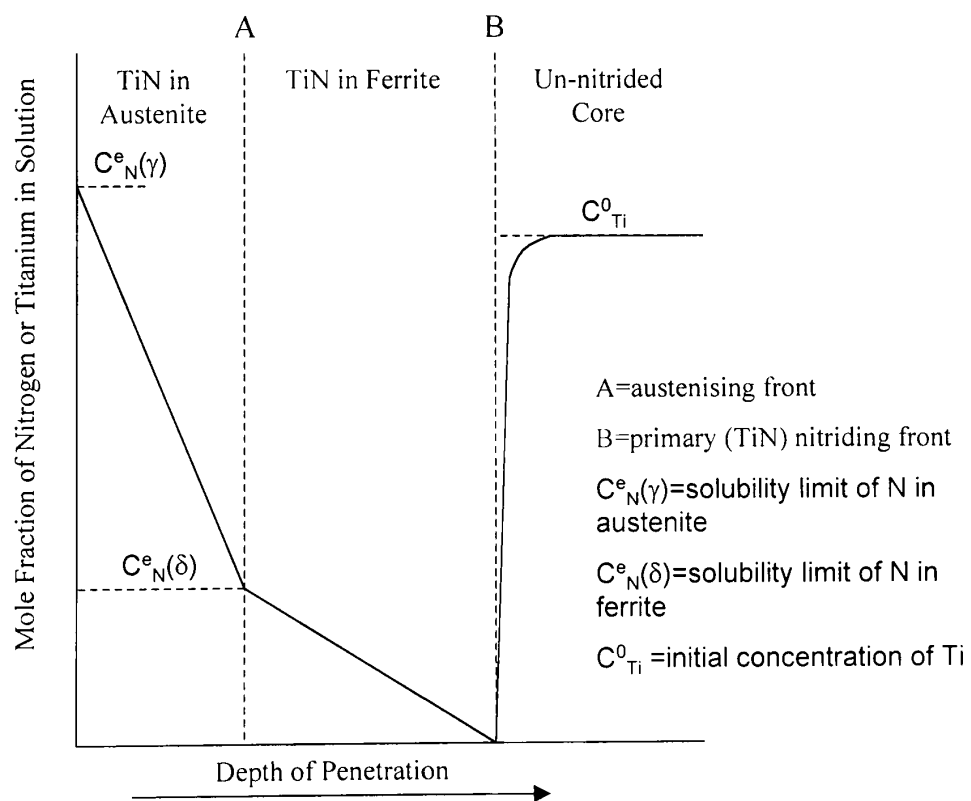
Figure 3.1 Schematic diagram illustrating the transformation to austenite behind the primary nitriding front

Owing to the higher solubility of nitrogen in austenite compared to ferrite, the nitrogen profile in the transformed austenitic region would be steeper than in the ferritic region.

The size of the titanium nitride precipitates formed were considerably larger than achieved in comparable work on 20:25 austenitic stainless steel. Ultimately, the relative coarseness of the titanium nitride dispersion formed in the steels was attributed to the effect of precipitation in a ferritic matrix and attention was focused on determining an alloy composition that would enable the steel to be austenitic at the nitriding temperature (1100-1150°C in this case), to ensure a fine titanium nitride dispersion, yet ferritic at operating temperatures. To counter the ferrite stabilising influence of the titanium, nickel was added. However, only limited nickel additions could be made without stabilising austenite down to the service temperatures. To further reduce stability of the ferrite phase, the chromium content was lowered to about 9%. This was the minimum thought necessary to maintain adequate corrosion resistance. Phase stability calculations yielded compositions 6137 and 6138 given in Table 3.1. Other than the specific changes noted above, the compositions are similar to FV448 and FI.

Wilson & Laing (1990) carried out the nitriding trials in nitrogen: hydrogen gas mixtures at 930-1050°C. This temperature range was lower than that of Wilson (1989a) on FV448 and FI. The alloys examined were duplex in their starting condition in that they contained a few volume % retained austenite in a predominantly delta ferrite matrix.

The nitrided case in alloy 6137 was found to contain mainly coarse, rod, plate or lath titanium nitride precipitates (approximately 35 x 200nm) in a martensitic matrix. A small amount of cruciform titanium nitride was also found to be present. No relationship was found between the orientations of the precipitates and the martensite laths. The un-nitrided core was ferritic.

In contrast, the nitrided case in alloy 6138 was ferritic and the dispersion of titanium nitride particles was found to comprise cruciform, intergranular precipitates (which were relatively fine). The precipitates exhibited preferred growth along <100> directions of the ferrite matrix, as well as precipitates formed on grain boundaries and stacking faults. The boundary between the nitrided case and the core was distinct. The grain structure was equiaxed in both regions and there was no

27

discontinuity in grain structure across the boundary. The average precipitate size was found to vary with the nitriding conditions (temperature and nitrogen partial pressure) as indicated by Table 3.2 from the work by Laing (1989).

Temperature °C	Proportion of N_2 in N_2:H_2 Mixture %	TiN Precipitate Size nm
1050	25	230
1000	25	160
950	9	90

Table 3.2 Variation in titanium nitride precipitate size with high temperature nitriding conditions after Laing (1989)

Laing proposed that the rod-like titanium nitride morphology in alloy 6137 indicated precipitation in a ferritic matrix. It was suggested that the removal of titanium from solution through the precipitation of titanium nitride, and the subsequent introduction of nitrogen into solution caused the matrix to transform to austenite. On cooling, this nitrogen-bearing austenite matrix then underwent a martensitic transformation. The process of titanium nitride precipitation followed by the matrix transforming to austenite is similar to that proposed by Wilson (1989a) in relation to high temperature nitriding of FV448 and FI.

In contrast, Laing found no evidence for any matrix transformation in the nitrided case of alloy 6138 during cooling from the nitriding temperature. This was taken to indicate a predominantly ferritic matrix at completion of the nitriding stage.

It was concluded that the apparently ready transformation to austenite in alloy 6137 during the nitriding process indicated that it was closer than alloy 6138 to the desired composition, i.e. a composition giving a fully austenitic structure at the nitriding temperature prior to the precipitation of titanium nitride.

3.2.3 Nitriding at Intermediate Temperatures using Ammonia

Kindlimann (1984) investigated the ammonia nitriding of cold worked, thin gauge strip (100-250μm) of a series of alloys containing 10-19%Cr. Typical examples of the compositions studied are given in Table 1 (Alloy 3 and Alloy 5). Alloy 5 is based

on the conventional 400 series ferritic stainless steel grades such as 409 and 439, both of which are titanium stabilised.

The temperature window within which nitriding produced an improvement in properties, i.e. a suitably fine dispersion of titanium nitride particles were precipitated, was 1500-1800°F (816-982°C). At nitriding temperatures above 1800°F (982°C) the particles became plate-like and were coarser than had been found for austenitic steels. This was attributed to the faster diffusion of titanium in ferritic steels. Nitriding at temperatures below 1400°F (760°C) resulted in heavy intergranular precipitation. The nitrided alloys were given a de-nitriding treatment in flowing hydrogen at 1100°C for 3 hours to remove the massive embrittling chromium nitrides that had formed during the nitriding stage.

Kindlimann measured significant improvements in tensile properties at 1000°F (538°C) and the time to 1% creep strain at 1400°F (760°C) in the nitrided alloys with respect to a standard type 409 alloy. In addition to the high temperature nitriding work, Laing (1989) also conducted low temperature nitriding at 300-550°C in 10% NH_3 in H_2 on Alloys 6137 and 6138. During the lower temperature ammonia nitriding, both chromium and titanium nitrides are stable. In this case, it is important to ensure that the NH_3: H_2 ratio is sufficiently low that iron nitrides do not form, Laing (1989). Since both chromium and titanium nitrides form, primary and secondary nitriding fronts will be present, Kindlimann & Ansell (1970). Under these conditions of constant activity nitriding the internal nitriding front is shown on Figure 3.2.
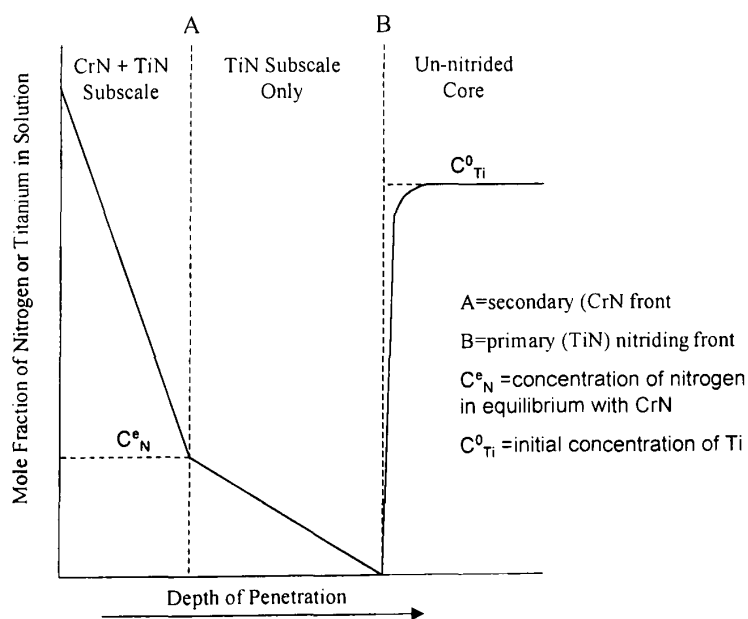
Figure 3.2 Schematic representation of internal nitriding in Fe-Cr-Ni-Ti alloys after Kindlimann & Ansell (1970).

29

To remove the chromium nitrides and excess nitrogen introduced during the ammonia nitriding, nitrided samples were given a reducing or de-gassing treatment, typically comprising an anneal of around 1000°C for 1-5 hours. The precipitate structures in the low temperature nitrided and reduced/de-gassed materials were found to be more complex than the high temperature nitrided material. The final nitride dispersion arose as a combination of three processes:

- A nitride dispersion formed during the low temperature nitriding step.

- Further nitride precipitates then form in the intermediate layer during the elevated temperature reduction treatment due to further nitriding reactions resulting from dissolving chromium nitrides and excess nitrogen already present in solution.

- A further nitride dispersion was attributed to precipitation during transformation of a nitrogen stabilised austenite region on cooling from the reducing temperature. Sheet like and Widmanstätten morphologies were attributed to this type of transformation.

Laing gives little detailed information about the intergranular dispersion but the precipitates appear substantially less than 100nm in size and perhaps only a few tens of nanometers. It was noted that these fine precipitates showed negligible coarsening during the reduction treatment.

3.3 SOLID STATE NITRIDING OF FERRITIC/ MARTENSITIC STEELS

Although some success was achieved in improving the strength due to the precipitation of fine titanium nitride particles, the kinetics of the internal oxidation/nitriding processes described in the previous section result in the dimensions of a component which can be successfully dispersion strengthened, being limited to thin section sheet. This is due to the precipitate dispersion becoming coarser with a consequent reduction in the strengthening capacity as the diffusion distance increases.

Birks & Meier (1983) described this as:

$$r \propto \frac{\nu N_B^0 X}{N_0^s D_o} \qquad (3.5)$$

Effectively the size r of the precipitates depends on the solubility of oxygen/nitrogen (N_o^s) at the source, the concentration (N_B^0) of the dissolved reactive solute, the distance (X) from the oxygen/nitrogen source, the diffusion coefficient of oxygen/nitrogen in the alloy (D_o) and the front velocity v.

This natural limitation on the dimensions of the component that can be strengthened successfully using gas nitriding has led to powder routes for nitrided alloy development. Using powder techniques, the maximum diffusion distance for nitrogen introduced at the powder particle surface is controlled by the powder particle radius. Production of bulk components using powder processing techniques are now well established and model headers (Hunter, 1999) have been produced using conventional advanced ferritic steels.

Wilson (1989b) applied this principal of powder metallurgy nitriding to 20%Cr 25%Ni 1.8%Ti gas atomised powder. The powder was gas nitrided using a fluidised bed furnace. The subsequently extruded bar showed high strength and refined titanium nitride particles compared with the equivalent gas nitrided AGR cladding material. However, problems with operations of a fluidised bed at elevated temperatures (1100-1150°C) resulted in this method of nitriding powders not being adopted for commercial development.

Instead an alternative method was developed in which the titanium containing steel powder is combined with a donor nitride which dissociates at or below the powder consolidation temperature to provide the nitrogen necessary to form the stable titanium nitride particles.

3.3.1 Nitrogen Donor

Jack (1973) first proposed the concept of a nitrogen donor, i.e. the use of a dissociable nitrogen containing compound as a source of nitrogen. Both Fe-Mo and Fe-Ti alloys were nitrided at low temperatures (e.g. 350°C) in NH_3/H_2 mixtures to give a thin layer of iron nitride (Fe_4N) at the surface. When aged under vacuum at higher temperatures (e.g. 580°C) the samples developed a hardness profile penetrating the depth of the sample. Jack proposed that such methods could be used to strengthen sections of unlimited size and similar nitrogen sources could be dispersed initially throughout the material.

Hamerton, Jaeger & Jones (1994a&b, 1995) have pioneered the use of chromium nitride as the solid state source of nitrogen. The composition of chromium nitride also makes it suitable as the chromium added by means of the donor addition is simply accounted for in the bulk chromium content of the titanium containing cast to achieve the final desired composition.

In this approach the titanium containing steel is converted to a powder but it is not nitrided using a gaseous source of nitrogen. Rather the nitrogen is provided by a donor nitride that is less stable than titanium nitride. The chromium nitride powder is mixed with the steel powder and dissolves when heated, releasing the nitrogen to diffuse to the titanium atoms. This is shown schematically in Figure 3.3.

Incorporation of donor in matrix

Nitrogen donor

Ti-containing steel matrix

Donor dissociation

TiN formation
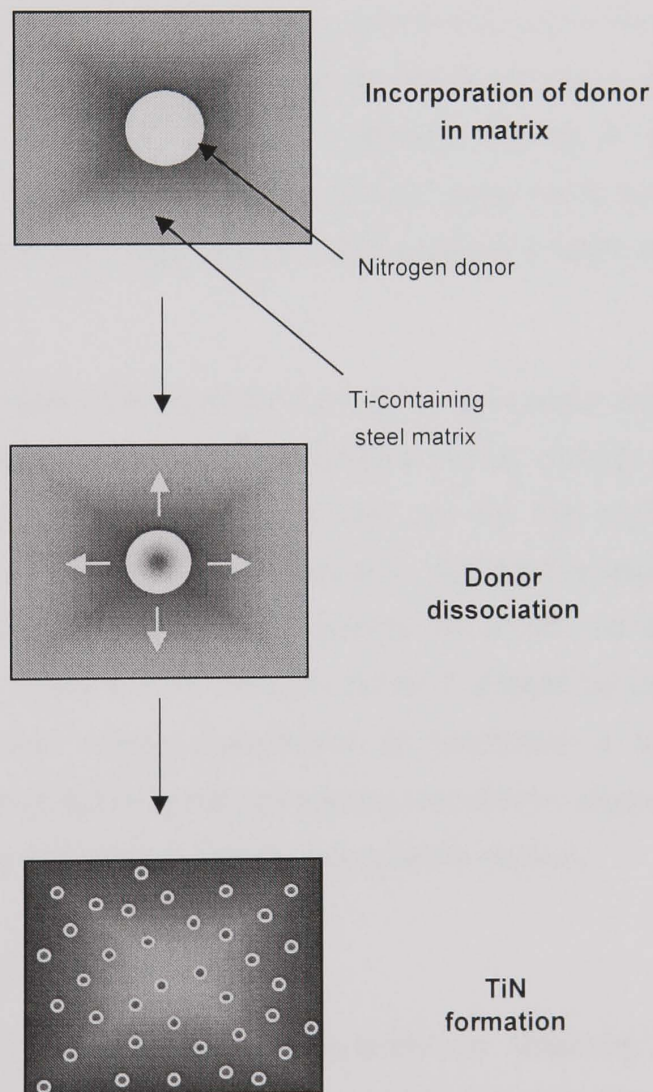
Figure 3.3 Internal nitriding using a solid state nitrogen donor

3.4 COMPARISON OF THE GAS NITRIDING PROCESS WITH POWDER METALLURGICAL DONOR ROUTES

In the powder metallurgical donor routes, dissolving chromium nitride particles act as the source of nitrogen to internally nitride the titanium containing matrix. The activity of nitrogen associated with this source is taken to be the nitrogen activity in solution for equilibrium between chromium nitride and the chromium containing matrix at the temperature and composition in question.

The effect of a high activity chromium nitride source can be seen by comparing the nitride dispersions produced under two different sets of conditions in Laing's work. Firstly, for high temperature nitrogen nitriding and secondly for ammonia nitriding in the intermediate layer produced during the reducing treatment. As previously discussed, the titanium nitride dispersion formed in the intermediate layer arises, at least in part, from a nitriding reaction caused by dissolving chromium nitride particles during the reducing treatment. It was a general finding in Laing's work that, although the microstructures of the intermediate layer were similar, the titanium nitride dispersion was finer. This reflects the high activity when chromium nitride is the nitrogen source.

There is a further similarity between the use of the solid-state nitrogen donor route and gas phase nitriding. For reasons discussed earlier, during ammonia nitriding, the formation of titanium nitride is governed not by the high nitrogen activity produced at the metal surface by the ammonia, but by the equilibrium activity of dissolved nitrogen associated with the internal chromium nitrides formed. The implication is that by using a solid nitrogen donor it should be possible to produce sufficiently fine titanium nitride dispersions to contribute a significant strength increment. This is provided that the processing conditions, especially temperature, under which the nitriding reaction occurs, are suitably chosen.

3.5 SUMMARY OF FINDINGS

To achieve a creep strength increase depends on obtaining a sufficiently fine dispersion of titanium nitride. There are several factors determining the precipitate size. The two that have undergone investigation in this previous work are the phase in which the precipitation reaction takes place and the precipitation temperature.

Regarding the phase in which precipitation takes place, the early development work by Wilson concentrated on trying to design alloys that would be austenitic at the nitriding temperature as earlier trials had revealed coarser titanium nitride precipitate in ferritic material than comparable austenitic material. Wilson attributed this to differences in the nucleation and/or coarsening kinetics for titanium nitride in matrices with the two different structures. It should be noted, however, that the temperatures used during nitriding of FV448 and F1 were relatively high (1100-1150°C). This in itself is likely to yield coarser precipitates. The work of Laing shows that, even though the desired fully austenitic condition was not thought to have been achieved in alloys 6137 or 6138, the results indicated that it is possible to precipitate a fine dispersion of equiaxed or cruciform titanium nitride particles in a ferrite matrix. The largest effect on particle size was found to be the precipitation temperature.

The Kindlimann work relates to the temperature window (approximately 820-900°C) within which nitriding produced a significant strength increment. This finding is consistent with the effect of temperature on titanium nitride precipitate size noted by Laing for high temperature nitrided alloy 6138. The coarse precipitates (>200nm diameter) formed at the upper end of the temperature range investigated (1050°C) would not be expected to contribute a significant strength increment. However, a reduction in nitriding temperature of only 100°C gives a more than two-fold reduction in precipitate size to 90nm. Thus, the nitriding should be performed at relatively low temperatures in order to achieve the desired fine nitride dispersion.

Although the gas phase work shows that nitriding should be performed at relatively low temperatures, in order to achieve the desired fine nitride dispersion in the experimental alloys undergoing solid state nitriding here, consideration will have to be given to the way in which the material is thermo-mechanically processed (TMP) e.g. by extrusion, rolling or hot isostatic pressing. The optimum conditions for the nitriding process and for alloy consolidation may well not coincide, therefore, a compromise set of conditions will have to be found or the processes separated. These issues are considered throughout the thesis.

The main points from this review are therefore:

- Significant improvement in elevated mechanical properties of high chromium ferritic steels can be achieved through precipitation strengthening by internal nitriding.

- The work suggests that precipitation in an austenitic phase is not a requirement to achieve a fine titanium nitride dispersion.

- In order to achieve a fine dispersion of titanium nitride particles, as low a temperature as processing allows should be used.

Chapter 4

Production routes of the research materials

The titanium nitride strengthened ferritic/martensitic steels studied within this thesis were produced in a multi-stage process as shown schematically in Figure 4.1. Firstly suitable feedstock was produced or purchased, the constituent parts of the feedstock were then combined to form the intermediate product which was subsequently consolidated before final heat treatment. During these various processes the reaction to form titanium nitride particles within the steel is accomplished.

Combination of feed stock by Osprey or Mechanofusion processes

Consolidation and heat treatment by extrusion or Hot Isostatic Pressing (HIP)

Feed Stock ⟶ Intermediate ⟶ Product

Ti Containing Steel and chromium nitride powder

Pre-form or Coated powder

Bar or plate
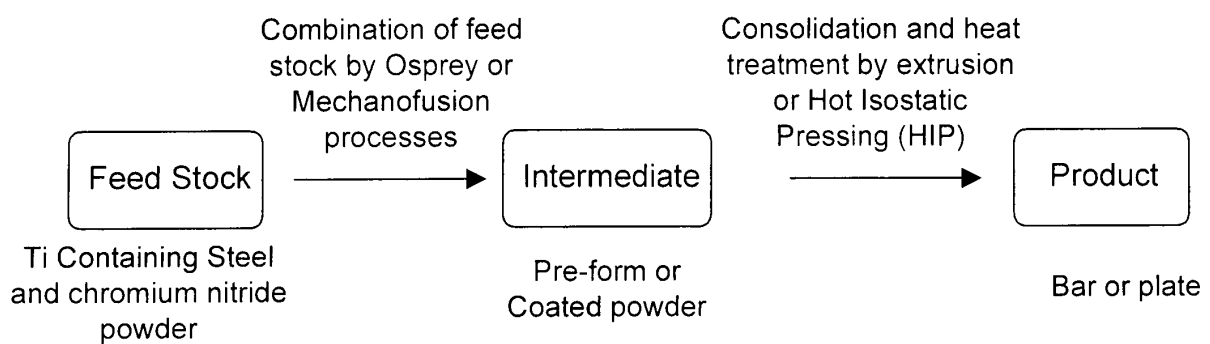
Figure 4.1 Flow diagram showing the production route of the experimental steel.

The main points of the various stages are described in the following sections.

4.1   PROVISION OF FEEDSTOCK

The feedstock consists of two elements, the titanium containing steel and the nitrogen donor material (chromium nitride). The titanium containing steel is not a standard production material and thus is produced specifically for this programme. Due to the requirement of high "free" titanium, i.e. titanium in solution not combined with oxygen, sulphur, carbon or nitrogen, this requires the steel to be produced in a vacuum or under a protective atmosphere. The nitrogen donor, chromium nitride, is a standard production material utilised in the hard metals industry. The chromium nitride powder particle size did, however, require some development as discussed in Chapter 5. An important aspect of the feedstock is to ensure that the combination of the titanium containing steel and the chromium nitride compositions result in the target final composition.

4.2   COMBINATION OF DONOR AND TITANIUM CONTAINING STEEL

The critical aspect of the solid state nitriding production process is the method of combining the nitrogen donor (chromium nitride) with the titanium containing steel in order to subsequently precipitate a fine dispersion of titanium nitride particles. In this research work two promising methods of mixing the constituent parts were identified:

a) The nitrogen donor can be injected into the liquid steel during spray forming (Osprey Process).

b) Hybrid powders can be produced where the nitrogen donor powder is coated onto the surfaces of the titanium containing alloy powder particles (Mechanofusion).

4.2.1 Spray Forming (Osprey Process)

In this technique the titanium containing steel is remelted and gas atomised (by utilising argon gas). These gas atomised droplets are then directed onto the collecting surface. Whilst these droplets are airborne, the chromium nitride powder is injected (through a separate injector) on a collision course with the molten steel spray. As a result of the collisions combined titanium containing steel and the chromium nitride particles form and the reaction to form titanium nitride occurs. This

reaction continues whilst the combined steel and chromium nitride particles are in flight and during their rapid cooling after impact on the pre-form.

Two spray forming units were utilised during this research work. The majority of the work was carried out on Osprey's OS5 research unit, whilst later plate preforms were sprayed on the OS8 semi-production plant.

A schematic diagram of the research plant OS5 is shown in Figure 4.2.
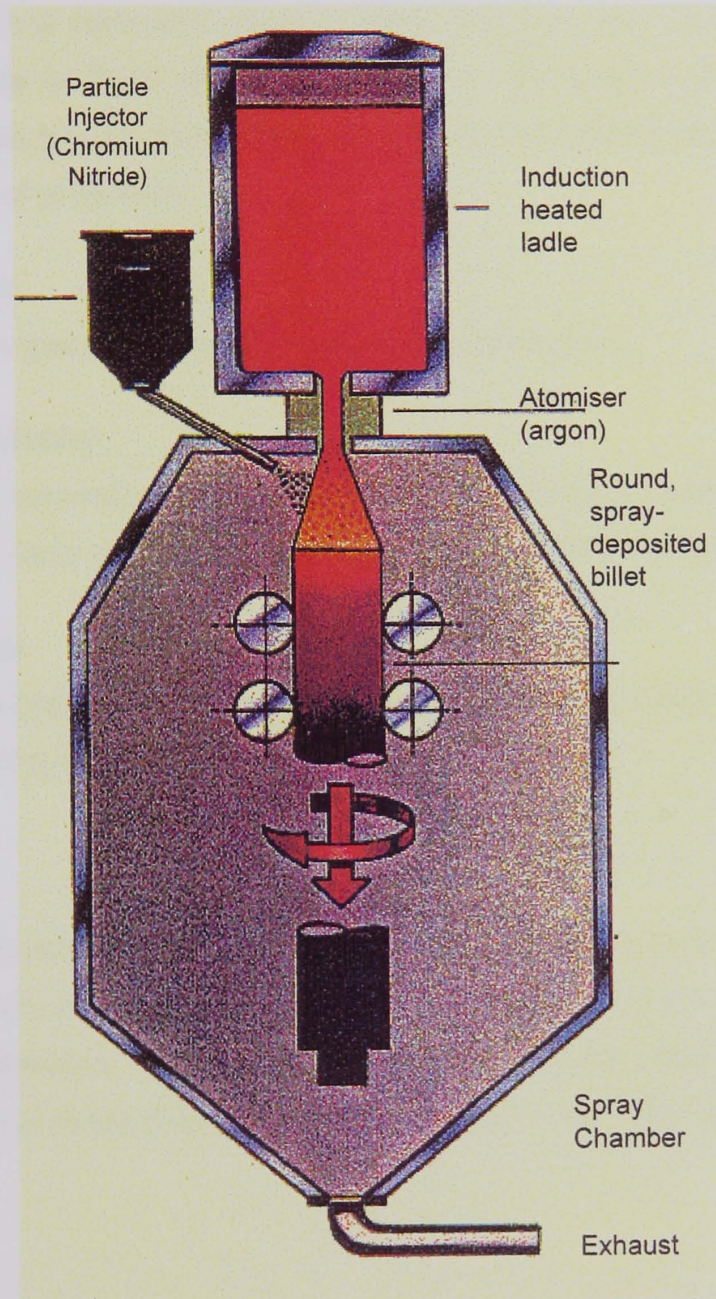
Figure 4.2 Schematic representation of the Osprey OS5 research unit

The plant comprises of the following systems:

Induction Melting/Dispensing System

A maximum 25 kg charge of pre-alloyed material is melted in the induction furnace under an inert atmosphere. The molten metal is dispensed from the base of the crucible via a zirconia nozzle directly into the preform units.

Atomiser

Gas atomising device which provides either argon or nitrogen gas for atomising the molten steel into a controlled spray shape. The gas also extracts heat from the atomised particle in flight and on deposition. The entire induction furnace and atomiser rises as the pre-form builds up in order to maintain powder flight distance for consistency of properties.

Spray Chamber

Within which the gas atomising and deposition takes place.

Preforming Collector

Upon which the sprayed material deposits. The preforming mechanism is pre-programmed to carry out the required movements under the spray.

Injection Device

It is through the injection device that the chromium nitride powder is added to the titanium containing metal spray.

The Osprey process is attractive as it is amenable to the production of large bulk components and could readily be employed to fabricate tube or pipe preforms and offers a cost effective, high volume route. Indeed, the Osprey Process is used commercially to produce stainless and nickel alloy tubing, Leatham (1996).

4.2.2 Powder Forming (Mechanofusion)

This is a mechanical blending technique with the aim of achieving an intimate mixture of the feedstock ingredients. The ingredients are the chromium nitride powder and also the titanium containing steel powder, which has been gas, atomised. The Mechanofusion system consists of a main chamber, which rotates at a speed of 30 ms^{-1} (this equates to approximately 2000 R.P.M.). Inside the chamber is a stator (shown in Figure 4.3a), the head of which is a smaller radius of curvature than of the internal wall of the chamber. The process operates by the powder mixture being compressed in the clearance between the stator head and the chamber wall as shown in Figure 4.3b. The powder mixture receives a combination of shearing, attrition, compression and rolling forces. After the material has passed the head of the stator it is released from the chamber wall by a scraper. The process occurs at room temperature and to minimise contamination of the powders the Mechanofusion process is performed in an argon atmosphere.
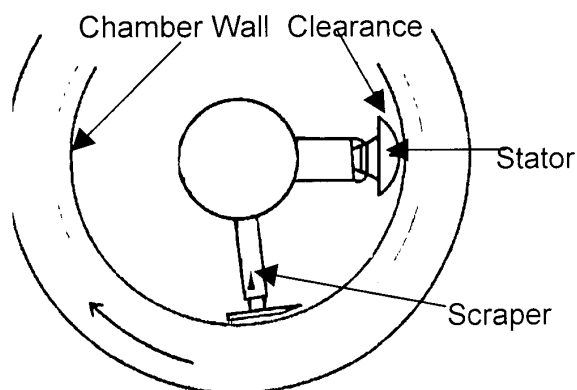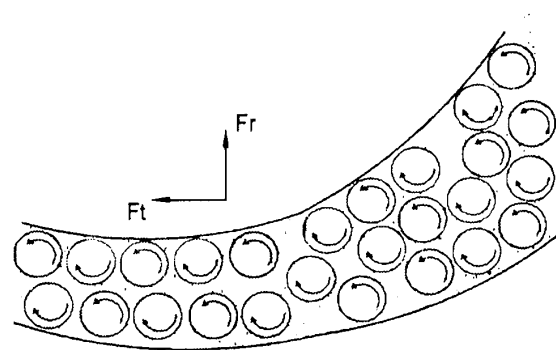
Figure 4.3a   Figure 4.3b

Figure 4.3a&b Schematic of Mechanofusion System

The result of the Mechanofusion process is that the hard chromium nitride particles are imbedded into the surface of the relatively soft titanium containing powder particles. Figure 4.4a shows the gas atomised titanium containing steel prior to Mechanofusion whilst Figure 4.4b shows the end result of the process. No titanium nitride particles are formed during the Mechanofusion process. The reaction to form titanium nitride only occurs as the powder mixture is heated during the consolidation processes of extrusion or hot isostatic pressing.

Steel Powder

50μm
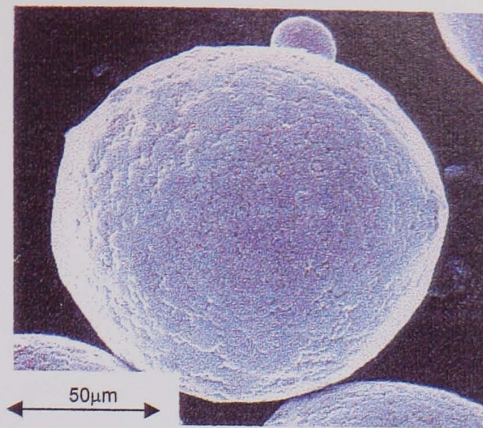
Figure 4.4a

Mechano-Fusion with chromium nitride

Coated Powder

50μm
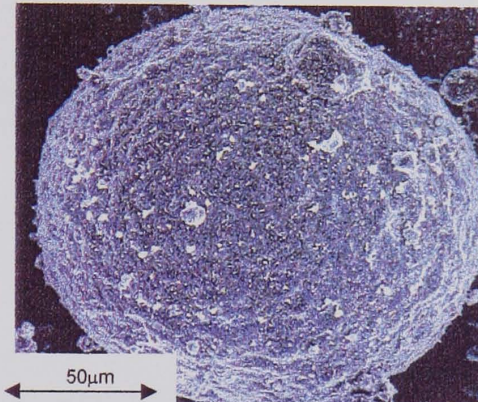
Figure 4.4b

Figure 4.4a&b Titanium containing powder sample before and after Mechanofusion.

4.3 CONSOLIDATION OF POWDER

4.3.1 Hot Isostatic Pressing

Consolidation of the Mechanofusion powder can be performed by Hot Isostatic Pressing (HIPping). HIPping also subsequently proved necessary in order to obtain acceptable densities in the Osprey sprayed material. With hydrostatic pressing the tensile stresses are reduced below their critical value for cracking while at the same time the flow stress is unaffected. The powders were poured into stainless steel cans (the can lids welded into place) and the air was evacuated through an attached tube. The HIP conditions utilised were 1150°C x 4 hours and 2000 barg pressure. The HIP cycle is shown in Figure 4.5. HIP routes could be used to produce near net shape components for high temperature plant, such as header sections which have been produced by this method using conventional alloy powders Hunter (1999).
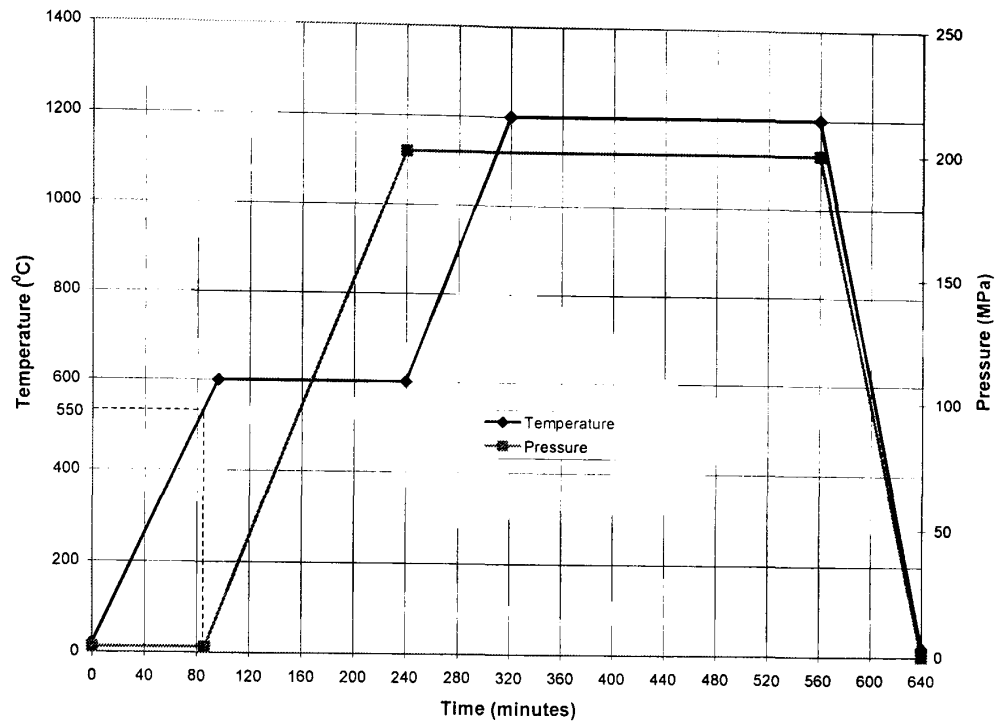
Figure 4.5 Typical HIP Pressure and Temperature Cycle

4.3.2 Extrusion

Extrusion of the canned and sealed powder was performed by direct extrusion. This was initially carried out at a 7:1 extrusion ratio to produce a 19mm diameter bar. Temperatures were varied between 1000 and 1200°C and the speed was set at 30mms^{-1} or 55mms^{-1}. Lubrication during the extrusion process was by fibreglass mat inserted into the die.

4.4   SUMMARY OF PROCESS VARIATIONS

A schematic diagram of the production methods is shown in Figure 4.6. As can be observed in Figure 4.6 there are several alternatives being investigated with this project for the production of the titanium nitride steels. The reason for this range of processes rather than concentrating on one process is because three possible final products are envisaged, namely, tubes, pipes and headers (headers are the collection devices for a bank of tubes; a typical header is shown in Figure 1.8). It is envisaged that the tube components or smaller diameter pipes will be produced either directly by the Osprey process or by a combination of the Osprey process or Mechanofusion process followed by extrusion. For the larger diameter pipes and more complex headers it is envisaged that the production route will be the

Mechanofusion combination of the titanium containing steel and the chromium nitride followed by HIP consolidation.

Feed Stock

Ti Containing Steel | Chromium nitride powder

Atomisation of the Ti containing steel and combination with the chromium nitride powder

Mechanofusion Process

Osprey Process

Combination Process

Mixing

Spraying

Powder Blend

Spray Preform

Consolidation and heat treatment by Extrusion or Hot Isostatic Pressing (HIP)

Product

Bar or plate for experimental purposes
Tube, pipe or header for commercial applications

Figure 4.6 Schematic Diagram Illustrating the Production Options

43

Chapter 5

Material design

5.1　BATCH 1 MATERIALS

Two approaches to developing a material with an appropriate microstructure for long term creep resistance were investigated within this work through the choice of two distinct alloy types. Both alloy types were designed such that the only strengthening precipitate present was titanium nitride. This is in order to determine clearly the influence that this precipitate has on the properties without other nitride, carbide and carbo-nitride precipitates confusing the situation. The effects of different matrix structures are, however, assessed. The first alloy type is a 9%Cr martensitic composition where the intention was to re-produce the tempered martensite sub-grain structure and high dislocation density present in conventional advanced martensitic steels, but replace the precipitated carbides and nitrides with titanium nitride particles. The second approach is to introduce the titanium nitride particles into a higher chromium (18%Cr) non-transformable ferritic steel typical of 430 grade. The alloy design and the philosophy employed for each alloy type is given in the following sections.

5.2　DESIGN CONSIDERATIONS

For each of the alloy types, in designing the alloy composition, due regard needs to be given to the chemical changes that will occur during the high temperature

nitriding reaction. In this nitriding reaction chromium and nitrogen enter solution as the chromium nitride dissolves and titanium and nitrogen are removed from solution as the titanium nitride is precipitated. The relative austenite and ferrite stabilising effects due to this reaction must be assessed in order to obtain the desired structure at the nitriding temperature and the desired final matrix structure.

The main influences in selecting the compositions for the two alloy types were:

I.   The nature of the phase (austenite or ferrite) in which the precipitation of the titanium nitride occurs as this may affect the precipitate size.

II.   The final alloy matrix.

5.3   CHROMIUM NITRIDE

A critical aspect of the design of the materials produced by solid state nitriding using chromium nitride as the donor are the characteristics of the chromium nitride powder used, principally the particle size range and composition.

5.3.1 Chromium Nitride Size

In order to get some indication for the expected diffusion paths of chromium and nitrogen during the thermal treatment, the average diffusion distance $\overline{X}$ was approximated using

$$\overline{X} = \sqrt{Dt} \qquad\qquad (5.1)$$

where D is the coefficient of diffusion and t is the diffusion time in seconds, Reed-Hill (1973). The relationships, after Smithells (1998), used for the diffusion coefficients of nitrogen and chromium in α and γ iron are given in Table 5.1. Taking for example, the planned precipitation and consolidation thermal cycle for the HIPping of Mechanofused powder at 1150°C x 4 hours, this would result in the average diffusion distances for the chromium and nitrogen given in Table 5.2.

Element/ Phase	A m^{2}s^{-1}	Q KJ$_{mol}$$^{-1}$	D $\propto$ 600°C m^{2}s^{-1}	D γ 1150°C m^{2}s^{-1}	Reference
N/$\propto$	5 x 10^{-7}	77.0	1.23 x 10^{-11}	-	Smithells
N/γ	9.1 x 10^{-5}	168.6	-	5.91 x 10^{-11}	"
Cr/$\propto$	8.52 x 10^{-4}	250.8	8.39 x 10^{-19}	-	"
Cr/γ	1.08 x 10^{-3}	291.8	-	2.10 x 10^{-16}	"

Table 5.1 : Diffusion data for nitrogen and chromium in ferrite and austenite

Element/ Phase	X HIP Process 1150°C x 4hrs	X Operation 600°C x 250,000 hrs
N/$\propto$	-	1 x 10^5 μm
N/γ	922 μm	-
Cr/$\propto$	-	27 μm
Cr/γ	17 μm	-

Table 5.2 Average diffusion distances for nitrogen and chromium during the HIP production route and operation

From Table 5.2 it is apparent that the high diffusion rate of the nitrogen should result in the saturation of typical gas atomised metal (powder size typically <150 μm). It is evident, however, that the diffusion path of chromium is negligible for the production route. Even considering the entire life of the power station (taken as 250,000 hours) under service conditions (~600°C) the total diffusion distance would only be 44.9μm. Although this estimate does not consider thermodynamic interactions, it illustrates very clearly that a homogeneous distribution of chromium cannot be achieved by the planned heating route. In order to minimise the inhomogenity of the chromium the initial introduction of the chromium must be as homogeneous as possible, thus, the maximum standard chromium nitride particle size of <45 μm was specified.

5.3.2 Chromium Nitride Chemistry

In designing the base alloy, it is essential that the nitrogen content of the chromium nitride powder be assessed. Chromium nitride can exist as CrN or Cr_2N; thus, the nitrogen content can vary from 11.9 wt% to 21.2 wt% depending on the mixture. As a result, in order to achieve the desired nitrogen content, the chromium content can, depending on the chromium nitride supply composition, vary considerably. This affects the base titanium containing feedstock as the total chromium in the alloy is a combination of the chromium content in the feedstock and the chromium added in the chromium nitride.

5.4 MARTENSITIC ALLOYS

It was intended to make use of the inherent strength of the martensitic matrix but to improve the conventional creep resistant martensitic steels by using the titanium nitride particles to stabilise the high dislocation density and sub grain boundaries. The alloy is designed to be fully austenitic at the titanium precipitation temperature (which is between 1050°C and 1200°C (for extrusion and HIP conditions) and fully martensitic upon cooling to room temperature and to maintain the martensitic structure at the operating temperature. Thus, ideally the material should have no delta ferrite present, have a Mf temperature above room temperature and have an A_1 temperature significantly above the maximum predicted operating temperature (650°C).

The reason for this design is so that firstly the titanium nitride precipitation reaction occurs in an austenite matrix, as Wilson (1989a) deduced that this resulted in a finer precipitate size. Secondly, it is essential, in order to achieve the optimum strength, that complete transformation to martensitic occurs, Pickering (1978). To avoid retained austenite and subsequent untempered martensite, the Mf temperature must be above room temperature. Another factor that limits the percentage martensite formed is the delta ferrite content. Kaltenhauser (1971), shows the effect of chromium and nitrogen on the phase stability of ferrite and austenite at temperatures between 800°C and 1400°C in Figure 5.1. As can be observed, if nitrogen is not considered, then exceeding 10%Cr, even at the optimum temperature of 1100°C, would result in delta ferrite being present. Delta ferrite is detrimental as it detracts from the potential strength of the steel. Additionally, as the delta ferrite tends to form as films around the austenite grains this limits the hot

Figure 5.1 Effect of N on austenite and ferrite regions after Kaltenhauser (1971)

ductility and can cause hot forming problems. Consequently, an industrial processing upper limit of 5% delta ferrite has been imposed.

The phase composition is determined by the amount of dissolved alloying element and the temperature. In the absence of the Thermocalc programme, a first approximation of the composition at room temperature can be arrived at by using chromium and nickel equivalent compositions, together with the well known Schaeffer diagram. However, as the alloys being considered here restrict carbon to its minimum possible level and nitrogen is a critical element in the composition and the titanium nitride precipitation, the Schneider (1960) modified Schaeffer diagram was utilised. These diagrams are empirical in nature and were originally developed as a guide to the constitution of castings and are now used extensively in welding.

The chromium and nickel equivalent values used are as follows:

Cr equivalent = Cr + 2Si + 1.5Mo + 5V + 5.5Al + 1.75Nb + 1.5Ti + 0.75W

Ni equivalent = Ni + Co + 0.5Mn + 0.3Cu + 25N + 30C

The amounts of alloying elements are in wt %.

This, however, is not the ideal diagram. Care should be taken in using the indication as to whether the austenite transforms to martensite because the coefficients for the elements for the Cr and Ni equivalents are not the same as those for the effects on the M_s and M_f temperatures. Thus, the composition of the steel must not only control the constitution, but also control the M_s-M_f temperature to above room temperature. Some effects of alloying elements on the M_s temperature specifically with regard to 12%Cr steels are given by Pickering (1978) in Table 5.3.

Element	Change in Ms (°C) per Mass %
C	-474
Mn	-33
Ni	-17
Cr	-17
Mo	-21
W	-11
V	-11
Cu	-10
Nb	-11
Si	-11
Co	+15

Table 5.3 Effect of alloying elements on the Ms temperature after Pickering (1978)

An empirical equation of the Ms temperature has been published by Pickering (1978).

$$Ms(°C) = 550°C - 474C - 33Mn - 17Cr - 17Ni - 11W - 11V - 10Cu - 11Nb - 11Si + 15Co$$

The interesting element Co, which whilst being an austenite former and thus capable of helping balance the composition, actually raises the Ms temperature. It, therefore, can be useful in steels containing large amounts of ferrite formers.

5.4.1 Alloys A and B

The target titanium feedstock composition and the target chromium and nitrogen contents of the final alloy after mixing and dissolution of the chromium nitride are shown in Table 5.4 and 5.5. Alloy A was chosen, as it is similar to the alloys

Alloy	C	Cr	Mo	Mn	Ni	Si	Ti	N
A	<0.02	7.6	0.6	0.8	1.0	0.4	2.0	0
B	<0.02	8.6	1.0	0.6	-	0.5	1.2	0
C	<0.02	15.6	1.0	0.5	-	0.3	2.0	0

Table 5.4 Target titanium containing steel compositions

Alloy	Final Cr	N in TiN	N in Solution	Total N
A	10.8	0.58	0.15	0.73
B	11.0	0.35	0.18	0.53
C	18.0	0.58	0	0.58

Based on chromium nitride 18.5 wt% N.

Table 5.5 Target chromium and nitrogen contents of final alloy

previously studied by gas nitriding as discussed in Chapter 3, while alloy B is similar to the base composition of conventional advanced martensitic steels, the major difference is that alloy A has the addition of 1% Ni. This is to lower the Ac_1 temperature and thus encourage an austenitic matrix at the titanium nitride precipitation temperature. Some effects of alloying elements on the Ac_1 temperature of 12% Cr steels are given by Pickering (1978) in Table 5.5.

Element	Change in Ac_1 °C per wt%
Ni	-30
Mn	-25
Co	-5
Si	+25
Al	+30
Mo	+25
V	+50

Table 5.6 Effect of alloying elements on the Ac_1 temperature, after Pickering (1978)

The start and final phase compositions as indicated by the Schneider diagram are shown in Figure 5.2. The start composition corresponds to the initial titanium containing alloy before the nitrogen has been released from the donor chromium nitride. After heating to the reaction temperature the chromium nitride becomes unstable and dissolves releasing chromium and nitrogen into solution. This is followed by the removal of titanium and nitrogen from solution as the stable precipitate forms, giving the final composition. Also shown in Figure 5.2 is the position of P92, the most advanced conventional martensitic creep resistant steel.
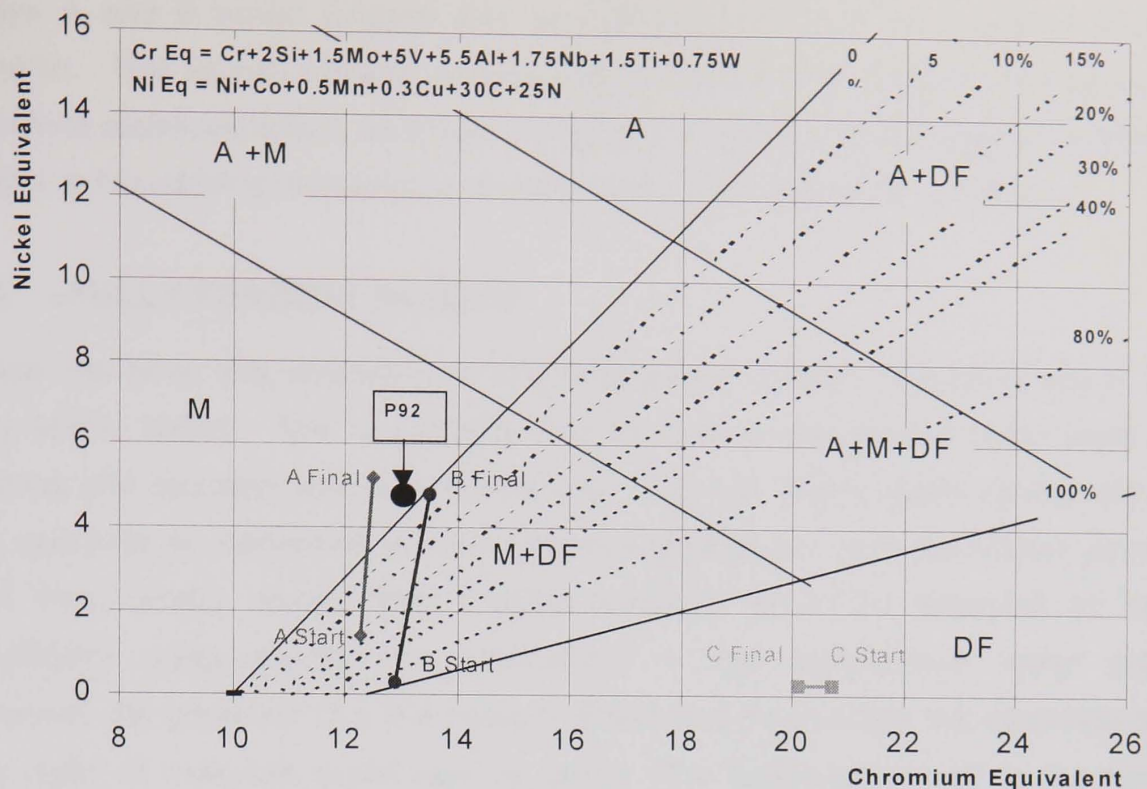
Figure 5.2 *Schneider modified Schaeffler diagram showing the start and final positions of experimental alloys A, B and C and also the position of commercial alloy P92.*

Thus, the alloy A has been designed to be fully martensitic after the precipitation of titanium nitride, whilst it is estimated that Alloy B will contain a minimal amount of δ ferrite. Utilising the data in Table 5.3 but replacing the carbon with the nitrogen content results in a calculated Ms temperature for alloys A and B after the complete precipitation of titanium nitride of 235°C and 232°C respectively.

As can be observed in Table 5.5 both alloys are designed to have excess nitrogen. It appears that there will be approximately 0.2% nitrogen in solution after all of the titanium has been precipitated. However, as it was found previously by Roberts & Evans (1992), the nitrogen level expected for stoichiometric titanium nitride is always exceeded, thus the amount of nitrogen in solution will be less. The apparent excess nitrogen required was revealed by Roberts & Evans to be due to the metallic constituent being increased by other elements, particularly chromium. It was found that although there are variations from particle to particle, the average composition gave ratios in atomic concentration of Ti : Cr : Nb : Si of 100 : 7.5 : 3 : 1.5. The wt% nitrogen uptake in these alloys was found to be around 14% greater than that required for stochiometric titanium nitride. Applying a similar extra uptake to the

alloys A and B would indicate that approximately 0.1% wt% nitrogen is still in solution. This excess nitrogen is designed to broaden the gamma loop due to its austenite stabilising effect, as shown in Figure 5.1, and thus encourage an austenite matrix at the nitriding temperature and ensure that no delta ferrite is formed.

5.5   FULLY FERRITIC ALLOYS

There has been little emphasis on the development of high strength levels in the fully ferritic steels. This is probably due to these steels mainly being used for forming and corrosion resistant applications. The fully ferritic steels cannot rely on the austenite to martensite transformation to develop the high dislocation density and thus, (under normal steel making practice), would be expected to have insufficient creep strength for applications in high temperature power plant. However, the presence of a fine titanium nitride dispersion offers the possibility that this class of materials could also be used. The additional benefit is the better oxidation resistance offered by the high chromium ferritic alloys.

The development of the ferritic alloys is based on the basic Type 430, which has a completely ferritic structure i.e. it is designed to be non-transformable. Since the principal alloying element is chromium, the iron chromium phase diagram in Figure 5.1 describes the metallurgical structures present. It indicates that at the final composition of 18% Cr, the structure would be completely ferritic at all temperatures.

The titanium containing feedstock target composition and final composition are shown in Tables 5.4 and 5.5. Unlike the martensitic variants, the ferritic alloy C is designed to have a stoichiometric nitrogen composition; it is thus designed to have no free nitrogen in solution. This is in order to avoid expanding the gamma loop, resulting in transforming the structure to austenite and subsequently to martensite. The start and finish positions of the ferritic alloy C are shown in the Schneider diagram in Figure 5.2. In order to retain the fully ferritic composition, allowance has to be made for the replacement of the ferrite former titanium in solution by additional chromium, as the precipitation reaction occurs. In addition to stabilising the ferrite phase, the high chromium content material will also possess greater oxidation resistance than the martensitic variants. The important role of oxidation resistance will be discussed in Chapter 10. In this section, the oxidation properties play an important role in the alloy selection criterion for batches 4 & 5.

Chapter 6

Batch 1 Material Production and Assessment

The first batch of titanium nitride strengthened material suffered many production problems. The root cause of the majority of the problems was the chromium nitride powder. However, the initial problems were encountered during the titanium containing feedstock production.

6.1 MELTING TRIALS

Initial melting trials at Osprey to produce the titanium containing feedstock from virgin elements highlighted the problems associated with melting ferrous alloys containing large concentrations of titanium, namely, the high reactivity of this element with the environment and the refractories. In the initial trials under an argon atmosphere, a thick viscous slag formed which led to pouring nozzle blockages. It was therefore necessary to produce the feedstock using vacuum induction melting. Here too, however, some problems were experienced due to titanium reaction with the refractories.

Having sub-contracted VIM production of the alloys A, B, and C, production trials using the Osprey and Mechanofusion routes were initiated.

6.2   PRODUCTION ROUTE

Alloys A, B and C were all produced in the Osprey process whilst alloy B' was produced by Mechanofusion. The entire production route for each material is described in Table 6.1.

Alloy	Combining Route	Product	Chromium Nitride Powder	Atomising Gas	Consolidation Route	Product	Diameter/ Thickness	Deformation Temp. (°C)
A	Osprey	Preform	CRN1	Ar	Extrusion	Bar	17mm	1100
B	Osprey	Preform	CRN2	Ar	Extrusion	Bar	17mm	1150
C	Osprey	Preform	CRN2	Ar	Extrusion	Bar	17mm	1150
B[1]	Mechano fusion	Combined Powder	CRN1	Ar	HIP	Bar	17mm	1150

Table 6.1 Summary of Batch 1 Production Routes

6.3   OSPREY PROCESS

6.3.1   Injection Problems

As discussed in Chapter 5, a critical aspect of production of the steels is the particle size range of the chromium nitride powder. The main market currently for chromium nitride powder is in the hard metals production industry, for which H.C. Stark routinely manufacture powder with a Fisher Sub-Sieve Size (FSSS) of 2-6 μm. It was however found that the standard material contains a wide range of particle sizes with some large particles up to 100 μm. As this size of particle would not fully diffuse into the steel matrix, it was necessary to place an upper limit on the particle size range. The first powder stock used (CRN1) was specified to be 100% < 45 μm. To achieve this size range, it appears that additional milling was used in the production of this batch, which resulted in a high proportion of fines. The particle size distribution analysed by Osprey revealed that 32% of the particles were less than 3μm in size.

The chromium nitride powder (CRN1) was initially used for Alloy A material. The fine particle size was, however, not suited to the Osprey fluidising injector system. The fine powder size was found to not fluidise correctly, and this resulted in the injection of the chromium nitride occurring in a pulsed fashion.

As a result of the chromium nitride powder not being available before the titanium containing steel was ordered, the average nitrogen content (18.5wt% N) given by H C Stark was used in the determination of the titanium containing feedstock chromium content. However, upon chemical analysis, it was determined that the actual nitrogen content was lower, being only 16.5 wt% N. As the nitrogen content is the determining factor, this resulted in excess chromium being added by the chromium nitride powder. The chemical composition of Alloy A is shown in Table 6.2. The accuracy of the chemical analysis for the principal elements was C 0.002wt%, Cr 0.1wt%, Mo 0.02wt%, Mn 0.02wt%, Ni 0.02wt%, Si 0.02wt%, Ti 0.02wt% and N 0.01wt%.

		C	Cr	Mo	Mn	Ni	Si	Ti	Tot N	Nf
Alloy A	Target	<0.02	10.8	0.6	0.8	1.0	0.4	2.0	0.73	0.15
	Actual	0.02	10.6-12.0	0.56	0.66	0.93	0.41	2.0	0.82	0.24
	Difference	---	-0.2-+1.2	---	-0.1	-0.1	---	---	+0.09	+0.09
Alloy B	Target	<0.02	11.0	1.0	0.6	-	0.5	1.2	0.53	0.18
	Actual	0.010	13.4	0.92	0.69	-	0.44	1.23	0.56	0.20
	Difference		+2.4	-0.1	+0.1	-	-0.1	---	---	---
Alloy C	Target	<0.02	18.0	1.0	0.5	-	0.3	2.0	0.58	0
	Actual	0.020	20.0	0.96	0.61	-	0.38	1.72	0.51	0
	Difference	---	+2.0	---	+0.1	-	+0.1	-0.3	-0.07	---
Alloy B'	Target	<0.02	11.0	1.0	0.6	-	0.5	2.0	0.73	0.18
	Actual	0.010	11.1	0.98	0.56	-	0.55	2.06	0.73	0.18
	Difference	---	+0.1	---	---		---	+0.1	---	---

Table 6.2 Target and actual chemical compositions for Alloys A, B, C and B'.

Although there was significant variation in the chromium content from the two analyses performed, the nitrogen content was similar. The nitrogen value was higher than predicted from the chromium nitride calculations. Investigations revealed that nitrogen gas had been used for atomising purposes rather than the argon specified. This resulted in nitriding occurring due to gas nitriding as well as the desired solid state nitriding. Although this may prove to be a future possible production adaptation to reduce the amount of chromium nitride added by injection,

the purpose of this research work is to investigate the properties that can be achieved by using this novel solid state reactive powder processing route.

Plotting the target and actual final range of composition on the Schneider diagram in Figure 6.1 revealed that although not achieving the target value, the increased chromium and nitrogen content, result in a predicted fully martensitic structure.
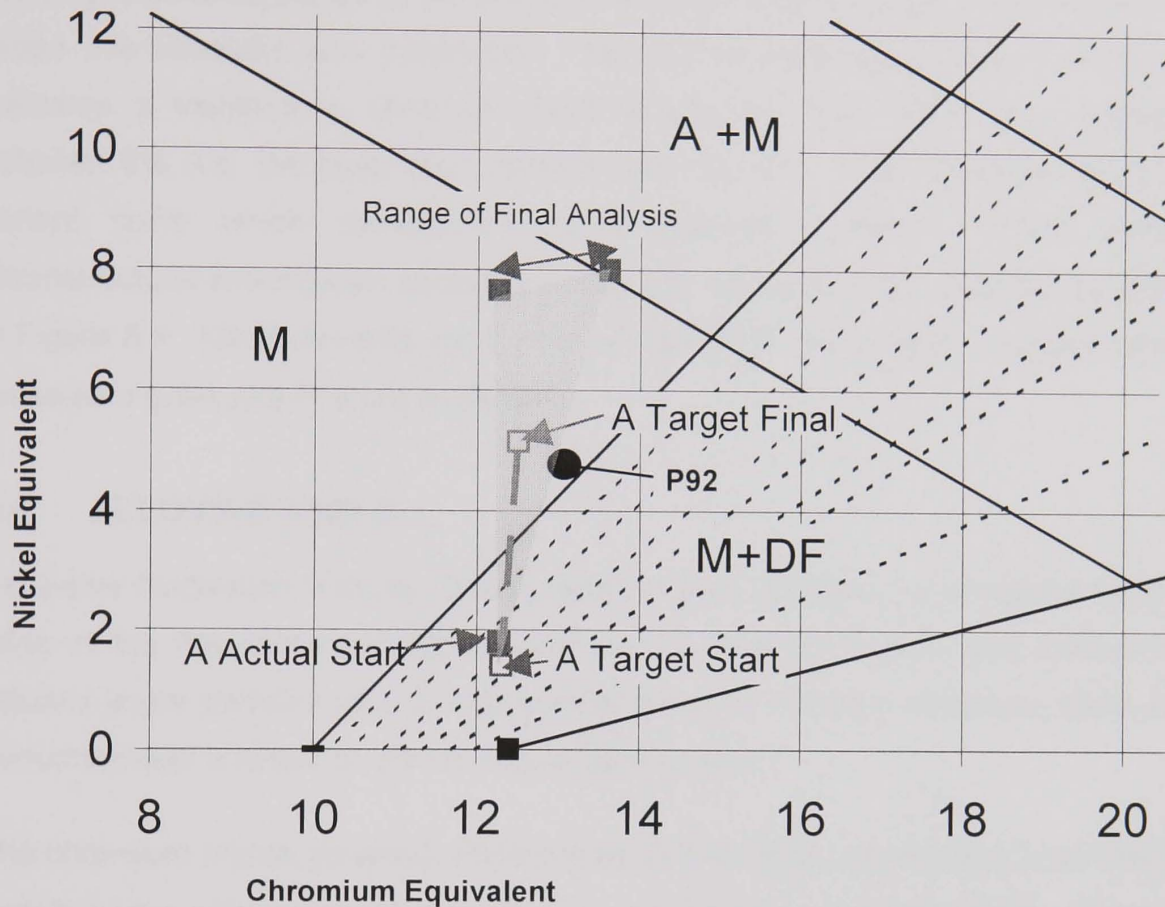
Figure 6.1 Schneider Diagram prediction for Alloy A

6.3.2 Preform Macro Examination

Examination of the sprayed preform revealed it to be porous, as shown in Figure 6.2. This porosity was caused by the processing conditions not being optimised. In order to achieve a dense preform, the mixed spray has to have sufficient fluidity such that upon impaction it deforms, giving a uniform layer. As there are recognisable atomised particles in the solidified preform, it is apparent that the atomised spray had largely solidified before impaction. This is a consequence of too long a flight time. As this structure is not suitable for assessment, the preform was extruded to 17mm diameter bars.

6.3.3 Extruded Bar Examination

Following from the chromium nitride injection problems, Alloy A has a distinct banded structure with light and heavy etched bands parallel to the extrusion direction and up to about 100 μm wide (Figure 6.3a). To confirm that this severe banding is a consequence of the uneven chromium nitride injection rate, an electron probe microanalysis was conducted. As can be observed in Figure 6.3b, this indicates a variation in chromium level across the bar, which was measured between 8% (i.e. the base alloy content) and 12 wt%. The exception being the central spike which corresponds to a residual chromium nitride particle. Microstructural examination revealed a very fine equiaxed grain structure as shown in Figure 6.4. Measurements conducted using ASTM A228 linear intercept method revealed a grain size of 4 μm in diameter.

6.4   ALLOYS B AND C

Extensive fluidisation trials by Osprey failed to give consistent controllable injection rates of the fine chromium nitride particles. Previously Osprey had successfully injected larger particles (due to the fact that these do fluidise), therefore, trials were performed with a larger chromium nitride particle size.

The chromium nitride obtained (Referenced CRN2) from London and Scandinavian metals had a size range of between 22 and 63 μm. Analysis of this chromium nitride revealed that the nitrogen content was only 10.46 wt% indicating that it was actually a chromium plus chromium nitride mixture. This supply of chromium nitride is not desirable as, due to the slow diffusion rate of chromium as discussed in Chapter 5; the optimum properties of the chromium nitride are fine particle size and low chromium content. Nevertheless, Alloys B and C were Osprey sprayed with this chromium nitride supply. Due to the low nitrogen content the percentage chromium nitride added had to be increased to get the required nitrogen content for titanium nitride precipitation, thus it was known that these materials would possess excess chromium. Fluidisation of this larger chromium nitride size proved successful, resulting in a constant discharge during the spraying process. The final chemical compositions are shown in Table 6.2.
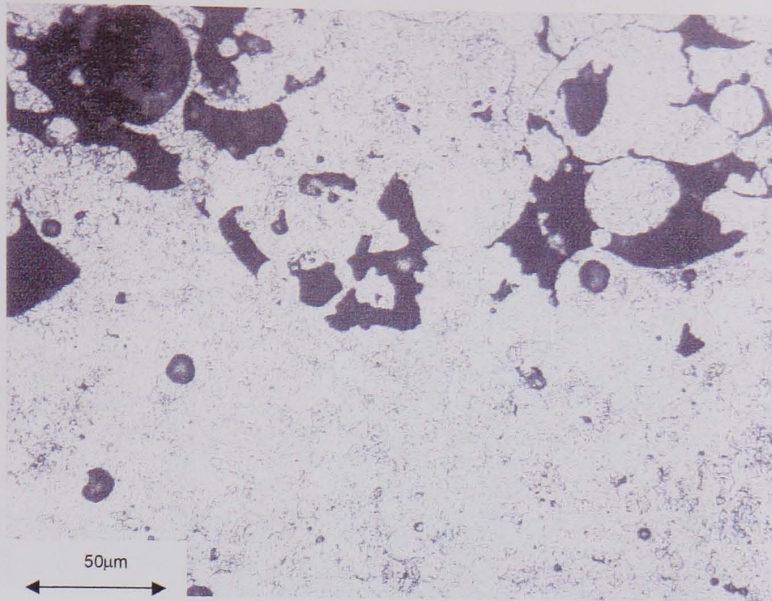
Figure 6.2 Porous Alloy A Osprey Preform
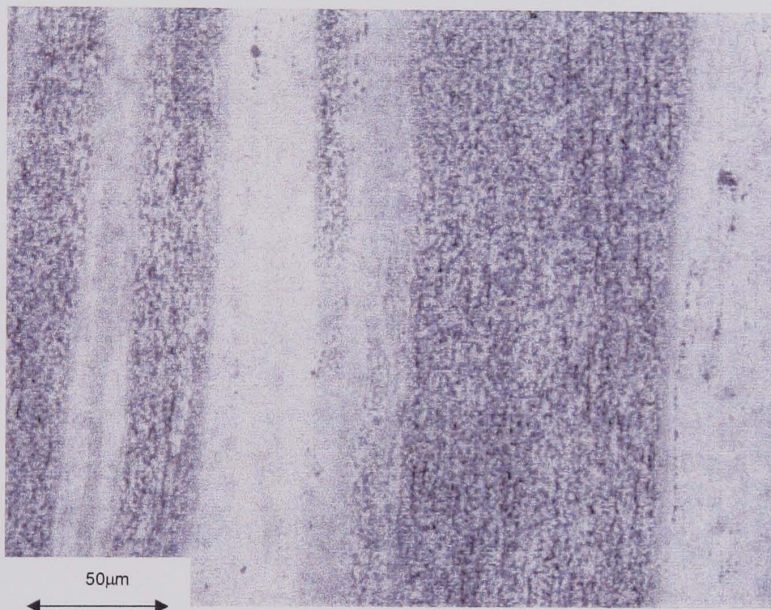
Figure 6.3a Alloy A showing banded etching response
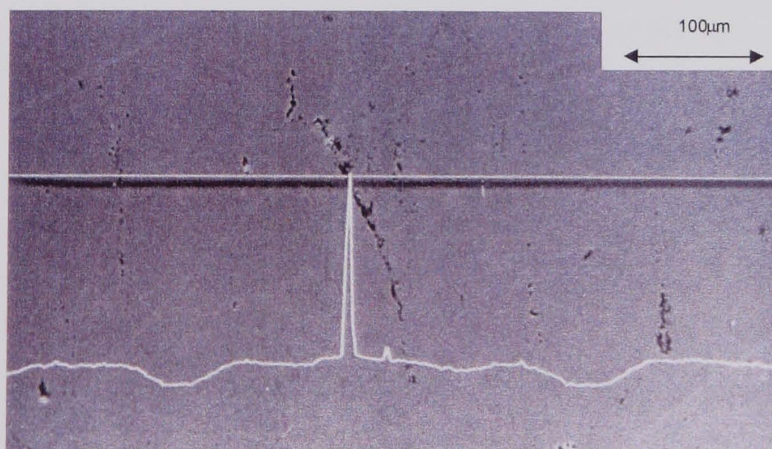
Figure 6.3b Electron microprobe trace indicating variation in chromium level across the sample. The measured Cr level varies between 8 and 12 wt% (except for the central spike which corresponds to a residual chromium nitride particle).
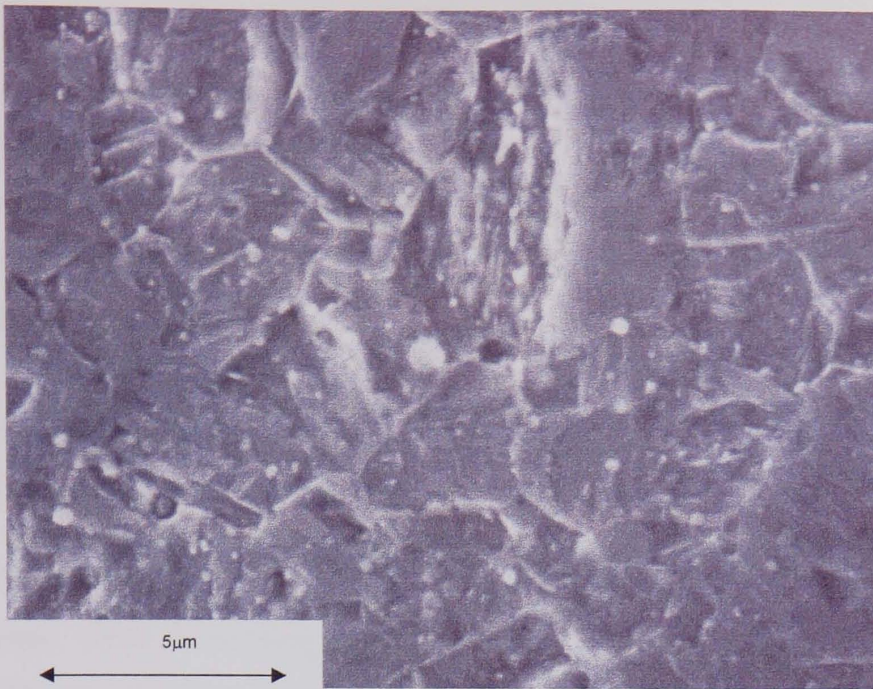
Figure 6.4 Alloy A showing fine prior austenite grain size.
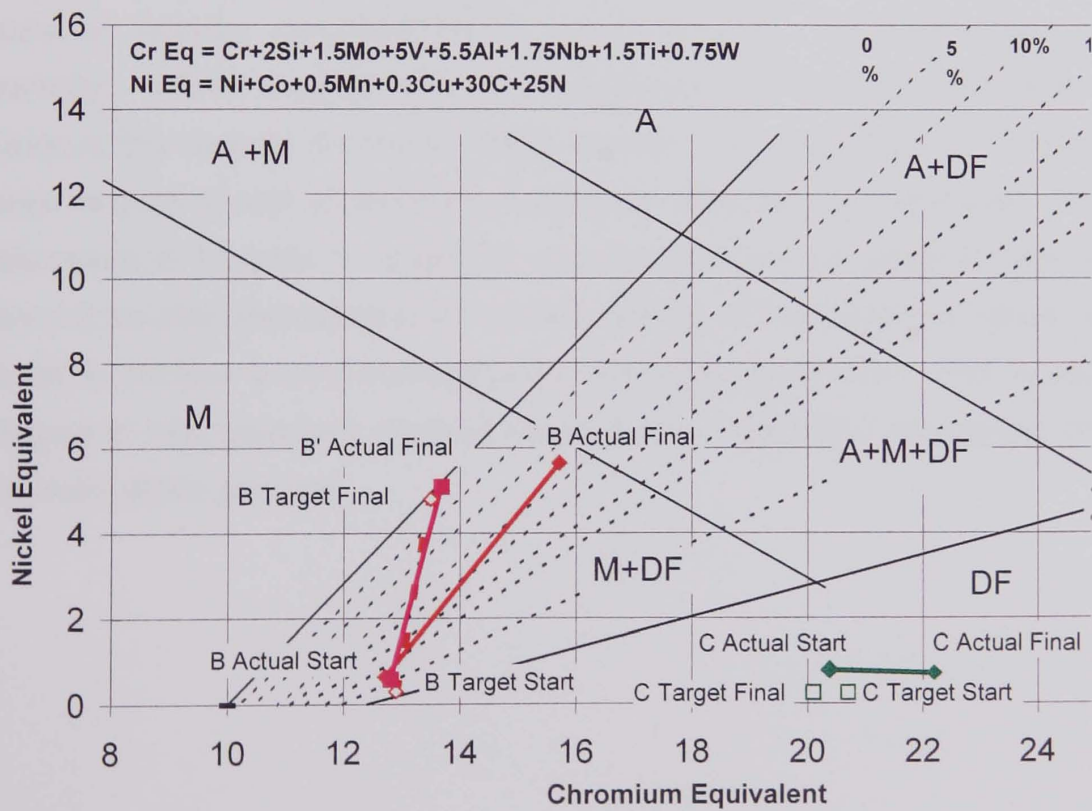
Figure 6.5 Schneider Diagram predictions for Alloys B, B' and C.

The change in atomising gas from nitrogen to argon was successful in avoiding nitrogen pickup; thus the final nitrogen content is determined by the chromium nitride only and, therefore, can be controlled. The target and final compositions are shown in the Schneider diagram in Figure 6.5. As can be observed, the low nitrogen, high chromium content, chromium nitride resulted in considerable deviation from the target compositions. For the Alloy C material, this is not detrimental as the desired fully ferritic phase is maintained. The higher chromium, however, resulted in the Alloy B material entering the martensite plus austenite plus delta ferrite field.

The final structure did not exhibit any evidence of the banding observed in Alloy A, however, what is apparent is the large amount of undissolved chromium nitride particles as shown in Figure 6.6 for Alloy C material. Due to the slow diffusion rate of chromium (discussed in Chapter 5), extensive time/temperature combinations would be required to give a homogeneous distribution of chromium. A trial 1200°C x 48 hr heat treatment was performed on a sample of the Alloy C material. The extent of the chromium diffusion path is clearly visible in Figure 6.7 with the dark etching zone of lamellar chromium nitride surrounding the remaining chromium nitride particles. EDAX analysis of this zone revealed a chromium profile that increased towards the original chromium nitride particle. Also observed in Figure 6.7 is an area of grain growth surrounding the particle after the heat treatment. This will be discussed in Chapter 7. Extensive time-temperature combination heat treatments are not a viable alternative to an intimate mixture of fine chromium nitride particles in order to achieve a semi-homogeneous chromium distribution. This is because the degree of heat treatment required would result in significant coarsening of even the titanium nitride particles.
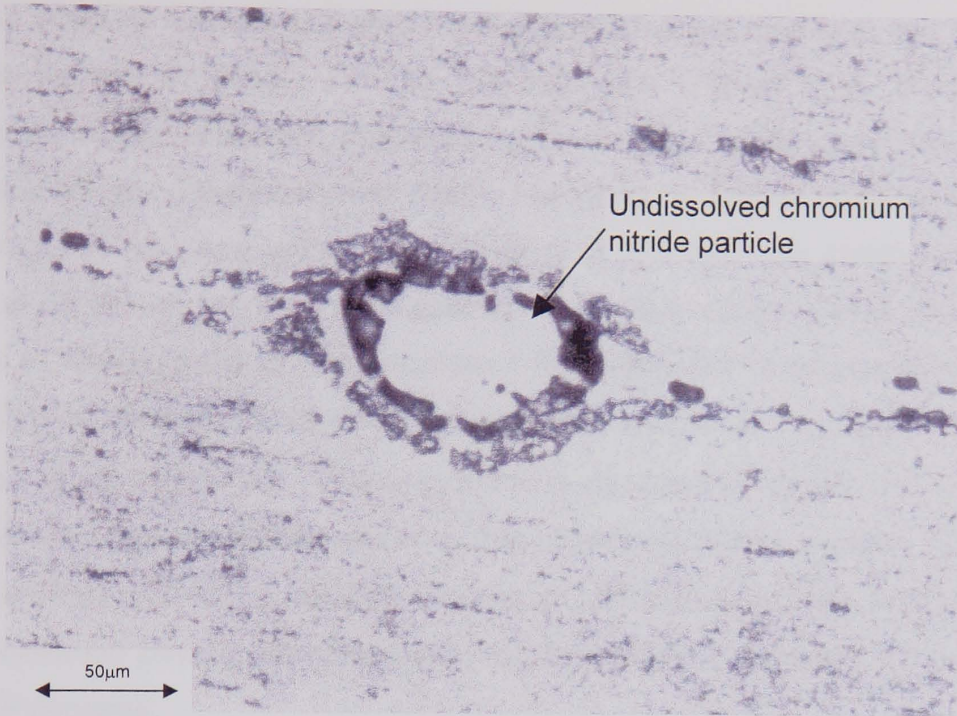
Figure 6.6 Typical coarse chromium nitride particle in Alloy C
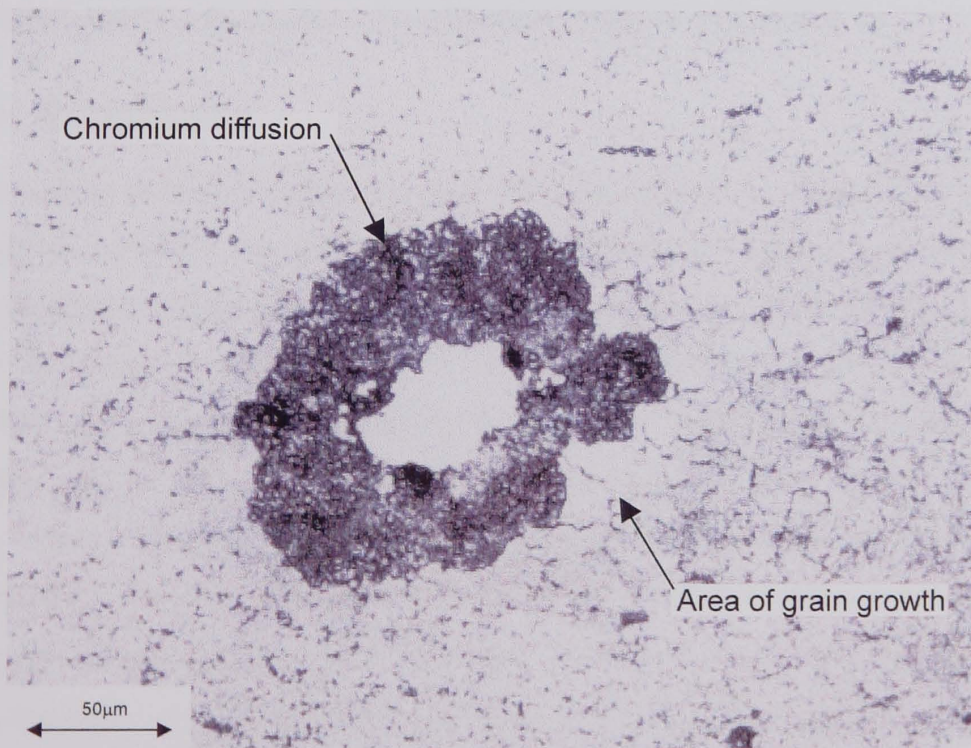
Figure 6.7 Chromium nitride particle after 1200^0Cx 48 hr heat treatment

6.5 MECHANOFUSION

Although the very fine chromium nitride powder size proved problematic to the Osprey injection system, the chromium nitride fines are ideally suited for use in the Mechanofusion Process. Due to the extensive Osprey trials to overcome the chromium nitride fluidisation problems there was no original Alloy A, B or C material available for the Mechanofusion trial. Therefore, a further material was sourced. The material obtained was similar to Alloy B but had the chromium reduced to accommodate the leaner than expected chromium nitride and a titanium content similar to Alloys A and C. To separate it from Alloy B this alloy was designated B'. The Alloy B' titanium containing feedstock was converted to powder by the Osprey process using argon gas. This resulted in a powder size range of 50-250 µm. The powder was then combined with the fine chromium nitride powder, (CRN1) by the Mechanofusion Process resulting in powder samples as shown in Figure 4.4a & b. The combined powder samples were subsequently consolidated to a plate form by the HIP process.

The final chemical composition of the Alloy B' is shown in Table 6.2. It can be observed that the target and actual compositions were relatively close, illustrating the level of control that can be achieved by using the Mechanofusion Process. The predicted matrix composition changes are shown in Figure 6.5.

6.5.1 Examination

Examination of the B' material in the HIPped condition revealed that depending on the plane on which the prior Mechanofused powder particles are sectioned, some prior powder particles clearly showed a variation in precipitate density giving a "halo" effect as shown in Figure 6.8. Scanning electron microscope (SEM) examination together with chemical microanalysis by EDAX was performed on this Alloy B' sample. As can be observed in Figure 6.9 the outer halo is darker and appears to have more particles than the centre region. The chemical composition was analysed by a series of point counts utilising EDAX apparatus. The active volume using 20 kV acceleration was in the order of a 2 µm. The critical element was found to be titanium. In a band extending approximately half the particle radius from the periphery of the particle towards its centre, the titanium content was found to be around 2% the bulk average composition. At the centre of the prior powder particles, the precipitate density was found to be generally very low, giving an

average titanium content of ~0.25%. When the SEM images were observed in detail this revealed a very dark region at the interface between the core from the outer halo. Upon investigating this region in a number of prior powder particles, this revealed the highest titanium level averaging at around 6.5 wt%. These results are shown in the schematic diagram in Figure 6.10. This characteristic halo effect of the precipitate density increasing towards the nitrogen source is indicative of counter diffusion.

6.6   COUNTER DIFFUSION

From Chapter 3 it was stated that the one of the conditions necessary for internal oxidation to occur is that the concentration of solute B is below that necessary to allow external oxidation, i.e. the formation of a continuous layer of oxide at the surface which blocks the passage of oxygen into the alloy. High temperature materials rely upon this selective oxidation for their oxidation resistance. In such cases, if the concentration of the selectively oxidised species falls below a critical level, a transition to internal oxidation and so-called breakaway oxidation can occur.

As discussed by Birks & Meier (1983), external oxidation will occur when the penetration velocity of the internal oxidation zone is sufficiently low that significant outward diffusion of the solute B can occur. The importance of the solute concentration N_B^o can be seen from its effect of the velocity in Equation (3.5). Birks & Meier suggest that the transition from external oxidation to internal oxidation will be enabled by conditions, which increase the inward flux of oxygen (e.g. higher N_o^S) or decrease the outward flux of solute.

In the classical internal oxidation processes, the interstitial specie (i.e. oxygen) is highly mobile with respect to the substitutional species with which it reacts. Thus, the distribution of the substitutional species is "frozen" on a macroscopic scale, leading to a homogeneous precipitate distribution. Wagner (1959) suggests that internal oxidation is to be expected when

$$N_o^S D_o >> N_B^o D_B \qquad\qquad 6.1$$
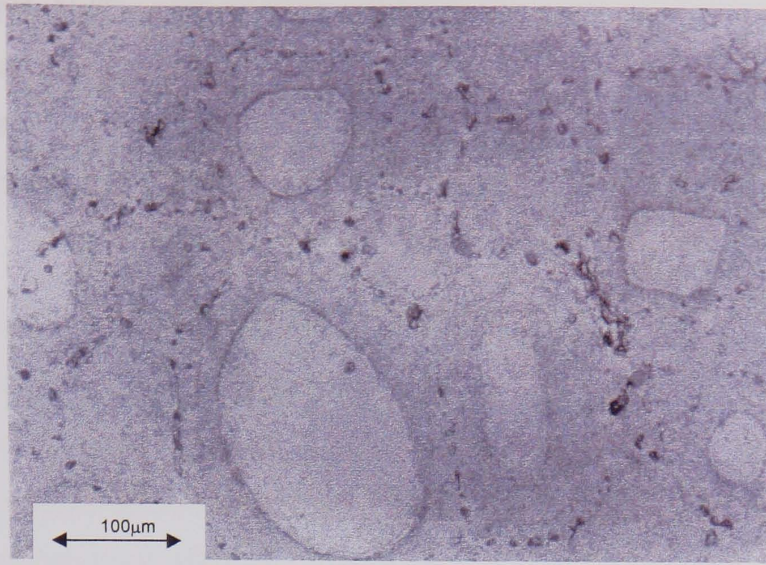
Figure 6.8 Optical micrograph showing "halo" structure of Alloy B'
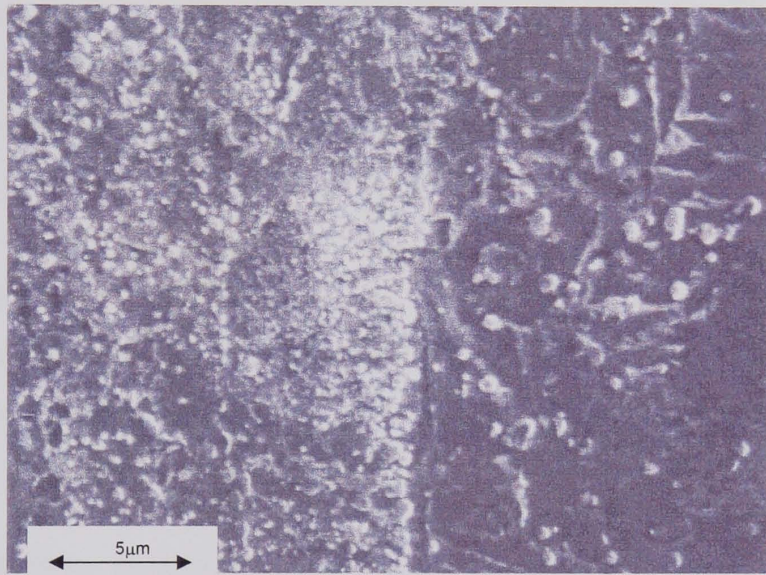
Figure 6.9 SEM micrograph of above at higher magnification

6 wt% Ti

0.25 wt% Ti

Approximate location of
Figure 6.9

2 wt% Ti

Band with higher particle
density at periphery of prior
powder particle

Lower precipitate density
in core of prior powder
particle
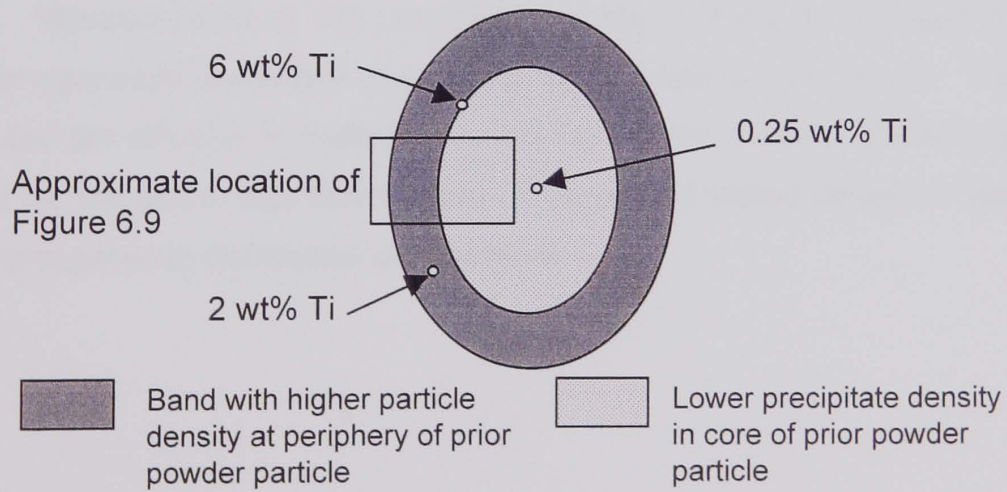
Figure 6.10 Schematic diagram of "halo" showing the EDAX results

where $N_o^S D_o$ and $N_B^o D_B$ are termed oxide and solute permeations. Wagner demonstrated that when condition 6.1 holds, the advance of the internal oxidation front is determined by oxygen diffusion alone. Diffusion of B is practically irrelevant and the molar fraction of the oxide formed is equal to that of solute B initially present.

Kindlimann & Ansell (1970) suggests that in the case of an 18/12 Ti stabilised austenitic stainless steel nitrided at 1050°C, equation (6.1) is not truly satisfied and the classical case described above can break down for large diffusion distances. This results in the substitutional species beginning to diffuse towards the nitrogen source, leading to macroscopic inhomogeneity in the precipitate distribution.

Thus, in any given system an intermediate situation can exist for a given set of conditions whereby the oxidation/nitriding is not purely internal (i.e. where solute B has limited mobility) and neither does it represent complete selective external oxidation/nitriding. In such cases there is limited counter diffusion resulting in some accumulation of oxide/nitride within the external layer. In the case of Kindlimann & Ansell (1970), effectively a titanium free zone was detected at the centre of 0.25mm thick sheet. Bilsby (1974) also cites evidence for counter diffusion of titanium in nitrided austenitic stainless steel. Here also, zones denuded in titanium nitride were reported to occur at the centre of 0.25mm steel.

The above explanation suggests that to achieve a homogeneous product requires either the concentration of titanium to be reduced or the diffusion distance to be reduced. Measurements of the precipitate density in Alloy B' revealed that the macro homogeneous distribution of precipitates extended for over 50 μm. Therefore to avoid counter diffusion in materials containing ~2wt% titanium, the prior powder size must be reduced to less than ~45μm. This has the added benefit of facilitating a more homogeneous distribution of chromium.

6.7 TRANSMISSION ELECTRON MICROSCOPE EXAMINATION

6.7.1 Experimental

A suitable specimen for transmission electron microscopy should present the following contradictory characteristics:

- The specimen should be thin enough to allow electrons to be transmitted without appreciable absorption and scattering in order to obtain suitable contrast.

- The specimen should be thick enough to be representative of the structure of the material being studied. For example, the dislocation density would be lower in thin areas than thicker areas.

Therefore, the usable thickness is limited to between 0.15-0.25 μm. The latter figure is considered the upper limit at 80 kV.

Slices of material >1mm thick were cut using resin bonded alumina discs on the Accutom machine. Three millimetre diameter discs were then cut from these slices using the Metals Research Servomet Spark machine. The discs were subsequently manually ground on emery papers down to around 100 μm. To obtain the thickness required for TEM examination, the discs were chemically polished with a solution of 8 vol% perchloric acid, 32 vol% 2-butoxyethanol and 60 vol% methanol at between -25 and -30°C and 20-25V using the "Tenupol" twin jet electropolishing equipment. Examination of the thin foil samples was carried out using a Philips EM400T TEM operating at 80 kV. No carbon replicas were utilised within this work. Whilst carbon replicas can facilitate a more accurate determination of particle size, they do not provide location information.

6.7.2 TEM Examination Results

Both Osprey and Mechanofused products were examined by TEM in the as consolidated condition (extruded or HIPped). These investigations have mainly concentrated on an initial assessment of the size, distribution and approximate chemistry of the particles present as well as the nature of the steel matrix. Illustrative micrographs are shown in Figure 6.11 a, b, c & d for Alloys A, B C and B' respectively.

Figure 6.11a Alloy A
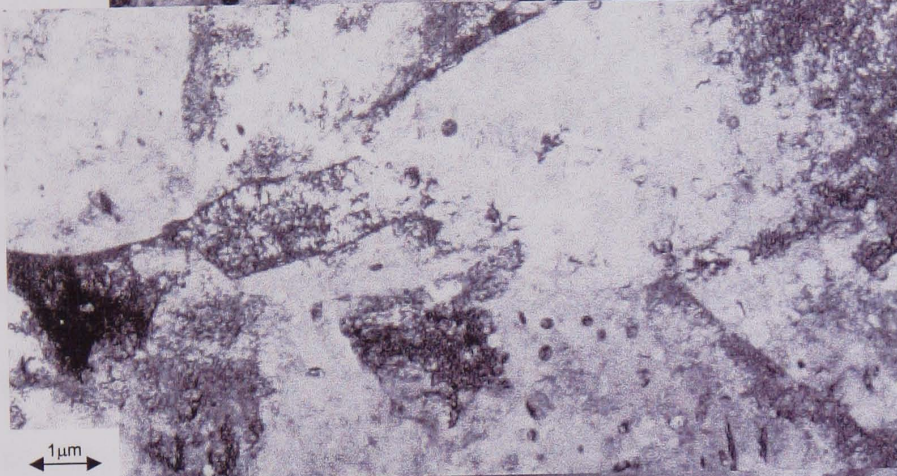
Figure 6.11b Alloy B

Figure 6.11c Alloy C
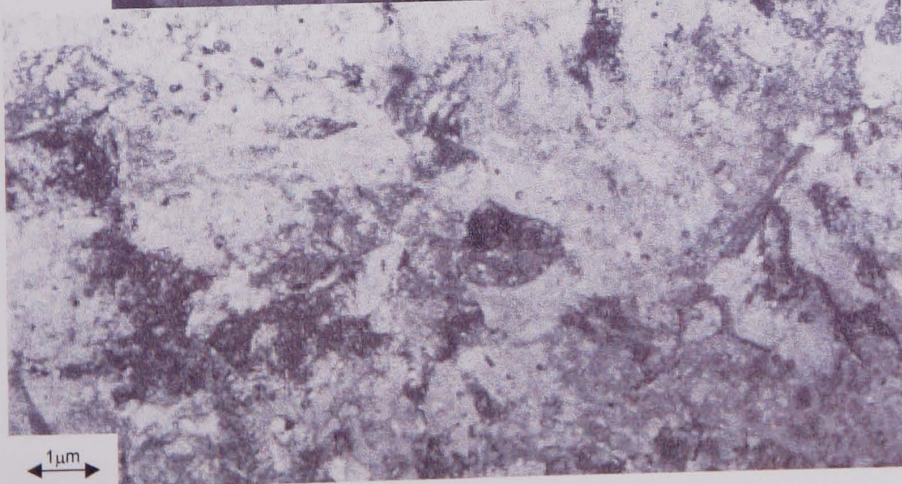
Figure 6.11d Alloy B'

6.7.2.1 Osprey Preforms

In the extruded pre-form samples of Alloys A, B and C, relatively large particle sizes typically in the range 100 to 300 nm were found. These particles took the form of both sphere and cube morphologies. The spherical particles tended to lie at the bottom end of the size range whereas at the upper end of the size range the precipitates increase their surface to volume ratio. The precipitate distribution tended to be very inhomogeneous with precipitate clustering and large precipitate free zones.

In Alloys A and B, heavily dislocated areas were present in the steel matrix as a direct result of the large strain produced by the martensitic transformation. Such areas were absent for Alloy C where only relatively dislocation-free ferrite was found. The absence of a martensitic transformation is consistent for this high chromium non-transformable variant.

6.7.2.2 Mechanofused Alloy B'

In Alloy B' the distribution of particle sizes was again inhomogeneous. In some areas the particles were typically in the size range 30-80 nm, whilst other areas contained large particles around 250 nm. Although there was evidence of clustering of the titanium nitride, the degree was far less than in the Osprey material. A typical edge to edge particle spacing was around 200nm and the matrix was predominantly martensitic.

6.7.2.3 General Observations

Chemical analysis using EDAX indicated that these particles contained a small amount of dissolved chromium. This has been observed previously by Roberts & Evans (1982) and is due to the similarity in atomic number of chromium and titanium. Thus, a limited amount of chromium will replace the titanium atoms in the FCC crystal structure.

Examination by TEM confirmed that the grain size found on these alloys was <5 µm. The reason for the very fine grain size was also apparent as shown in Figure 6.11c. Here it can be observed that the fine grain size is due to the titanium nitride particles pinning the grain boundaries, which is the primary function of titanium nitride particles in micro-alloyed steels. The presence of particles on the grain boundary decreases the grain boundary area and thus the overall grain boundary energy.

Consequently, it takes considerable energy to move the grain boundary away from the particle.

6.8   MECHANICAL TESTING

6.8.1   Test Condition

Stress rupture tests were performed on three prototype steels (A, B and C). Alloy B' was not tested due to the counter diffusion experienced during production. The martensitic A and B variants were tempered at 750°C x 1 hour in a similar fashion to conventional martensitic creep resistant steels. This reduced the hardness value to 200-240 Hv_{10} for both materials. The Alloy C3 material was tested in the as extruded condition.

Uniaxial test specimens were machined from the extruded bars and were tested on constant load stress rupture machines within the Mitsui Babcock Creep Laboratory. Testing was carried out at 600°C and the initial stresses chosen were 120 and 100 N/mm^2 which would result in around 30K and 100K hour test durations for P91 material.

6.8.2   Results

Early failures were experienced in all of the titanium nitride strengthened materials; as a result the applied stress was reduced. The results are given in Table 6.3. Figure 6.12 compares the stress rupture data at 600°C for the titanium nitride strengthened steels and for the PD6525 (1992) data for P22 and P91. As can be observed from Table 6.3 and Figure 6.12 the titanium nitride strengthened steels show very low rupture strengths and very high elongations and reductions in surface area i.e. high rupture ductility.

6.8.3   Test Specimen Examination

The reduction in cross sectional area was relatively uniform over the entire gauge section as shown in Figure 6.13. Unlike a conventional material where a neck forms and all the strain is concentrated in the neck, there appears to be a "diffuse" neck covering the entire gauge length with uniform elongation. SEM examination of the failed stress rupture specimens revealed that no large scale changes in the grain shape occurred during the creep elongation. The structures shown in Figure 6.14

demonstrates that the microstructure was fine and equiaxed before and after testing, i.e. the aspect ratio of the grains does not reflect the total strain in the specimen.

Alloy	Temperature (°C)	Stress N/mm^2	Rupture Life (hrs)	Rupture Strain (%)
A	600	120	69	88
	600	100	100	84
	600	80	216	80
	600	60	870	96
B	600	120	434	56
	600	100	625	74
	600	80	1145	76
C	600	120	554	92
	600	100	596	95
	600	80	1239	108

Table 6.3 600°C stress rupture results for Alloys A, B and C
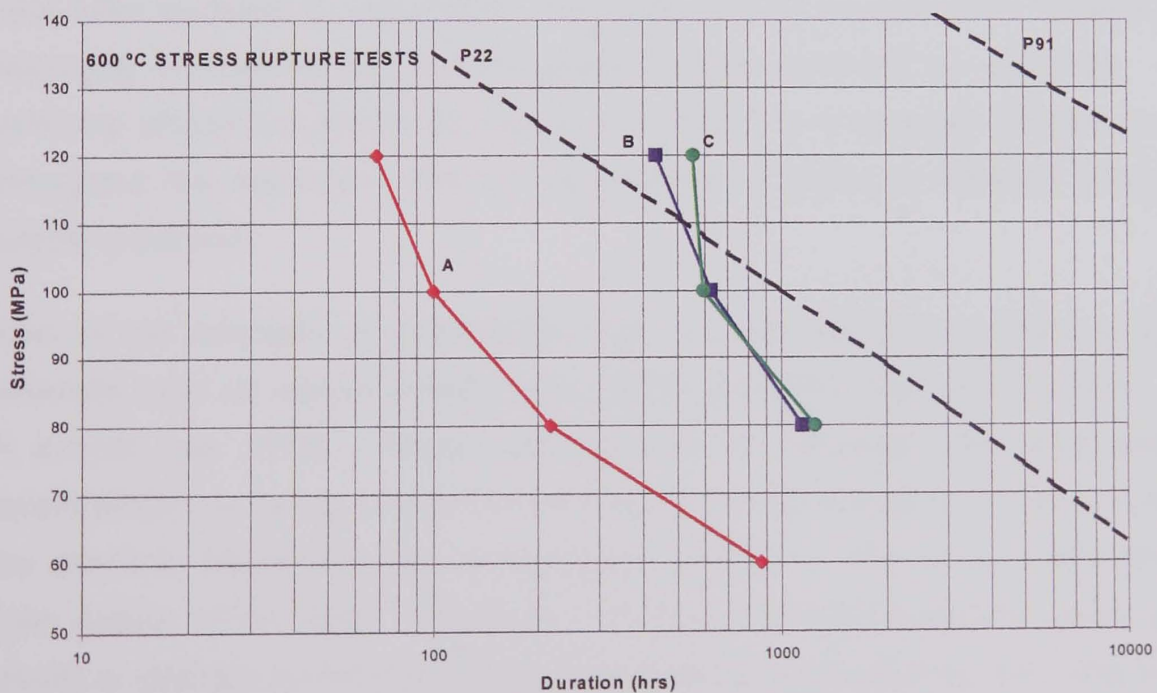
Figure 6.12 600^{0}C stress rupture results for Alloys A, B and C in comparison with P22 and P91

6.9 SUPERPLASTIC FEATURES

The diffuse neck and non-deforming grains are classical features of superplastic flow, although the elongations observed here are far less. Superplastic materials can accommodate strain in the order of many hundreds of percent elongations. It does, however, appear that the flow mechanism is similar. Superplastic flow has been observed as a general property of ultrafine grained materials under certain conditions of test. In the review by Hazzledine & Newbury (1973) the critical aspects required for superplastic flow are as follows:

- The grain size (diameter) must be less than 10 μm and equiaxed

- The grain size must be stable, i.e. resistant to recrystallisation.

- The test temperature must be greater than 0.4 Tm.

- The strain rate generally was between $10^{-4}s^{-1}$ and $10^{-3}s^{-1}$.

Deformation is by grain boundary sliding, as the grain boundaries, which are imperfectly bonded, are weaker than the ordered crystalline structure of the grains for the conditions given above. In superplastic flow, the movements of the grains have been modelled by Lee (1970). The grain centres move as if the material was deforming homogeneously, but the grains remain equiaxed by switching. The switching process is shown on Figure 6.15 and it is envisaged that this occurs throughout the specimen, with various clusters of grains in different stages of switching process.

Most of the examples of superplastic flow, concern alloys not related to boiler materials, such as lead-tin eutectic Hart (1967), Zn 40%Cr Melton et al (1974), Mg-Al eutectic Lee (1969). These alloys achieve the necessary fine grain size for superplasticity by using a two-phase structure such as a eutectic. With a eutectic the chemical dissimilarity can prevent grain growth i.e. one phase obstructs the grain growth of the other. There are, however, notable exceptions where grain growth is retarded by thermally stable dispersed particles such as with yttria in MA ODS alloys. These alloys deform superplastically at elevated temperatures (>1050°C) Luton (1986), Fawley (1972) when in the fine grained, as extruded condition. Fine grained (0.5 - 1.5 μm) ultra high carbon steels containing a fine dispersion of carbide have also been shown to behave superplastically at 650°C,

Sherby et al (1975). Fukuyo et al (1991) developed a model for superplasticity in precipitate strengthened alloys. The model was developed for ultrahigh carbon steels containing large volume fractions of carbides (VC~25vol%) and is based on grain boundary sliding accommodated by slip.

It is apparent from the foregoing review that the low creep strength of the titanium nitride strengthened materials (A, B, and C) is a result of the strengthening effect of the precipitates being masked by the fine grain size which promotes grain boundary sliding and high rupture ductility. The phenomenon depends on the material having a small grain size and thus a large volume fraction of grain boundary material. The small grain size ensures that the relative movement of two adjacent grains is small and that they may, therefore, slide under a low imposed stress at a low overall strain rate.

The excellent creep properties of the MA ODS alloys are only fully realised by the formation of a coarse anisotropic grain structure which develops upon elevated temperature heat treatment of the as extruded material, Jaeger & Jones (1994). Therefore, in order to realise the potential of the titanium nitride particle strengthening materials it is necessary to minimise the grain boundary sliding effect by minimising the amount of grain boundary. To achieve this, i.e. to grow the grains, sufficient energy will be required to overcome the high grain boundary pinning forces imposed by the titanium nitride particles.
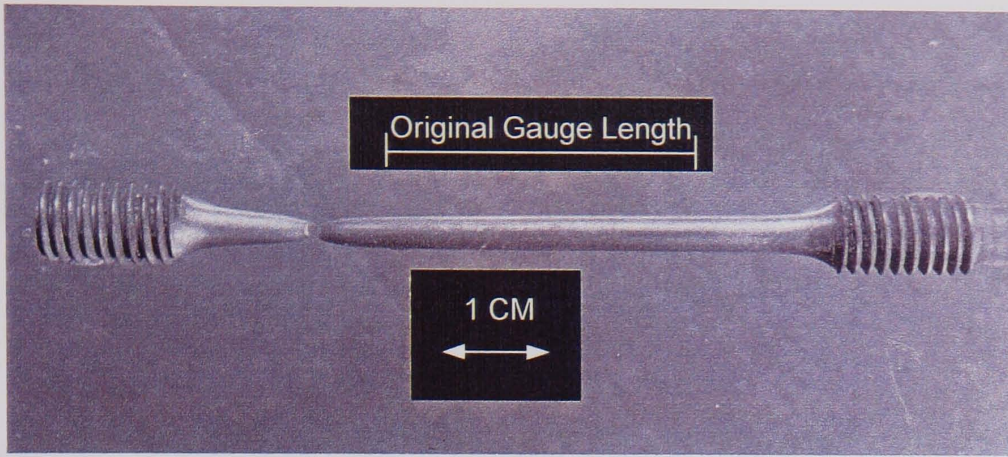
Figure 6.13 Alloy C failed stress rupture specimen (600^{0}C/80MPa/1239hrs/108%El)
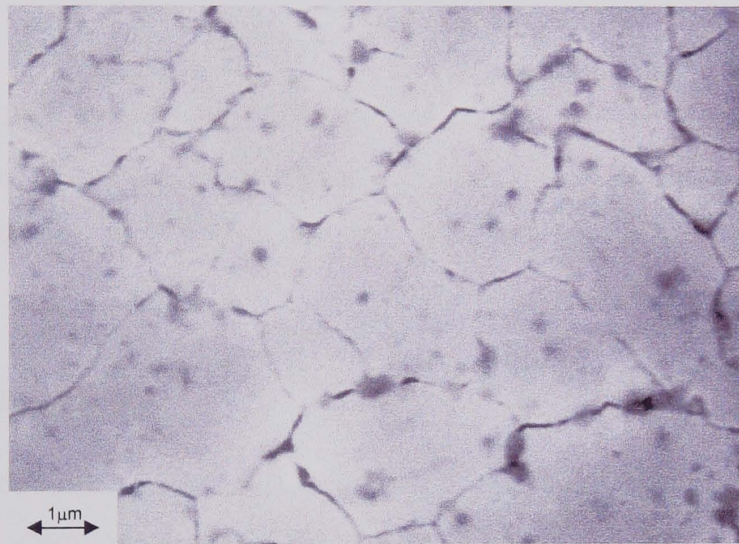
Figure 6.14 Fine equiaxed grain structure remains after stress rupture testing.
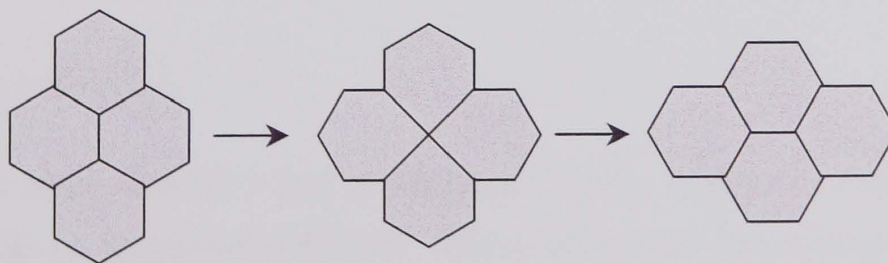
Figure 6.15 Grain Switching. The grains remain approximately equiaxed while the specimen deforms. After Lee (1970)

73

Chapter 7

Grain Growth Trials

A feature of all materials produced thus far in the project no matter whether the alloy is martensitic or ferritic or if it is HIPped or extruded, has been a fine, equiaxed grain structure, typically <5 μm in diameter (prior austenitic grain size in the martensitic variants).

7.1   GRAIN PINNING

The incredibly fine grain sizes obtained in the Batch 1 A, B, and C alloys are a consequence of grain boundary pinning by the titanium nitride precipitates. The relationship between the titanium nitride particle radius r, and the volume fraction vf of the pinning particles and the matrix grain radius R was first developed by Zener (1948).

$$R = \frac{4}{3} \frac{r}{vf}$$
(7.1)

Applying the basic data for r and vf obtained for Alloy A gives a maximum grain radius that can be restrained of 6.2 μm. This is larger than the observed grain size (~5μm). The reason for this differential is most probably due to the assumptions made in the Zener equation, which includes assuming that it is an isolated grain.

Grain growth essentially ceases when the driving force for grain boundary migration equals the Zener pinning force. Using this equation the most effective grain

boundary pinning and thus the finest grain size is achieved by the maximum volume fraction of the finest particles which is exactly the same aim as the precipitation of particles to give the maximum strengthening.

As demonstrated in Chapter 6, the fine grain size has a significant effect upon the mechanical properties of the titanium nitride strengthened steels. This is due to the fact that the stress rupture properties of a material are a balance between the grain strength and grain boundary strength. At low temperature, a fine grain size increases strength due to the grain boundaries acting as a barrier to dislocation movement i.e. the slip planes are weaker than the grain boundaries. As the temperature is raised there comes a point, where for a given strain rate, the grains and grain boundaries have equal strength (equicohesive temperature). Above this temperature, as observed in Chapter 6, grain boundary sliding can be the dominant strain accumulation process in stable fine grained material. As the titanium nitride steels are being designed for high temperature operation, it is imperative that grain boundary sliding is minimised. To achieve this, the grain boundary area must be minimised by maximising the grain size.

In conventional creep resistant ferritic steels the material would be heated to a temperature where the principal grain boundary pinning precipitate would become unstable and be taken back into solution. The material would then be held at this temperature until the required grain size was achieved, before cooling and re-precipitating the strengthening (and grain boundary pinning) particles. With the titanium nitride strengthened steels however, the stability of the titanium nitride particles preclude this. Effectively, once the titanium nitride particles have precipitated in the alloy they can only coarsen, therefore, no wholesale re-solution is possible.

7.2 GRAIN GROWTH HEAT TREATMENT TRIALS

In order to investigate if heat treatment could provide sufficient energy to detach the grain boundaries from the pinning particles, Alloys A and C were subjected to annealing temperatures of 1000°C & 1350°C and for durations of one and six hours. The result of these heat treatments was that minimal grain growth was only possible after heat treating at 1350°C x 6 hour by adjusting the factor of r/vf due to particle coarsening. The observed increase in particle size (via SEM) is shown in Figure 7.1a-c.
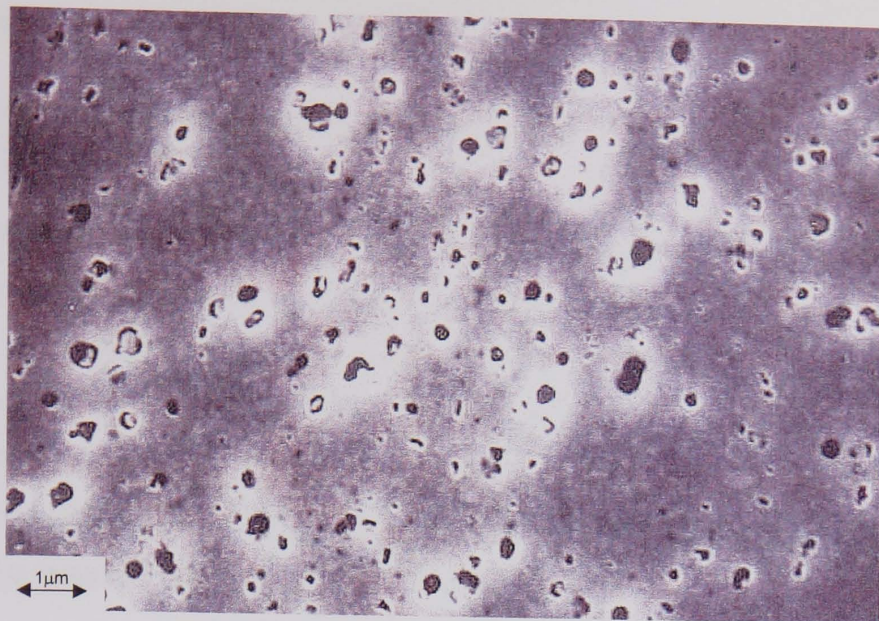
Figure 7.1a Alloy C 1000°C x 6 hours
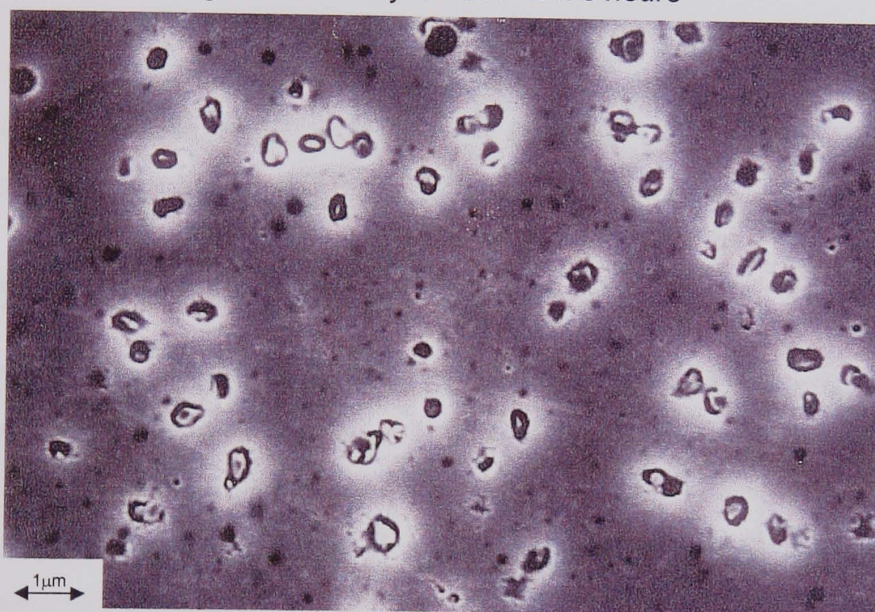
Figure 7.1b Alloy C 1350°C x 1 hour
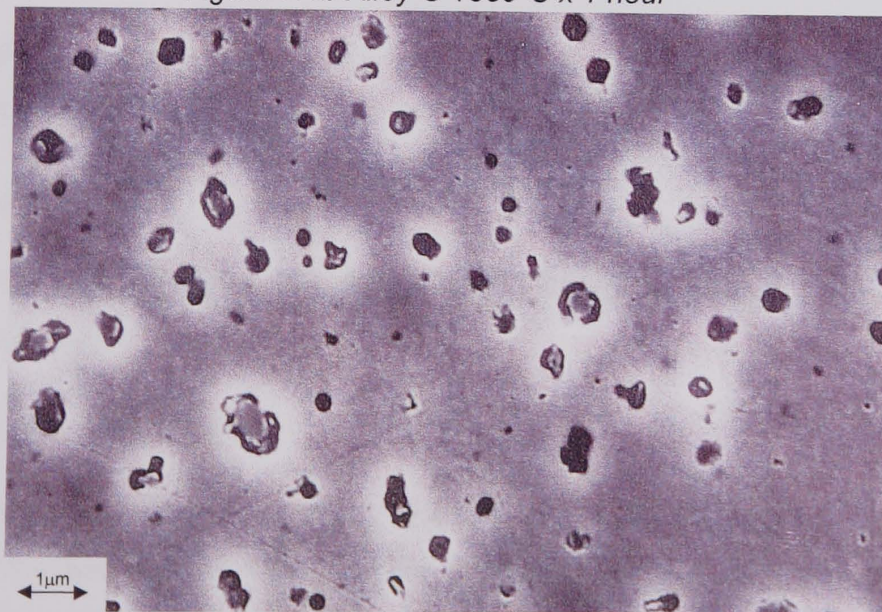
Figure 7.1c Alloy C 1350°C x 6 hours

As fine titanium nitride particles are necessary to impart high temperature strength, increasing the grain size by coarsening the pinning particles is not a feasible option.

In the Alloy C material, larger grains were observed in the immediate vicinity of some of the large chromium nitride particles as shown in Figure 6.7. Similar large grains adjacent to widely spaced coarse particles have also been observed by Humphreys (1977) and Leslie, Michalak & Aul (1963) reviewed by Cotterill & Mould (1976). This was found to be due to the large particle accelerating the nucleation process of primary recrystallisation by the large amount of deformation produced in the vicinity of the large non deformable particle. As the larger grains are restricted to the immediate vicinity of the large non-optimum chromium nitride particles, this is also not a feasible method of increasing the grain size.

This fine grain size problem was also faced by some of the most successful mechanically alloyed materials including the oxide dispersion strengthened iron based and nickel based superalloys. For these alloys it was found to be possible to induce a coarse grain structure by means of secondary recrystallisation.

7.3 SECONDARY RECRYSTALLISATION

The following section will review the salient features affecting the development of a secondary recrystallised grain structure. Emphasis will be placed on relating the features found in MA ODS alloys to these titanium nitride strengthened steels. Throughout the section, reference will be made to certain phenomena associated with general recrystallisation and grain growth.

The basic definitions which are based on those given by Cahn (1966) and Cotterell & Mould are as follows:

Recovery

The density and distribution of dislocations change without any movement of the grain boundaries.

Primary Recrystallisation

This is the process in which new strain free grains are nucleated and these then grow at the expense of the deformed material until this is all consumed. At this stage the migrating boundaries will have impinged on each other. Primary

recrystallisation is then complete and the metal has a minimum recrystallised grain size, which is dependent on the degree of prior deformation, heat treatment temperature, particle distribution and composition. The driving force is the removal of the strain energy associated with the deformed state.

Grain Growth

This involves the further migration of grain boundaries through the recrystallised material to produce a grain size that is larger than at the end of primary recrystallisation. The driving force is the reduction in the overall internal energy associated with the grain boundaries within the strain free material.

Grain growth can be further divided as follows:

Normal Grain Growth

This is the more usual form of grain growth in which the rate of boundary migration is approximately uniform throughout the material, with the result that at any instant the grains are roughly similar in size.

Secondary Recrystallisation

This is a deviation from normal grain growth such that the growth process is restricted to a relatively small number of grains, whilst the remainder are virtually unaltered until they are consumed.

As secondary recrystallisation did not occur during the heat treatment trials conducted on Alloys A and C, chemical and processing alterations were made to the Batch I alloys in an attempt to make them more susceptible to this mechanism of grain growth.

7.4 BATCH II ALLOYS

In order to investigate if it was possible to induce secondary recrystallisation in the family of titanium nitride strengthened steels, changes were made to the titanium nitride content and the processing route. The flow diagram outlining the Batch I

alloys, the modification philosophy, the method and the Batch II alloys, is shown in Figure 7.2.

Batch I	Objectives	Method	Batch II
Alloy A (2% Ti) Alloy B (1.2% Ti) Alloy B' (2% Ti)	1. Finer TiN precipitates 2. Coarser grains 3. Less counter diffusion 4. Fabricability	a) Stabilise austenite (1) b) Reduce Ti (1-3) c) Reduce "free" nitrogen (4)	ALLOY D (0.6%Ti, 3%Ni)
Alloy C (2% Ti)	1. Coarser grains 2. Less counter diffusion	Reduce Ti	ALLOY C3 (0.6%Ti,)
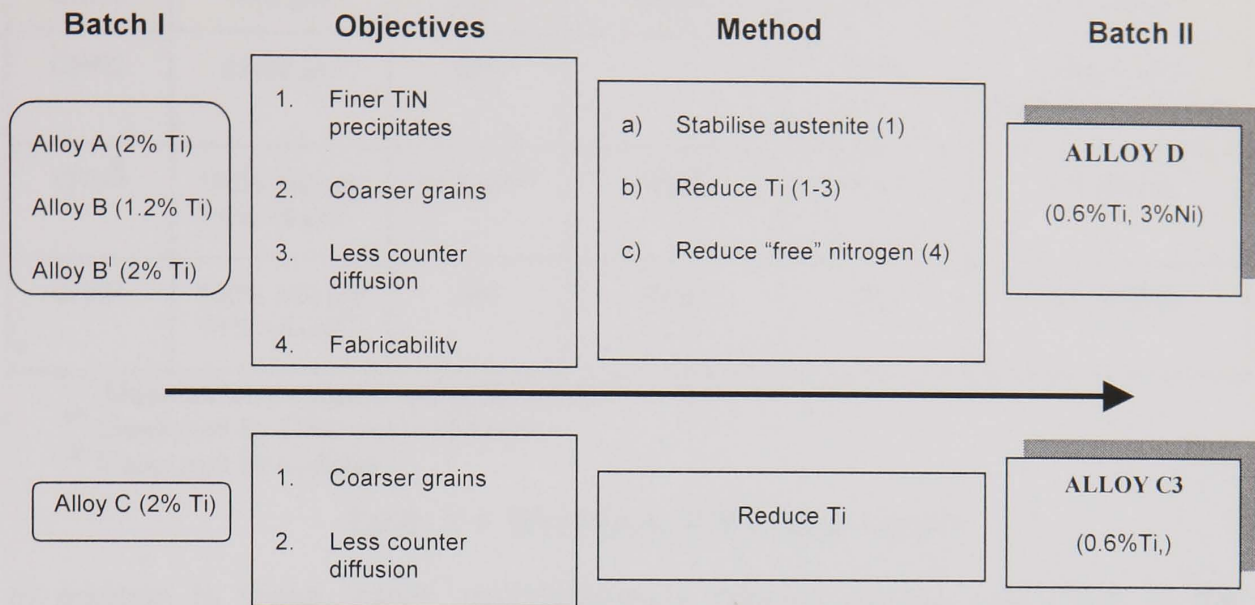
Figure 7.2 Development of batch II alloy composition

7.4.1 Chemical Modifications

To decrease the degree of grain boundary pinning the volume fraction of titanium nitride particles was reduced from ~3% to ~1% by reducing the levels of titanium from ~2wt% to 0.6wt% and commensurate reduction in the nitrogen content.

To avoid the chromium nitride problems experienced in Batch I two new batches of chromium nitride powder were ordered. Details of the chromium nitride properties are given in Table 7.1. Two batches of chromium nitride were obtained to suit the differing needs of the Osprey and Mechanofusion processes i.e. very fine particles for the Mechanofusion process and coarser particles for the Osprey process. The nitrogen content of the chromium nitride was determined before the titanium containing feedstock materials were specified in order to adjust the chromium contribution accurately and thus avoid the problems experienced with the Batch I alloys due to the chromium nitride being lean in nitrogen.

Number	Size Range	Mean Size	Specified N /wt%	Measured N /wt%	Source
CRN1	<45 μm	3 μm	16-21	16.5	H.C. Starck
CRN2	22-63 μm	NK	-	10.46	London and Scandinavian Metals
CRN3	100% <45 μm 7.5% <5 μm[1]	16.8 μm[2]	16-21	18.1[3]	H.C. Starck
CRN4	100% <10 μm 71% <5 μm[1]	NK	16-21	18.1	H.C. Starck

[1] Measured by supplier using Microtrac.
[2] Measured by OML using Malvern.
[3] Measured by supplier.

Table 7.1 Chromium nitride supply details

In addition to these "batch" modifications a specific change was made to the martensitic alloy. This change involved increasing the nickel content from 1wt% to 3wt%. The reason for this addition is to determine if the relatively coarse titanium nitride precipitate size observed in Alloys A & B (which were similar in size to the fully ferritic Alloy C material) was due to precipitation in the ferritic phase. Thus by lowering the A_{c1} further this should ensure that precipitation occurs in the austenitic phase. Finally, due to joining problems experienced with the original martensitic alloys the "free" nitrogen was reduced to 0.1wt%.

In fact, due to the problems discussed earlier with titanium additions, the actual D and C3(1) materials fell short of their titanium targets. For Alloy C3(2) the titanium containing stock material was closer to the target composition of 0.6%wtTi. The target and actual chemical analysis for Alloys C3(1), C3(2) and D are given in Table 7.2. For Alloy C3(2) the composition presented in Table 7.2 is not the average composition of the entire plate. Due to the reoccurrence of chromium nitride spray problems in the Osprey Process, 70% of the plate was scrapped. The remaining 30% of the plate was rolled down to a thickness of 15mm for examination and testing. The positions of the Alloys C3(1), C3(2) and D on the Schneider diagram are shown in Figure 7.3. As can be observed, all materials achieved their target compositions.

		C	Cr	Mo	Mn	Ni	Si	Ti	N	Nf
Alloy C3(1)	Target	<0.02	17.5	1.0	0.5	-	0.3	0.6	0.17	0.00
	Actual	0.020	17.0	0.85	0.55	-	0.3	0.4	0.13	0.01
	Difference	-	-0.5	-0.1	-	-	-	-0.2	-0.04	+0.01
Alloy C3(2)	Actual	0.02	16.8	0.89	0.54	-	0.31	0.61	0.21	0.03
	Difference	-	-0.7	-0.1	-	-	-	-	+0.04	+0.03
Alloy D	Target	<0.02	9.2	0.5	0.8	2.8	0	0.6	0.28	0.10
	Actual	0.018	8.9	0.52	0.97	2.74	0.07	0.6	0.29	0.11
	Difference	-	-0.3	---	+0.2	-0.1	+0.1	-	+0.01	+0.01

Table 7.2 Chemical compositions for alloys C3(1), C3(2) and D
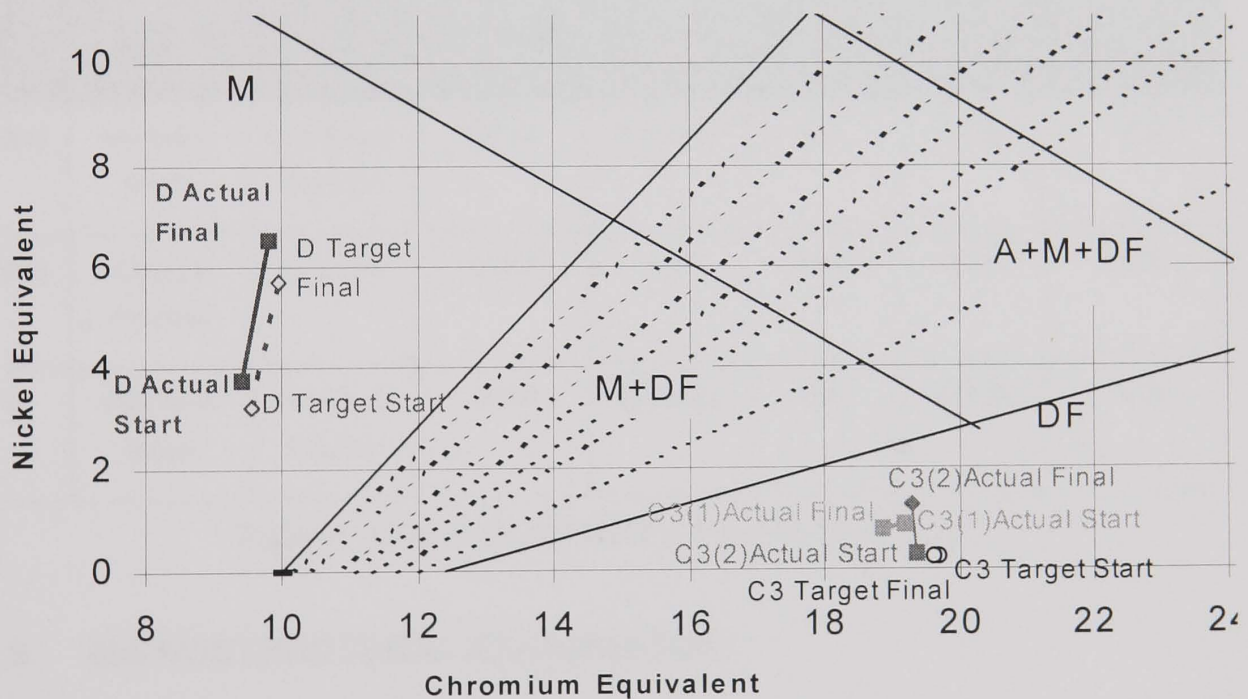
Figure 7.3 Schneider diagram for Alloys C3(1), C3(2) and D.

7.4.2 Process Route Modifications

In addition to the measures identified above, the extrusion practice was altered to simulate the high plasticity process developed for the iron based Mechanically Alloyed Oxide Dispersion Strengthened (MAODS) steels (Jaeger private communication). To achieve the desired high plasticity to create a high level of

stored strain energy, a high extrusion ratio, high strain rate and "low" temperature were employed.

Typical extrusions in Batch I were:

- extrusion ratio: 7 : 1 (giving a 19mm diameter bar from the 50.8mm can.
- extrusion speed: 30mm s^{-1}
- extrusion temperature: 1050 - 1200°C

The Batch II extrusion conditions were:

- extrusion ratio: 16 : 1 (giving a 12.7mm diameter bar)
- extrusion speed: 55mm s^{-1}
- extrusion temperature: 1000°C

The entire production route of alloys D and C3 are summarised in Table 7.3

Alloy	Combining Route	Product	Chromium Nitride Powder	Consolid- ation Route	Product	Diameter/ Thickness	Deformation Temp. (^{0}C)
C3(1)	Mechano fusion	Combined Powder	CRN4	Extrusion	Bar	12.7mm	1000
C3(2)	Osprey Process	Preform	CRN3	HIP	Plate	15mm	1150
D	Mechano fusion	Combined Powder	CRN4	Extrusion	Bar	12.7mm	1000

Table 7.3 Summary of Batch II Production Routes

7.5 MICROSTRUCTURAL EXAMINATION

7.5.1 Alloy D

Examination of the Alloy D material by TEM revealed a typical high dislocation martensitic structure. A detailed assessment of the titanium nitride particle size was performed by measuring the particle diameters and nearest neighbour interparticle spacings over twenty random areas. This revealed that the average particle size was 229nm. The particle distribution was not homogeneous; there were areas of finer 50-80nm particles and other areas of coarse 200-350nm particles as shown in Figure 7.4a & b.

7.5.2 Alloy C3

Examination of the alloy C3 material post extrusion by TEM did not reveal the classical features of a highly deformed microstructure i.e. high dislocation density, and generally convoluted microstructure. The observed microstructure contained equiaxed grains largely free of dislocations as shown in Figure 7.5. It is thus apparent that the material has dynamically recrystallised at least once during the course of the extrusion. The product of the primary recrystallisation is the very fine grain size. The as-extruded hardness value of 230 Hv_{30} reflects the fact that dynamic primary recrystallisation has occurred. Although this extruded structure is dissimilar to the iron based ODS materials, it is similar to the nickel based ODS alloys which can undergo successful grain growth.

Examination of the particle size was performed on the C3 material in a similar method to that performed on Alloy D. For Alloy C3(1) this revealed a similar non-homogeneous particle distribution and a similar particle size distribution to alloy D. The actual figures for Alloy C3(1) were 238nm and 884nm for the average particle diameter and interparticle spacing respectively. In the case of Alloy C3(2) the average particle size was 256nm which is coarser than the material produced via the Mechanofusion process, but due to the higher volume fraction titanium nitride the average interparticle spacing (676nm) is finer.

7.6   SECONDARY RECRYSTALLISATION HEAT TREATMENT TRIALS

It was intended to base the heat treatment schedule to induce grain growth on that used for the industrial process performed by Plansee Gmbh who are the manufacturer of both iron and nickel based MAODS alloys. However, heat treatment schedules are considered proprietary information and only a broad window of heat treatments was supplied by the manufacturer.

Post extrusion, the two bars (Alloy D and C3(1)) were sheathed by the extruded carbon steel can of around 0.5mm in thickness. Prior to sectioning, to obtain suitable samples for heat treatment trials, the bars were ground to remove the sheath. Heat treatments were performed at temperatures between 900 and 1350°C and for times between 1 and 100 hours. The extents of heat treatments applied to each alloy were tailored to the materials behaviour. Heat treatments were performed in a carbolite tube furnace in a protective argon atmosphere.

Figure 7.4a Area of coarse particles in Alloy D
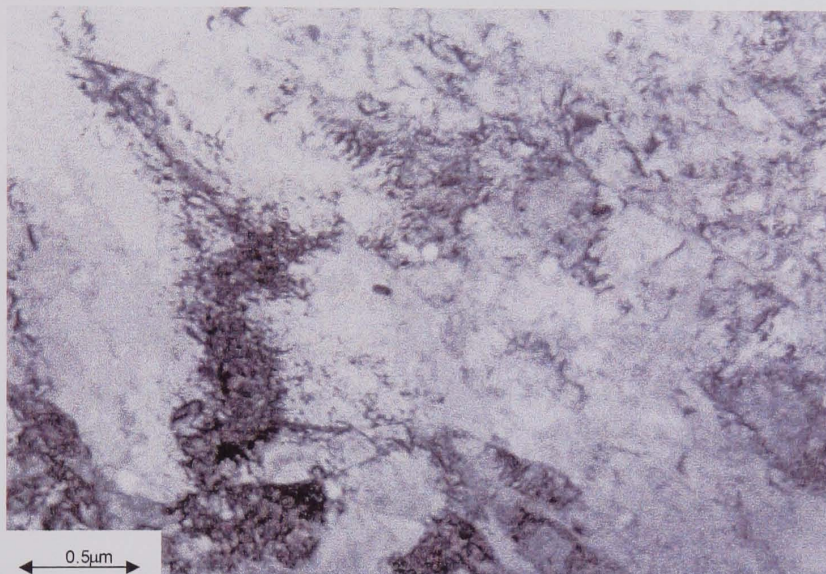
Figure 7.4b Area of fine particles in Alloy D

Figure 7.5 Area of coarse particles in Alloy C3(1)

A schematic diagram of the apparatus is shown in Figure 7.6. The heating rate for all samples was 400°C/hr and all samples were air cooled.
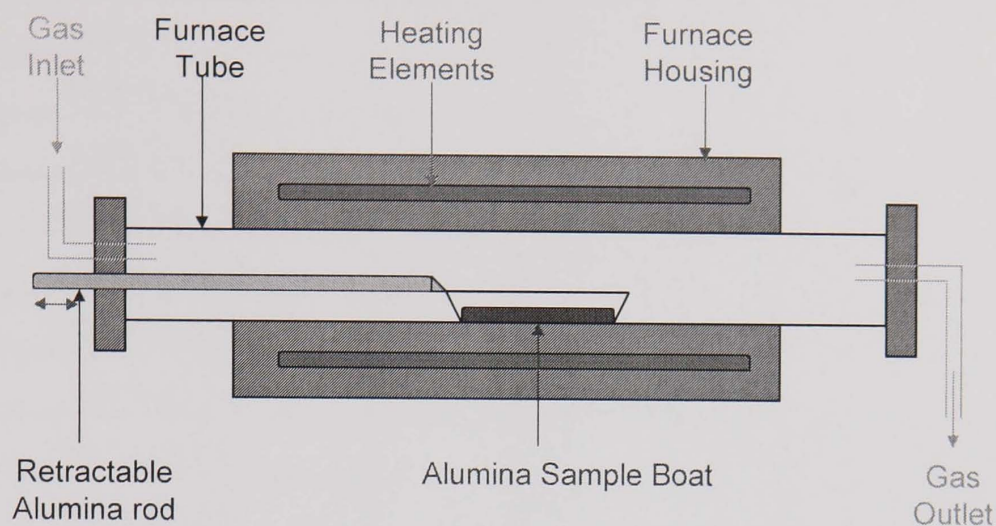
Figure 7.6 Schematic diagram of heat treatment apparatus

7.6.1 Secondary Recrystallisation Heat Treatment Results

7.6.1.1 Alloy C3

For the Alloy C3 material, two distinct regimes were apparent: no grain growth at lower temperature, and extensive columnar grain growth of a few grains at higher temperatures after an incubation time, as shown Table 7.4. Secondary recrystallisation produced very large grains (up to 10mm in length and 1mm in diameter were observed). The highly anisotropic structure closely resembles a directionally solidified structure with the elongated columnar grains aligned along the extrusion axis. The grains boundaries were found to be serrated due to the pinning of particles, resulting in an interlocking nature in the longitudinal direction as shown in the optical micrographs in Figures 7.7 a & b.

In order to investigate if a critical value of "thermal energy" is required before the onset of secondary recrystallisation, the Hollomon parameter, Hollomon & Jafee(1945), was used to combine the effects of time and temperature.

$$Hp = T(20 + \log t) \tag{7.2}$$

where t is the heat treatment time in hours and T is the absolute temperature. The Hollomon parameter values are included in Table 7.4.

Heat Treatment Procedure	Hollomon Parameter $(\times 10^3)$	Grain Growth	Hardness (HV_{30})
(As-extruded)			236
1350°C x 10 hrs	34.08	Yes	158
1350°C x 5 hrs	33.59	Yes	162
1350°C x 1 hr	32.46	Yes	172
1200°C x 100 hrs	32.41	Yes	167
1200°C x 10 hrs	30.93	Yes	169
1200°C x 6 hrs*	30.61	Yes	165
1200°C x 5 hrs	30.49	Yes	172
1200°C x 4.5 hrs*	30.42	Partial	231
1200°C x 4 hrs*	30.35	No	228
1200°C x 2 hrs *	29.90	No	234
1200°C x 1 hr	29.46	No	235
1150°C x 168 hrs*	31.63	No	222
1150°C x 100 hrs*	31.31	No	219
1150°C x 10 hrs*	29.88	No	222
1150°C x 5 hrs*	29.45	No	225
1150°C x 1 hr*	28.46	No	232
1100°C x 100 hrs	30.21	No	227
1100°C x 10 hrs	28.83	No	230
1000°C x 100 hrs	28.01	No	234
1000°C x 10 hrs	26.73	No	232
1000°C x 5 hrs	26.35	No	229
1000°C x 1 hr	25.46	No	232
900°C x 100 hrs	25.81	No	234
900°C x 10 hrs	24.63	No	234
900°C x 5 hrs	24.28	No	235

* ADDITIONAL TESTS

Table 7.4 Results of Heat Treatment for Alloy C3(1)
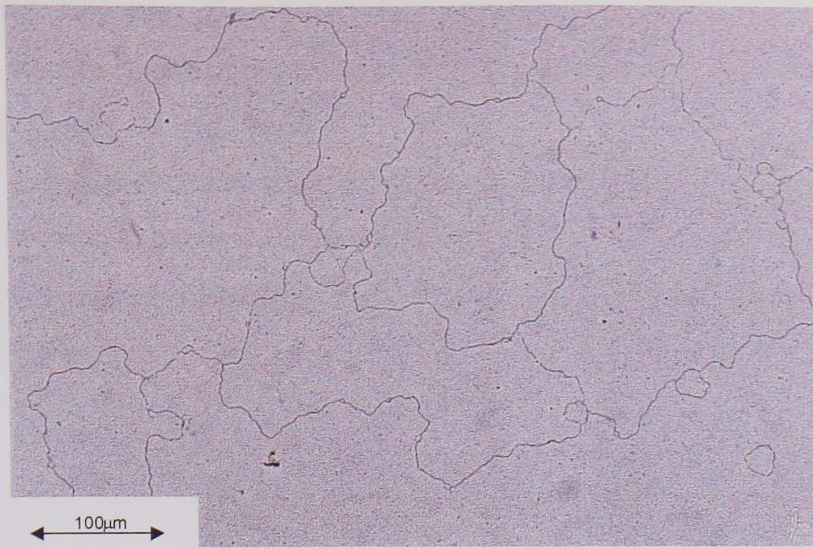
Figure 7.7a Transverse view of Alloy C3(1) Coarse secondary recrystallised structure

Figure 7.7b Longitudinal view of above
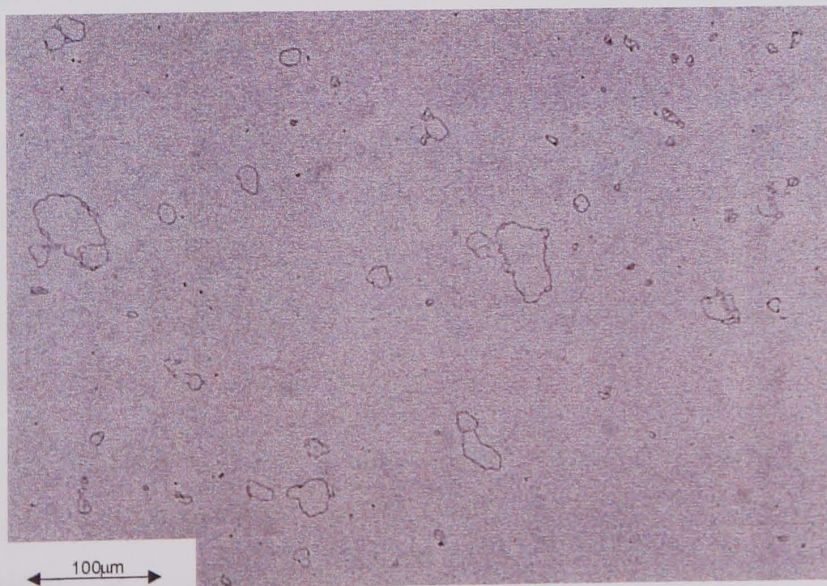
Figure 7.8 Initiation of secondary recrystallisation

It was found, however, that the Hollomon parameter only predicted the conditions necessary for the onset of secondary recrystallisation above the critical temperature, which was found to be 1200°C. Above this, a Holloman parameter value of ~30.5x10^3 corresponded to secondary recrystallisation conditions. Below this critical temperature no secondary recrystallisation occurred even though heat treatment time / temperature combinations gave greater Hollomon parameter values. The factors controlling the "triggering" of secondary recrystallisation are discussed in Chapter 8.

In addition to the distinctive features of grain growth in this titanium nitride strengthened alloy, the minimum temperature necessary to induce secondary recrystallisation was also surprising. The secondary recrystallisation temperature of 1200°C corresponds to approximately 0.8Tm which is significantly higher than the 0.5Tm value commonly observed for grain growth (albeit for normal grain coarsening) in this alloy type without the titanium nitride particles.

Investigation of the behaviour of the materials at the minimum observed heat treatment temperature for additional times around the observed incubation time resulted in mainly two alternatives; no growth or complete grain growth to the elongated structure described above. Only in one instance (1200°C x 4.5hrs) was partial secondary recrystallisation observed. In this case a few grains have begun to grow within the fine equiaxed matrix observed (Figure 7.8). At no stage was an equiaxed intermediate sized grain structure present. This indicates that only a few grains grow and when grain growth starts, it rapidly reaches completion. The results of this survey are included in Table 7.4.

The grain growth in the samples corresponds with a decrease in hardness of around 60 Hv$_{30}$ points, as shown typically in Table 7.4 and Figure 7.9. The excess energy stored by the material in the as extruded condition is primarily in the form of grain surfaces and, to a lesser extent, due to dislocations. Thus, after the secondary recrystallisation, this energy is minimised.

The features observed here as a result of the C3 grain growth studies are similar in many ways to secondary recrystallisation. The characteristic features of secondary recrystallisation, as summarised by Cahn (1966) are as follows:

I. Secondary recrystallised grains are particular grains of the initial structure, which have become enlarged and are not freshly nucleated.

II. There is a significant incubation period before the onset of secondary recrystallisation.

III. It is generally accepted that the "grains to grow" are larger than the average grain size and that they have orientations different to those within the primary recrystallised structure.

IV. Normal grain growth must be inhibited for secondary recrystallisation to occur.

V. The texture of the secondary recrystallised structure usually differs from the primary texture.

VI. There is usually a well defined minimum temperature, which must be exceeded for secondary recrystallisation to occur which is dependent on the prior thermo-mechanical processing.
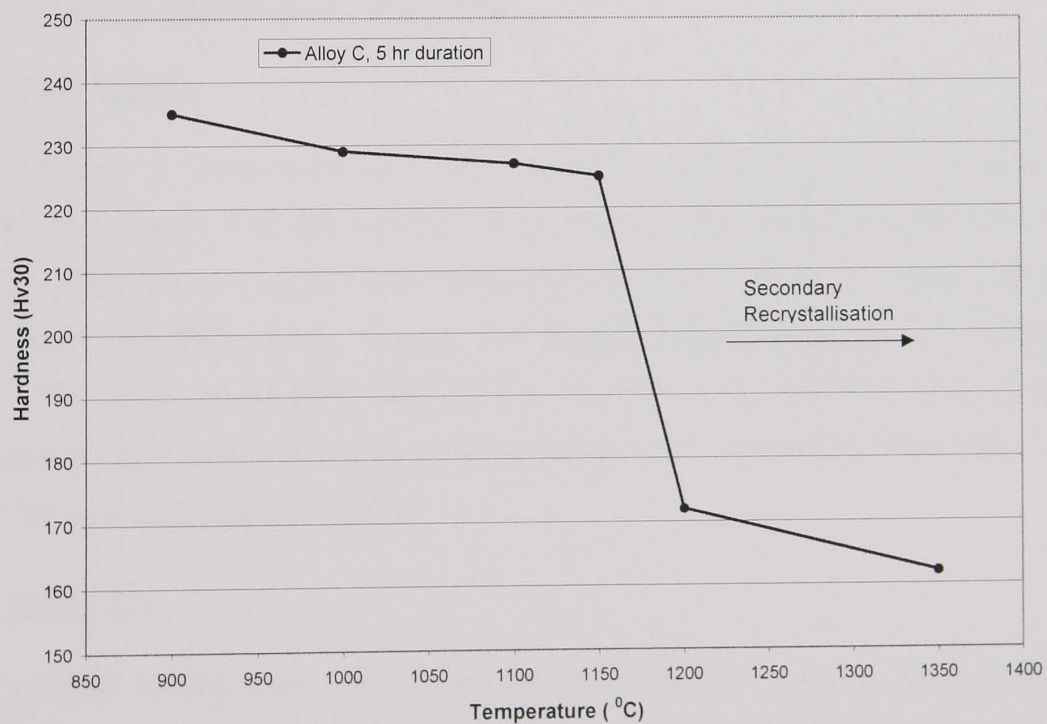
Figure 7.9 Decrease in hardness due to secondary recrystallisation

7.6.1.2 Martensitic Alloy D

The martensitic alloy D material was subjected to a similar heat treatment schedule to that performed on Alloy C3. In this case the material did not secondary recrystallise under any of the heat treatments. At the highest temperatures and times, there was a minor amount of grain growth, typically from 5μm to 9μm. This, however, is due to precipitate coarsening as was observed with the Batch I alloys.

The major difference between this material and the C3 material is that the Alloy D material undergoes a phase transformation from martensite to austenite at around 720°C. This temperature is lower than conventional martensitic creep resistant steels due to the addition of 3wt% nickel. The result is that the high dislocation density observed in the samples post extrusion due to the transformation to martensite will be removed by the re-ordering during the transformation to FCC austenite. At the recrystallisation temperature the sub-micron equiaxed austenitic grains are effectively strain free. Reasons for the martensitic alloy D not recrystallising to the large interlocking grains is discussed in Chapter 8 where the various factors affecting/controlling the triggering of secondary recrystallisation are discussed.

7.7   STRESS RUPTURE TESTING

7.7.1 Test Matrix

As per Chapter 6, tests were performed at 600°C and 120 N/mm². In addition, it was also considered that the strengthening effect of the dispersed titanium nitride could be apparent at higher test temperatures and, therefore, some iso-stress rupture tests (58 MPa) were carried out at test temperatures in the range 600-700°C. The stress of 58 MPa was chosen, as this is the BS1113 codified design stress (the design stress contains a safety factor over the actual test stress range) for P91 for 100,000 hours at 600°C.

7.7.2 Alloy C3

Stress rupture testing was carried out on the alloy C3 material after secondary recrystallisation at 1200°C x 5 hrs. This is the minimum time to result in secondary recrystallisation at the "cut off" minimum recrystallisation temperature. This minimum time and temperature combination was chosen to minimise the degree of

titanium nitride precipitate ripening that will occur and still achieve the coarse interlocking grain structure.

For the alloy C3 material a typical creep curve is shown in Figure 7.10. What is evident is the high initial strain, which equated to around 3%; this is approximately five times that of comparable P91 tests. This large difference is due to the need to form pinned dislocation networks in the dislocation free recrystallised ferritic steel, whereas these are already present in P91 due to the martensitic transformation. Once this strain had accumulated, a limited degree of constant secondary strain rate was apparent before tertiary creep and failure occurred.

Examination of the failed specimens revealed that they all possessed a distinctive crimped "neck" region surrounding the failure as shown in Figure 7.11. The reduction in area was not relatively uniform along the gauge length as observed with the Batch I fine grained materials, but was concentrated in this crimped neck region. The ridges of the neck correspond to the large interlocking grain boundaries. An optical examination of the cross section of the fracture surface (Figure 7.12) revealed the fracture path to be both along the grain boundaries and through the grains.

The results of the tests are presented in Figures 7.13 & 7.14 and Table 7.5. Although the tests revealed that the material still possessed very poor creep properties, the creep limiting process of grain boundary sliding resulting in almost superplastic behaviour has been overcome. The secondary recrystallised Alloy C3(2) material possessed superior properties than Alloy C3(1). This is due to the increase in titanium content and thus titanium nitride particles resulting in the observed decrease in interparticle spacing (despite larger average particle size).

7.7.3 Alloy D Material

The alloy D material was tested in the extruded and tempered (700°C x 2 hrs) condition, and after 1350°C x 4 hrs followed by the same tempering heat treatment in order to determine if the slight amount of normal grain growth has been sufficient to avoid extensive grain sliding. It is accepted that the titanium nitride particle coarsening resulting from the 1350°C x 4 hrs heat treatment has largely removed any strengthening effect that the titanium nitride particles could impart.

Both heat treated conditions revealed a low rupture strength, high strain rate and high final elongation. Thus, similar to the earlier tests, the creep rupture properties are still controlled by grain boundary sliding. Test results are shown in Figures 7.13 & 7.14 and Table 7.5.

Alloy	Temperature (°C)	Stress N/mm^2	Rupture Life (hrs)	Rupture Strain (%)
C3(1)	600	120	123	45
	600	100	235	37
	600	58	2305	35
	625	58	174	48
	650	58	26	32
	700	58	2	75
C3(2)	600	58	6337	42
	625	58	846	43
	650	58	139	43
	675	58	35	45
D Extruded + temper (700°C x 2hrs)	600	120	87	98
	600	100	110	85
	600	80	215	92
	600	60	1168	93
D 1350°Cx4hrs + temper	600	100	56	108
	600	80	154	91

Table 7.5 Batch II Alloys Stress rupture results

Test Temp	600C
Stress	100 N/mm
% Elon	37.6
Duration	255 hrs
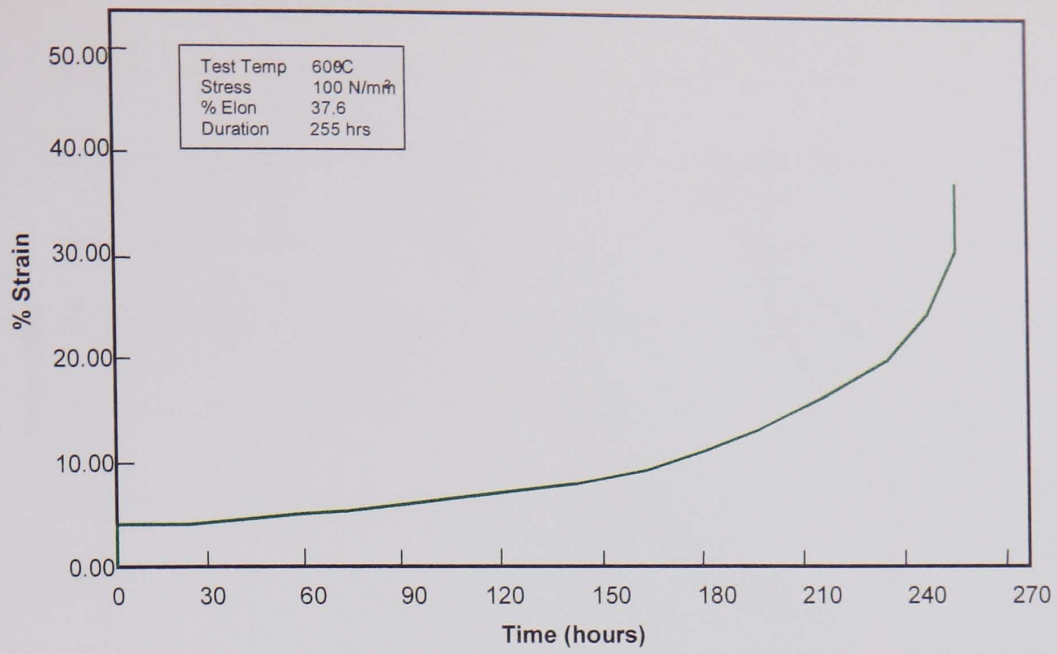
Figure 7.10 Typical Alloy C3 creep curve

1 CM
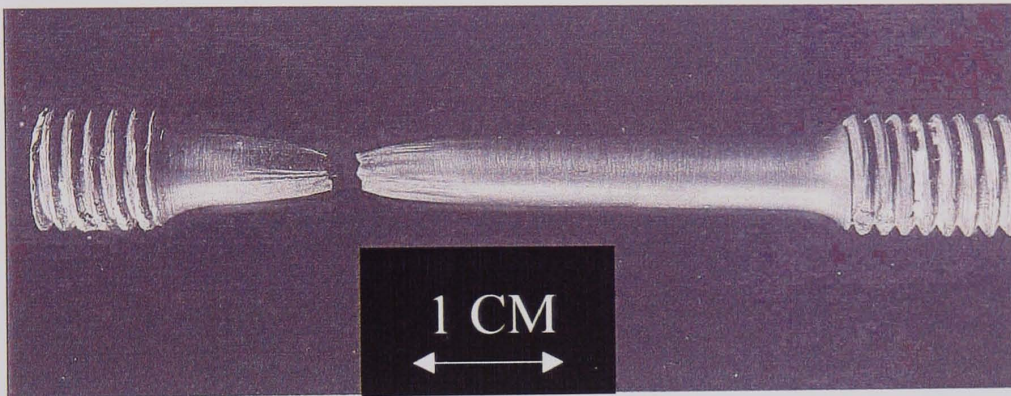
Figure 7. 11 Alloy C3 typical "Crimped" rupture morphology

200µm

Figure 7.12 Cross section of Alloy C3(1) stress rupture failure
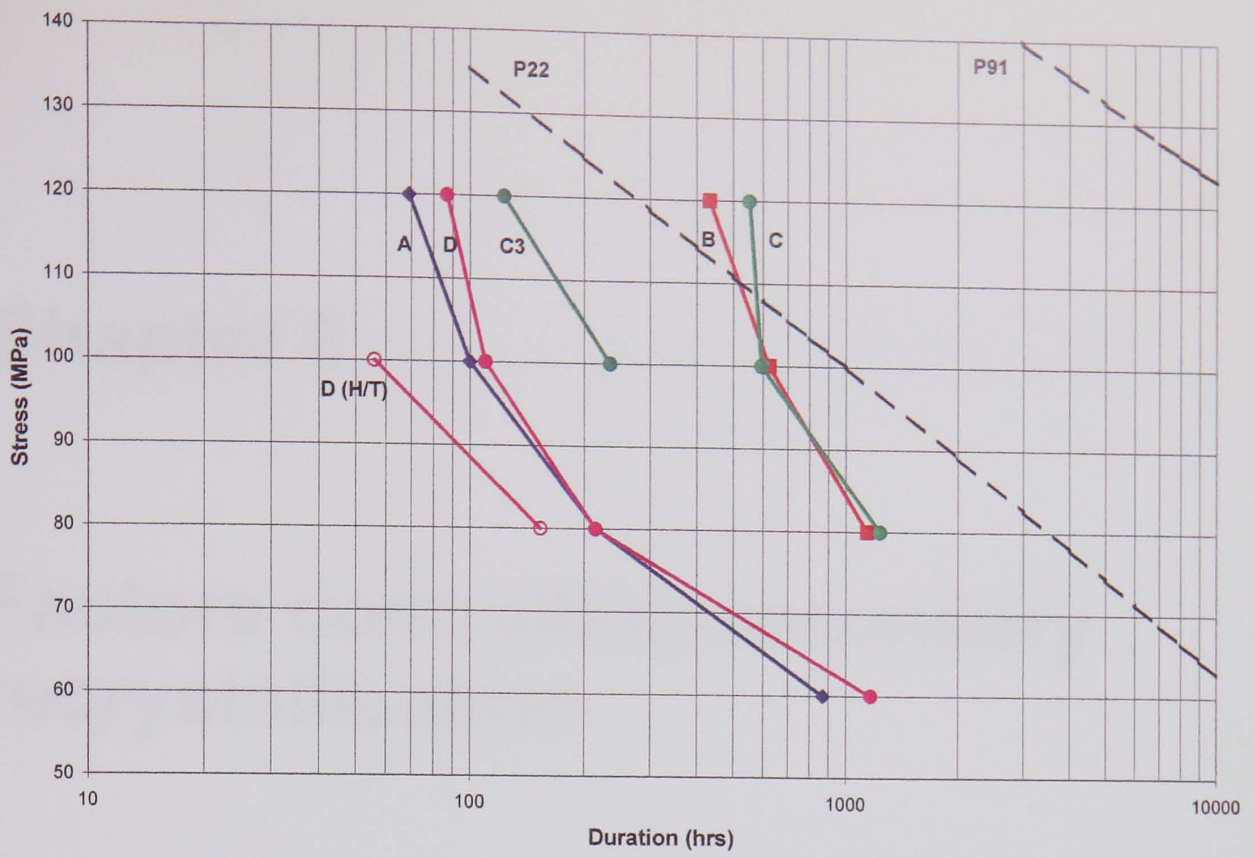
Figure 7.13 Iso-temp (600°C) stress rupture results
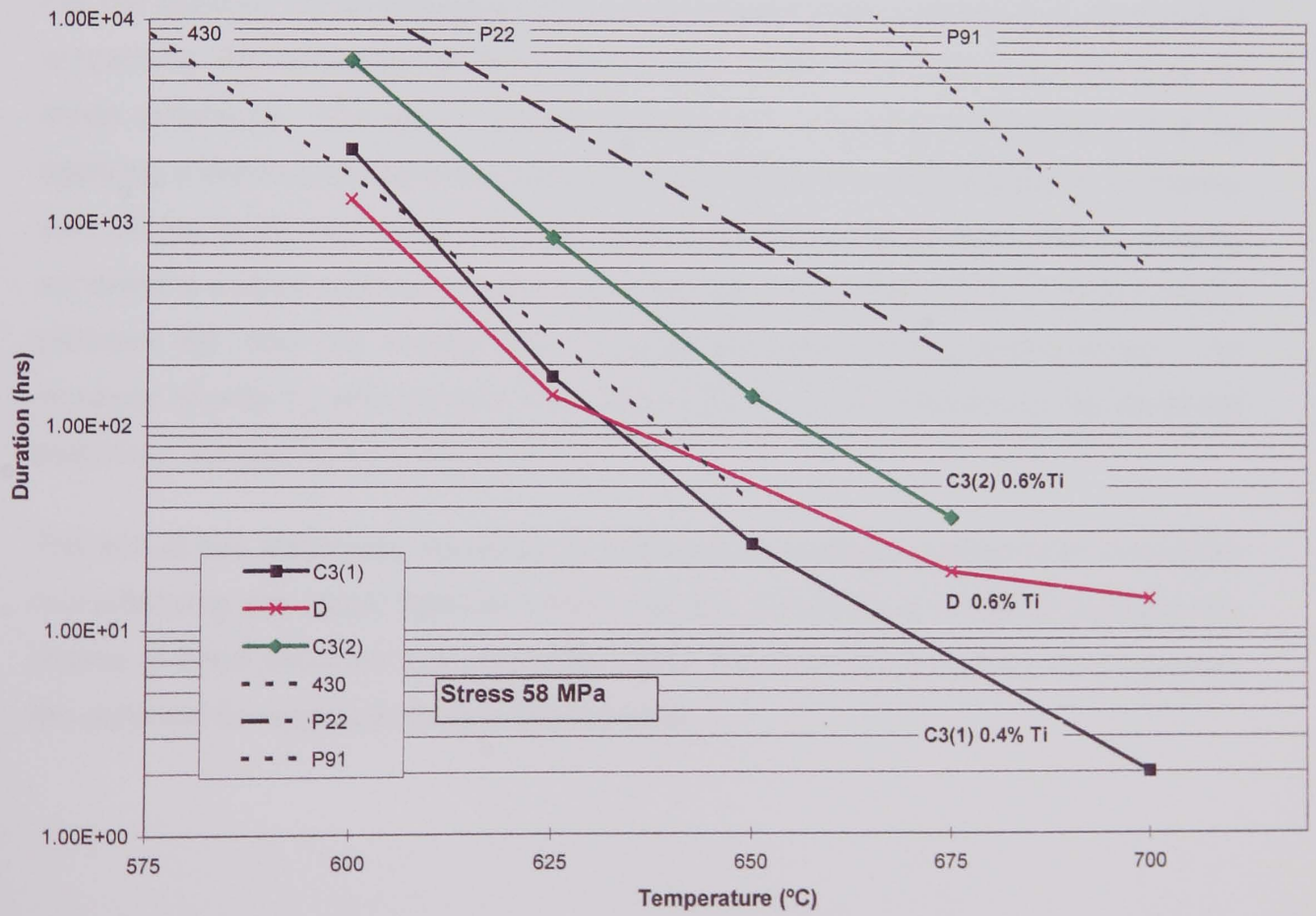
Figure 7.14 Iso-Stress (58 MPa) stress rupture results for Batch II alloys

Chapter 8

Factors controlling secondary recrystallisation

For the titanium nitride strengthened steel developed here to achieve its objective of surpassing the conventional ferritic/martensitic steels, this alloy must increase its creep resistance. The alloy C3 trials have proven to be very successful in that, by applying a thermo-mechanical treatment it can secondary recrystallise in a manner very similar to the high creep strength oxide dispersion strengthened alloys. Having achieved a coarse grained structure, the strengthening effect of the titanium nitride particles are now not masked by the grain boundary sliding phenomenon. An increase of only 0.2wt% titanium from Alloy C3(1) to C3(2) resulted in the life of the specimen increasing by a factor of five.

The aim at this stage was, therefore, to utilise the knowledge gained from secondary recrystallising the lower titanium nitride content C3 steels in order to produce the coarse grained structure in a steel with higher titanium nitride content and therefore the potential for appreciable strength increase.

8.1 ALLOY C4 DESIGN

The composition of the alloy chosen was similar to Alloy C3 but the titanium was increased to 1.5wt% and the nitrogen was increased to achieve a stoichiometric composition. The target composition is shown in Table 8.1.

Material	Cr	Si	Mo	Ti	Ni	Mn	N	C
Target C4	18	0.3	1.0	1.50	0	0.5	0.44	<0.02
Alloy C4	18.5	0.37	1.07	1.12	0.003	0.35	0.47	0.009
Difference	-	+0.1	+0.1	-0.4	-	-0.1	+0.03	

Table 8.1 Alloy C4 chemical composition

8.2 ALLOY C4 PRODUCTION

The production route for Alloy C4 was as follows:

Base alloy produced by Special Melted Products: 10% additional titanium added to compensate for titanium lost to refractories.

Converted to powder by gas atomisation at Osprey Powder: In order to minimise the degree of counter diffusion, the nitrogen diffusion distance was decreased by decreasing the powder particle size. To achieve this the titanium containing feedstock was converted to powder at the Osprey powder production plant using argon gas as the atomising agent. The Osprey powder plant produces powder typically <100μm diameter which is finer than that produced on the Osprey spray production plant described in Chapter 4. This powder was then classified to sub 45μm powder diameter by Osprey. This resulted in approximately half of the material weight being discarded.

Mechanofusion by AEAT: In order to minimise the degree of retained chromium particles the chromium nitride was restricted to at least 18% nitrogen content and less than 10μm diameter. Utilising chromium nitride supply CRN4 achieved this.

Extrusion to bar by Inco: Minimum temperature and hold time (1000°C x 1 hr) used to minimise titanium nitride coarsening. High extrusion ratio used 16:1 to maximise the amount of deformation.

8.2.1 Production Results

Even though additional titanium was added to the melt stock, analysis after casting at Special Melted Products revealed that the titanium content present was 1.32wt%. After re-melting in order to atomise the stock to powder, an additional 0.2wt% was lost. In both cases, the titanium losses were to the refractories during the melting processes.

Plotting the final chemical composition (Table 8.1) on the Schneider diagram (Figure 8.1) revealed that the alloy is very near the delta ferrite/austenitic plus martensite plus delta ferrite boundary. Metallographic examination and the Permascope retained austenite meter revealed the alloy to be fully ferritic.
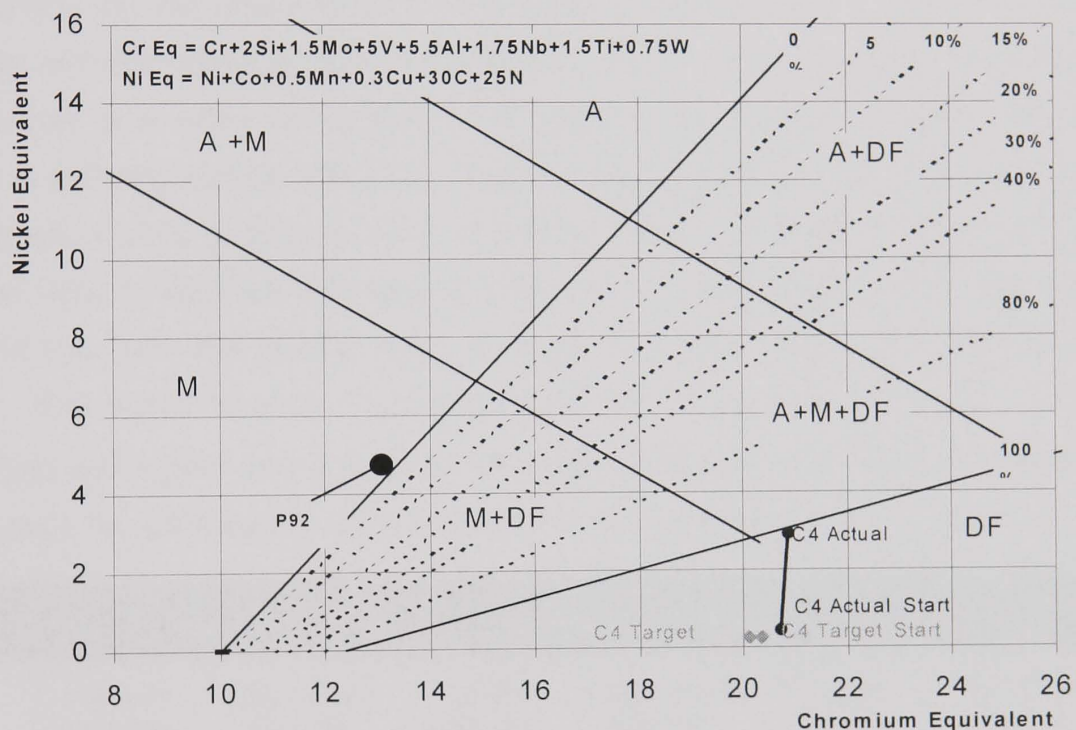
Figure 8.1 Schneider diagram prediction for Alloy C4

8.3   ALLOY C4 MICROSTRUCTURE

8.3.1 Optical Examination

Optical examination of the material in the as extruded condition revealed a relatively homogeneous structure (Figure 8.2). There is still some evidence of the prior powder particles; however, there is no evidence of the counter diffusion of the titanium. Within the microstructure there are some retained chromium nitride particles. These are agglomerations of sub 10μm chromium nitride particles rather than individual particles and are dispersed throughout the material.

8.3.2 TEM Examination

Examination was carried out on thin foils taken perpendicular to the extrusion direction. Investigations were undertaken to assess the microstructure and to measure the particle size and interparticle spacing of the titanium nitride precipitate.

As with Alloy C3, the particle size and the edge to edge nearest neighbour distance was determined from 20 random fields. Table 8.2 gives the results of the measurements carried out on the Alloy C4 material and the baseline measurements taken on the Alloy C3 (1) and (2) materials. Although only the maximum, minimum and average values are quoted, the particle distributions are recorded and will be published. The evolution from Alloys C3 to C4 has reduced the interparticle spacing considerably by the combination of increased volume fraction of titanium nitride particles and decreased powder particle size. It is proposed that the decrease in particle size is a direct consequence of reducing the nitrogen diffusion distance (aimed at avoiding counter diffusion). This decrease in particle size is in accordance with equation (3.5) derived by Birks & Meier (1983). Although the particle size obtained here for the Alloy C4 material produced by the Mechanofusion route is less than half that from the Osprey route, in dispersed particle terms it is still relatively coarse. The matrix microstructure is similar to that observed for Alloy C3 in that it possesses a fine grain size ($\sim$5μm) and a largely dislocation free structure indicating that primary recrystallisation has occurred. A typical area is shown in Figure 8.3.

	C3 (1)		C3 (2)		C4	
	Particle Diameter (nm)	Edge-Edge Spacing (nm)	Particle Diameter (nm)	Edge-Edge Spacing (nm)	Particle Diameter (nm)	Edge-Edge Spacing (nm)
Max	390	1650	430	2230	200	540
Min	190	630	160	150	61	90
Average	238	884	256	676	126	287

Table 8.2 Titanium nitride particle diameter and interparticle spacing measurements

8.4   SECONDARY RECRYSTALLISATION HEAT TREATMENT TRIALS

Heat treatment trials similar to those conducted on Alloy C3 (Table 7.4) i.e. temperatures between 900°C and 1350°C and durations between 1 and 100 hours did not result in any secondary recrystallisation. Similar to the alloy D martensitic

material some normal grain coarsening was apparent at the highest temperatures and times, however, the extent of this grain growth would not be large enough to avoid appreciable grain boundary sliding as found with alloy D.

8.5 ANALYSIS OF SECONDARY RECRYSTALLISATION TRIGGERING

In order to investigate the cause of the non-recrystallisation of Alloy C4 and Alloy D, the resistance to recrystallisation and the factors influencing the "triggering" of secondary recrystallisation were investigated.

The general model for grain growth is that "nucleation" occurs by the bowing of a grain boundary. The fact that secondary recrystallisation only occurs at very high temperatures (in the order of 0.8 of the melting point Tm as opposed to normal grain growth at about 0.5 Tm in the material without titanium nitride particles) and the fact that it occurs by the very fast growth of only a few grains to a very large size, points to a very large activation energy for the process.

This was investigated by Sha & Bhadeshia (1997) who calculated that the previous models based on the Johnson-Mehl-Avrami approach reviewed by Christian (1975) do not accurately predict the transformation temperature. This was due to the model failing to consider the nucleation process and thus the origin of the high activation energy. The assumption that there are a fixed number of nucleation sites at time zero gives too low an activation energy and thus transformation temperature calculated by Sha and Bhadeshia was too low.

The model proposed by Sha & Bhadeshia accounts for the very high activation energy by considering the additional effect that the very small grain size has. It was noted that there was less constraint on a grain boundary bulge when the grain junctions are spaced at distances greater than the critical bulge size. This applies to a "normal" grain size as shown in Figure 8.4a. With the very fine, micron-sized grains found in mechanically alloyed metals or in the titanium nitride strengthened materials, the grain junctions are themselves pinning points as shown in Figure 8.4b. Thus the pinning from the particles and the grain junction make it very difficult to form large enough bulges to nucleate grain growth. The model, therefore, takes cognisance that individual grains cannot be considered to be topologically independent when the grain size becomes sufficiently small.
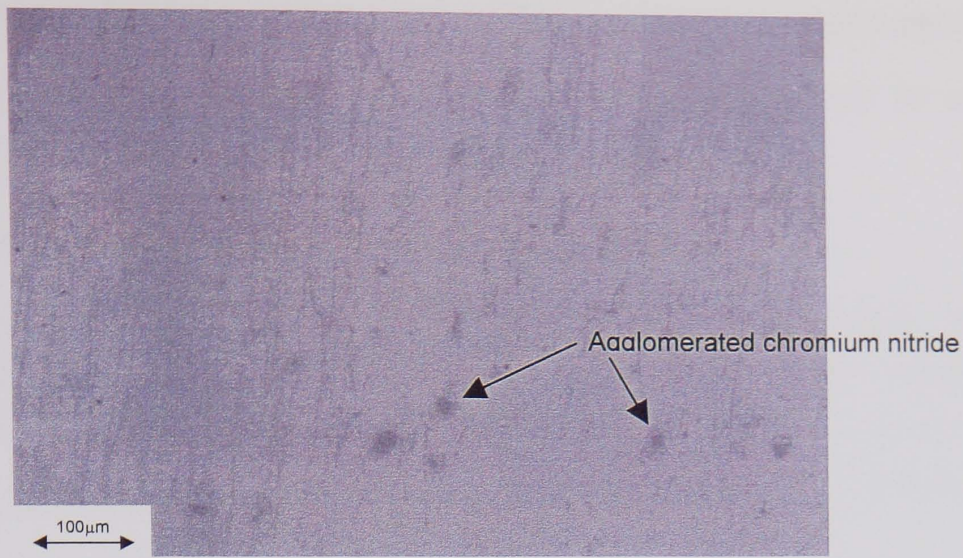
Figure 8.2 Microstructure showing areas of agglomerated chromium nitride
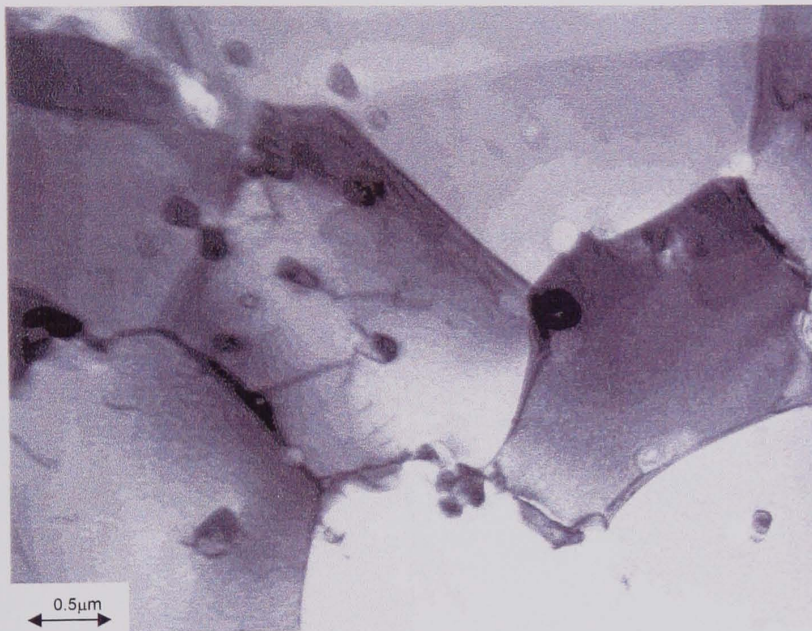
Figure 8.3 Alloy C4 particle size and distribution
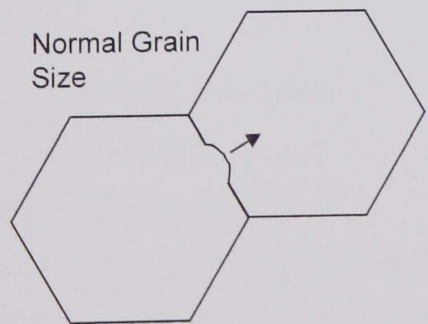
Figure 8.4a&b   Schematic of grain boundary bulging in a)conventional alloys and b) stable fine grain sized alloys, after Sha & Bhadeshia (1997)

8.5.1 Factors Affecting the Onset of Secondary Recrystallisation

There are a number of factors that apparently affect the "triggering" for secondary recrystallisation; these are discussed in the following sections.

8.5.1.1 Influence of the dispersoids and precipitates:

According to Gladman (1966) and Gladman & Pickering (1967), the grain coarsening temperature for the onset of secondary recrystallisation represents the temperature at which some of the particles pinning the grain boundaries reach a critical size by coarsening, thus releasing the grain boundary. The critical radius is given by:

$$r_{crit} = \frac{6R_o F_v}{\pi} \left(\frac{3}{2} - \frac{2}{Z} \right)^{-1} \tag{8.1}$$

The critical pinning size is very dependent on the volume fraction F_v and the matrix grain radius R_o. Thus a grain boundary will be able to migrate despite the presence of dispersed particles if the energy released, per particle, by the migration process is equal to or greater than the energy increase which is associated with the boundary particle separation process. An investigation of the grain growth process by Novikov (1997) using modelling techniques for general alloys found that complete secondary recrystallisation can be achieved provided the pinning force decreases in two stages, first, slowly by particle coarsening, and then far more rapidly by particle dissolution.

Hotzler & Glasgow (1980) deduced that secondary recrystallisation in nickel based MA alloy MA6000 which is dual dispersed with yttria and γ' was due to particle dissolution rather than particle coarsening. It was found that the secondary recrystallisation temperature was close to the γ' solvus and thus it was deduced that dissolution of the γ' led to the reduction in the pinning force, resulting in secondary recrystallisation as discussed above. Singer & Gessinger (1982) refuted Hotzler & Glasgow's findings by performing recrystallisation experiments on both MA6000 and MA760. MA760 which contains similar amounts of yttria, but only a very low level of γ', showed similar recrystallisation temperatures. Thus, it was deduced that the dissolution of γ' does not influence the onset of secondary recrystallisation.

101

Mino, Nakagawa & Ohtomo (1987) suggested that it was the coarsening of the yttria that was acting as a trigger for secondary recrystallisation. The "coarsening" noted by Mino et al was only from 20-30nm to 30-50nm. However, although the particle size of the yttria increases slightly during high temperature heat treatments Krautwasser et al (1994) found that this was not due to coarsening driven by interface energy minimisation, but complicated effects originating from the reactions between the yttria, aluminium and oxygen. It was found that, although the particle size increases slightly, the volume fraction of particles also increases, whereas any large alumina particles tend to dissolve as the alumina reacts with the yttria. Therefore, the growth of the yttria based dispersoids are unlikely to trigger secondary recrystallisation.

From the work carried out within this study, it is apparent that particle coarsening does influence the triggering of secondary recrystallisation, but not in the manner postulated by Gladman, Hotzler, Mino et al. It was found from Alloy C4 that the coarsening of the titanium nitride precipitates allowed some normal grain growth (for $\sim 4\mu m$ to $\sim 7\mu m$) but no secondary recrystallisation occurred. This grain growth has two contradictory effects. Firstly, with increasing grain size, the effective resistance to significant bowing decreases, therefore secondary recrystallisation becomes easier. Secondly and concurrently, the driving force for recrystallisation, i.e. energy stored in grain boundaries, is also reduced. The relative effects of each driving force will determine if secondary recrystallisation will or will not occur. This argument only holds if it is assumed that there is a cross over point. The cross over point is the theoretical minimum energy for secondary recrystallisation. It is therefore proposed that the small amount of normal grain growth that occurred due to the particles coarsening was sufficient to reduce the driving force (from the grain boundary area) to a level where it was insufficient to overcome the activation energy (albeit reduced) for secondary recrystallisation. Thus, following this logic, no secondary recrystallisation will occur even with extensive high temperature treatments.

8.5.1.2 Influence of strain

In order to recrystallise Alloy C4, methods have to be found to increase the driving force for secondary recrystallisation or decrease the activation energy. Therefore, to secondary recrystallise Alloy C4 either the stored energy for secondary recrystallisation has to be increased or the pinning force has to be decreased.

The influence of strain on secondary recrystallisation has been investigated in several studies. Jaeger and Jones (1994), in considering the iron based ODS alloy directly related the degree of strain energy to the driving force for the generation of secondary recrystallisation type structure. They discussed the fact that the development of the coarse grain microstructure was more akin to primary recrystallisation (to a very large grain size) due to the fact that the driving force was the reduction in strain energy.

Alamo, Regle & Bechade (1992) and Regle & Alamo (1993) conducted extensive studies regarding the effect of cold deformation on the recrystallisation behaviour of MA956 and MA957. Two deformation processes were used, swaging and drawing, with reductions ranging from 10-60%. In all cases, deformation led to a reduction in the secondary recrystallisation temperature, the effect being the greatest for cold drawn samples. For MA956 the maximum reduction in secondary recrystallisation temperature was 600°C (1350-750°C) and for MA957 the reduction was 200°C (1450-1250°C). In order to investigate if a similar effect could be imparted to the alloy C4 by means of cold straining the material, the following experiment was performed.

8.6   COLD STRAIN EXPERIMENT

In order to examine the effect of strain on the onset of secondary recrystallisation, eight tensile specimens (60mm gauge length) were manufactured from the C4 extruded bars and the Alloy D material. The specimens were then strained at room temperature on the Zwick tensile tester at $3.79 \times 10^{-4} s^{-1}$ strain rate to the desired elongation. Tests were conducted at 2% strain intervals up to the maximum allowable. The strain was measured during the test by means of linear voltage displacement transducers attached to the gauge length. The tests were stopped when the calculated elastic plus plastic elongation was reached. Measurements were then made on the specimens by means of the pre-marked grid to ensure that the elongation was uniform over the area from which the specimens were removed. For Alloy C4, the material properties allowed uniform strains up to 12%. Beyond 12%, necking occurred in a localised area. The maximum strain to failure over the entire gauge length was 15%. The martensitic Alloy D material possessed lower ductility, however, by removing specimens from the necked region it was possible to obtain similarly strained specimens.

After testing, 5mm sections of the gauge length were removed. The actual strain measurements for the individual tensile samples were 2.0%, 3.9%, 5.9%, 8.0%, 9.9%, 11.9% for Alloy C4 and 1.9%, 3.9%, 5.9%, 7.9%, 9.9%, 12.2% for Alloy D. All the strained sections of gauge length were then subjected to heat treatments at 1000, 1050, 1100,1150,1200, 1250, 1300 and 1350°C for durations of 1, 2, 4, 8, 16, and 24 hours. Heat treatments were carried out in the carbolite furnace described earlier using the same protective argon atmosphere and temperature measurement apparatus. The heating rate was 400°C/hour and all samples were air cooled.

8.6.1 Results

This survey revealed that it was possible to induce secondary recrystallisation in Alloy C4 by cold straining prior to heat treatment. The parameters necessary to induce complete secondary recrystallisation were, however, confined to a limited range of conditions involving high prior deformation and a narrow range of high temperatures. The complex effect on the grain size that arises as a result of the variation in pre-strain and heat treatment temperature and time is shown on the three dimensional graph shown in Figure 8.5 where the average grain size is plotted against the pre-strain and temperature for 24 hour duration. As can be observed, complete secondary recrystallisation is restricted to pre-strains of 10 and 12%, which are close to the plastic limit for the material. The results of heat treatment matrix for the 12% strain are shown in Table 8.3.

Temperature	Time (hrs)					
(°C)	1	2	4	8	16	24
1000	X	X	X	X	X	X
1050	X	X	X	X	X	X
1100	X	X	X	X	X	X
1150	X	X	X	X	X	X
1200	X	X	PR	R	R	R
1250	X	X	PR	R	R	R
1300	X	R	R	R	R	R
1350	R	R	R	R	R	R

X - No effect   PR – Partial Recrystallisation   R - Secondary Recrystallisation

Table 8.3 Results of secondary recrystallisation heat treatment matrix on 12% strained samples

8.6.1.1.1   Partial Secondary Recrystallisation

Between the boundaries of secondary recrystallisation and non secondary recrystallisation, partial secondary recrystallisation conditions were observed. This is not incomplete secondary recrystallisation as observed in Alloy C3 (Figure 7.8) but complete secondary recrystallisation of only part of the cross sectional area of the bar. As can be observed in the optical micrograph in Figure 8.6, it is apparent that secondary recrystallisation nucleated at positions near the outer wall then proceeded to grow around the tube circumference. This effect has also been observed by Uhbi (1980) in MA956 sheet, Korb & Sporer(1990) in PM2000, Murakami et al (1993) in MA6000 bar and Jaeger & Jones (1994) in ODM331 tube.

Murakami et al suggests that selective growth was due to a greater alignment of oxide particles in the extrusion direction near the surface rather than in the bulk. Murakami proposed that the alignment of the particles is such that grain boundary pinning is reduced and so grain boundary migration is favoured. Whilst stringers of titanium nitride particles have been observed in the Alloy C4 material there is no evidence from examination of metallographic sections for preferential alignment at the surface. A different explanation has been proposed by Uhbi, Jaeger & Jones and Korb & Sporer. Their explanation is that in the production process the outer surface of the tube or bar receives the greatest degree of plastic deformation. This can be observed in the deformation pattern as a result of the extrusion as shown by Schey (1977) in Figure 8.7. In Figure 8.7 elements at the centre of the billet essentially undergo pure elongation into extruded rod, however elements near the surface undergo extensive shear deformation due to container wall friction. From examination of the extruded bars, the protrusion of the C-steel can stub into the final ~50mm of the bar is indicative of the degree of bar centre to surface deformation mismatch. In the Alloy C4 material it is, however, apparent that during hot extrusion the material dynamically recrystallises removing the effects of the greater surface deformation. Greater surface deformation can also be introduced by the uniaxial cold tensile deformation. As the surface is not constrained by triaxial stresses it will yield earlier and experience greater strain than the centre portion near the failure event. In the case of Alloy C4, this could be the reason for the outer surface partial secondary recrystallisation.

8.6.1.2 Intermediate Strains

For the 6% and 8% strained samples, secondary recrystallisation did occur, but only in the outer fibres of the samples as described above after high temperature long duration treatments as shown in Table 8.4.

Temperature	Time (hrs)					
(°C)	1	2	4	8	16	24
1000	X	X	X	X	X	X
1050	X	X	X	X	X	X
1100	X	X	X	X	X	X
1150	X	X	X	X	X	X
1200	X	X	X	X	X	X
1250	X	X	X	X	X	X
1300	X	X	X	X	PR	PR
1330	X	X	X	PR	PR	PR

X - No effect   PR – Partial Recrystallisation   R - Secondary Recrystallisation

Table 8.4   Results of secondary recrystallisation heat treatment matrix on 8% strained samples

8.6.1.3 Low Strains

Below 6% strain, the cold deformation has no effect upon the secondary recrystallisation response and thus, no secondary recrystallisation was detected. Similar to the earlier work on as-extruded material at the higher temperatures and times, minimal normal grain growth from ~5μm to ~7μm occurred. The plastic strain energy at these relatively low levels did not appear to have any effect upon the extent of normal grain growth.

8.6.1.4 Alloy D Material

No secondary recrystallisation occurred in any of the strained samples even after the most onerous heat treatment cycle.
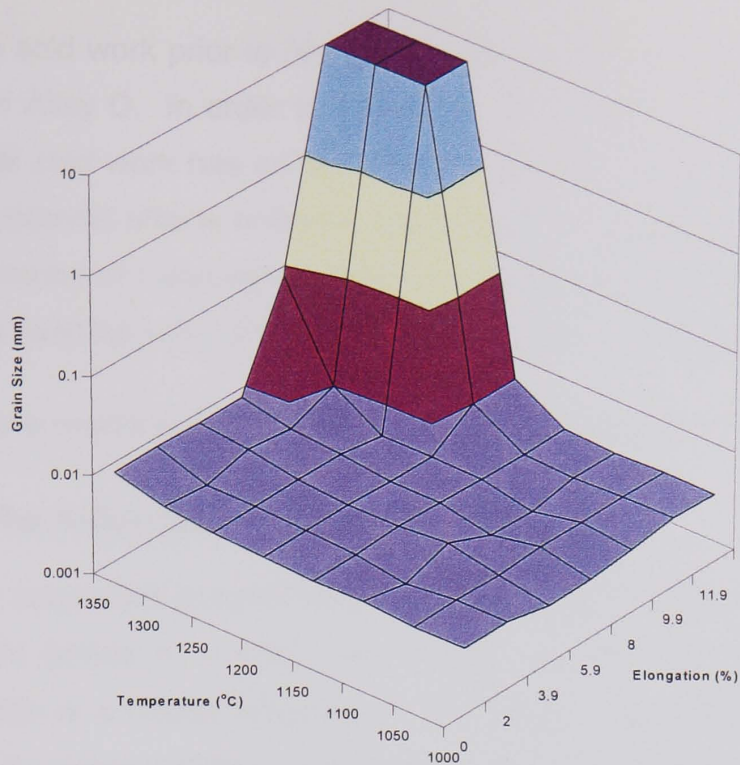
Figure 8.5 Relationship between grain size, deformation and temperature for 24 hour duration
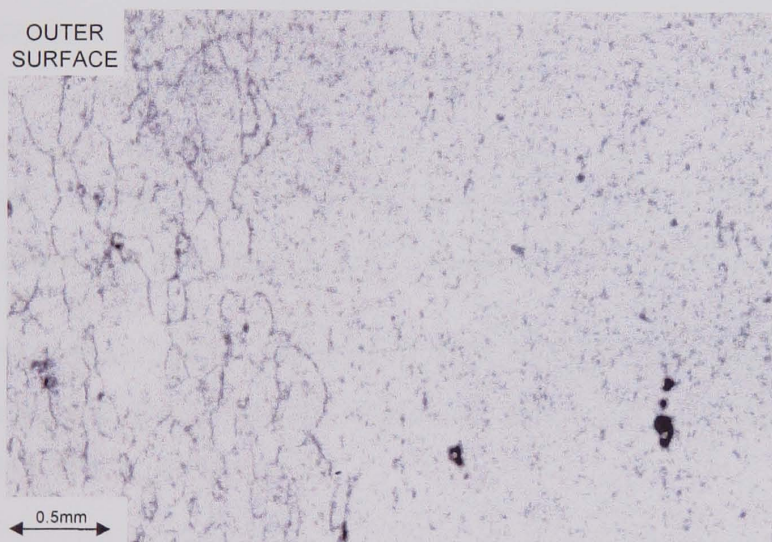
Figure 8.6 Secondary recrystallisation of outer area of bar only. 12% pre-strain/1250ºCx4hours
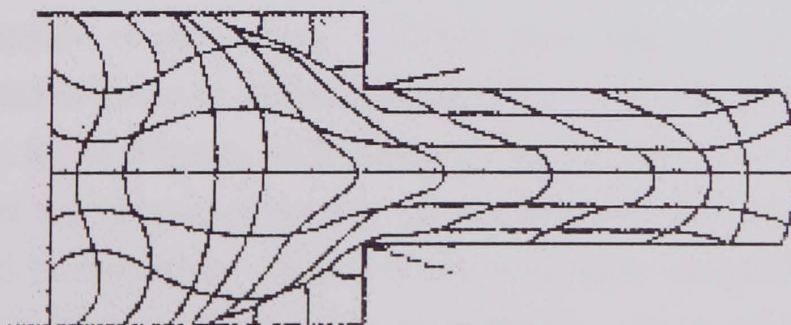
Figure 8.7 Patterns of metal deformation in extrusions after Schey(1977)

8.7 COLD WORK EFFECT

Although cold work prior to heat treatment resulted in recrystallisation in Alloy C4, it did not in Alloy D. In order to determine the reason for this differing behaviour the effect that cold work has on secondary recrystallisation has been analysed. There are two potential effects of the increased strain on secondary recrystallisation. Firstly the generation of dislocations increases the driving force and secondly the strained materials develop sufficient texture to decrease the pinning effect.

The relative merits of each process are described in the following sections.

8.7.1 The Influence of Dislocation Density

Although secondary recrystallisation is defined as the growth of a limited number of strain free grains in a strain free matrix, the fact that the level of prior plastic deformation is a critical influence on the onset of secondary recrystallisation led to Jaeger & Jones (1994) postulating that the driving force for secondary recrystallisation is in fact a combination of the driving force for primary recrystallisation (a reduction in the strain energy associated with the dislocation structure) and the driving force for secondary recrystallisation (a reduction in the surface energy associated with the overall energy of the grain and subgrain boundaries). Thus, it was postulated that secondary recrystallisation was in fact primary recrystallisation to a coarse directional grain structure.

Sha & Bhadeshia (1997) also utilised the combination of the stored energy from the dislocations and the grain boundaries in order to calculate the driving force for recrystallisation as given by

$$\Delta G = \Delta G_{dislocation} + \Delta G_{grain\ boundary} - \Delta G_{particle\ pinning}$$

Sha & Bhadeshia do not differentiate between primary and secondary recrystallisation in their paper. Rather they refer to the typical secondary recrystallised structure as recrystallisation to a coarse anisotropic grain structure. If secondary recrystallisation were triggered by the additional stored energy from dislocations then this would explain the non secondary recrystalllisation of Alloy D. As Alloy D is martensitic, heating to the secondary recrystallisation temperature results in a phase transformation to austenite. As a result of the austenitic transformation, the material effectively loses its dislocation network.

It was found by Chou (1997) in his assessment of the recrystallisation behaviour of MA956 material that the measured stored energy (by means of differential scanning calorimeter) did not increase with deformation. In fact, it was found that deformation led to a reduction in stored energy. There was no clear explanation of these results; however, they led to Chou concluding that the crystallographic texture change observed has a more pronounced effect on the secondary recrystallisation behaviour than the stored energy. In addition, it has also been found the cold work can retard secondary recrystallisation.

8.7.2 Cold Work Retarding Recrystallisation

Several authors have found that rather than induce secondary recrystallisation the converse is true in that additional work actually retarded secondary recrystallisation. This was found to be the case by, Mino, Nakagawa & Ohtomo (1987) who compressively deformed the nickel base MAODS alloy TMO-2 followed by 1280°C for 30 minutes heat treatment. The results show that secondary recrystallisation did not occur in the most heavily deformed areas, but did occur in the areas with least strain.

Work by Singer & Gessinger (1982) on nickel based MA6000 also found that their material could not be recrystallised after pre-straining. It was considered that during the secondary recrystallisation heat treatment the strained grains had enough energy to allow them to grow to a size where secondary recrystallisation would not take place. It was postulated that straining increased the degree of normal grain growth by increasing the coarsening rate, by increasing the diffusivity of the matrix by vacancy creation and/or increasing the diffusivity of the matrix. The response was observed by Sporer & Lang (1994) who produced a processing chart (shown in Figure 8.8) for Ni base ODS alloys. It was noted that this chart does not apply to ferritic materials, however, no explanation for the differing response was presented in the paper.
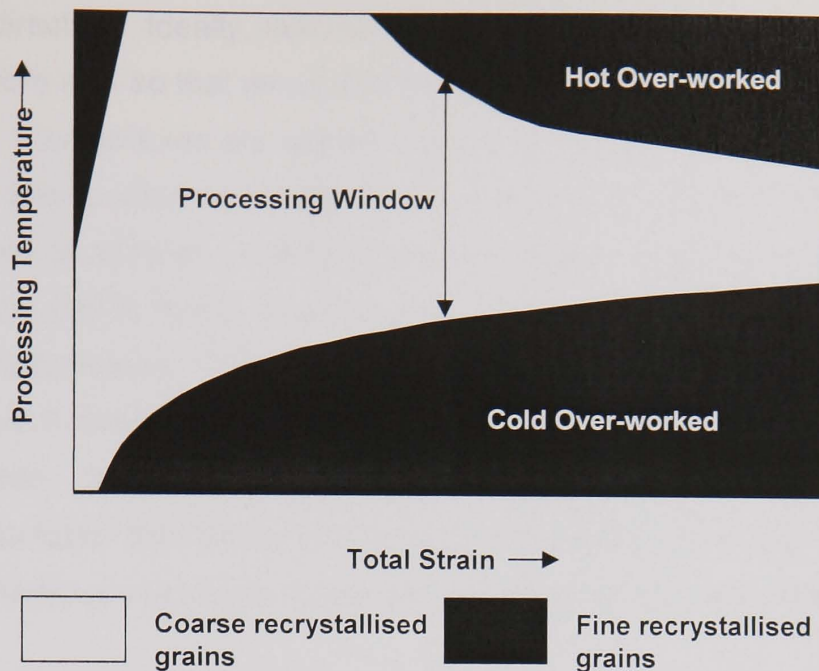
Figure 8.8 Processing chart for Ni-base ODS after Sporer & Lang (1994)

The common aspect of all the cases described above where secondary recrystallisation was retarded by cold work is that the materials were all nickel based. The reason for this may lie with the differing behaviour of high and low stacking fault energy materials. For the high stacking fault energy ferritic materials there does not appear to be an upper limit on the level of plastic deformation to induce secondary recrystallisation. This work has shown that the lower limit of plastic deformation to induce secondary recrystallisation is relatively high. It is postulated that the reason for this is that the high stacking fault energy allows dislocation re-arrangement to occur relatively easily due to processes such as climb within the deformed metal as it is heated. Whereas for the Ni base ODS alloys, recrystallisation occurs as the dislocation re-arrangement processes are extremely difficult in low stacking fault energy alloys. Primary recrystallisation results in removal of dislocations, but it also alters the texture.

8.7.3 The Influence of Texture

A material which has undergone a severe amount of deformation such as extrusion and cold tensile pulling will develop a preferred texture in which certain crystallographic planes tend to orientate themselves in a preferred manner with respect to the direction of maximum strain.

These are generally referred to as fibre textures and are described by specifying the crystallographic direction or directions that lie parallel to the principal strain axis or

the flow direction. Ideally, materials having a fibre texture have rotational symmetry about a fibre axis so that all crystal orientations about the axis are equally probable. However, fibre textures are seldom ideal and the orientation distribution around the specified axis is often non-uniform. According to Smallman (1990) BCC structures irrespective of material variants always develop a <110> fibre texture. Hatherly & Hutchinson (1979) found that the texture increases in sharpness with increasing levels of deformation. Texture induced secondary recrystallisation was first reported by Burgers & Basart (1929) and is associated with the texture inhibition of normal grain growth. Juul-Jenson & Kjems (1983) showed that the growth rate for textured grains was faster than those with random orientation. This is in agreement with the general theory of orientated growth as discussed by Cotterell & Mould (1976).

The critical aspect of texture on secondary recrystallisation has been demonstrated on the iron based MA ODS alloy PM2000 by Korb & Sporer (1990). The material consolidated by hot isostatic pressing followed by some primary deformation by extrusion, showed no evidence of texture and, significantly, no secondary recrystallisation response. Further deformation of the same material to levels greater than 90% resulted in an extremely fine grain structure and a strong <110> fibre texture. In this condition, secondary recrystallisation was achieved. Regle & Alamo (1993) also arrived at a similar conclusion in that they found that the texture derived by the cold work process was much more important in secondary recrystallisation than the actual level of cold work reached.

There is little doubt that texture influences secondary recrystallisation. When texture is considered in relation to the Sha & Bhadeshia (1997) nucleation model, it is possible that the texture could lead to the clustering of adjacent grains into similar orientations. This could lead to an increase in the effective grain size, making the nucleation of secondary recrystallisation easier.

Texture based considerations could also explain the markedly different secondary recrystallisation responses to strain energy as observed by iron based and nickel based materials as discussed above. The results of these deductions are that the texture obtained during recovery gives rise to low angle boundaries (Cotterell & Mould (1976) and Juul-Jensen, Hansen & Humphreys (1985)), therefore, encouraging secondary recrystallisation by the mechanism described by Sha & Bhadeshia. However, for the Ni base alloys dynamic recrystallisation leads to

randomly orientated grains with high angle boundaries. Consequently, secondary recrystallisation is more difficult.

Work by Uenishi & Takeda (1990) on Ni base MA alloys has also indicated that the primary recrystallisation texture is likely to play an important role in encouraging secondary recrystallisation. The authors heat treated highly textured MA alloy sheet in which hardness indents had been introduced. Microscopy revealed that around the next grain, the structure was fine and equiaxed, whereas away from the indent the grains were typical of a secondary recrystallised structure. The explanation for this was that the indent introduced a higher degree of stored energy into the material, thereby decreasing the size of the recrystallised grains and changing their shape to equiaxed. However, it is also possible that the indent destroyed the texture local to the indent. Only at some distance away from the indent would the texture become strong enough to produce the elongated structure.

Texture controlled secondary recrystallisation would also explain the non secondary recrystallising martensitic alloys. In the course of the α to γ transformation during heating to the recrystallisation temperature, the material not only lowers its stored energy with the loss of the high dislocation martensitic structure, but it also modifies the texture it possessed due to the phase transformation to austenite.

In his assessment of the secondary recrystallisation studies on MA956 and MA957, Chou (1997) found that the texture effect in MA956 was stronger than in MA957. This resulted in MA956 having a lower secondary recrystallisation temperature compared with MA957. This occurs even though MA957 has a lower yttria content. The composition of MA957 is such that it may just enter into the γ loop (Fig 5.1) at the secondary recrystallisation temperature, thus a small amount of austenite may be present, modifying the texture as described above.

Chou (1997) investigated this by adding nickel to MA957 to increase the austenite content. Although the percentage austenite is not stated it is likely to be relatively small. It did, however, have a great effect on the secondary recrystallisation response increasing the start temperature from 1250°C to 1350°C.

8.8   SUMMARY

From the review carried out with respect to the secondary recrystallisation of the titanium nitride strengthened alloys, it is obvious that secondary recrystallisation is a complicated phenomenon and depends on a range of finely balanced variables. It is important that thermo-mechanical processes involved to produce secondary recrystallisation in one alloy be analysed for that alloy system. This is due to the fact that it is apparent that a particular thermo-mechanical process designed to produce secondary recrystallisation in one alloy can actually retard the secondary recrystallisation process in another. Thus, separate consideration should be given to the iron-based secondary recrystallised alloys and the nickel based secondary recrystallised alloys and not the generality of ODS alloys.

There is still no unified theory on the factors affecting the initiation process for secondary recrystallisation. This author has found that the Sha & Bhadeshia grain pinning model which, it has been postulated is strongly influenced by texture, can provide a rational explanation for the varying circumstances that can lead to the development of the coarse interlocking directional structures, a non optimised structure, or the complete loss of a materials ability to undergo secondary recrystallisation.

Chapter 9

Alloy C4 properties

The properties of the secondary recrystallised Alloy C4 were assessed by means of tensile and stress rupture tests.

The specimens for both sets of tests were manufactured by:

    I. Machining specimens from the extruded bars to give a 44mm gauge length and 25mm^2 cross sectional area.

    II. Tensile pulling the specimens to a plastic elongation of 10%.

    III. Heat treating in an argon atmosphere to 1200°C x 5 hours

    IV. Full secondary recrystallisation was confirmed by polishing, etching and metallurgically examining the structure by means of replication.

The results of the tensile and stress rupture tests are as follows:

9.1   TENSILE TESTS

The tensile tests were carried out using a Zwick electromechanical universal test machine equipped with a focused infrared clamshell furnace. Specimens were held within ±2°C of the target temperature for 20 minutes prior to testing. Tests were carried out at temperatures of 20°C and 600°C at a constant cross head speed equivalent to a nominal strain rate of $3.79 \times 10^{-4} \text{s}^{-1}$.

The results of the tests on the alloy C4 secondary recrystallised material and also the results of the tensile tests on the C3(1) and (2) secondary recrystallised materials are presented in Table 9.1 and in Figures 9.1 and 9.2 for the 20°C and the 600°C tests respectively. Also presented in Table 9.1 and Figures 9.1 and 9.2 are the Grade 430 and P92 material minimum properties at 20°C and 600°C.

Material	20°C		600°C		650°C		700°C	
	YS N/mm^2	UTS N/mm^2	YS N/mm^2	UTS N/mm^2	YS N/mm^2	UTS N/mm^2	YS N/mm^2	UTS N/mm^2
GD 430(min)	310	517	111	237				
C3(1)	282	467	168	268				
C3(2)	355	512	182	272				
C4	411	670	210	258	146	151	93	95
P92(min)	440	620	251	341				

Table 9.1 Room and elevated temperature tensile results (strain rate $3.79 \times 10^{-4} s^{-1}$)

The tensile results at 20°C show the tensile properties increasing significantly with increasing titanium content such that the fully ferritic Alloy C4 material properties approach the minimum properties of the martensitic P92 material.
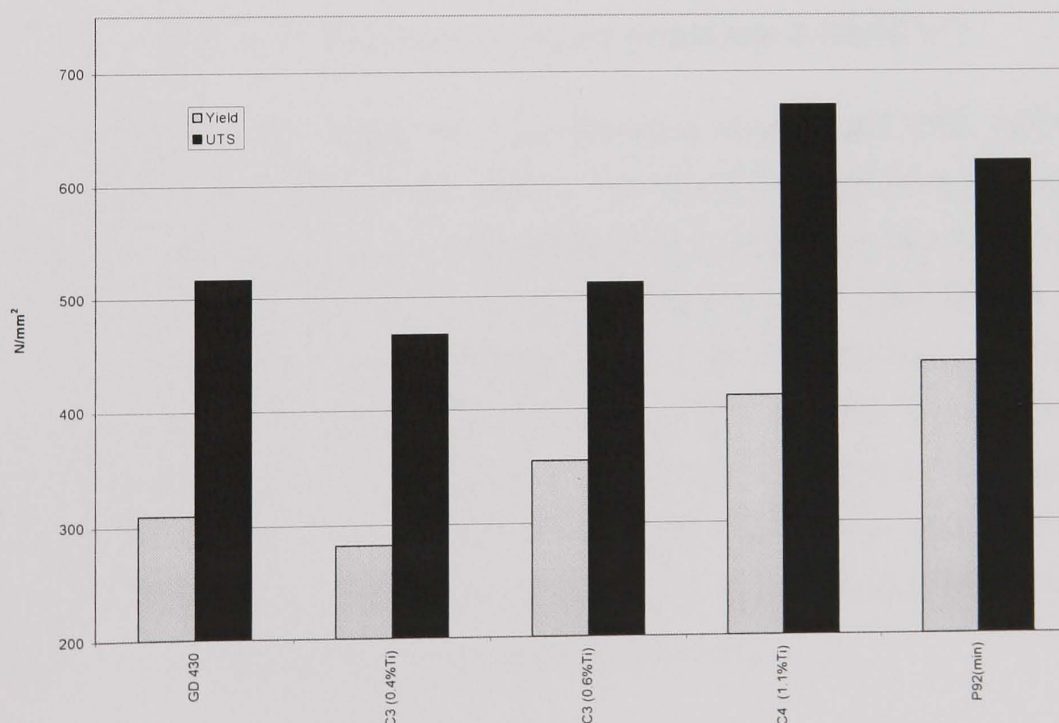
Figure 9.1 Room temperature tensile results (strain rate $3.79 \times 10^{-4} s^{-1}$)

At 600°C, however, the difference between the P92 material and the titanium nitride strengthened steels becomes more polarised. The development of the grade 430 basic material by adding increasing amounts of titanium nitride has increased the yield strength with very little effect on the ultimate tensile strength (UTS).
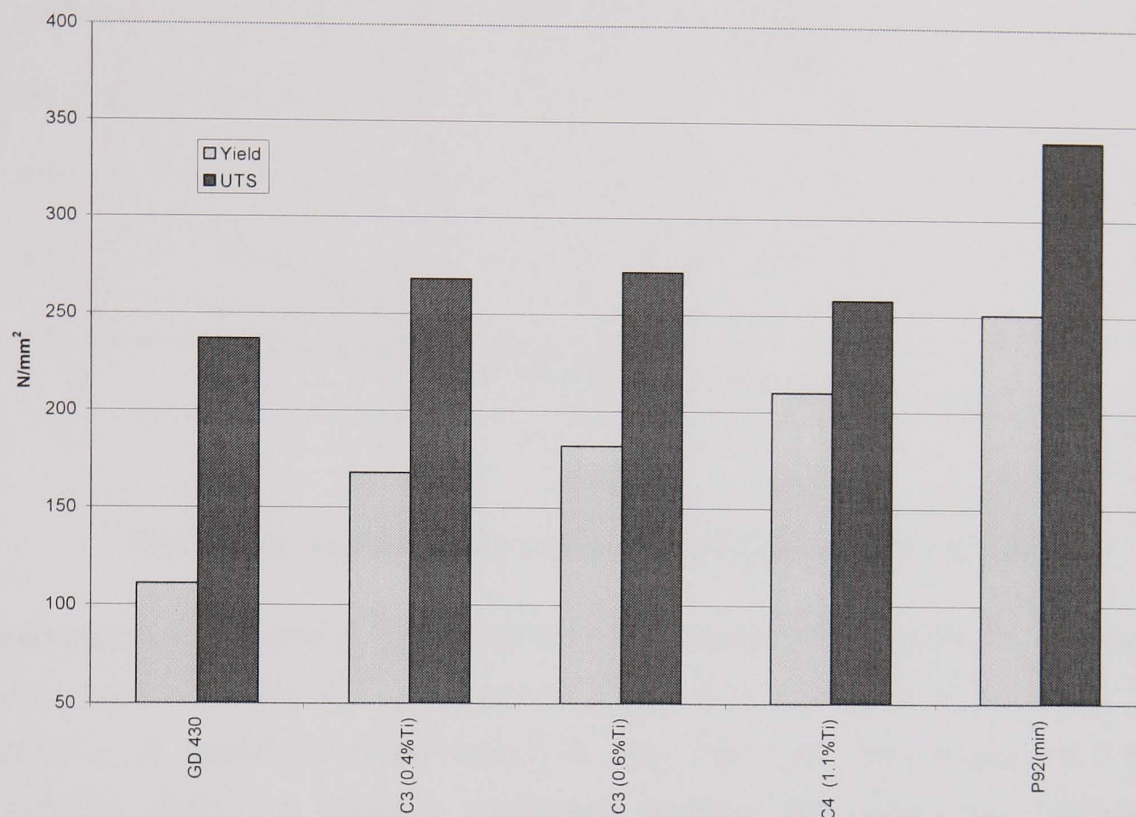
Figure 9.2 600°C tensile results (strain rate 3.79x10⁻⁴s⁻¹)

In order to examine this difference in performance of yield and UTS, further tests were also performed at 650°C and 700°C. The results of these tests are also given in Table 9.1. To aid the analysis, the stress strain curve properties were examined (Figure 9.3). From Figure 9.3 it is apparent that at room temperature, yield is followed by considerable work hardening until the UTS is reached. At 600°C and 650°C the amount of work hardening decreased, such that after the yield point has been reached there is only marginal work hardening followed by a continuous decrease in stress until fracture. At 700°C, the strength of the material cannot be expressed by the standard method, as a yield and an ultimate tensile strength, because the maximum stress occurs at the yield point.
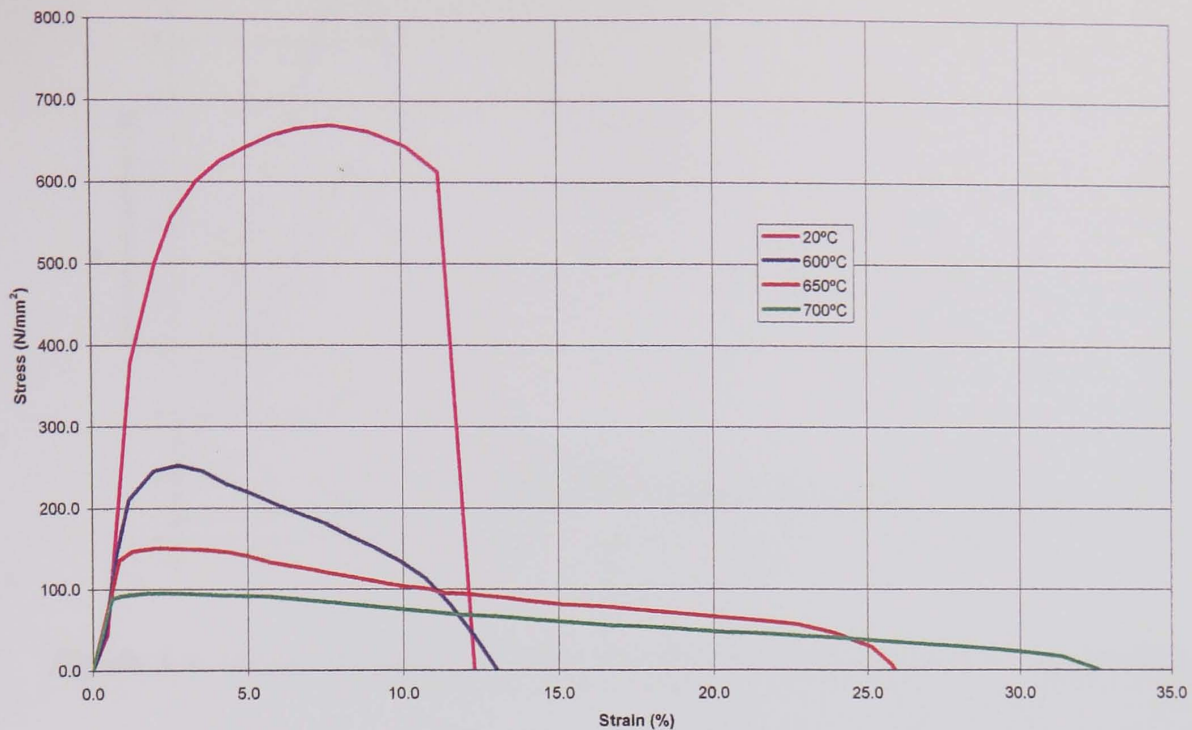
Figure 9.3 Alloy C4 stress strain curves at 20, 600, 650 & 700°C

Examination of the strain, to account for this shape of hot tensile curve reveals that the uniform reduction of cross-sectional area due to elongation at the onset of the reduction of maximum stress would be very low, thus, this would not have a significant effect. In order to investigate whether this continuous decrease in maximum stress was due to the onset of a localised reduction in area (necking) at low strains, the following experiment was performed.

A specimen was prepared with the diameter measured at 5mm intervals along the gauge length. The specimen was then tested at 650°C, but at regular intervals of approximately 2% strain, the specimen was unloaded, cooled and the diameter along the gauge length was re-measured at the reference positions. The results of this experiment are shown in Figure 9.4. This work confirmed that at elevated temperatures, localised deformation was occurring at a very early stage. In the case of the sample tested, localised necking occurred at strains as low as 4%.
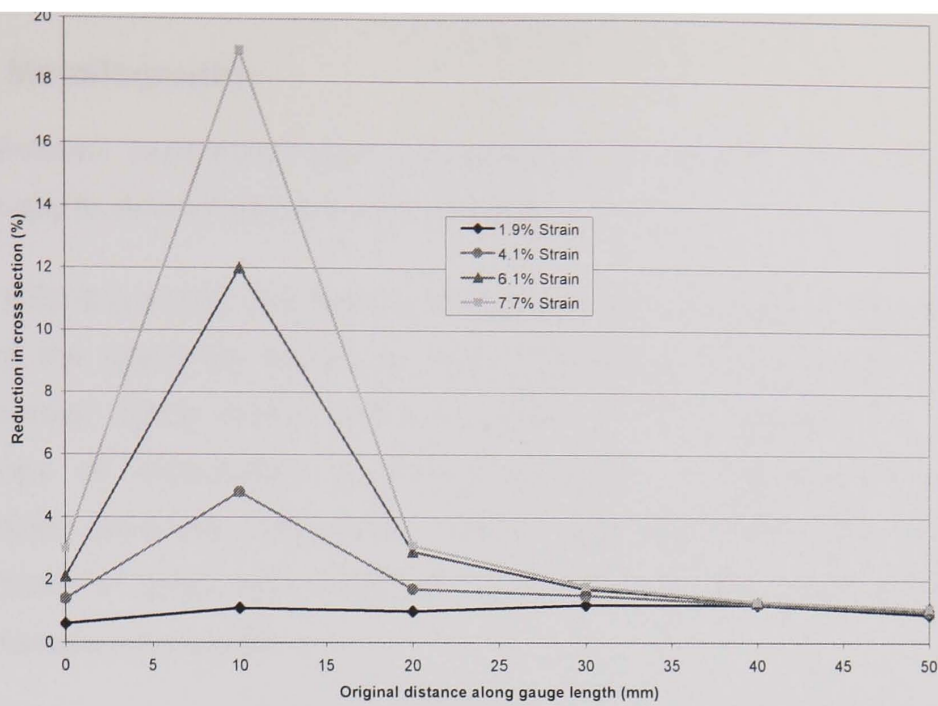
Figure 9.4 Onset of necking in Alloy C4 (650°C test at $3.79 \times 10^{-4} s^{-1}$ strain rate)

The effect of strain rate on the tensile properties was also investigated at 650°C. Tests were conducted at three additional cross head speeds equivalent to strain rates of 3.79×10^{-5}, 1.36×10^{-3} and $0.019 s^{-1}$. These tests revealed that the Alloy C4 material properties are sensitive to strain rate. The tests show that with decreasing strain rate the maximum stress increases and ductility decreases. Figure 9.5 shows the maximum stress as a function of the strain rate.
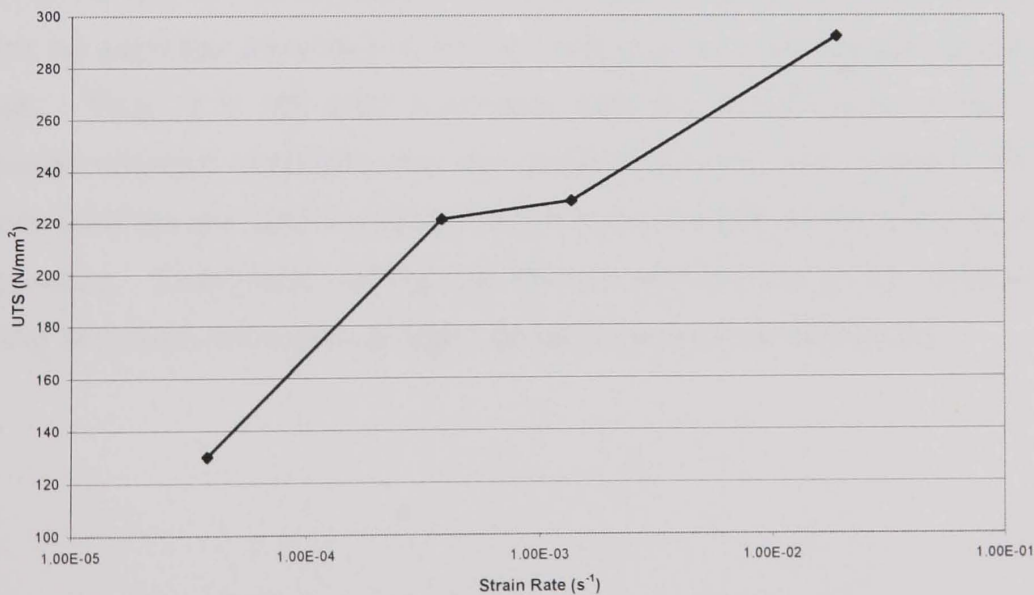
Figure 9.5 UTS variation with strain rate (650°C tests)

9.1.1 Metallography

The fractured specimens were all examined by optical and scanning electron microscopy to determine the fracture modes.

Figure 9.6a & b shows the fracture surface and a cross section through the fracture zone of the specimen tested at room temperature. This figure illustrates the transgranular brittle mode of this material at room temperature. Pronounced anisotropy of deformation is clearly revealed in the photomicrographs, the deformation observed is associated with the individual grains. It is apparent that at the $3.79 \times 10^{-4} s^{-1}$ strain rate, room temperature tensile tests are below the ductile to brittle transition temperature.

At 600°C and above, the fracture exhibited a ductile transgranular and intergranular failure as shown in Figure 9.7a & b. The straining at temperature formed pores within the grains and particularly at the grain boundaries. The pores at the grain boundaries appear to have a marked influence on the fracture appearance, leading to the parting of the grain boundaries in the fracture zone. Each grain appeared to neck down producing longitudinal cracks along the grain boundaries. The behaviour of the material is analogous to the tensile response of wire rope. This grain boundary weakness could be avoided if the formation of pores could be prevented. The reason for the occurrence of pores has been investigated. The pores generally occur in the vicinity of chromium nitride particles or coarse titanium nitride particles. Where no particles were found, this is likely due to drop out during the polishing stages. Thus, it is not only imperative that the particle size is kept small for increased strength purposes, but the coarse particles also weaken the material. Coarse particles are also implicated in the early necking of the material at elevated temperature. Examination of the test sample post tensile failure revealed that the necking occurred in a region of high coarse chromium nitride density.

Figure 9.6a Fracture surface of room temperature tensile test

Figure 9.6b Cross section of room temperature fracture surface
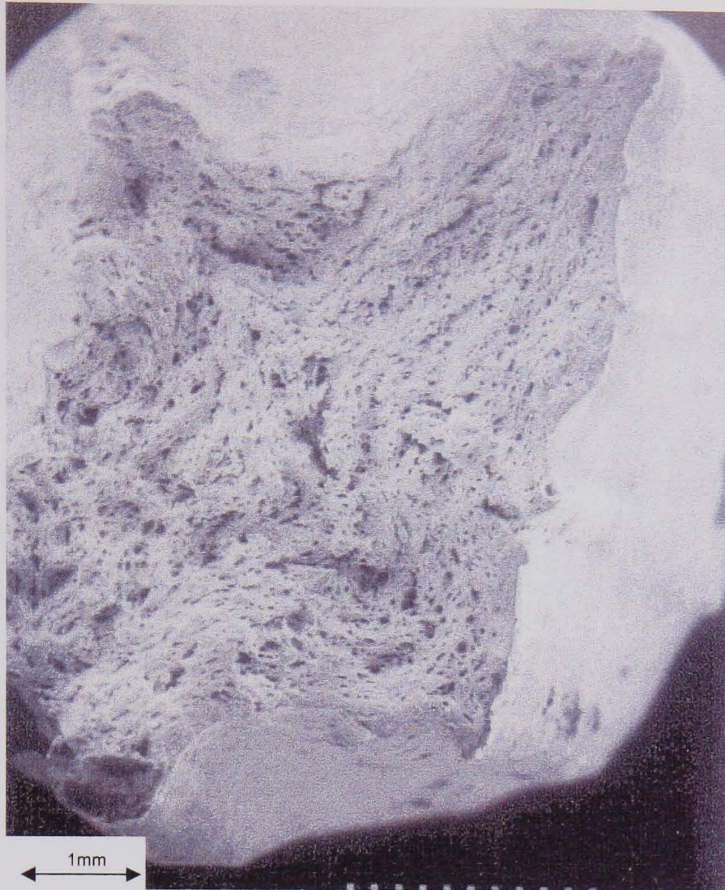
Figure 9.7a Fracture surface of 600°C tensile test

Coarse particles at
grain boundary

1μm
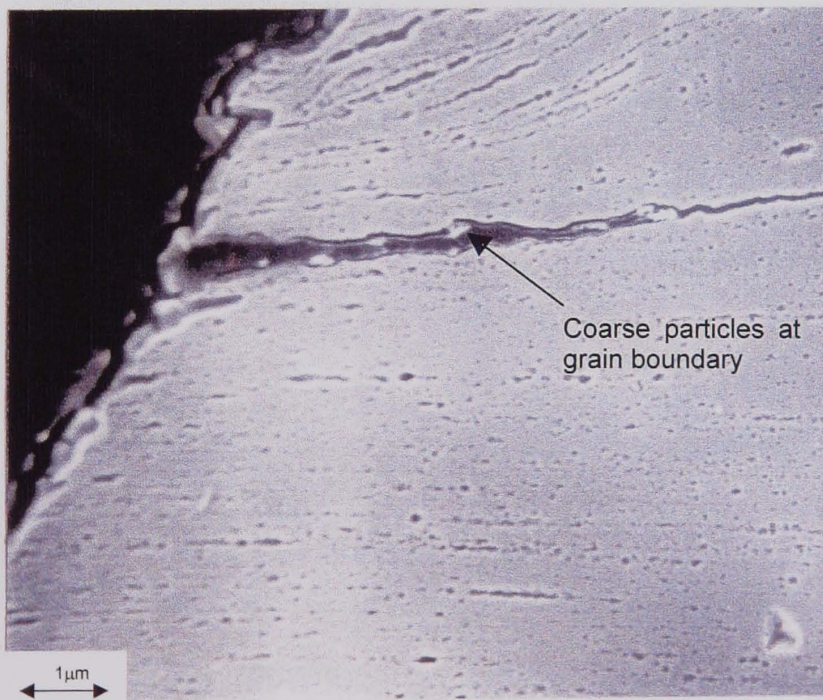
*Figure 9.7b Cross section of fracture surface showing coarse
particles at a fractured grain boundary*

9.2 CREEP PROPERTIES

Creep tests were carried out at 600°C and also the 58MPa iso-stress tests at 650, 675 and 700°C in a similar fashion to the testing performed on the earlier alloys. A characteristic of the earlier creep tests on secondary recrystallised material was the high primary strain. This is due to the complete recrystallisation to produce the necessary coarse grain, results in low dislocation densities. In order to investigate if the creep performance could be improved by the introduction of dislocations by plastic deformation prior to creep testing, a pre-strain experiment was carried out.

Two nominally identical secondary recrystallised C4 creep rupture specimens were chosen. One specimen was given a plastic deformation of 8% pre-strain and was then re-machined to remove any necking that had occurred, whilst the other was tested in the as secondary recrystallised condition. Both specimens were heated to the creep temperature of 700°C and held at this temperature for 1 hour prior to loading. This temperature will allow dislocation recovery and re-arrangement to occur without causing recrystallisation.

The results in Table 9.2 and Figure 9.8 show that the 8% pre-strained material exhibited significantly lower primary strain, lower minimum creep rate and increased creep rupture life. The negative aspect is that the pre-strained material exhibited decreased creep ductility. The pre-strain removes to a large extent the plastic component of the initial strains on loading. Any plastic deformation that does occur adds to the dislocation density already present. The dislocation densities at the start of the test and at the onset of secondary creep are thus significantly higher than on the non pre-strained sample. The high dislocation density pinned by the titanium nitride particles increase the creep resistance by restricting deformation of the large grain interiors. The relative contribution of the grain interiors and thus the overall creep rate decreases. As a result of this pre-straining experiment, all other creep samples were given an 8% strain prior to creep testing.

Alloy C4	Temperature (°C)	Stress N/mm²	Rupture Life (hrs)	Rupture Strain (%)
As SR	700	58	94	38.7
8% Pre-strained	650	58	5336	2.8
	700	58	264	22
	600	120	181	25
	600	100	421	30.3
	650	70	125	30.5

Table 9.2 : Alloy C4 creep and stress rupture test results
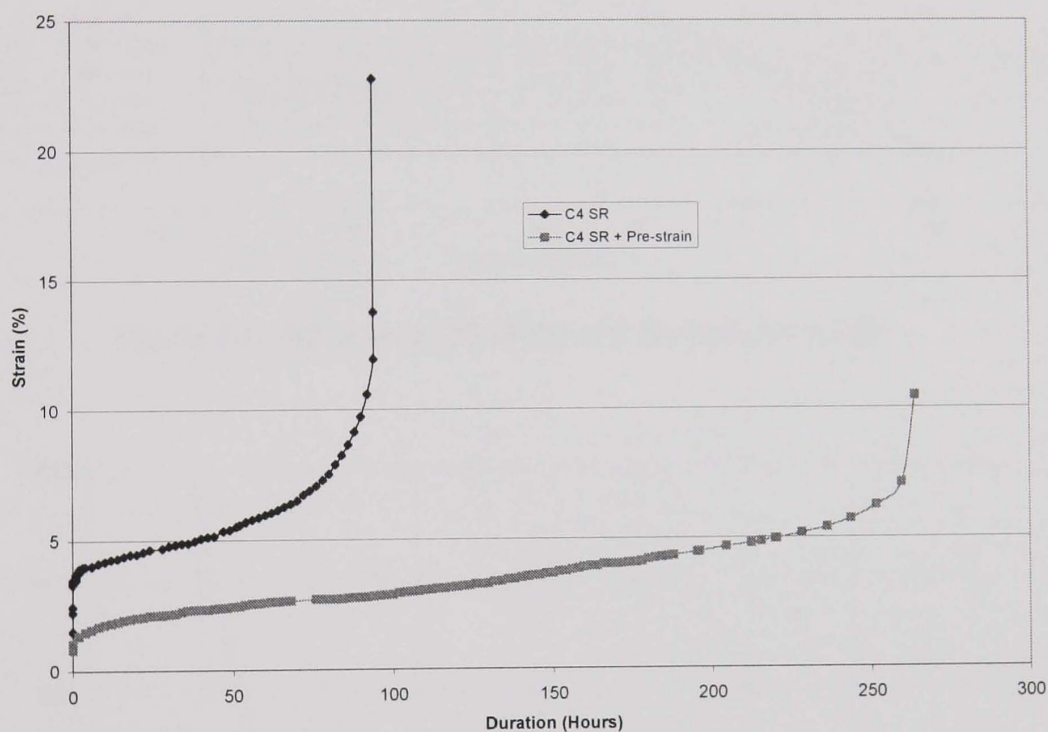
Figure 9.8 Comparison of 8%pre-strained and as SR creep curves, (58MPa/700°C)

In comparison with the earlier secondary recrystallised alloys in the iso-stress tests, Alloy C4 exhibits significantly superior creep performance as shown on Figure 9.9. The chemical and processing alterations from Alloy C3(2) to Alloy C4 resulted in an increase in life by a factor of 40. The Alloy C4 at 650°C is now almost within the -20% (on stress) scatter band for P91 material. These three Alloy C materials are all fully ferritic and have similar secondary recrystallised grain structures and base chemical compositions. The only difference between the alloys is the volume fraction of titanium nitride, the particle size and thus the controlling factor of interparticle spacing. Plotting the measured interparticle spacing for each alloy

against their durations at 650°C and 58 N/mm^2 results in an exponential increase in life with decreasing interparticle spacing as shown in Figure 9.10.
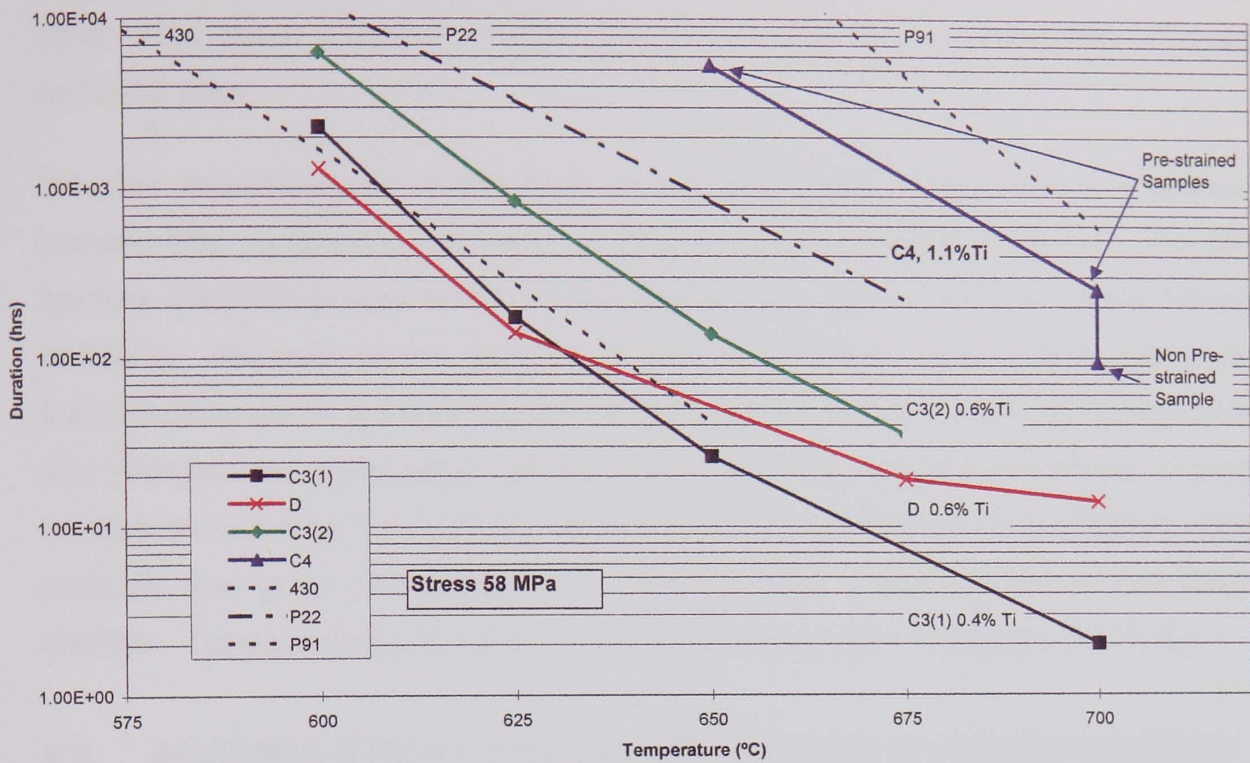
Figure 9.9 Iso-stress (58 MPa) stress rupture results
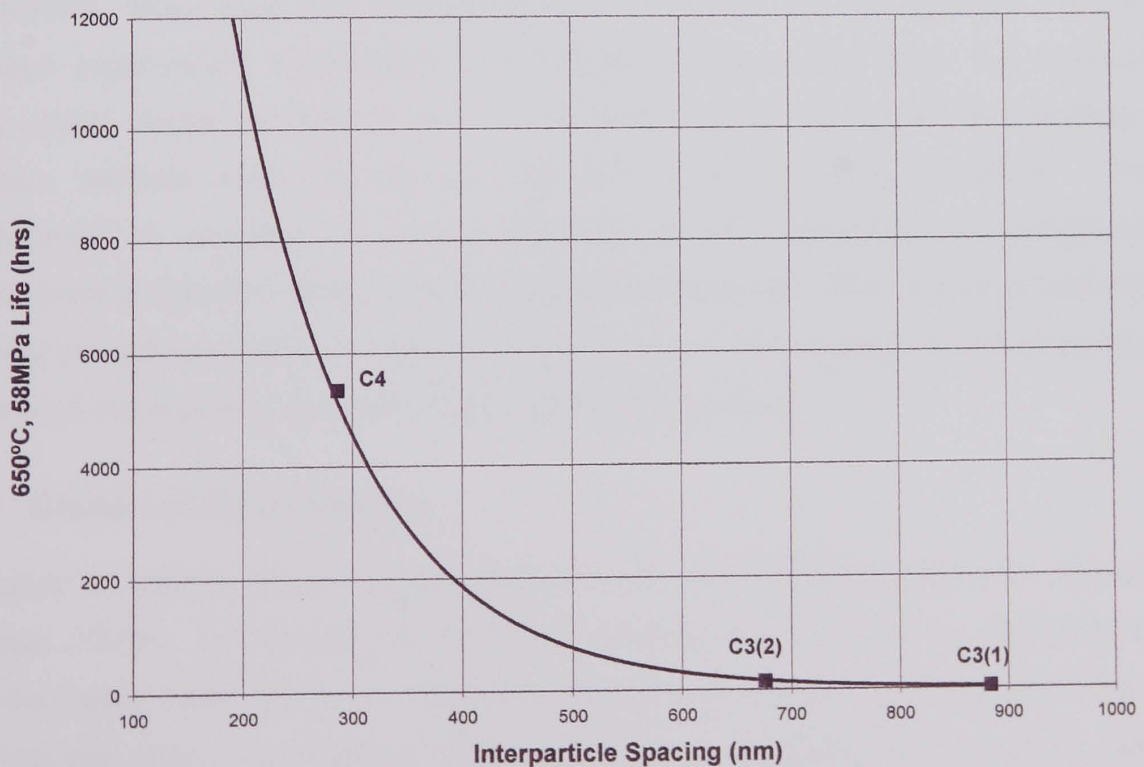
Figure 9.10 Test duration (650°C/58MPa) as a function of interparticle spacing

9.2.1 Creep Rupture Characteristics

The creep rupture behaviour of the Alloy C4 material can be categorised into short time, high strain rate tests and long time, low strain rate tests. The short term high strain rate tests displayed higher elongations and higher reductions in cross sectional area.

Fracture microstructural examination of the short time creep rupture specimens showed little evidence of cavitation in the transverse grain boundaries. The final fracture morphology was similar to the medium and slow strain rate tensile failures at 650°C. However, in the relatively long term (5336hrs) creep rupture specimen, fracture occurred in a brittle manner (Figure 9.11a) with a mixture of transgranular and intergranular crack paths. In this specimen there was some evidence of creep cavities surrounding the relatively coarse chromium nitride particles, titanium nitride particles and grain boundaries in a very localised area adjacent to the failure position. Typical areas are shown in the SEM micrographs in Figures 9.11b & c.

9.3   ACCUMULATION AND ACCOMMODATION OF CREEP DAMAGE

The failure mode of the titanium nitride strengthened fully ferritic steel in the stress rupture tests depends on a number of parameters such as the operating temperature, strain rate and microstructure. Whereas the fine grained Alloy C exhibited superplastic deformation characteristics, the similar Alloy C4 material tested under similar conditions, but in a coarse grained secondary recrystallised condition, exhibits extremely low ductility and failure by cavity formation. The development of cavitation is clearly important in understanding the operational performance of titanium nitride creep resistant ferritic steels. The following sections describe the accumulation of creep damage and how the damage is influenced by the various mechanisms by which it may be accommodated.

9.3.1 Creep cavity nucleation

Nucleation of cavities always occurs where deformation is inhomogeneous, Goods & Brown (1979). In non-particle hardened systems this takes place generally at grain boundary triple points. In particle strengthened alloys, cavitation also takes place at the grain boundaries. Dyson (1983), in studying Nimonic 80A, has proposed the formation of cavities due to interaction of slip planes and the locked serrated grain boundary. Diffusion in the grain boundary reduces the stresses, but it

125
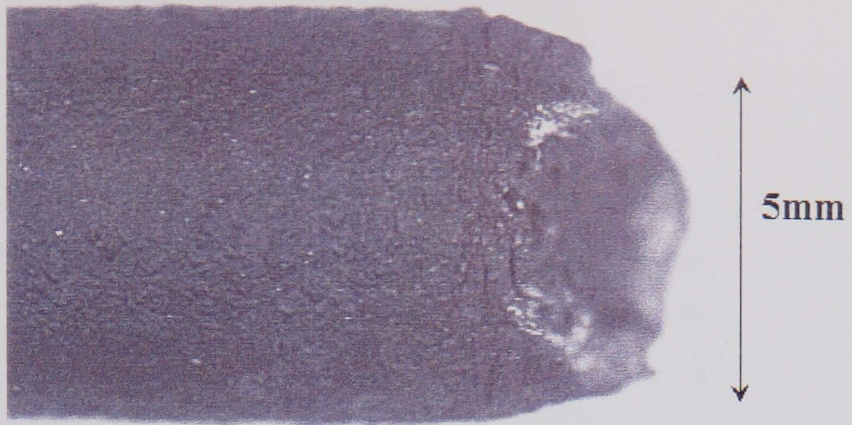
Figure 9.11a Alloy C4, 650°C/58MPa/5336hr/2%El stress rupture specimen
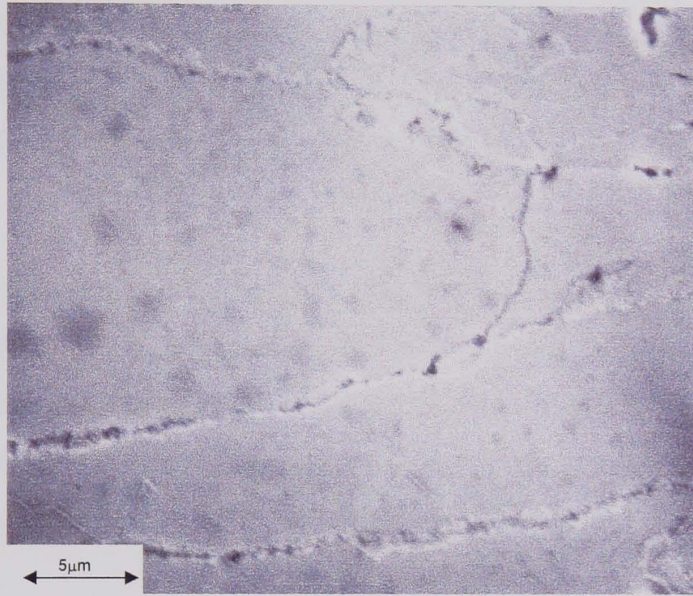
Figure 9.11b Alloy C4 creep cavitation at grain boundaries local to failure
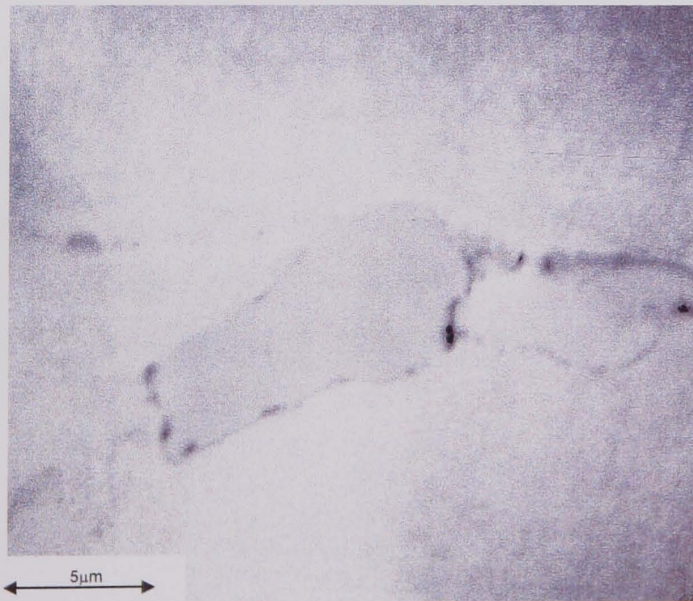
*Figure 9.11c Alloy C4 creep cavitation surrounding coarse chromium nitride
particle*

126

has been shown that cavity nucleation can occur if the magnitude of the stress and the rate of internal loading are both sufficiently high.

In the titanium nitride strengthened steel, cavity nucleation appears mainly to be associated with any remaining chromium nitride particles or indeed the titanium nitride particles themselves. Goods & Brown have suggested that nucleation can take place by mechanical decohesion between the particle and the matrix. This mechanism is favoured by most workers, for example Harris (1965), Rukwied (1973) and Fleck, Taplin & Beevers (1975), and involves the particle behaving as a discontinuity in the boundary plane and acting as a stress concentrator in the event of grain boundary sliding. Other workers, for example Machlin (1956) and McLean (1957) have suggested that nucleation may take place through stress directed vacancy condensation at the particle matrix interface particularly under situations of low stress and high temperature where the concentration and mobility of vacancies are high.

The nucleation of cavities within grains has been observed in a wide variety of dispersion strengthened alloys including thoriated nickel, Wilcox & Clauer (1966), ODS copper, Humphreys & Stewart (1972). Here too, as discussed above, it is conceivable that the nucleation can occur by vacancy condensation (now at the particle-matrix interface) or by the mechanical decohesion between the particle and matrix.

9.3.2 Cavity growth

Extensive studies of cavity growth mechanism, be it nucleated by vacancy condensation at the particle matrix interface or plastic flow of the matrix, will generally grow by vacancy diffusion when they are small, Cocks & Ashby (1982), but as they become larger, power law creep becomes the dominant growth mechanism. From Nix (1988) Figure 9.12 shows schematically the mechanisms of diffusion controlled cavity growth and dislocation creep controlled growth.

(a)   (b)
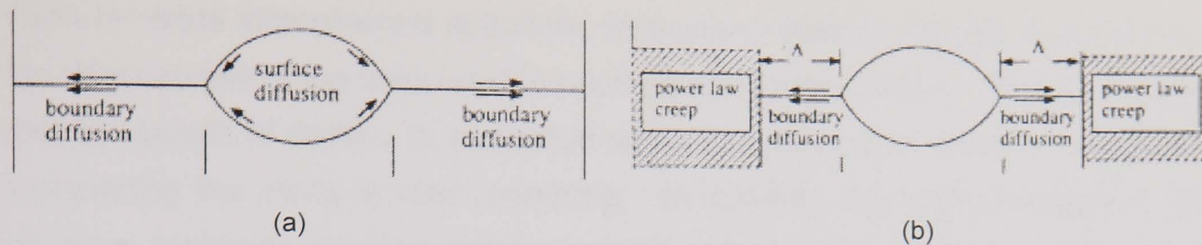
Fig. 9.12 Schematic of cavity growth mechanisms, after Nix (1988)

Where boundary diffusion alone controls growth, Figure 9.12a matter diffuses out of the growing void and deposits onto the grain boundary. The void is assumed to maintain its spherical shape during growth because surface diffusion is generally fast compared to grain boundary diffusion. This assumption may not be wholly justified under conditions where void growth is controlled by surface diffusion as when surface diffusion is slow, the void ceases to grow as a sphere. Atoms transferred by diffusional growth processes are deposited on adjacent grain boundaries. Creep can enhance the growth of cavities by decreasing the length over which diffusion must occur, Figure 9.12b. This is generally referred to as coupled cavity growth. This growth mechanism only takes place when the void has reached a specific size. Hence, this mechanism is only likely to be of significance at high loadings or large accumulations of creep damage.

Dyson (1976) proposed that diffuse cavitation on an isolated grain boundary facet can be constrained by creep of the surrounding material. It was proposed that if the displacements associated with diffusion growth of cavities on the grain boundary facet are not matched by creep displacements in the surrounding material, the load is shed from the cavitating facet to the surrounding material.

9.3.4 Creep damage in titanium nitride strengthened ferritic steels

Grain boundary cavitation requires displacement of material within the microstructure. This displacement of material needs to be accommodated to maintain compatibility and can be achieved by the mechanisms described in the previous section, namely: grain boundary sliding; stress directed diffusion; or dislocation creep of the surrounding matrix. More reasonably, the accommodation mechanisms are likely to be a combination of the above, as indicated by Raj & Ghosh (1981) and Timmins & Arzt (1988). These accommodation mechanisms may also control the rate of cavity growth, so, by limiting one or more of these

128

mechanisms cavity growth will be limited and the creep strength increased. In titanium nitride strengthened materials, dislocation creep is strongly suppressed by the effectiveness of the dispersoid in resisting dislocation motion. This will therefore limit the growth of cavities in a situation where the dislocation creep of the material surrounding the cavity is rate controlling. In addition, the highly elongated grain structure containing serrated grain boundaries will limit grain boundary sliding by the keying in of the serrations and, therefore, cavity growth controlled by sliding is also limited. Grain boundary sliding is further inhibited as the resolved shear stresses necessary for sliding will be greatly reduced when the grain boundary is aligned parallel to the stress direction. Cavity growth by stress directed diffusion of vacancies may also be inhibited when the grain size is large because the diffusion distances between vacancy sinks and sources are large.

9.4   SUMMARY

In tensile and creep rupture behaviour, this work has shown that temperature and strain rate affects the mechanical properties and fracture mode of the coarse grained titanium nitride strengthened alloys. It is thus apparent that the strengthening of the material due to the content and size of the titanium nitride particles has reached a level where at low strain rates, deformation must occur by microvoid formation coalescence and crack link up. It is thus energetically more favourable to deform in localised areas rather than through the larger volume as in high strain rate testing.

The review of the literature concerning creep cavitation has revealed there is no unified view as to the mechanism for creep cavity nucleation. It is apparent, however, that the various conditions necessary for creep cavity initiation and growth are restricted by the Alloy C4 grain structure and titanium nitride particles. This therefore accounts for the relatively sparse localised cavitation observed at the fracture surface.

The behaviour of the secondary recrystallised Alloy C4 material suggests that there are critical strain rates for these alloys where fracture modes change significantly. Correlation of the tensile and creep rupture behaviour of the secondary recrystallised Alloy C4 material at 650°C reveals a shift in fracture behaviour from low ductility to moderate ductility back to low ductility as the strain rate is increased from very low secondary creep rates through moderate creep rates and tensile strain rates to very high tensile strain rates. The elongations observed for the varying strain rates are shown in Figure 9.13. In the case of the creep specimens, the strain rate is the average strain rate to failure.
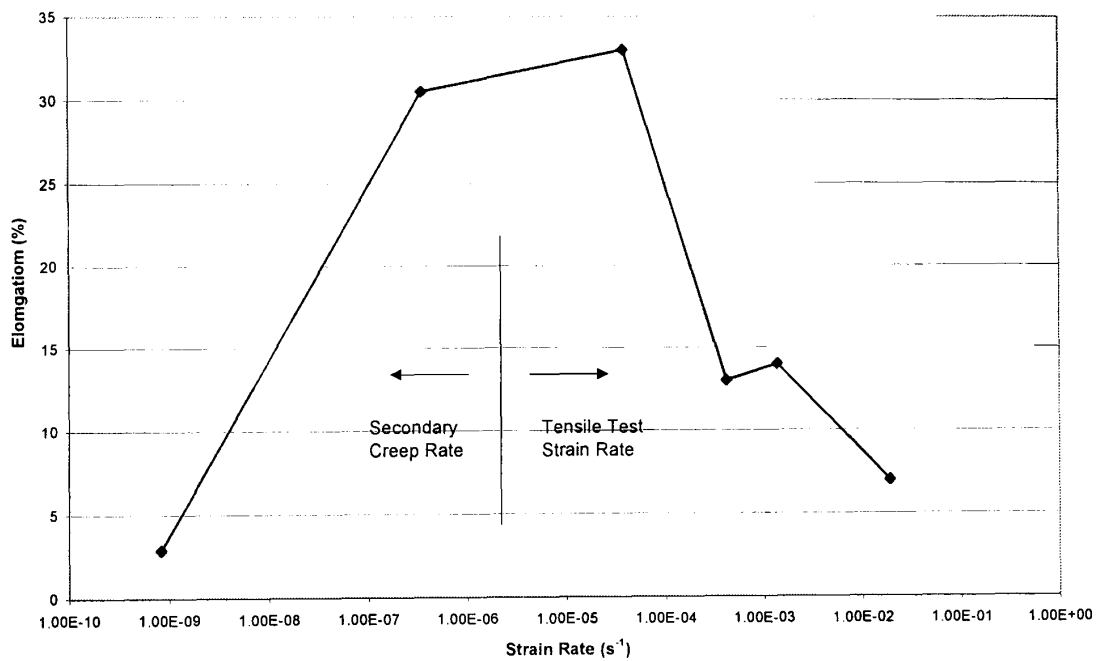
Figure 9.13 Alloy C4 (650°C) test elongations as a function of strain rate

Chapter 10

Selection of material type for further development

At this stage in the project, the two alloy types, martensitic and fully ferritic, were reduced to one to allow concentration of effort in order to develop the chosen alloy type to a stage where it could be considered a commercially feasible option. Additionally, at this stage, the production variables were reviewed and the most appropriate route was chosen for the remainder of the alloy development.

10.1 MARTENSITIC ALLOYS

At the inception of the project, it was envisaged that the martensitic grade would be the preferred choice of material. This was due to the fact that selection of this material would result in the project being more evolutionary, in that, although the major strengthening precipitates would be replaced by titanium nitride particles, the base composition of the conventional advanced creep resistant materials that are in widespread use would be maintained. Development of the fully ferritic alloy would be more revolutionary as there are no non-transformable ferritic materials in use today within the boiler industry for creep resistant components.

The reason that martensitic steels have, and are continuing to receive the majority of the world wide development activity is due to the enhancement in the properties from the martensitic transformation. The important aspect of the diffusionless

131

transformation from austenite to martensite is the strain associated with the transformation. This strain energy is minimised by the generation and motion of dislocations giving plastic deformation. The very high dislocation density increases the strength, and by pinning the dislocations with precipitates and solid solution elements, this strength is maintained at high temperatures and durations. The transformation from face centred cubic (FCC) austenite to body centred tetragonal (BCT) martensite also increases the strength due to solution hardening by interstitial elements, such as carbon and nitrogen as they create greater strain in the BCT lattice.

The decision was, however, taken not to proceed with the titanium nitride strengthened martensitic variant. This decision was taken because the creep properties of this material type are determined not by the strengthening effect due to the interaction of the titanium nitride particles with the dislocations, but, by the weakening effect of the fine grain size which is a consequence of the titanium nitride grain boundary pinning. Unlike the ferritic variant, the phase transformation from martensite to austenite has resulted in secondary recrystallisation not being achieved and thus the coarse grain size not being achieved.

10.2 FERRITIC ALLOY

The decision to develop the fully ferritic titanium nitride strengthened steel presents a greater challenge than developing the martensitic variant as the starting position of the material in terms of creep strength is at a significantly lower level. The enforced selection of the non-transformable alloy may, however, prove to be a major positive influence in the adoption of the titanium nitride precipitate strengthening. This is because it is now apparent that the maximum operational temperature of conventional martensitic materials are limited by their oxidation resistance rather than their creep strength. This has significant implications regarding the cycle efficiencies that are achievable as discussed in Chapter 14.

10.2.1 Oxidation Resistance

Up to this point, emphasis has been on achieving adequate mechanical properties, especially creep strength, but the oxidation properties can be equally important as the operational temperatures are increased. Although 9%Cr steels are very resistant to oxidation in air, an experimental superheater installation at the

Wilhelmshaven Power Station consisting of various 9% Cr steels conducted by Zabelt, Wachter & Melzer (1996) revealed that under typical boiler conditions the 9% Cr steels are susceptible to excessive oxidation when exposed to steam at temperatures above 600°C. The limitation on service temperature is due to the decrease in heat transfer as the oxide is an efficient insulator (Figure 10.1). The decrease in heat transfer leads to such an increase in the tube wall temperature that the creep properties are significantly reduced. The reduction in wall thickness resulting from the scale formation is a second order effect.
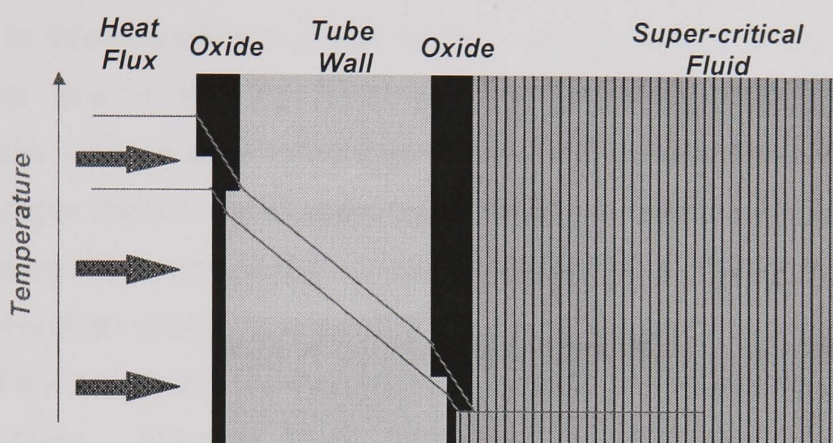
Figure 10.1 Schematic representation of the metal temperature increase due to increased oxide thickness

Due to the oxidation rates observed in the steamside being very much higher than those observed in air, fundamental studies were performed by Quadakkers and Ennis (1998) to investigate the effects of H_2O in more detail. This study confirmed that the oxidation of Chromium steels above 600°C is strongly affected by water vapour. The higher oxide growth rates are due to the presence of the water vapour causing the breakdown of the protective scale followed by an approximately linear oxidation of porous $(Fe,Cr,Mn)_3O_4$. It was found by Quadakkers and Ennis that the enhancement of the isothermal oxidation by the presence of water vapour did
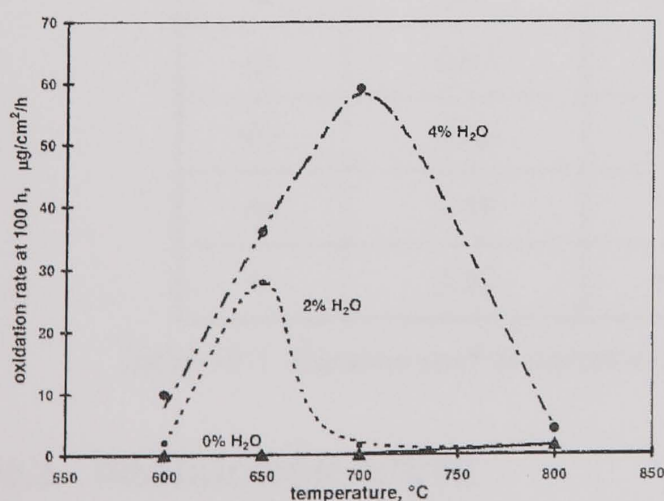
Figure 10.2 Influence of water vapour on the rate of oxidation of P91, after Quadakkers & Ennis (1998)

not continuously increase with increasing temperature as shown in Figure 10.2. Figure 10.2 demonstrates that the oxidation rate reaches a maximum at 700°C. The reason for the drop off beyond this temperature is due to the diffusion of chromium into the scale becoming sufficiently rapid to allow a protective oxide consisting of $(Fe,Cr)_3O_4$ and Fe_2O_3 to form.

Increasing the chromium content offers greater protection; thus the emphasis for the development of advanced martensitic steels is to obtain the strength of the 9%Cr martensitic steels such as E911 and P92 but increase the chromium content to 12wt% to allow operation above 600°C. As discussed in Chapter 5, this causes problems due to forming delta ferrite. To counter this, the most advanced martensitic conventional steels being developed in the Thermie 700 and the COST 522 projects contain up to 4wt% cobalt. This element stabilises austenite without surpressing the austenite transformation temperature; however, the cost of cobalt is considerable as shown by the comparison in Table 10.1. As a result, the production costs of the advanced conventional ferritic steels are now greater than the austenitic variant costs. The fully ferritic titanium nitride strengthened ferritic steels being developed within this project contain 18wt%Cr and therefore will not suffer from water vapour enhanced oxidation even at 700°C operation.

Element	Relative Cost	Element	Relative Cost
Ni	1	Co	6.37
Al	0.32	Mg	0.7
B	2.3	Mo	3.04
Cr	0.87	Nb	2.89
Cu	0.29	Si	0.27
Fe	0.18	Ti	0.71
V	2.08	W	1.65

Table 10.1 Relative cost of elements (taking Ni as unity) at 18/2/00

10.3 PRODUCTION ROUTE

At this stage in the project, decisions were also taken regarding the production routes for future alloys. It was apparent at this stage in the project that the Osprey

preform spraying process did not possess the degree of control necessary to inject the fine chromium nitride particles at a rate to precisely match the feedstock spray rate in order to obtain the target chromium and nitrogen contents throughout the billet. Additionally, the titanium nitride particles formed during the Osprey Process were found to be consistently coarser than the particle size produced via the Mechanofusion followed by extrusion or HIP route.

Due to the control and the flexibility offered by the Mechanofusion Process to produce accurately small development batches of material, this process was selected as the means of manufacturing all alloys designed to improve the creep strength from this point onwards.

Chapter 11

Increased titanium nitride content

11.1 BATCH IV ALLOYS

Although the creep properties of the Alloy C4 titanium nitride strengthened alloys had been increased by a factor of 40 in life over the alloy C3 recrystallised material, the creep life still falls below the properties of P91. This is a reflection of how low the base properties of a typical grade 430 ferritic material are and the fact that, whilst the titanium nitride particles are now significantly increasing the creep strength, a great deal more is required if this is to be a commercially feasible alloy.

The critical step in achieving the required creep performance from the titanium nitride strengthened steel is to ensure that the particle size and interparticle spacing are sufficiently fine to act as effective barriers to dislocation movement. The particle size, interparticle spacing and the volume fraction of titanium nitride are all inter-related. A simple relationship between these variables was developed by Shaw et al (1953) in Equation (11.1).

$$\lambda_{(s)} = R'\left\{ \cfrac{1}{1 - \sqrt{1 - \left(\cfrac{r}{R'}\right)^2}} - \cfrac{r}{R'} \right\} \qquad (11.1)$$

In this relationship the interparticle spacing is defined as the edge to edge measurement between any particle and its nearest neighbour. When this formula was applied to the volume fraction titanium nitride and particle size data obtained by TEM examination for Alloys C3(1), C3(2) and C4, this resulted in the calculated interparticle spacings being greater than the measured values as shown in Table 11.1. This is most probably due to the fact that this formula is based on the assumption that the particles are distributed in a geometrically regular array, whereas, the actual distribution was irregular and random. The spacings have therefore been re-assessed in terms of formula based on the assumption of random distribution contained within the review of interparticle spacing (IPS) formula, conducted by Corti, Cotterell & Fitzpatrick (1974). This revealed that the Hertz equation (11.2) provided a good correlation with the measured values as shown in Table 11.1.

$$\lambda_{(H)} = \Delta - 2r = r\left\{ 0.5\left(\frac{2\pi}{3Fv}\right)^{\frac{1}{2}} - 2 \right\} \qquad (11.2)$$

	Ti (wt%)	Measured Particle Dia (nm)	Measured IPS (nm)	Shaw IPS (nm)	% Diff.	Hertz IPS (nm)	% Diff
C3 (1)	0.4	238	884	1306	+ 48	869	- 2
C3 (2)	0.6	256	676	1228	+ 82	717	+ 6
C4	1.1	126	287	494	+ 72	228	- 21

Table 11.1 Comparison of Shaw and Hertz predictions with measured values

The values obtained by the Hertz equation leads to numerical values, which are smaller than those given by the Shaw analysis by a factor of ~0.45 and are significantly closer to the measured edge to edge interparticle spacing. The Hertz equation can thus provide a design model for selecting the titanium content to achieve the desired interparticle spacing for a given particle size.

In order to aid the optimisation of the design of the Batch IV alloys, the Hertz model was produced as a 3D graph (Figure11.1) relating the particle size, interparticle spacing and vol% titanium nitride (which has been converted to wt% titanium content, assuming stoichiometric nitrogen is added). The particle size was assumed to be that of the Alloy C4 material. Therefore, utilising Figure 11.1, it can be predicted that increasing the wt% titanium from 1.1 in Alloy C4 to 1.5, 2.0 and 2.5 will reduce the interparticle spacings from ~230nm to ~180nm, ~140nm and ~110nm respectively.
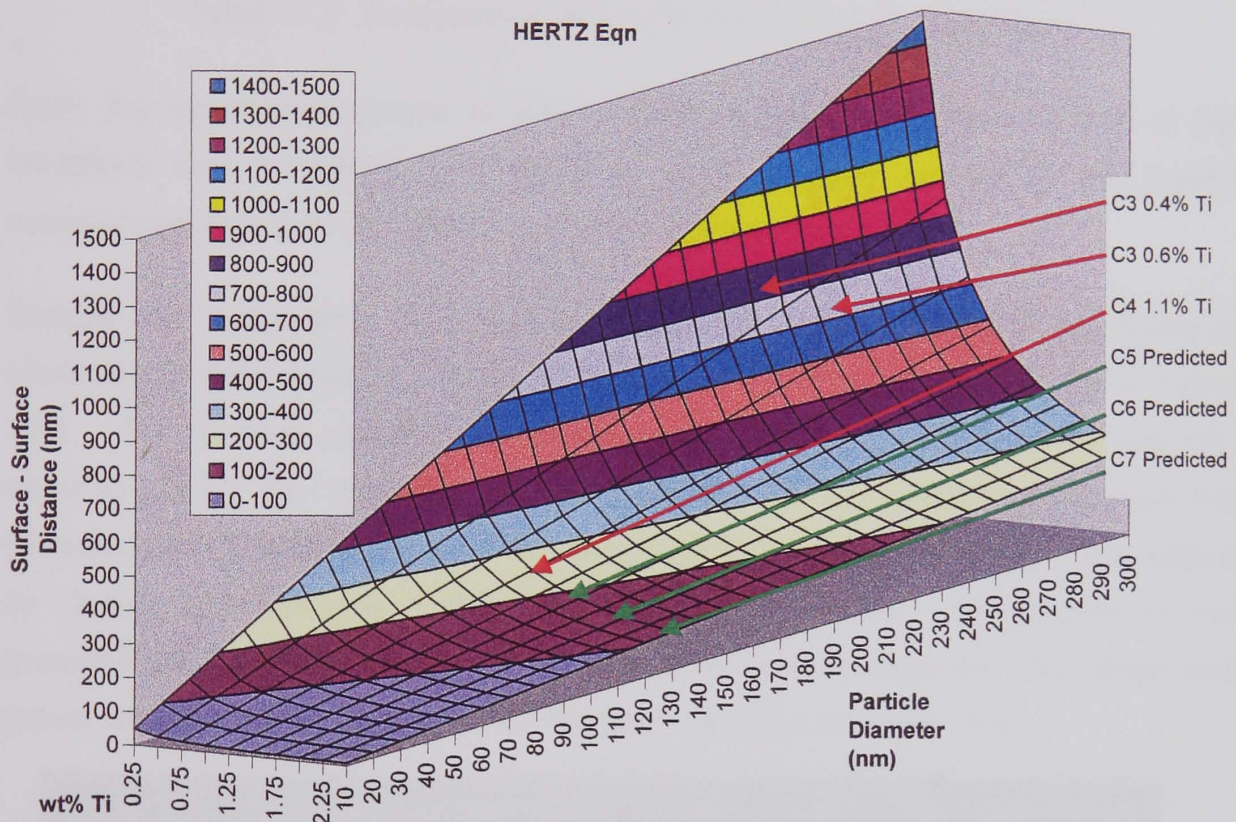
Figure 11.1 Graph depicting the Hertz interparticle spacing, titanium content and particle diameter relationship

As observed with earlier titanium nitride strengthened materials, it is necessary to generate a coarse grained structure in addition to a fine titanium nitride size and interparticle spacing. As it was not known if there existed an upper limit on the volume fraction titanium nitride that would allow secondary recrystallisation, all three alloys (containing 1.5, 2.0 and 2.5wt% titanium) were produced. These alloys were designated C5, C6 and C7.

11.2 MATERIAL PRODUCTION

The Alloy C5, C6 and C7 materials were produced in a similar fashion to the Alloy C4 materials including the upper limit of 45μm on the titanium containing feedstock powder production. The production details are given in Table 11.2.

Alloys	Feedstock	Powder Prod	Powder Classifi cation	Chromium Nitride Powder	Combining Route	Consoli dation Route	Extrusion Ratio	Extrusion Temp
C5, C6 & C7	Man. by SMP	Osprey	< 45μm	CRN5	Mechano-fusion	Extrusion	16 : 1	1000°C

Table 11.2 Summary of Alloys C5, C6 & C7 production route

From the experience gained in earlier alloys the target titanium content of the feedstock was increased by 0.1wt% in order to take account of the losses experienced during re-melting to convert the billet to powder

Despite the experience of producing the earlier alloys, the feedstock material produced by SMP failed to achieve the desired titanium contents as shown in Table 11.3. The titanium content was low by less than 0.1% in Alloys C5 and C6, however, in C7 the loss was greater (0.5wt%). In an attempt to increase the titanium content of alloy C7, a further amount of industrial grade titanium was added by Osprey into the melt during the production of powder. Introduction of the granules did, however, require the removal of the argon purged lid. The target and actual chemical compositions for the feedstock is given in Table 11.3.

Alloy		C	Cr	Si	Mo	Ti	Ni	Mn	N
C5	Target	<0.02	15.8	0.3	1.0	1.6	0	0.5	0.0
	Actual	0.003	15.8	0.27	0.99	1.51	0	0.27	0.0
	Diff.	-	0	-	-	-0.1	0	-0.2	-
C6	Target	<0.02	15.0	0.3	1.0	2.1	0	0.5	0
	Actual	0.002	14.9	0.28	1.0	2.02	0	0.2	0
	Diff.	-	0.1	-	-	-0.1	0	-0.3	0
C7	Target	<0.02	14.3	0.3	1.0	2.6	0	0.5	0
	Actual	0.003	14.3	0.26	1.0	2.1	0	0.2	0
	Diff.	-	-	-	-	-0.5	0	-0.3	0

Table 11.3 : Ti containing feedstock composition

139

Although the addition of titanium to the powder melt in Alloy C7 increased the total titanium content, it did not increase the wt% titanium in solution for subsequent solid state transformation to titanium nitride. Analysis of the C7 powder revealed that it contained 0.3% nitrogen. A microscopic examination of the powder particles revealed coarse titanium nitride cubes. Thus, even though the argon purged lid was only removed briefly during the re-melting of the ingots to introduce the powder, sufficient exposure to the air occurred for the high nitrogen affinity of the titanium to result in precipitation of titanium nitride particles in the liquid state. This failure in the production process resulted in alloy C7 not being produced to any further stages.

Quality checks of C5 and C6 alloys did not reveal any nitrogen in the composition nor precipitated particles in the powder. The remaining production was carried out in a similar fashion to Alloy C4 resulting in Alloy C5 and C6 bars. The comparison of the actual and target compositions is given in Table 11.4.

Alloy		C	Cr	Si	Mo	Ti	Ni	Mn	N	Nf
C5	Target	<0.02	18	0.3	1.0	1.5	0	0.5	0.44	0.00
	Actual	0.009	17.8	0.24	0.87	1.45	0	0.36	0.45	0.02
	Diff.	-	-	-0.1	-0.1	-	0	-0.1	+0.01	+0.02
C6	Target	<0.02	18	0.3	1.0	2.0	0	0.5	0.58	0.00
	Actual	0.002	17.9	0.28	0.96	1.9	0	0.23	0.57	0.02
	Diff.	-	-	-	-	-0.1	0	-0.3	-0.01	+0.02

Table 11.4 Target and Final Alloy Composition

11.3 SECONDARY RECRYSTALLISATION

Secondary recrystallisation trials were performed on Alloys C5 and C6 in a similar fashion to that conducted on Alloy C4. The variables are thus as follows:

Pre Strain: Samples were given approximately 0%, 2%, 4%, 6%, 8%, 10% and 12% elongations prior to sectioning to form samples.

Heat Treatment:

Temperature (°C)	Durations (h)
900	1, 5, 10
1000	1, 5, 10
1100	1, 5, 10
1200	1, 2, 3, 4, 5, 6, 10
1300	1, 5, 10

The result of this survey was that secondary recrystallisation was possible in both Alloy C5 and C6 materials. The response was similar to alloy C4, in that secondary recrystallisation only occurred in the high pre-strain and high heat treatment temperature condition. The minimum elongation and temperature to achieve complete secondary recrystallisation through the cross section was 10% and 1200°C respectively. The incubation time at 1200°C was, however, less than Alloy C4 in that for Alloys C5 and C6 recrystallisation occurred after 3 hours as opposed to 5 hours with alloy C4.

Due to secondary recrystallisation being achievable in both alloys the highest volume fraction titanium nitride material, namely, Alloy C6 material was chosen for the test programme.

11.4 TESTING

11.4.1 Test Condition

Tests were conducted on the Alloy C6 material that was secondary recrystallised at 1200°C for 3 hours after 10% elongation. Prior to stress rupture testing the secondary recrystallised material was pre-strained to 8% elongation. Stress rupture testing was performed in the established matrix of 58 MPa stress tests at various temperatures.

11.4.2 Results

Testing of Alloy C6 material revealed that the creep strength did not increase from alloy C4 as anticipated, in fact, the creep properties were inferior. This is demonstrated in Figure 11.2 and Table 11.5.

Alloy	Temperature °C	Stress N/mm^2	Rupture Life (hrs)	Rupture Stress (%)
C4	650	58	5336	2.8
C6		58	973	26
Decrease in Life			81.8%	
C4	700	58	264	32
C6		58	20	38
Decrease in Life			92.4%	

Table 11.5 : Comparison of Alloy C4 and C6 stress rupture results.
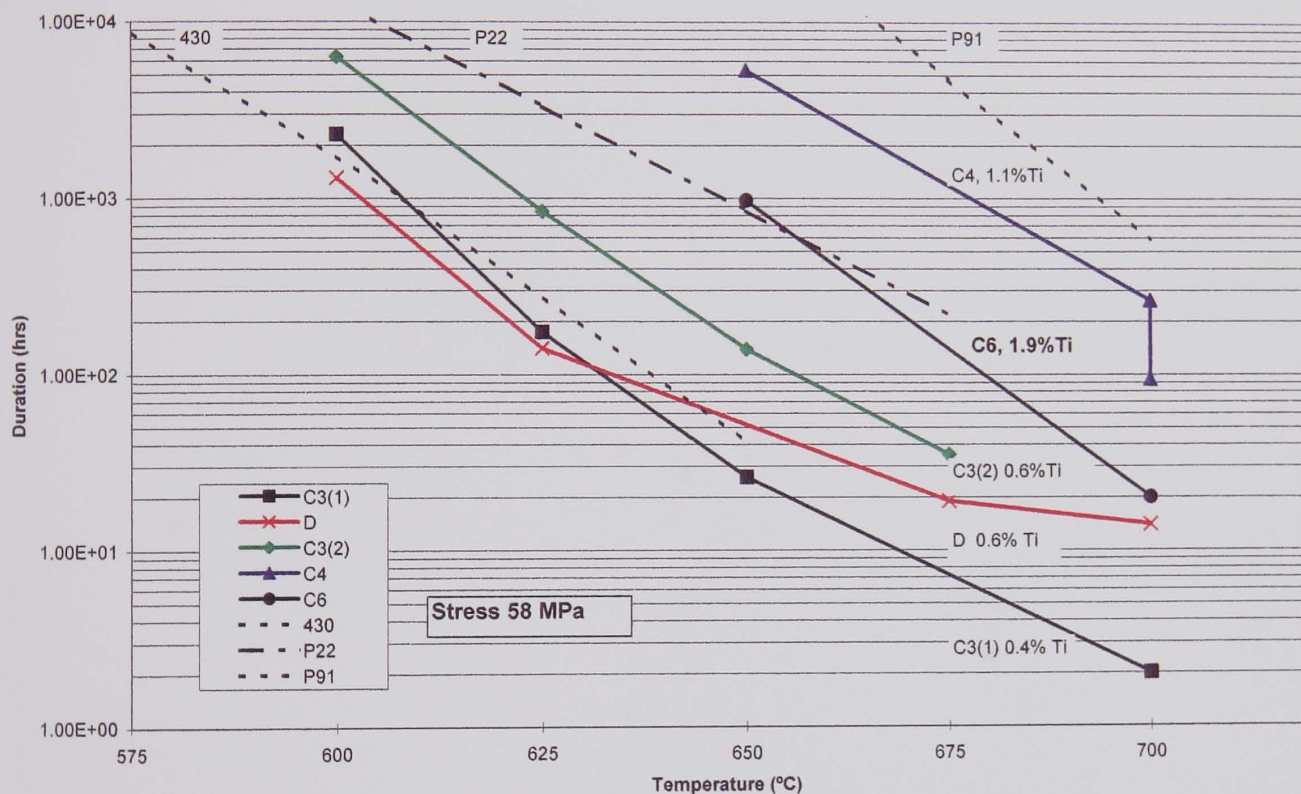
Figure 11.2 Iso stress (58MPa) stress rupture tests

11.4.3 Examination

Optical examination of the failed samples did not reveal the origin of the reduction in properties as the material did not fail in a grain boundary sliding manner. The reason for the decrease in properties was, however, apparent when the as extruded samples reached the transmission electron microscopy examination stage. This examination showed that the majority of the titanium nitride particles had precipitated on the grain boundaries and their size was greater than those observed in the Alloy C4 material (as shown in Figures 11.3a &b). Measurement of the

nearest neighbour distance in twenty random fields revealed that there was still relatively large variation in particle size and spacing but the mean size had increased from 126nm to 211nm. As a result the increased titanium content and thus volume fraction titanium nitride particles has had limited influence on the interparticle spacing, but has resulted in an increased number of large particles that are effective grain pinners but offer very little resistance to dislocation movement.
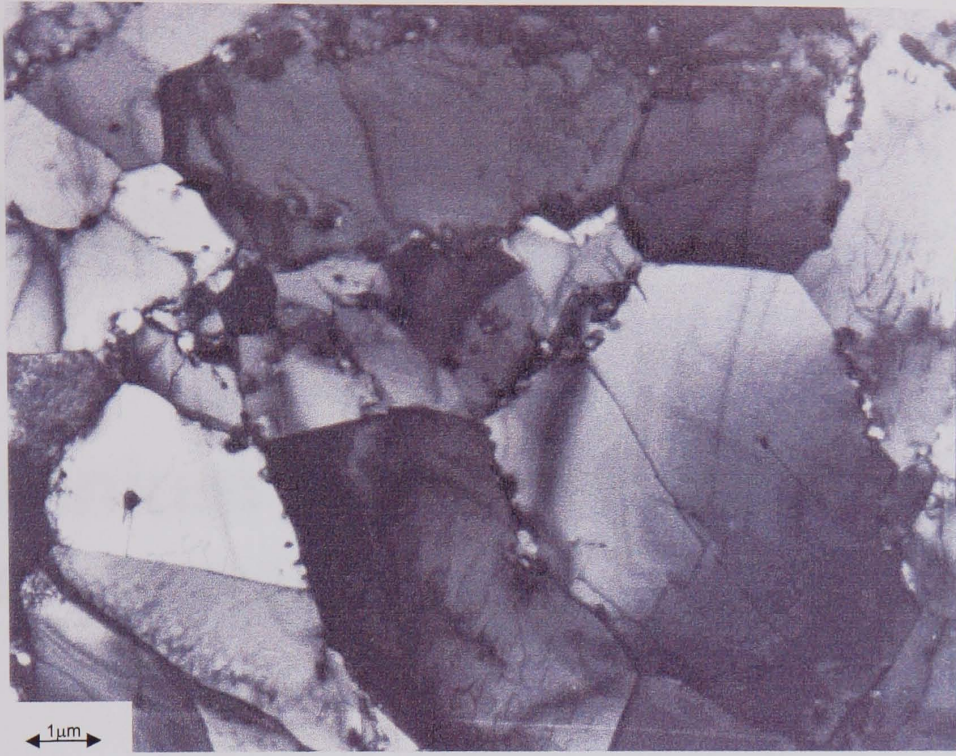
Figure 11.3a Alloy C6 grain structure with mainly grain boundary precipitates
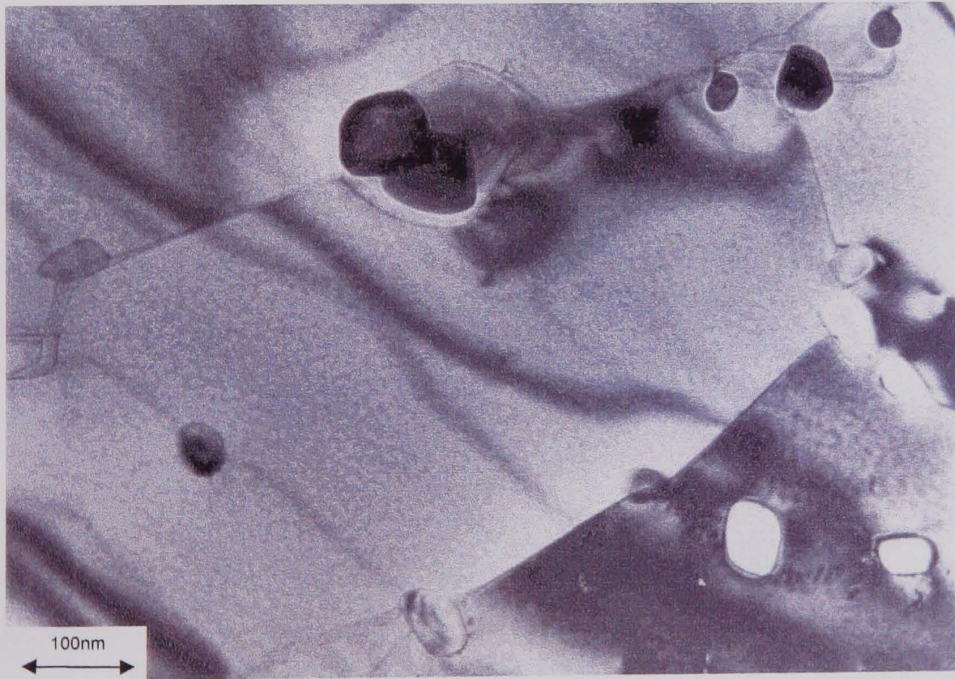
Figure 11.3b Precipitates on and near grain boundaries

Chapter 12

Titanium Nitride Particle Refinement

The large precipitate particle sizes observed in Chapter 11 may appear surprising for titanium nitride precipitates due to their very low coarsening rate as demonstrated in Chapter 2. It is, however, explained by the fact that coarsening only takes over as the particle size controlling process when the growth process is close to an end i.e. when almost all of the titanium has been removed from solution by precipitation. Before this stage the growth rate v depends on the concentration gradient at the interface and the rate at which the atoms can move, therefore from the analysis be Zener (1949):

$$v = \frac{D}{C_{Ti} - C_e} \cdot \frac{dc}{dx} \qquad (12.1)$$

Where C_{Ti} is the titanium concentration in the precipitate and C_e is the equilibrium concentration. D is the interdiffusion coefficient.

As the titanium nitride particle grows, this decreases the concentration of titanium and nitrogen in solution. Where the diffusion field of separate precipitates begin to overlap, growth will decrease and finally end when all the titanium and nitrogen have

been removed or reached the equilibrium solubility level which for titanium nitride is virtually zero, as shown on Figure 12.1a and b.
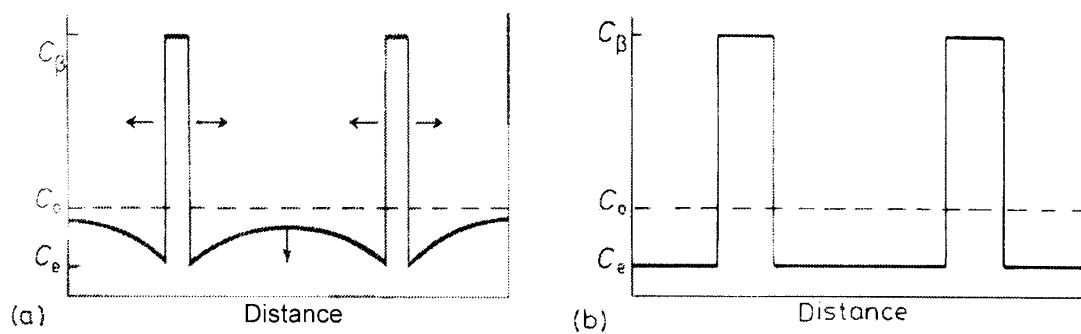
Figure 12.1(a) Interference of growing precipitates due to overlapping diffusion fields at later stage of growth. (b) Precipitate growth is complete

Therefore, it is only near the end of the growth stage shown in 12.1a that coarsening is the growth controlling mechanism. The particle size is thus largely determined by a competition between the rate of nucleation (as the nitrogen becomes available to the titanium) and the growth rate of the particle. Once a particle has nucleated, growth of the particles then depends on the rate at which the titanium can diffuse to the site of the nucleus. Meanwhile, nitrogen will continue to diffuse into the alloy until a further nucleation event occurs ahead of the first. At this point, the supply of further titanium to the first nucleus is cut off and growth ceases. The longer a nucleated particle has to grow before the next nucleation event (which will deplete the supply of titanium), the larger will be the particle. What this, in fact, means is that the nucleation rate of the titanium nitride will control whether there can be a significant strengthening effect of the particles.

On this basis, Birks & Meier(1983) suggest that the precipitate size will depend on the time available between nucleation events, which itself is inversely proportional to the speed of the oxidation front. Hence, particle radius r will vary according to equation (3.5). Thus, with all other variables remaining constant, increasing the titanium concentration will increase the particle radius. The increase in particle size from Alloy C4 to C6 was from 126nm to 211nm because of increasing the titanium content from 1.1wt% to 1.9wt%. This effect was also observed by Roberts & Evans (1992) in titanium nitride dispersion strengthened 20Cr25Ni stainless steel. It was found that with high temperature gas nitriding (95%N_2, 5%H_2) alloys containing

0.51wt% to 3.08wt% titanium, there was no beneficial creep strengthening effect of increasing the titanium beyond approximately 2wt%.

Previously, for the production of Alloy C4, in order to reduce counter diffusion of titanium, the powder size was reduced to <45μm, thus reducing the nitrogen diffusion distance (X) which also resulted in a particle size decrease. Powder sizes can be reduced further; however, this would further significantly decrease the powder yield. At present classifying the powder to sub 45μm results in the loss of 50% of the material by weight. As the aim is to develop an industrial process, this option was not pursued.

In order to increase the creep properties of the titanium nitride strengthened material much beyond those exhibited by Alloy C4, a method of decreasing the interparticle spacing, increasing the volume fraction titanium nitride and thus, decreasing the particle size must be developed. From the literature, the two influences on the titanium nitride precipitate size are the alloy composition and the nitriding temperature.

12.1 EFFECT OF ALLOY COMPOSITION ON PRECIPITATE SIZE

In the development of gas phase nitriding routes, attention was given to the design of alloys, which would be austenitic at the nitriding temperature prior to precipitation of titanium nitride. The reason lay in the observation by Wilson (1989a) of relatively coarse titanium nitride precipitation in nitrided FV448 and F1 alloys in comparison to earlier work on a nitrided austenitic steel. Wilson attributed this to differences in the nucleation and for coarsening kinetics for titanium nitride in matrices with the two different structures, but the reasons were not established in detail.

From first principles, the critical nucleus size of the titanium nitride particle in austenite would be smaller due to the relative packing density. Maurickx & Taillard (1988) quantified the differences in nucleation in austenite and ferrite with the use of the Jesser (1969) criterion. This uses the misfit parameter "δ" to indicate loss of coherency. The value of the misfit parameter "δ" for titanium nitride precipitation in austenite is 0.18. This indicates a very high interfacial energy, which correlates with a measured critical radius of 15-20nm. In contrast, the energy of the interface of titanium nitride particles in ferrite is rather low. The misfit parameter "δ" in this case

147

being 0.048, resulting in a critical radius for the loss of coherency being double that for austenite.

With regard to the supposition by Wilson (1989a) that the coarsening kinetics of titanium nitride in ferrite are greater, the data presented in Chapter 2 would indicate that the reverse is true due to the significantly lower solubility of titanium in ferrite with respect to austenite. The nucleated titanium nitride particles will, however, grow at a higher rate than corresponding particles in the austenite matrix due to the higher diffusion rate of titanium (and nitrogen) in a ferritic matrix.

It should be noted that the temperatures used during nitriding of FV448 and F1 were relatively high (1100-1150°C). The effect of temperature is discussed below.

12.2   EFFECT OF TEMPERATURE ON PRECIPITATE SIZE

The work of Kindlimann (1970) demonstrates that it is possible to improve the creep performance of high chromium ferritic steels through precipitation strengthening with titanium nitride. The important conclusion to be drawn from Kindlimann's work relates to the temperature window (approximately 820-980°C) within which gaseous nitriding produced a significant strength increment. This finding is consistent with the effect of temperature on titanium nitride precipitate size noted by Laing (1989) for nitrided alloy 6138. The coarse precipitates (>200nm diameter) were formed at the upper end of the temperature range investigated (1050°C). A reduction in nitriding temperature of only 100°C gave Laing a more than two-fold reduction in precipitate size to 90mm. In Kindlimann's case, the precipitate dispersion is likely to have been finer still and, therefore, potentially capable of significantly enhancing the materials strength.

It is deduced from the review of previous work that temperature appears to be the primary controlling factor on the titanium nitride precipitate size in ferritic steel. Although the composition in which the precipitation occurs will affect the nucleation and growth kinetics, this is a second order effect.

12.2.1 Reduced Temperature Precipitation: Homogeneous Nucleation

In order to investigate the effect of temperature, the classical theory of homogeneous nucleation is considered. The essential driving force is the difference in free energies of the initial supersaturated solution containing titanium and nitrogen

148

and the final composition where all the titanium and nitrogen form the titanium nitride precipitate, given stoichiometric amounts of nitrogen.

The classical total free energy change of the system accompanying the formation of a precipitate in a solid is as follows:

$$\Delta G = -\Delta G_v + \Delta G_s + \Delta G_m \qquad (12.2)$$

Where ΔG_v is the free energy associated with the formation of the volume of titanium nitride. ΔG_s is the energy of the surface created between the titanium nitride particle and the ferrite. ΔG_m represents the strain energy arising from the formation of the particle. Figure 12.2 illustrates the free energy of a precipitate particle as a function of its radius.
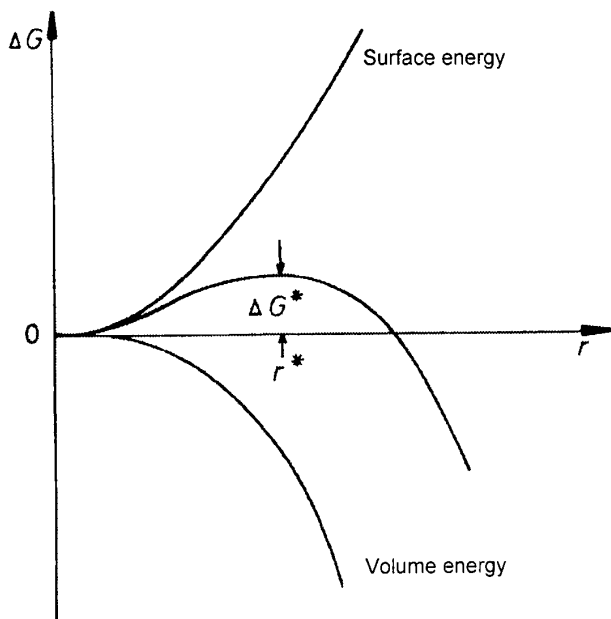
Figure 12.2. The variation of ΔG with r for a homogeneous nucleus, after Porter and Easterling (1988)

The activation energy barrier ΔG^* and the critical radius r^* are shown. For particles with an r value less than r^* they dissolve and go back into solution whereas above r^* the free energy decreases with increasing radius therefore the particle is stable and continues to grow. As detailed above growth is controlled by the concentration gradient.

The incubation time for nucleation t_p will therefore be controlled by the activation energy for nucleation and the activation energy for diffusion. The precipitation incubation equation quoted by Koster (1974) is as follows:

$$t_p = AP \exp\left(\frac{Q_P + Q_D}{RT}\right) \qquad (12.3)$$

149

where AP is a factor which includes an entropy term and a geometric factor. Q_p is the activation energy for the nucleation of the titanium nitride and Q_D is the activation energy for diffusion.

As the temperature is reduced, to a first approximation the surface energy does not change with temperature. However, the volume free energy varies with temperature, becoming more negative as the temperature is reduced as the supersaturation increases. The effect is shown in Figure 12.3 where it can be observed that the activation energy barrier is reduced and therefore the critical stable particle radius is reduced. Consequently, the rate of homogeneous nucleation is increased.
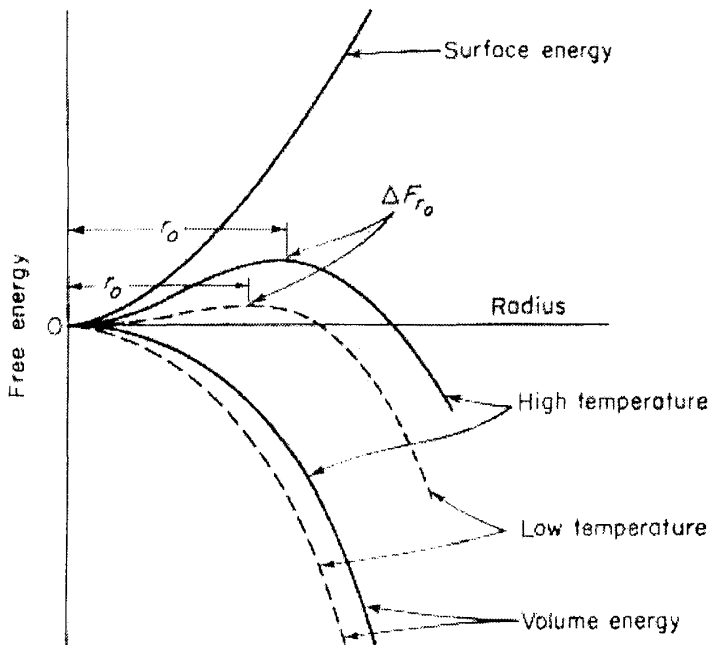
Figure 12.3 Effect of temperature of precipitation on the free energy of a precipitate particle as a function of its radius, after Reed-Hill (1973)

On reducing the temperature the nucleation rate is still determined by the activation energy. However, the activation energy decreases more than linearly with temperature, this gives a rapidly increasing nucleation rate as the undercooling increases. The growth rate, however, is controlled by an activation energy, which does not vary appreciably with temperature, and hence the rate decreases as the temperature decreases due to slowing of diffusion. These opposing factors give an overall transformation rate, which first increases to a maximum at a temperature below the equilibrium transformation temperature and then decreases again as temperature falls further. This results in the classic precipitation "C" curves.

A precipitation time temperature (PTT) diagram for titanium nitride in an austenite matrix is shown in Figure 12.4 for various concentrations of titanium.
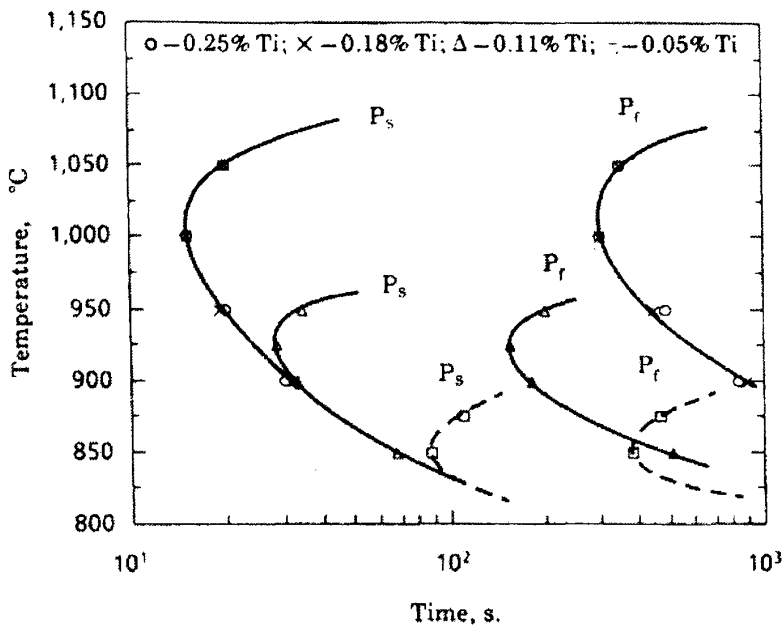
Figure 12.4 PTT curves for titanium nitride, after Lui & Jonas (1988)

This PTT diagram was constructed by Lui & Jonas (1988) using a stress relaxation technique. In this technique as precipitation takes place in solution treated titanium bearing steels dislocations are pinned. After a certain number of precipitates have been formed, relaxation is arrested and the initiation of precipitation is indicated. The PTT curves showed the classical C shaped curve for all the titanium containing steels tested. From this technique, P_s and P_f cannot really be measured experimentally and the nitrides plotted are more realistically some percentage after the start and before the finish e.g. $P_{0.05}$ and $P_{0.95}$.

12.2.2 Reduced Temperature Precipitation: Heterogeneous Nucleation

Although the above shows the effect of decreasing the temperature on homogeneous nucleation, nucleation of precipitates in solids is almost always heterogeneous. Suitable heterogeneous nucleation sites in order of decreasing ΔG^* from the review by Porter & Easterling (1988) are:

I.   homogeneous sites

II.   vacancies

III. dislocations

IV.   grain boundaries

V.   free surfaces

151

Nucleation will occur more rapidly at sites at the bottom of the list. The reason that the activation energy is reduced is because the "defects" listed above all increase the free energy of the material. Precipitating a particle on the defect, results in the destruction of part of the defect, thus releasing some free energy. This free energy reduces (or even removes) the activation energy barrier (ΔG^*). Evidence that heterogeneous nucleation dominates the precipitation of titanium nitride is clearly observed throughout this thesis in the TEM examinations (Figure 11.3a & b for example) where precipitation on the original fine ferrite grain boundaries dominates.

12.2.2.1　Sites for Precipitation

The greatest effect of lowering the temperature in the titanium nitride strengthened alloys could be to increase the sites for heterogeneous nucleation. If precipitation could be performed at a temperature below the primary recrystallisation temperature then this would provide a vast number of dislocation sites for heterogeneous nucleation. The effects of precipitating on a dislocation are twofold, firstly as described above, the effect is to reduce the total strain energy of the embryo ΔG_s, thus the driving force is increased, decreasing ΔG^*. Secondly the growth of the embryo beyond the critical size is assisted by dislocation pipeline diffusion.

The powder particles after the Mechanofusion Process with the chromium nitride powder will have a very high dislocation density due to the extent of room temperature plastic deformation that occurs with this process. The objective therefore is to determine the conditions that will allow precipitation to occur on the dislocation before the dislocations are removed by primary recrystallisation.

In order to determine the conditions necessary for dislocation precipitation a review of the recovery and primary recrystallisation process was conducted.

12.3　RECOVERY AND PRIMARY RECRYSTALLISATION

The descriptions of recovery and recrystallisation are as follows:

Recovery

Recovery always precedes recrystallisation. The driving force for recovery is the release of stored energy associated with the deformed state.

Microstructural changes during recovery are associated with the rearrangement of dislocations. Cell boundary dislocations become less tangled and low angle boundaries begin to form. Dislocation glide takes place from the cell interiors to the cell walls. Some dislocation annihilation also occurs.

Primary Recrystallisation

Primary recrystallisation as defined in Chapter 7 involves the nucleation and growth of new grains within the deformed structure until all the deformed material is consumed by strain free grains.

12.3.1 Kinetics of Primary Recrystallisation

A formal theory of recrystallisation kinetics is presented by Burke & Turnbull (1952). The main features are that primary recrystallisation has three distinct phases, as shown in Figure 12.5.
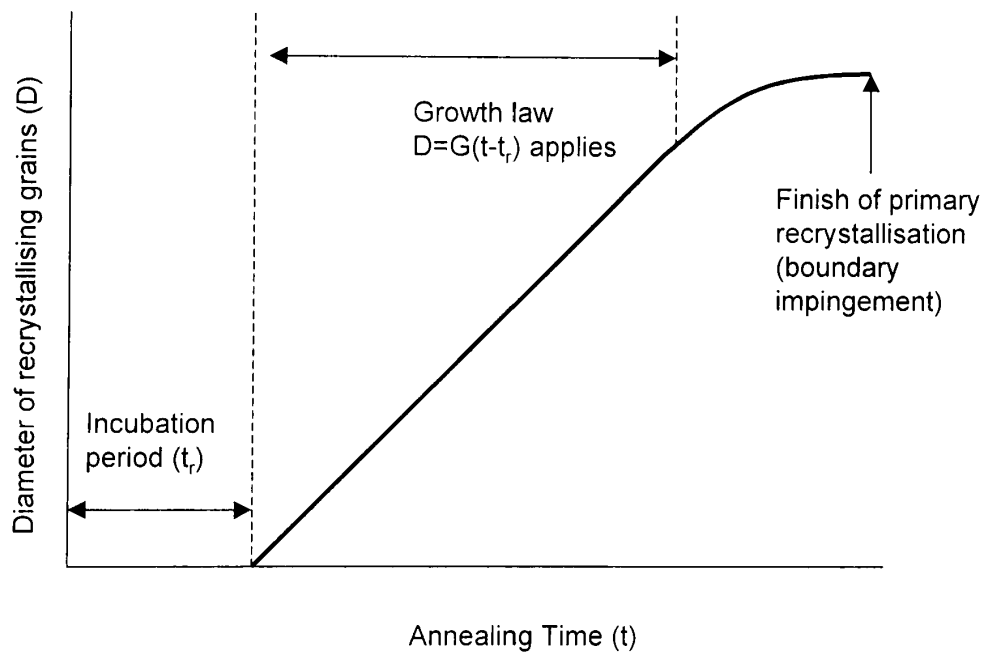
Figure 12.5 The characteristic features of an expanding grain during primary recrystallisation under isothermal annealing conditions, after Burke & Turnbull (1952)

The incubation time t_r is inversely related to the nucleation rate N, i.e. the number of new grains appearing per unit time in a unit volume of unrecrystallised metal. From the work by Anderson & Mehl (1945) on aluminium:

$$t_r = A(N)\exp\left(-\frac{Q_R}{RT}\right) \qquad (12.4)$$

A(N) is a factor that combines the driving force for recrystallisation, an entropy term and various geometric factors. Q_R is the activation energy for the formation of a mobile recrystallisation front. As described in Section 12.3.3 there is more than one process involved in primary recrystallisation, thus the recrystallisation activation energy is generally considered to be an empirical constant.

The linear rate of growth is described by

$$D = G(t - t_r) \qquad (12.5)$$

Where D is the diameter of the growing grain, G is the linear rate of growth and t is the annealing time.

The fraction of material recrystallised can be calculated by the Johnson-Mehl-Avrami expression, proposed by Johnson & Mehl (1939) and developed by Avrami (1941).

$$X = 1 - \exp(-bt^k) \qquad (12.6)$$

X is the fraction recrystallised, t is the time in seconds, and b and k are constants.

12.3.2 Primary Recrystallisation Variables

The variables that influence primary recrystallisation have been summarised by Burke & Turnbull (1952) and are described as follows:

- A minimum amount of deformation is required for primary recrystallisation.

- The lower the amount of deformation, the higher the temperature/time factor is required to be.

- The larger the original grain size, the greater the amount of deformation that is required to give the equivalent recrystallisation time and temperature

- Increasing the primary recrystallisation temperature decreases the incubation time.

- After the incubation time, primary recrystallisation builds up to a maximum rate after which it finishes slowly.

- The final grain size depends mainly on the degree of deformation and, to a lesser extent, on the temperature.

12.3.3 Formation of Nuclei

The process of subgrain formation is normally complete after the recovery stage. Nucleation of new grains occurs at the maximum energy area, i.e. high lattice strain positions where there is strong lattice curvature and in areas close to grain boundaries.

A number of models have been developed to describe the formation of a small strain free volume that can grow out and consume the deformed matrix surrounding it. It is not the purpose of this thesis to consider in detail all the proposed nucleation models. Three proposed mechanisms are described briefly below.

12.3.3.1   Abnormal Subgrain Growth

This mechanism is described by Smallman (1990). After deformation, recovery occurs by polygonisation, resulting in several regions in the lattice where the strain energy is lower than the surrounding matrix. Initially as the subgrains grow, the angles between them are a few degrees; in this case, the growth of any subgrain at the expense of others is very slow. However, upon further growth, the boundary the subgrain makes with the deformed matrix can be large, $\theta \cong 30\text{-}40°$. High angle boundaries have high mobility and are able to grow at a faster rate than the surrounding subgrains and thus can act as the nucleus of a recrystallised grain. Further increases in size result in greater differences in orientation between the nucleus and the matrix until it finally becomes recognisable as a new strain free grain separated from its surroundings by a large angle boundary.

12.3.3.2   Subgrain Coalescence

This is the combination of subgrains to form a strain free region large enough in size to grow. As postulated by Hu (1963) the elimination of a subgrain boundary must result in a relative rotation of the two subgrains that are combined. This process is shown schematically by Li (1962) in Figure 12.6.
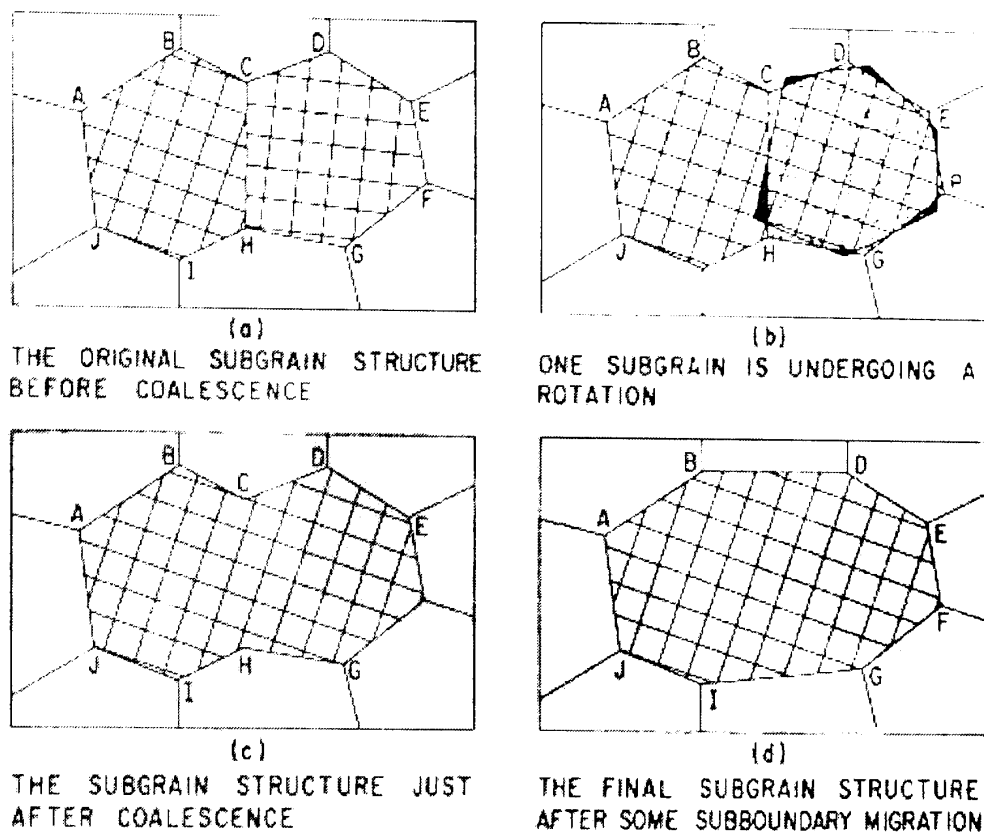
Figure 12.6 Subgrain coalescence by rotation of one subgrain, after Li (1962)

(a) Represents the initial structure with the misorientations indicated by the hatched lines. To remove the sub-boundary there must be a relative rotation of one or both subgrains (b). (c) shows the two subgrains united.

The subgrain coalescence is the effective movements of the dislocations from the original boundary CH into the remaining surface of the combined subgrains, raising the energy of the surface. An extension of this process eventually results in a small grain surrounded by a high angle boundary with sufficient energy to grow progressively into the polygonised matrix that surrounds it.

12.3.3.3   Strain Induced Boundary Migration

Strain induces boundary migration, Beck & Sperry (1949), differs from the previous primary recrystallisation mechanisms discussed in that no new grains are formed. Rather, this process describes the growth of one grain into its neighbouring area becoming strain free in the process and is shown schematically in Figure 12.7.

For the process to occur, it is assumed firstly that the boundary is capable of high mobility due to a large misorientation between the two grains (A and B in Figure 12.7).

156
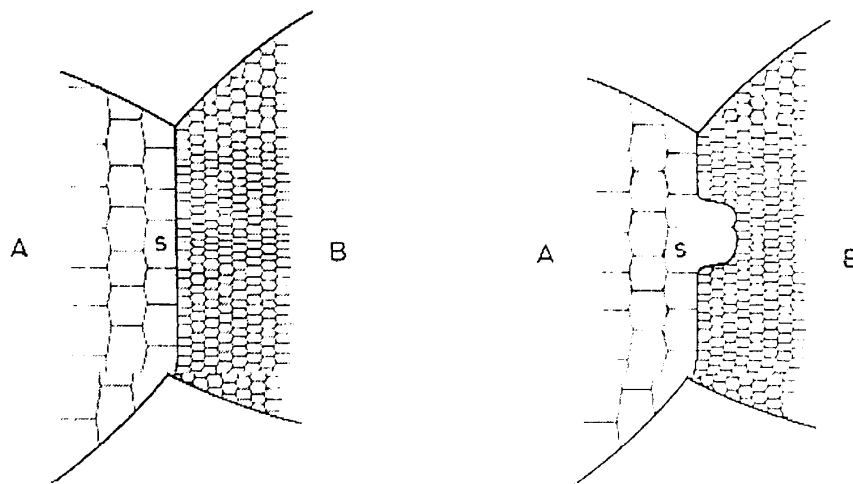
Figure 12.7 Schematic of strain induced boundary migration, after Beck & Sperry (1950)

Secondly, there is a significant strain difference between the two grains. Nucleation of recrystallisation is initiated by the grain boundary bowing at the large subgrain in the lesser-strained grain (A). The direction of growth is into the more heavily deformed grain as this represents a reduction in internal energy of the system.

12.3.3.4 Summary

These models are in agreement in two critical points:

- A region of a crystal can become a nucleus and grow only if its size exceeds a minimum value.

- The nucleus must be surrounded at least in part by the equivalent of a high angle grain boundary (for the mechanism proposed by Beck & Sperry, it occurs at regions where high angle boundaries already exist).

12.3.3.5 Effect of Precipitation

Although not included in the above description, it is well established that dispersed incoherent particles can either retard or accelerate recrystallisation. Primary recrystallisation is retarded in a material containing a dispersion of fine closely spaced particles (Doherty & Martin 1963). Whereas, as observed in Chapter 6 primary recrystallisation can be accelerated by large widely spaced particles. Thus, in order to maximise the incubation time prior to primary recrystallisation it is necessary to eliminate any coarse chromium nitride particles.

12.4 KINETICS OF NUCLEATION AND GROWTH OF PRECIPITATES AND STRAIN FREE GRAINS

It is apparent from the foregoing investigation that in actual fact the system comprises of the competing processes of nucleation and growth of strain free grains in a strained matrix and the nucleation and growth of titanium nitride precipitates on the strained matrix dislocations. If the conditions are such that precipitation occurs before primary recrystallisation, then the fine precipitates will retard primary recrystallisation. If, however, primary recrystallisation occurs before precipitation, then precipitation is retarded by the removal of the heterogeneous sites.

For primary recrystallisation, it has been found that the incubation period for recrystallisation t_r is given by equation (12.4) from the Anderson & Mehl (1945) work on aluminium. In the case of the precipitation of particles, the incubation time t_p is given in equation (12.3) Figure 12.8 below plots a schematic of the interaction of the two competing processes.
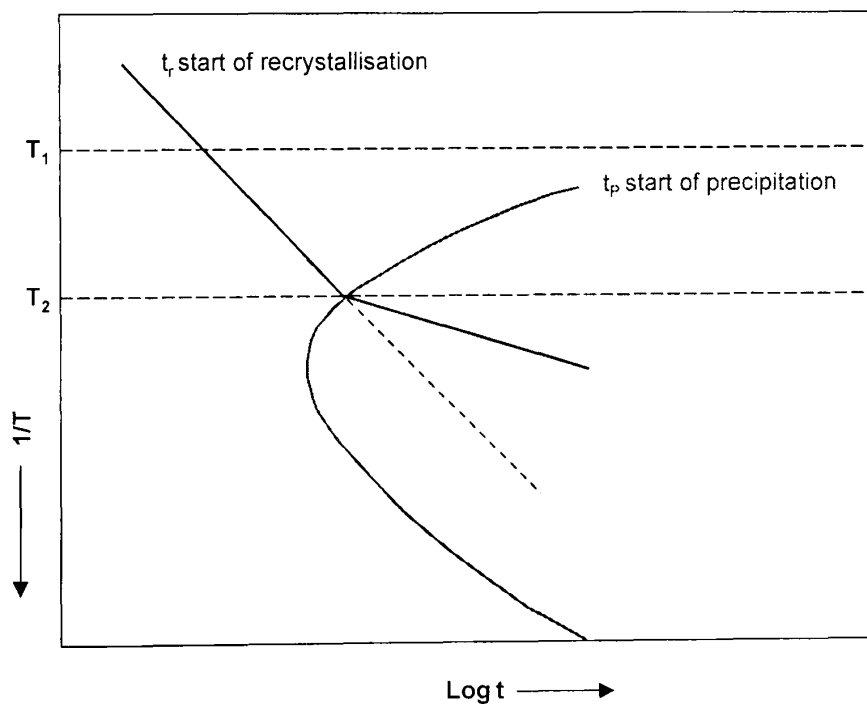
Figure 12.8 Schematic showing possible relationship between the incubation periods for precipitation (t_p) and recrystallisation (t_r) as a function of the annealing temperature, after Koster & Hornbogen (1968).

At T_1, $t_p > t_r$, The incubation period for recrystallisation is less than that for precipitation, hence, recrystallisation can occur unhindered by titanium nitride particles. Precipitation of titanium nitride occurs at longer times but the high density

of dislocations, heterogeneous nucleation sites will have been removed resulting in significant grain boundary precipitation.

At $T < T_2$ The incubation period for precipitation is less than that for recrystallisation ($t_r > t_p$) and thus precipitation is able to occur on the recovered dislocation network, giving a fine homogenous dispersion of particles necessary for creep strength. The precipitation of titanium nitride particles will significantly interact with the recrystallisation reaction.

If the precipitation temperature is reduced sufficiently below T_2, then it is possible for the particle density to be so high that a significant proportion of the dislocations are pinned. In the discussion by Kreye & Hornbogen (1970) the precipitates considered were of relatively low stability, therefore, primary recrystallisation occurred after holding for a period at the recrystallisation temperature when the coarsening of the particles reached a critical level. The stability of the titanium nitride particles is such, that for a given dislocation density and a sufficiently low precipitation temperature, primary recrystallisation may not occur. This is discussed in Chapter 13. If, however, the dislocation density is increased by further work, it is possible to decrease t_r sufficiently to induce primary recrystallisation. As discussed in Chapter 8, this is more likely in low stacking fault materials (nickel based alloys) that cannot reduce the driving force by sufficient recovery.

12.5 MODIFICATIONS TO THE PROCESS ROUTE

Prior to this stage, precipitation of the titanium nitride has always been carried out during the consolidation process of the powder, namely the extrusion, HIPping or Osprey billet spraying process. These processes all require a minimum operation temperature in order to achieve a consolidated product, i.e. to reduce the degree of porosity. As such, it has been this production limitation that has governed the precipitation kinetics.

It is apparent, though, that each of the titanium containing powder particles after being "coated" with chromium nitride during the Mechanofusion process contain all the ingredients necessary for precipitation. In fact, the sub 45 μm Mechanofused powder can be regarded as a micro system for the entire alloy.

In order to investigate the minimum temperature that precipitation can be performed to maintain the maximum dislocation density, and also to carry out the reaction in a timescale that would be conceivable for an industrial application; the following factors had to be considered:

(1)   Will the chromium nitride dissociate, releasing the necessary nitrogen for the reaction?

(2)   Will the titanium diffuse to the precipitate within a reasonable timescale?

12.5.1 Chromium Nitride Dissociation

This was studied by Lee (1998) in assessing a model for internal solid state nitriding of austenitic stainless steels. Lee utilised the nitrogen potential pressure data from Pearson & Ursula (1953) and the dissociation pressure function developed by Wilson & Wilson (1980). Utilising these relationships allows the nitride dissociation pressure to be calculated with respect to metal activities at the various temperatures being considered here (Table 12.1). Table 12.1 shows that at various temperatures the dissociation pressures of the chromium nitrides far exceed that of titanium nitride and thus thermodynamically a driving force for the dissolution of the chromium nitrides and precipitation of titanium nitride exists.

	N_m	500°C	600°C	700°C	800°C	1000°C	1200°C
$2Ti+N_2 \rightarrow 2TiN$	0.028	3.0×10^{-33}	4.9×10^{-28}	6.7×10^{-24}	2.0×10^{-20}	2.6×10^{-15}	1.4×10^{-11}
$4Cr+N_2 \rightarrow 2Cr_2N$	0.196	5.8×10^{-5}	1.2×10^{-3}	2.2×10^{-2}	1.5×10^{-1}	4.0	44.0
$2Cr+N_2 \rightarrow 2CrN$	0.196	2.2×10^{-6}	1.4×10^{-4}	2.4×10^{-3}	2.3×10^{-2}	7.4×10^{-1}	13.1

Table 12.1   Nitride dissociation pressure (atm.) with respect to metal activities at various temperatures.

An alternative assessment is by considering the standard stability data. Calculating the $\Delta G°$ values over a similar temperature range (Table 12.2) confirms that titanium nitride is considerably more stable than chromium nitrides at all the temperatures.

		500°C	600°C	700°C	800°C
$2Ti+N_2 = 2TiN$	$\Delta G^\circ = -160500+44.40T$	-126179	-121739	-117299	-112859
$4Cr+N_2 = 2Cr_2N$	$\Delta G^\circ = -44000+24.0T$	-25448	-23048	-20648	-18248
$2Cr+N_2 = 2CrN$	$\Delta G^\circ = -51000+33.4T$	-25182	-21842	-18502	-15162

Table 12.2 ΔG° calculated values at various temperatures.

12.5.2 Titanium Diffusion

The calculated interparticle spacing based on a target 80nm particle diameter for the 1.9wt% titanium Alloy C6 equates to 120nm based on the Hertz model discussed in Chapter 11. Therefore, the maximum diffusion distance for the titanium under these circumstances would be 60nm. Utilising equation (5.1) an estimation of the duration required for the titanium to diffuse to the precipitate in α iron at various temperatures can be calculated. The resultant graph is shown in Figure 12.9.
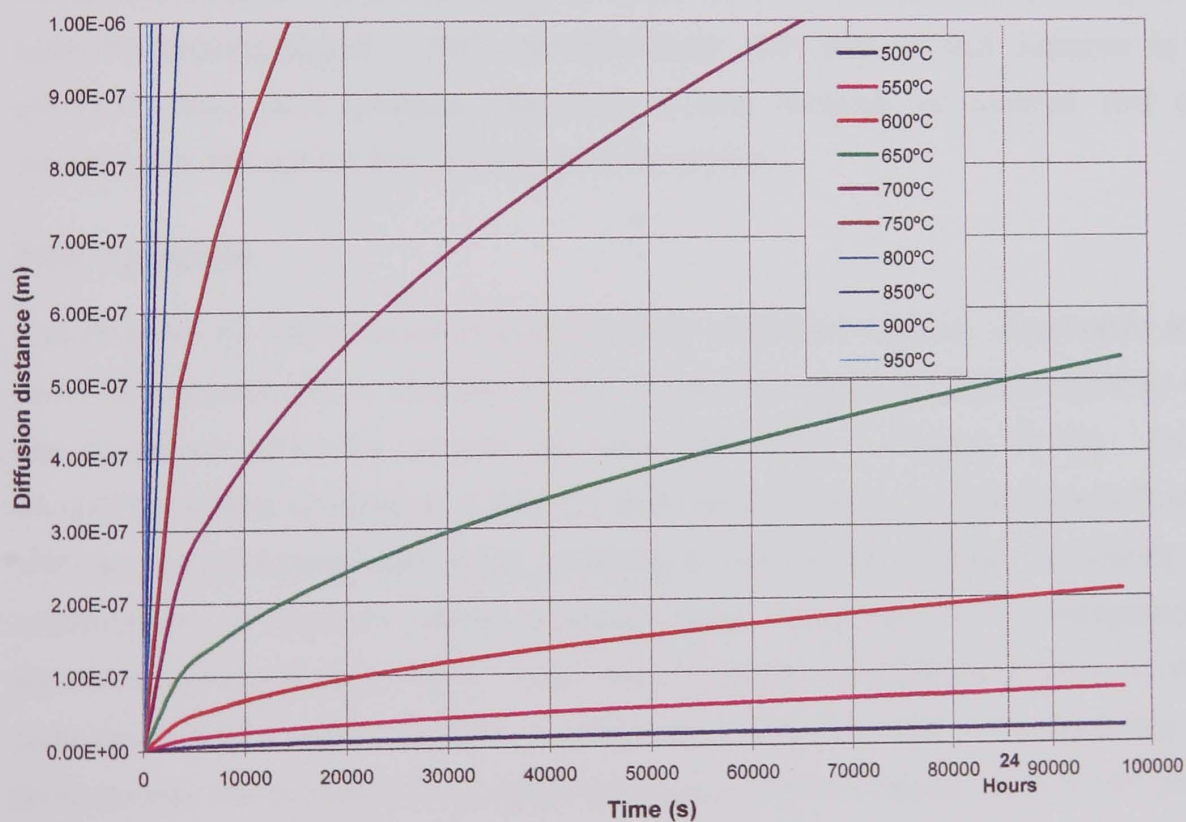
Figure 12.9 Relationship between titanium diffusion time and temperature for equation (5.1)

Considering the data in Sections 12.5.1 and 12.5.2, in order to complete the precipitation within a reasonable industrial time frame e.g. 24hours, a precipitation

temperature of 600°C was selected. This is significantly below the minimum primary recrystallisation temperature for Grade 430 material.

12.6 LOW TEMPERATURE PRECIPITATION EXPERIMENT

The apparatus used was that discussed in Chapter 7. The powder was heated at a rate of 400°C/hour and held at constant 600°C ± 1°C. Powder samples were removed at one hour intervals. The samples being cooled in an argon draught

Metallurgical preparation was by mixing the powder in cold setting reagent and polishing in the normal manner. Previously, the materials had been etched electrolytically using oxalic acid. As the powder particles are not set in a conducting resin and are not in intimate contact with each other, it was not possible to use the electrolytic etching process. Trials were conducted on typical samples to determine the most appropriate "swab" etch. This revealed that a reagent containing one part hydrofluoric acid, five parts nitric acid and thirty parts water gave very good repeatable results. Etching times at 20°C were controlled at 20s to give the optimum etching depth. This non-electrolytic etch was in fact superior to the previous oxalic acid process, therefore, it was adopted for powder and solid components throughout the remainder of the project.

12.6.1 Results

Examination by SEM revealed that the heat treatment had no observable effect upon the powder until a duration of four hours was reached. At this duration etch pits appeared within the powder particles, as shown in Figure 12.10b. This is thought to be due to clusters of titanium and nitrogen atoms forming Guiner-Preston (GP) zones producing local strain, resulting in preferential etching. Clustering and precipitation of titanium nitride particles were observed and investigated by Rickerby, Hendry & Jack (1986). They found that the precipitation of titanium nitride particles in 0.5, 1.0 and 2.0 wt% Ti (alloys gas nitrided in $NH_3 - H_2$ mixtures) was preceded by the formation of a stable dispersion of disc shaped Fe-Ti-N GP zones. The population of the etch pits and thus the postulated GP zones increased as the hold time increased until the titanium nitride embryos reached their critical radii and became incoherent visible precipitates, Figure 12.10c. The etch pits surrounding the incoherent particles were negligible, indicating a reduced strain field in comparison to the coherent GP zone. The number of visible particles increased with

holding time and the extent of etch pitting decreased with increasing holding time (Figures 12.10d and e). After 17 hours at 600°C, the process appeared to be complete. The resultant microstructure, Figure 12.10f, was an extremely homogeneous array of fine titanium nitride particles. The fact that the fine precipitates are distributed within the grains with no apparent clustering at the grain boundaries would indicate that the heat treatment has been successful in inducing precipitation on the recovered dislocations' sub structure before primary recrystallisation initiated. The extended hold period agrees well with the diffusion time for titanium to cluster from a homogeneous distribution in the steel matrix.

2μm

a) As mechanofused
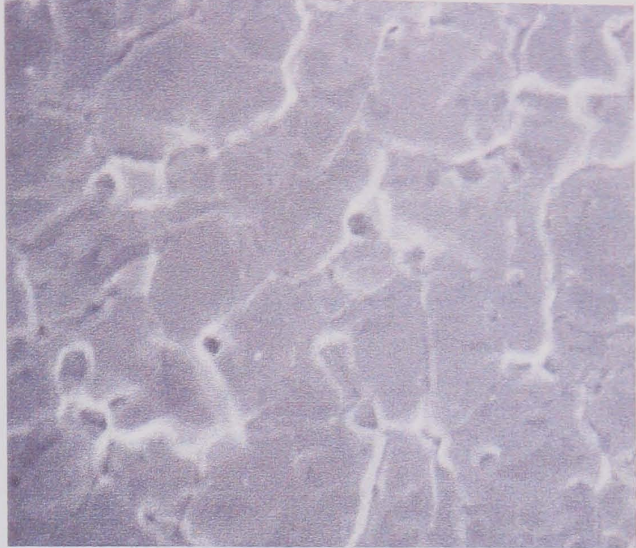
b) 600°C x 4 hours

c) 600°C x 6 hours
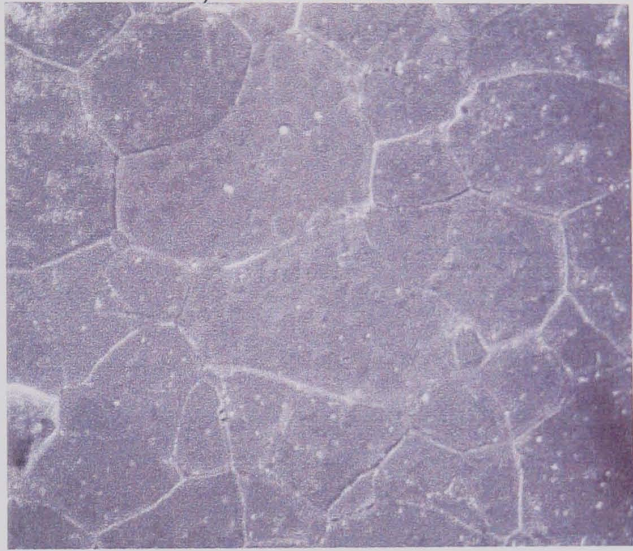
d) 600°C x 8 hours
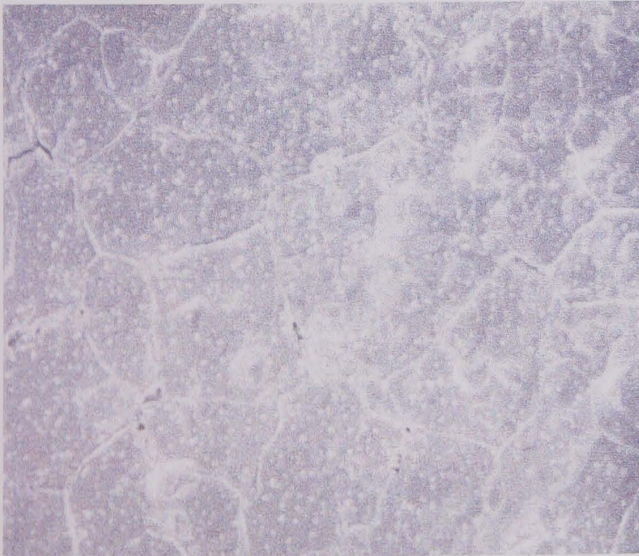
e) 600°C x 12 hours
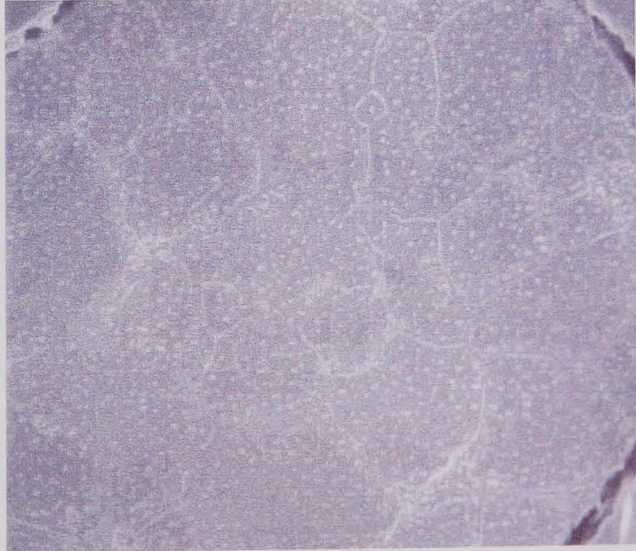
f) 600°C x 17 hours

Figure 12.10a-f Alloy C6 powder precipitation heat treatment trials

Chapter 13

Final alloy production and properties

As a result of the work in the previous chapter, an additional heat treatment step was added into the processing route for Alloy C6B. This additional step was inserted after the Mechanofusion (of the titanium containing feedstock material and the chromium nitride) and before extrusion of the powder to bar form. The additional heat treatment of 600°C for 17 hours was performed on the canned powder material before it was heated to 1000°C for extrusion.

The first noticeable difference in the production of this alloy was that 20% greater pressure was required to extrude the material as bar when compared to the Alloy C6 which is of identical composition but without the additional heat treatment. All other parameters, e.g. temperature, extrusion rate, reduction rate and initial can size were identical for both alloys.

13.1 ALLOY C6B EXTRUDED MATERIAL

Post extrusion, the material exhibited significantly greater hardness than the earlier C3, C4, C5 and C6 alloys as shown in Figure 13.1 which relates the extruded hardness against titanium content for the ferritic materials.
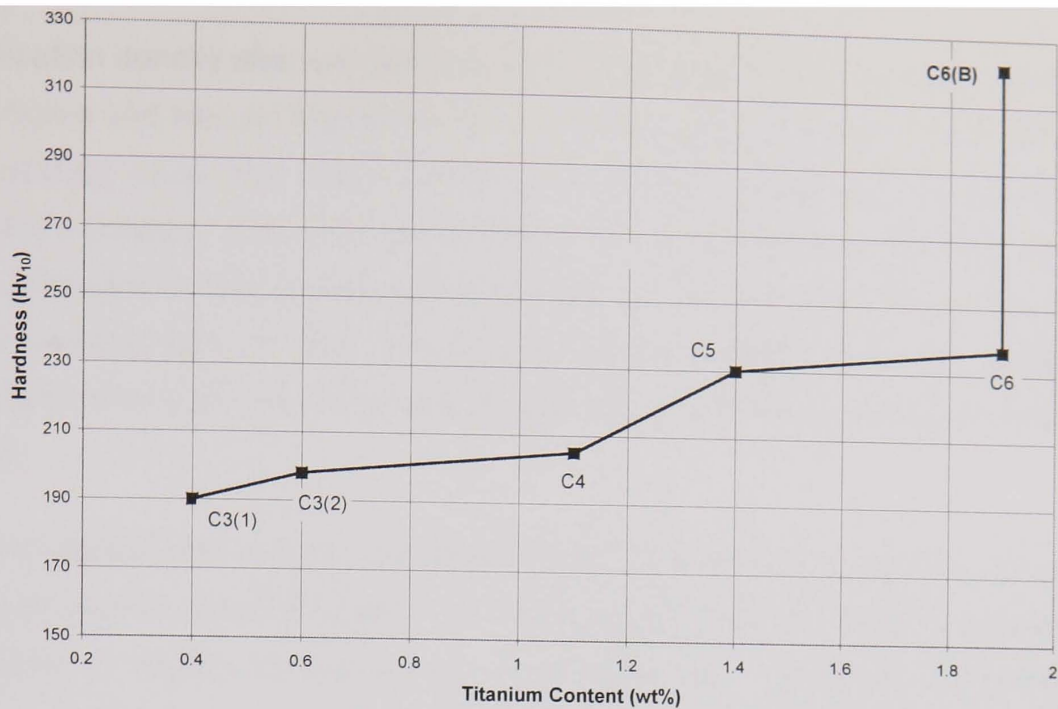
Figure 13.1 Hardness of as extruded alloy C materials

One possible explanation for this increase of $83Hv_{10}$ points over the highest ferritic hardness to date, was that the material structure consisted in part of untempered martensite. As the powder material was taken from the same source as the fully ferritic Alloy C6, this could possibly occur by having an excessive amount of chromium nitride. Thus, the final structure would have "free" nitrogen present, increasing the nickel equivalence and thus allowing the final composition to lie in the martensite plus austenite plus ferrite phase field. However, chemical analysis revealed that the final composition was almost exactly at the target values shown in Table 13.1, indicating that the Alloy C6B material had nominally the same composition and thus the same base structure as the Alloy C6 material which was fully ferritic. The Schneider diagram also indicates that Alloy C6B material would be fully ferritic.

	C	Cr	Si	Mo	Ti	Ni	Mn	N	Nfree
Target	<0.002	18	0.3	1.0	2.0	0	0.5	0.58	0.00
Actual	0.002	17.9	0.28	0.96	1.9	0	0.23	0.56	0.01
Difference	-	-	-	-	-0.1	0	-0.3	-0.02	+0.01

Table 13.1 Chemical composition of Alloy C6B

The reason for the high hardness value was revealed by the TEM investigation. Unlike the earlier as extruded structures, the alloy C6B material contained a high

dislocation density after extrusion, as shown in Figure 13.2a. As can be observed in this figure and also on Figures 13.2b & c the critical aspect of the Alloy C6B material processing route has been achieved with a fine dispersion of titanium nitride particles present. Also importantly the additional precipitation heat treatment stage has produced a material with a particle distribution which is relatively homogeneous. The development of the "as-extruded" microstructure may be explained by consideration of the microstructural events that occur during extrusion of the powder billet.

In commercial hot working operations producing high strain, dynamic recovery and recrystallisation generally result. This was the case with the earlier production alloys resulting in largely dislocation free microstructures. However, in the Alloy C6B titanium nitride strengthened alloys after extrusion at 1000°C and an extrusion ratio of 16:1 with respect to the cross sectional area, it appears that dynamic recrystallisation did not occur.

The evidence for this relates to the grain structure and the dislocation density after extrusion. Firstly, the grain structure, unlike the earlier alloys which exhibited fine equiaxed grain after extrusion, the Alloy C6B grains, whilst fine, are elongated in the extrusion direction. Given the extrusion ratio of 16:1 the mean grain size would increase in length by a factor of 16 and the diameter of the grains would consequently reduce in diameter by a factor of $\sqrt{16}$. The spread of measured values encompasses this aspect ratio of grains.

With regard to the very high dislocation density observed, the material during the extrusion process would have to dynamically recover and recrystallise followed by further deformation of the newly recrystallised structure to form the highly deformed grain structure observed. Whilst it is possible for a material to dynamically recrystallise and "re work" several times during a hot extrusion process, it would seem unlikely that the resultant condition of the 1m long bar would be a consistent heavily worked structure as indicated by the 320 ± 10 Hv_{10} hardness value measured at 50mm intervals along the length. Therefore, although the processing conditions used to produce the Alloy C6B bar, in theory, favour dynamic recrystallisation, the microstructural evidence via optical, SEM and TEM indicates that it does not take place in the production of the Alloy C6 bar.
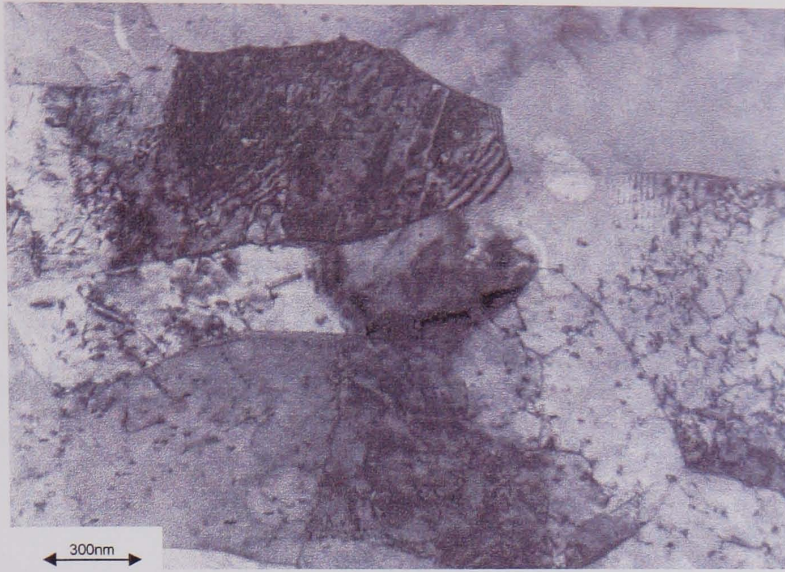
Figure 13.2a High dislocation structure of Alloy C6B after extrusion
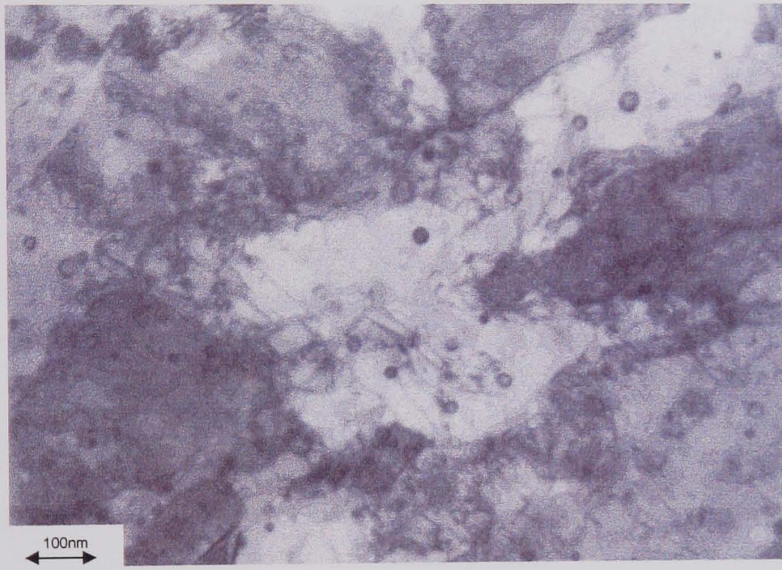
Figure 13.2b Interaction between precipitates and dislocation structure
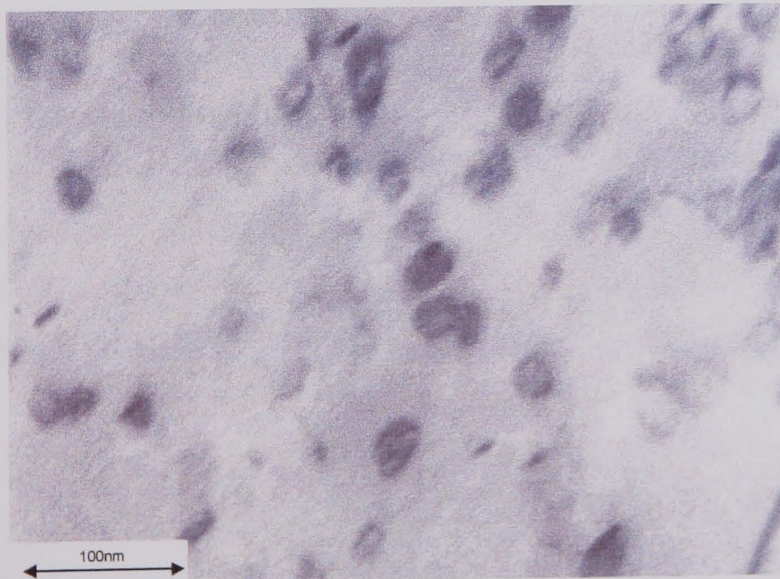
Figure 13.2c Alloy C6B fine homogeneous distribution of titanium nitride precipitates

Recrystallisation can be retarded or completely inhibited by closely spaced particles. The retarded recrystallisation by fine closely spaced particles is associated with reductions in both the nucleation and growth rate, Doherty and Martin (1963) shown in Figure 13.3. They concluded that for recrystallisation to occur the nuclei must attain the critical conditions for growth whilst being smaller than the interparticle spacing. For small interparticle spacings this was difficult, therefore recrystallisation was retarded. Pinning of subgrains by fine particles has also been cited as a mechanism for retarding nucleation of recrystallisation in TD nickel by Kimmel and Inman (1969).
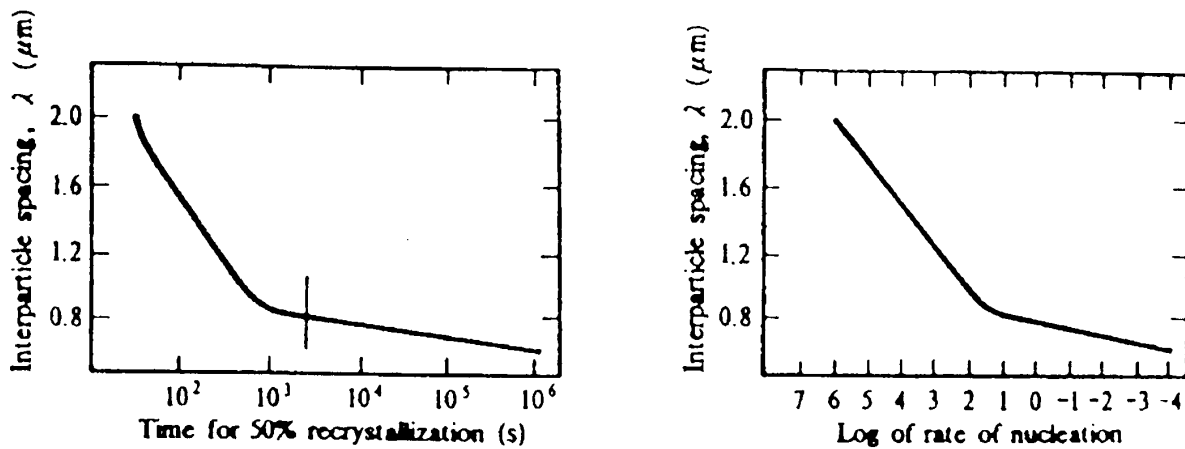
Figure 13.3 Variation of particle spacing with time for 50% recrystallisation in Al-CuAl₂ alloys, after Doherty & Martin (1963)

13.1.1 Particle Size Distribution

The additional heat treatment stage to precipitate the titanium nitride particles on the dislocation sub-structure prior to extrusion has been successful in significantly altering the particle size and also the particle distribution. As can be observed as a result of the heterogeneous dislocation nucleation sites being available during the precipitation reaction, there is a more homogeneous distribution of fine particles rather than the particles previously being precipitated predominantly at grain boundaries. The size of the precipitates is also significant, as the low temperature process to stimulate nucleation and retard growth of titanium nitride particles has succeeded in producing fine particles with the majority in the 20-60nm range which is below the 80nm target value. The average particle size and interparticle spacing from twenty random fields is presented in Table 13.2. The development of the particle size and spacing from Alloy C3 to C6B is shown in Figure 13.4.

169

	C3 (1)		C3 (2)		C4		C5		C6		C6B	
	Dia. (nm)	Spacing (nm)	Dia. (nm)	Spacing (nm)	Dia. (nm)	Spacing (nm)	Dia. (nm)	Spacing (nm)	Dia. (nm)	Spacing (nm)	Dia. (nm)	Spacing (nm)
Max	390	1650	430	2230	200	540	250	742	284	423	94	168
Min	190	630	160	150	61	90	60	20	84	12	20	81
Av.	238	884	256	676	126	287	175	271	211	259	61	122

Table 13.2 Measured particle diameters and edge to edge interparticle spacings for the alloy C materials
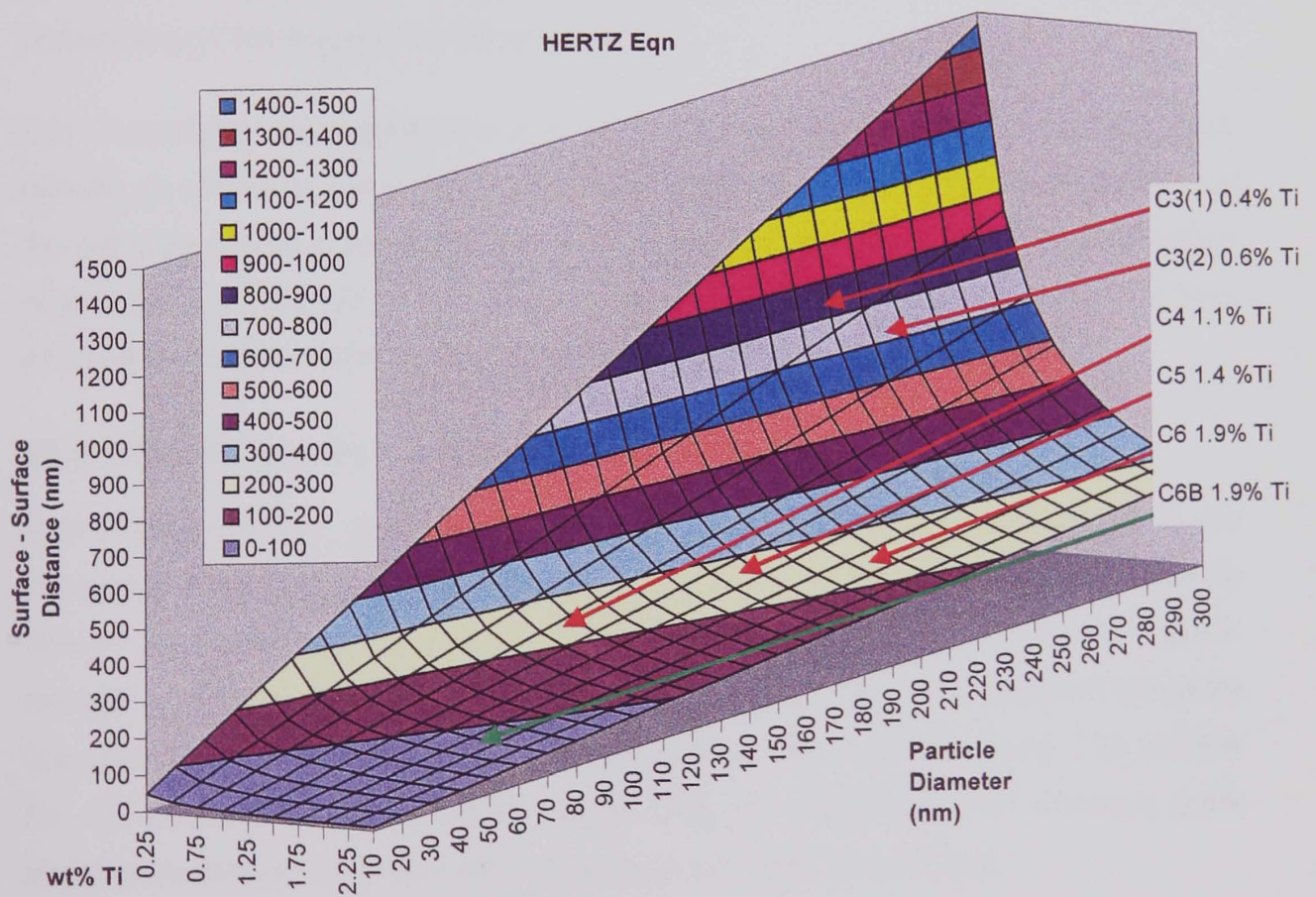
Figure 13.4 Actual alloy C parameters plotted on Hertz interparticle spacing, particle size and vol% particles relationship.

13.2 SECONDARY RECRYSTALLISATION OF ALLOY C6B

The Alloy C6B material also recrystallised markedly differently from the earlier alloys. Firstly, it was found that the material secondary recrystallised without the need for any additional cold deformation, as was the case with the Alloys C4, C5 and C6. Secondly, the heat treatment matrix (similar to that performed on the earlier alloys) revealed that the material fully secondary recrystallised with lower thermal energy (time temperature combination) than had been observed previously. Secondary recrystallisation occurred at 1200°C after two hours. As a result, additional heat treatments were performed at quarter hour intervals between one and two hours at 1200°C and some higher temperature heat treatments were discarded. In all cases the heating rate was 400°C/hour. The additional heat treatments revealed that the minimum time at 1200°C to achieve secondary recrystallisation was 90 minutes. Thus, this heat treatment was chosen as the secondary recrystallisation treatment for the alloy C6B material to minimise the coarsening of the titanium nitride precipitates.

After secondary recrystallisation the TEM examination revealed a low dislocation density as would be expected for completely recrystallised material. Examination of the particle size revealed that the 1200°C x 90 minutes secondary recrystallisation heat treatment resulted in minimal precipitate coarsening of the particles and thus similar interparticle spacings before and after secondary recrystallisation.

13.2.1 Secondary Recrystallised Grain Structure

Examination of the secondary recrystallised grain structure revealed it to be marginally different from the earlier grain structures. Although the grain structure viewed by optical microscopy will to some extent depend on the section taken, enough sections were taken to indicate that there were clear differences in the grain size and shape between the Alloy C6B material (shown in Figure 13.5a & b) and the C4, C5 and C6 materials viewed earlier (Figure 7.7a & b). The complex grain structure makes an accurate determination of the grain size difficult.
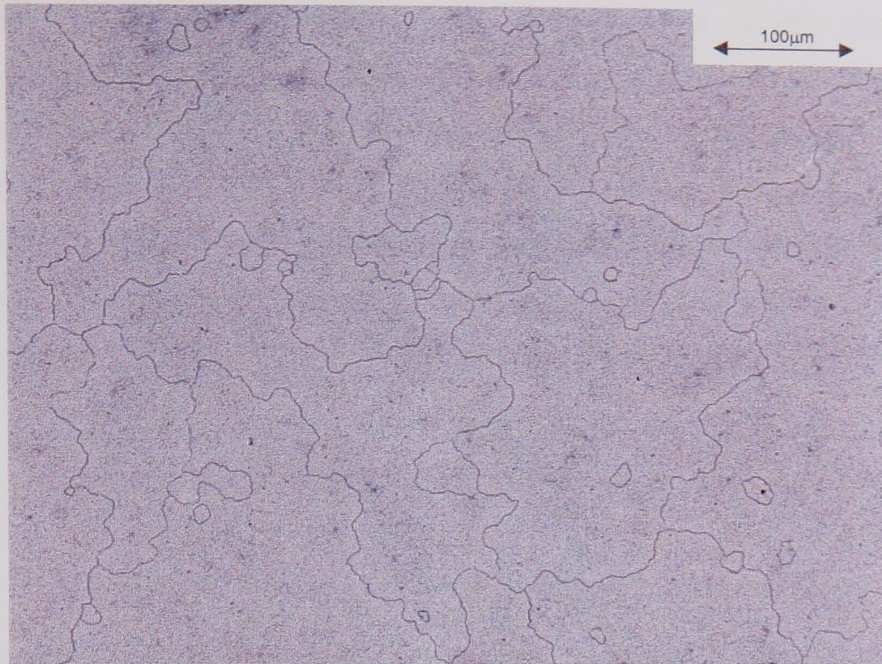
Figure 13.5a Transverse view of Alloy C6B secondary recrystallised structure
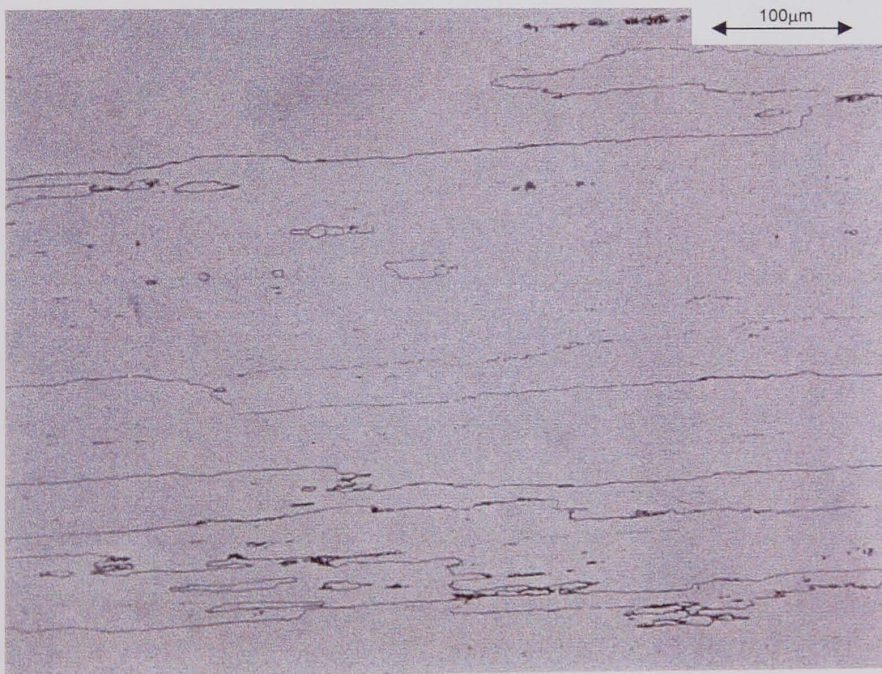
Figure 13.5b Longitudinal view of above

Due to the highly anisotropic grain structure the standard grain size measurement techniques such as ASTM comparison and mean linear intercept methods are not appropriate in their standard form. For the purposes of this investigation, the average longitudinal intercept length (L) and the average transverse intercept length (d) are quoted for this alloy and also for Alloys C3, C4, C5 and C6 in Table 13.3. Several authors including Wilcox & Clauer (1972) have demonstrated that it is the grain shape developed during secondary recrystallisation that is more important for the elevated temperature stress rupture strength than grain size. The common measure of grain shape is the grain aspect ratio (GAR) defined as

$$\text{Grain Aspect Ratio (GAR)} = \frac{L}{d} \qquad (13.1)$$

Alloy	Wt% Ti	Average Longitudinal Intercept Length (L) mm	Average Transverse Intercept Length (d) mm	GAR
C3 (1)	0.4	3.31	0.221	14.9
C3 (2)	0.6	3.38	0.269	12.8
C4	1.1	3.10	0.198	15.6
C5	1.4	2.31	0.212	10.9
C6	1.9	3.02	0.231	13.1
C6B	1.9	1.78	0.128	13.9

Table 13.3 Grain structure parameters

The effect of size and volume fraction of dispersoid on the secondary recrystallised structure and material properties was investigated by Benjamin & Bomford (1974) in relation to the secondary recrystallised structure produced and the effect this has on the stress rupture properties. The alloy under investigation was a Y_2O_3 dispersion strengthened nickel base superalloy IN853. The volume fraction of dispersoid added ranged from 0.70% to 4.55%, while the average dispersoid particle size ranged from 15-58nm. It was found, as shown in Figure 13.6 that the GAR increases with increasing average Y_2O_3 particle size and decreasing volume percent of Y_2O_3. As can be observed the dispersoid greatly affected the development of the GAR.
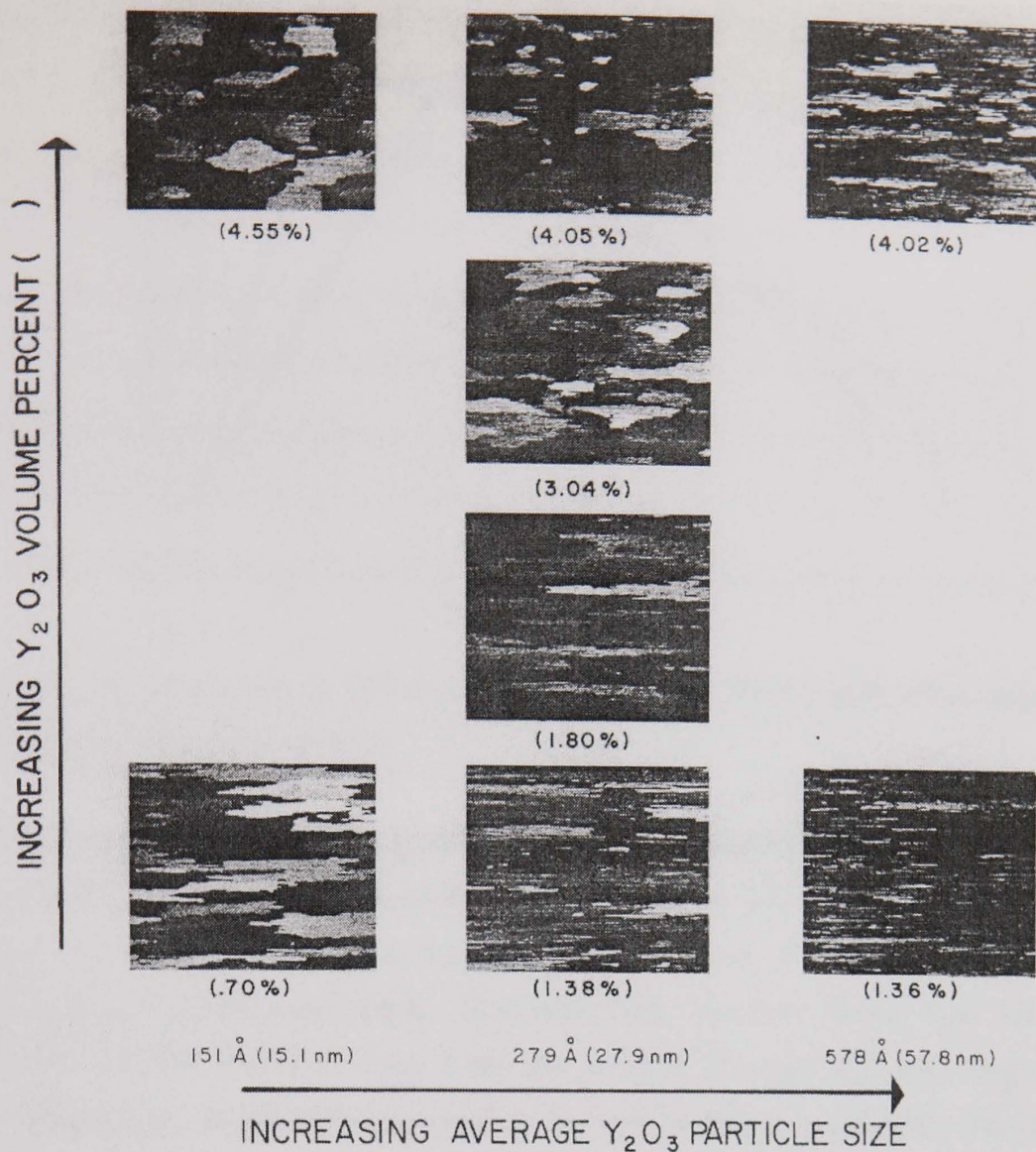
Figure 13.6 Relationship between dispersoid parameters and grain structure, after Benjamin & Bomford (1974)

This in turn influenced the rupture properties. For IN853 with a GAR less than 6, the 1900°F (1038°C) rupture strength was controlled by the GAR while at higher GAR it was found to be controlled by a dispersoid parameter ratio vf/dv where vf is the volume fraction and dv the average oxide particle size. The variation in the 100 hour rupture life at 1038°C with volume fraction of Y_2O_3 is given in Figure 13.7. Here it can be observed that the greatest rupture strength is obtained with a 1-2% volume fraction of ~16nm particles.
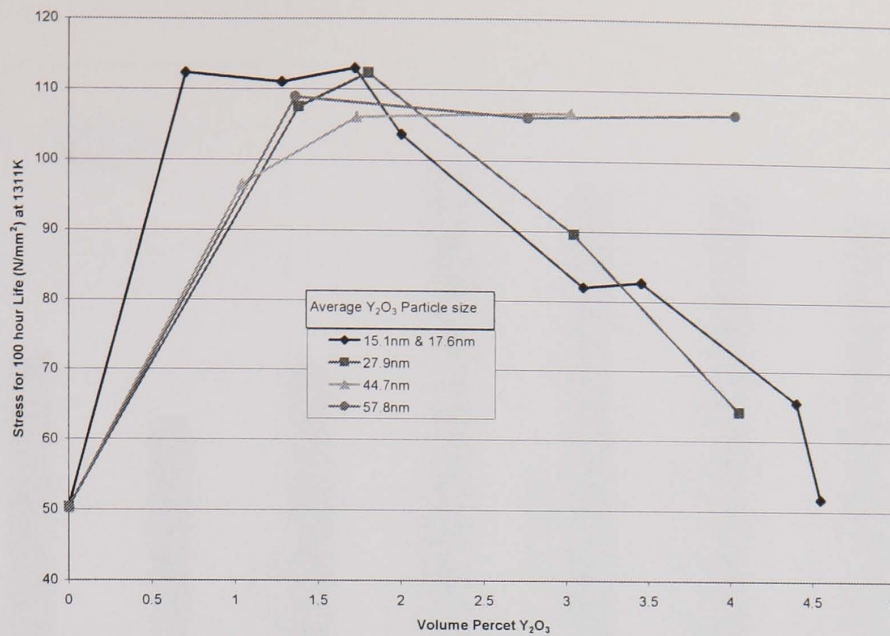
Figure 13.7 Variation in 100 hour rupture stress at 1311K with yttria volume %, after Benjamin & Bomford (1974)

The findings of Benjamin & Bomford (1974) in regard to the effect of particle size on the GAR are not replicated by this work on Alloys C3, C4, C5, C6 and C6B. This work has not found any clear trend in the GAR value with volume percent or size of the titanium nitride precipitate. This work has, however, found that the length and breadth of the grains in Alloy C6B are smaller (though still very large by normal comparisons. A possible explanation for this is that it is not only the particle size, but also the particle distribution that is important. Due to the heterogeneous nature of the particles in Alloys C3, C4, C5 and C6, relatively large particle free regions exist. This could result in preferred secondary recrystallisation nucleation sites, leading to fewer sites actuated and thus larger grains. Whereas observations of Alloy C6B suggest that the structure is more homogeneous, thus, at a given activation energy there will be more nucleation sites resulting in a larger number of smaller grains.

13.3 TENSILE PROPERTIES

13.3.1 20°C Tensile Properties

Room temperature tensile tests were performed at $3.79 \times 10^{-4} s^{-1}$ strain rate in a similar manner to the tensile tests described in Chapter 9. The 20°C tensile results are shown in Figure 13.8.
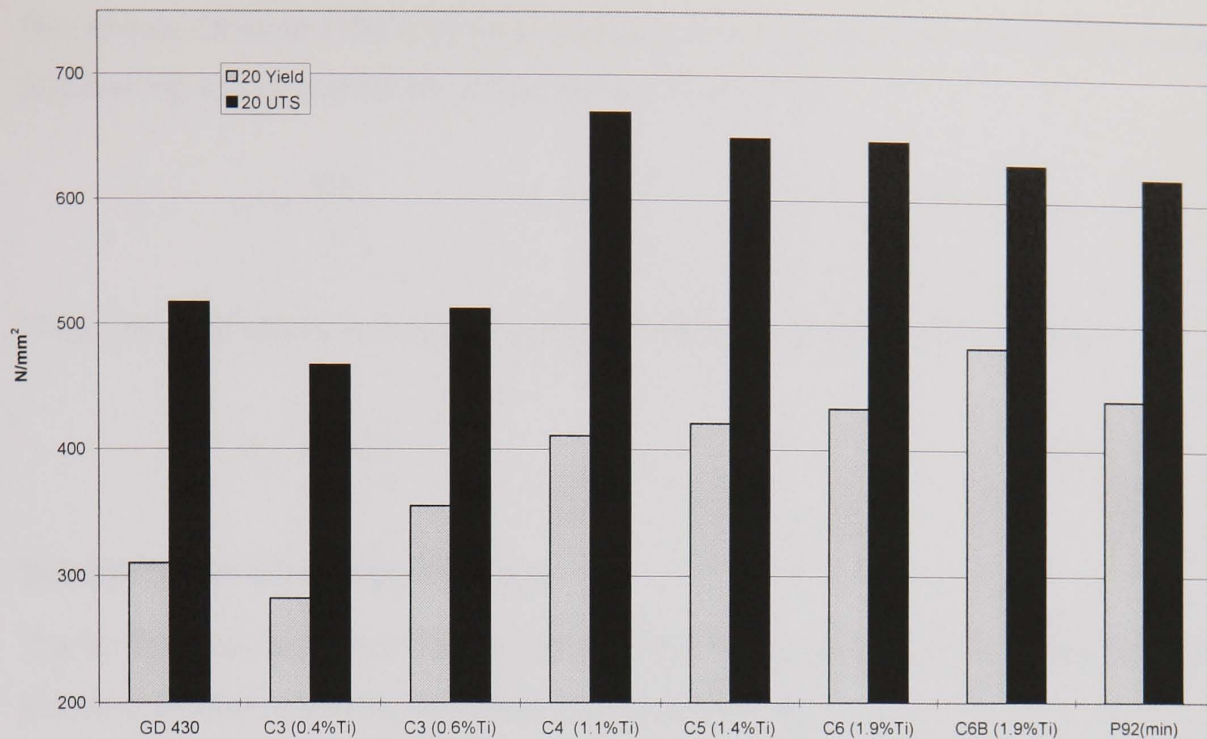
Figure 13.8 Room temperature tensile test results

13.3.1.1 Yield Strength

As can be observed, the yield strength of the material increases as the design and processing of the alloys have evolved from Alloy C3 to Alloy C6B. The yield stress is the minimum stress required to send dislocations through the matrix and as such, it is the threshold stress for plastic flow. The yield strength is the sum of all the constituent strengthening mechanisms. Thus:

Yield strength = dislocation strengthening + precipitation strengthening + solid solution strengthening + Internal strength + grain size effect.

Considering these strengthening mechanisms individually

Dislocation Strengthening (σ_d)

As dislocations interact with one another (i.e. the interaction between a gliding dislocation and another dislocation not lying on the primary slip plane) increases the pinning effect. Within a given grain dislocation/dislocation interactions are given by:

$$\sigma_d \propto Gb\sqrt{\rho} \qquad\qquad (13.2)$$

176

Precipitation Strengthening (σ_p)

The simple Orowan (1947) process of dislocation bypassing mechanism by bowing and leaving a loop surrounding the particles is given by:

$$\tau = \frac{Gb}{\lambda} \qquad (13.3)$$

Thus, the yield stress is inversely proportional to the inter-particle spacing λ

$$\sigma_y = K\frac{1}{\lambda} \qquad (13.4)$$

Solid Solution Strengthening (σ_{ss})

The solid solution strength is a function of the misfit strain and the concentration of the solid solution element, Fleischer (1963), such that

$$\tau_{ss} = AG\varepsilon^{3/2} C^{\frac{1}{2}} \qquad (13.5)$$

Grain Size ($K_y d^{-\frac{1}{2}}$)

A general relationship between yield strength and grain size was proposed by Hall (1951) and expanded by Petch (1953)

$$\sigma_y = \sigma_o + K_y d^{-\frac{1}{2}} \qquad (13.6)$$

Thus, the yield strength can be calculated from: $\sigma_y = \sigma_o + \sigma_d + \sigma_p + \sigma_{ss} + K_y d^{-\frac{1}{2}}$

13.3.1.2   Yield Stress Calculation

Conventional precipitation strengthened, high strength, tempered martensitic steels consist of carbides and nitrides precipitated on the dislocations at the fine grain and subgrain boundaries. As a result, it is by no means certain which strength controlling parameter will dominate; therefore, a complete assessment of all of the strengthening mechanisms detailed above would have to be conducted in order to predict the Yield strength.

In the case of the titanium nitride strengthened steels in the fully secondary recrystallised condition, however:

σ_d will be negligible, as the materials are virtually dislocation free in the recrystallised condition.

σ_{ss} & σ_o will be similar for all alloys, as the basic composition is the same.

$K_y d^{-\frac{1}{2}}$ strengthening due to grain size will be small and relatively constant for the large secondary recrystallised structure.

Thus for titanium nitride strengthened steels, their yield strength should be related to their structure by means of an Orowan equation. The simple Orowan equation has, however, been demonstrated to overestimate the strength due to particles by an order of magnitude. For the purposes of calculating actual yield strength increments due to the presence of impenetrable particles, a more refined version of the equation has been derived by considering the mean interparticle spacing, dislocation dipole effect and the line tension of the dislocation. These three parameters have been incorporated in (13.2) by Foreman, Hirsch & Humphreys (1970) to provide a more exact theoretical estimate of the Orowan stress.

$$\tau = \frac{0.81 Gb}{2\pi(1-r)^{\frac{1}{2}}} \frac{\ln(2r_s/b)}{(\lambda_s - 2r_s)} \qquad (13.7)$$

The Orowan relationship is verified if the plot of yield stress against $\ln(2r_s/b).(\lambda_s - 2r_s)^{-1}$ is linear and the slope gives predicted values in agreement with experimental values.

Torronen (1976) determined that the yield strength of Cr-Mo-V pressure vessel steel containing 0.18%C was being controlled essentially by the particle dispersion. The Cr-Mo-V as quenched bainitic microstructure was tempered over a range of temperatures and times to produce a range of particle sizes of MC, M_2C_3 and $M_{23}C_6$ carbides. Using the same assumptions, the strengthening of the titanium nitride steels were calculated. The critical resolved shear stress was calculated utilising the TEM thin foil particle size and spacing measurements in accordance with equation (13.7). The shear yield stress calculated from the measured proof stress is plotted against the function of the planar spacing of the titanium nitride particles in Figure 13.9. This shows that there is a linear agreement. The comparison between the observed and calculated delta shear yield stress is shown in Figure 13.10 against a 1:1 correlation line. This illustrates the good agreement and thus it can be

concluded that the changes in size and spacing of the titanium nitride particles alone determine the changes in mechanical properties in the secondary recrystallised condition.
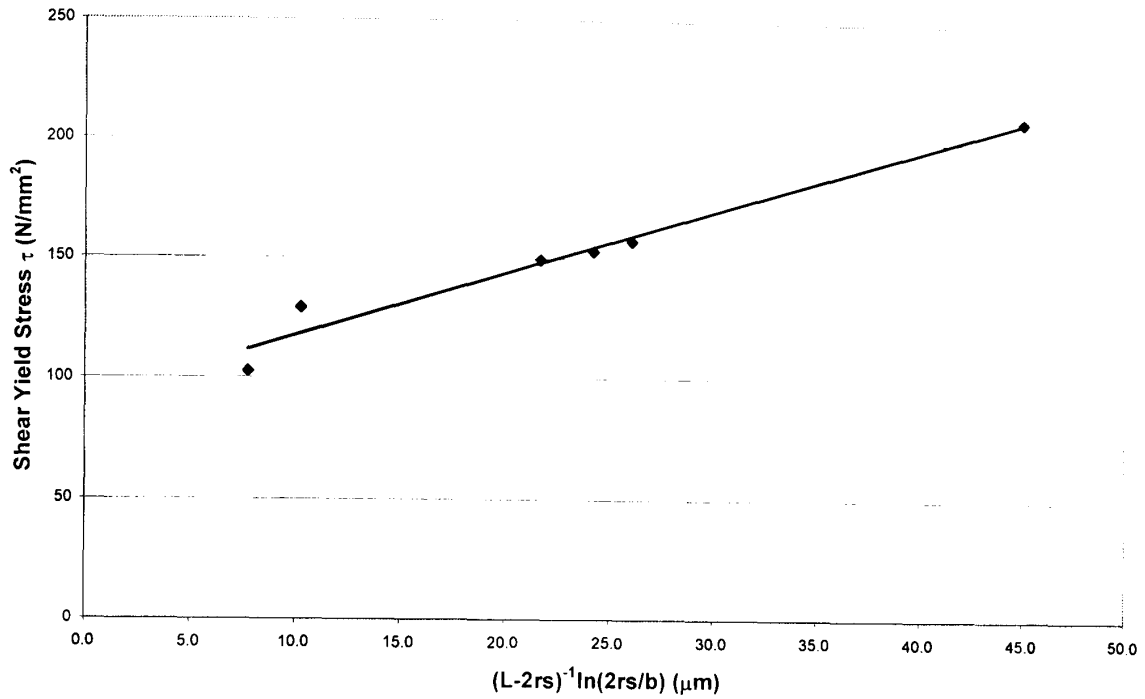
Figure 13.9 Shear yield stress calculated from measured particle data
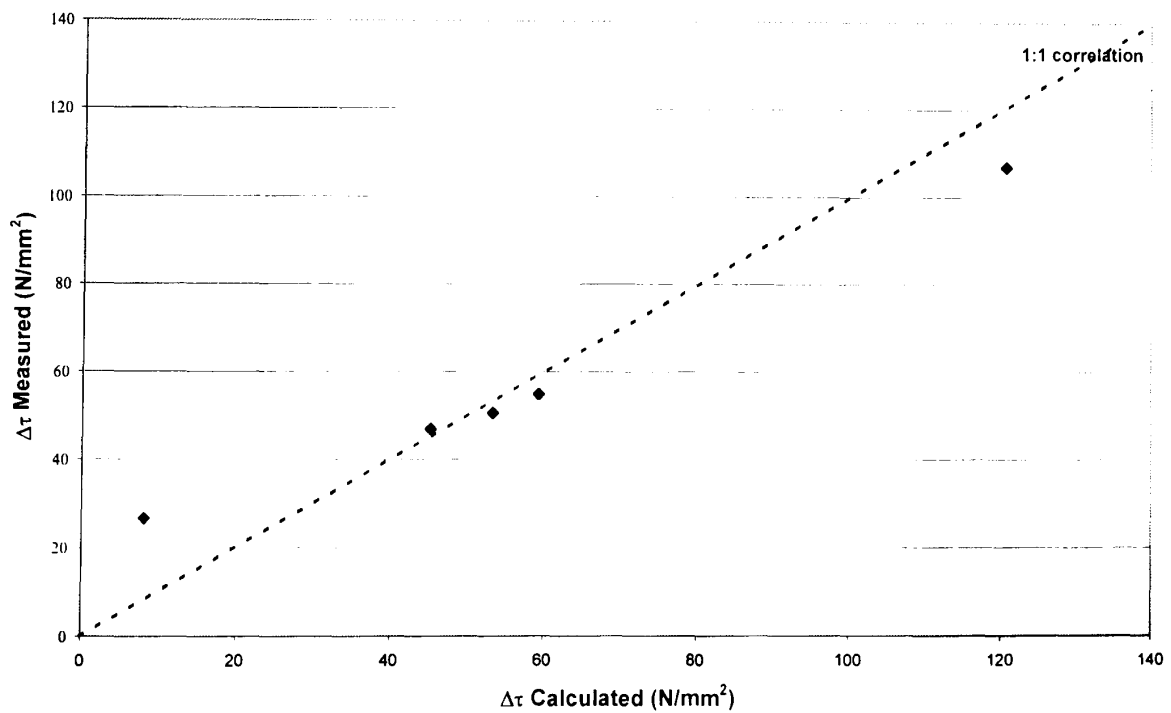
Figure 13.10 Correlation between calculated and measured shear stress values

179

13.3.1.3 Work Hardening

Post yield work hardening occurs, i.e. the shear stress required to produce slip constantly increases with increasing shear strain. Work hardening is caused by the dislocations interacting with each other and with the fine titanium nitride particles, which act as effective barriers. The impediment of dislocation leads to generation of more dislocations by the applied stress from existing dislocations, by for example, the Frank-Read mechanism.

13.3.2 600°C Elevated Temperature Tensile Tests

At elevated temperature, there is a substantial fall in the yield strength as the force required to detach the dislocation from the titanium nitride particles is sensitive to temperature. The 600°C tensile data is shown in Figure 13.11.
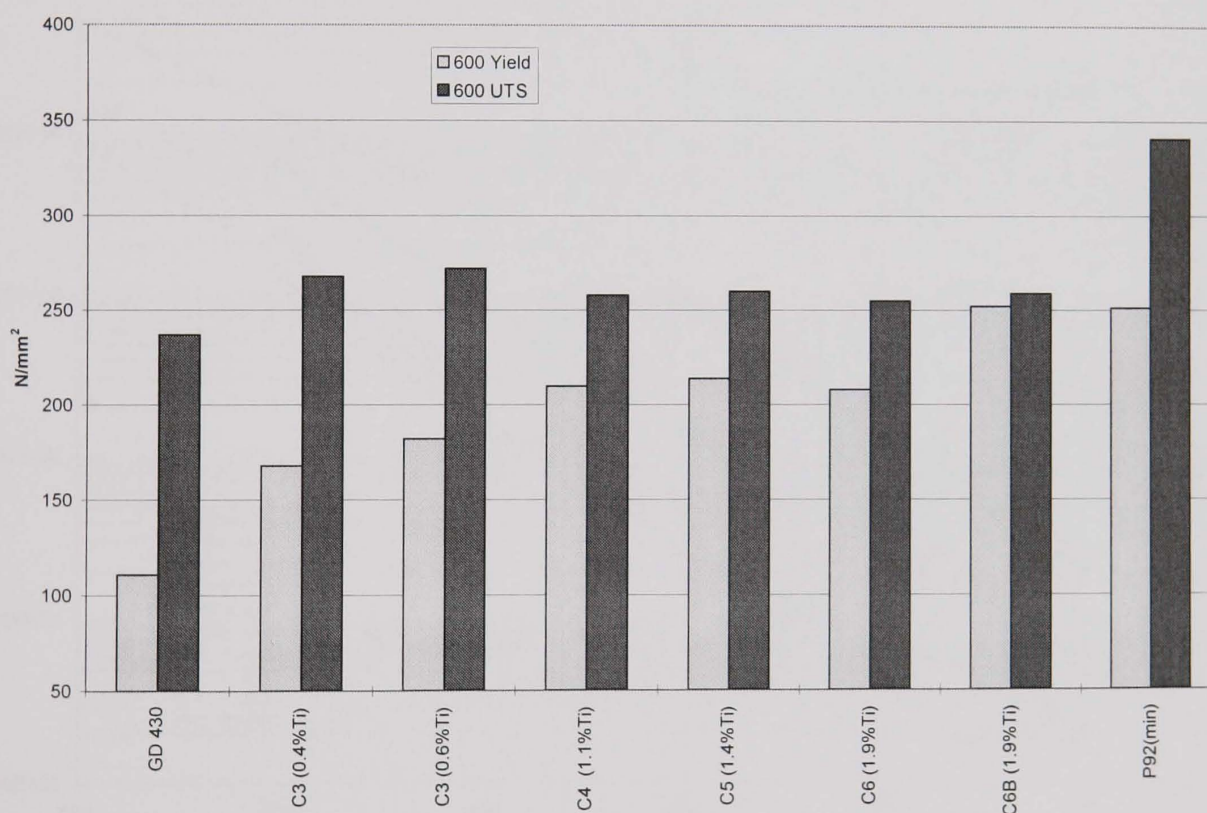
Figure 13.11 600°C tensile data (strain rate $3.79 \times 10^{-4} s^{-1}$)

As can be observed the fine titanium nitride size has significantly increased the yield strength such that it is now comparable with the minimum properties of the martensitic P92 material. Also evident in Figure 13.11 is the small increase in UTS over the yield strength as discussed in Chapter 12.

13.4 CREEP RUPTURE PROPERTIES

13.4.1 Stress Rupture Tests

Creep specimens were prepared from the secondary recrystallised bar sections. Prior to testing, all the specimens were pre-strained to 8% elongation. Initially, the stress rupture tests selected, namely 600°C/100 N/mm^2, 650°C/58 N/mm^2, 675°C/58 N/mm^2 and 700°C/58 N/mm^2 were similar to the tests carried out on previous Alloy C materials.

All of the above tests are continuing, and as of 31/01/00 all tests have exceeded 17,500 hours duration. The iso-stress plot previously shown in Chapter 11 is reproduced with the C6B alloy added (Figure 13.12).
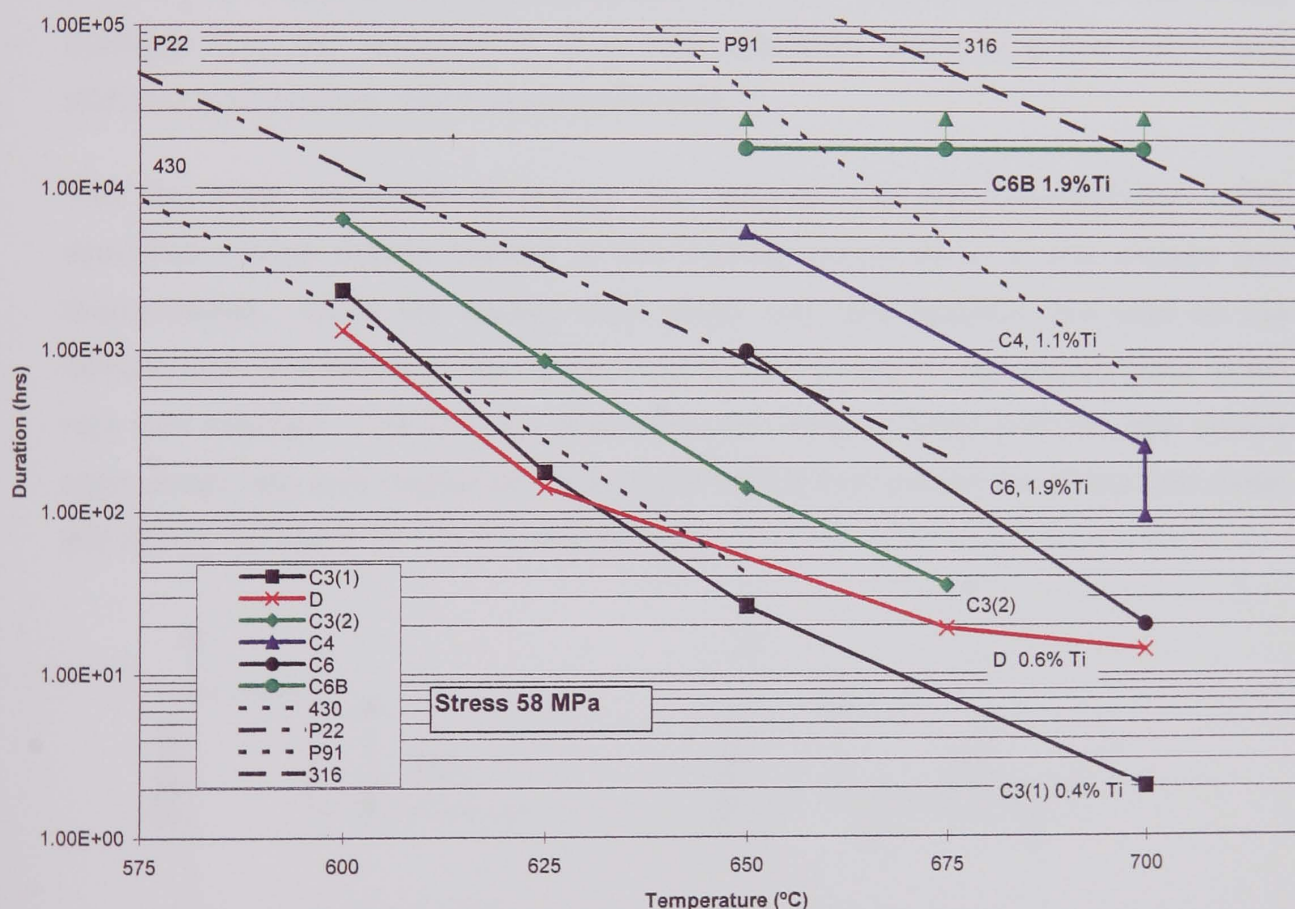
Figure 13.12 Iso-stress (58MPa) tests (Alloy C6B test durations at 31/01/00)

As can be observed C6B exhibits significant improvement in creep life over the earlier alloys. It must be stressed that all the "C" type alloys presented in Figure 13.12 possess similar secondary recrystallised grain structure and essentially the same base chemical composition comprising of a 18%Cr fully ferritic steel. The only difference is the titanium and nitrogen content. With regard to the Alloy C6, this

181

alloy is from the same cast as C6B and is mixed with the same amount of chromium nitride and, therefore, the chemical composition is identical (within chemical analysis scatter). The improvement of greater than a factor of 875 in life is solely due to the decreased titanium nitride particle size and interparticle spacing resulting from the precipitation heat treatment performed before consolidation.

Due to the significantly increased life of the Alloy C6B tests, a further test was performed. This test was conducted at 700°C/80 N/mm² and had a duration to failure of 1003 hours. This indicates that although the life of the tests at 58 N/mm² are significantly increased, a small increase in stress results in a large change in life.

13.4.2 Dip Tests

In order to maximise the data obtained from the limited number of specimens available from the extrusion of Alloy C6B, Dip tests, Ahlquist & Nix (1971) and Williams and Wilshire (1973) were performed.

The Dip tests consisted of testing the material with full extensometry. The specimens were initially loaded at the highest stress level at the chosen test temperatures. Once the steady state creep rate was reached, the load on the sample was decreased in the range 5-10 N/mm² where a new steady state strain rate was reached. The Dip test was performed several times until the new steady state strain rate was negligible. Schematic of Dip test graphs for stress and strain are shown in Figure 13.13a & b respectively.
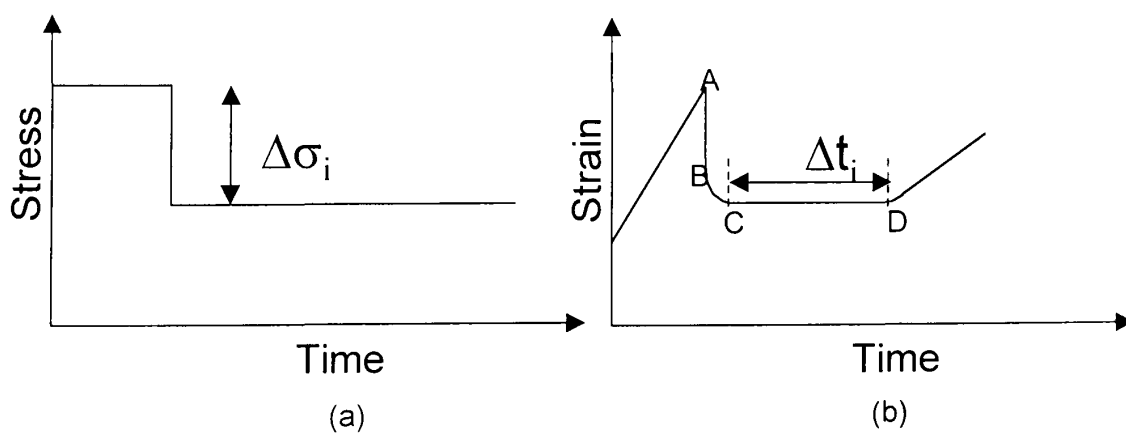
Figure 13.13a & b Schematic of the stress and strain of the dip test

Two tests were performed, one at 650°C and the other at 700°C. The results of these tests are shown in Table 13.4.

Material	Temperature °C	Stress N/mm^2	Strain rate s^{-1}
C6B	650	85	6.5×10^{-10}
		75	-
		65	-
		60	-
	700	85	7.4×10^{-9}
		75	2.1×10^{-9}
		65	4.6×10^{-10}
		60	9.4×10^{-11}

Table 13.4 Results of the "dip tests" on Alloy C6B material

13.4.2.1   650°C Test

The 650°C test failed at the extensometer notch, which was within the gauge length of the specimen. The features observed by SEM examination (shown in Figure 13.14a & b) indicate a relatively slow crack growth process which propagated inter and trans-granularly. As a result of the stress concentrating notch and highly pinned dislocation density, it is possible that at this lower test temperature, failure occurred by creep crack growth. This is discussed further in Chapter 14.

13.4.2.1   700°C Test Data Analysis

The variation in creep rate $\dot{\varepsilon}$ with applied stress σ is usually described by a Norton (1929) type relationship:

$$\dot{\varepsilon} = A\sigma^n \left(-\frac{Q}{RT} \right) \tag{13.8}$$

The high temperature creep deformation behaviour of the titanium nitride strengthened Alloy C6B can be characterised as unusual in that the strain rate sensitivity to the applied stress is high.

Surface oxide indicating slow growth rate

Extensometer notch
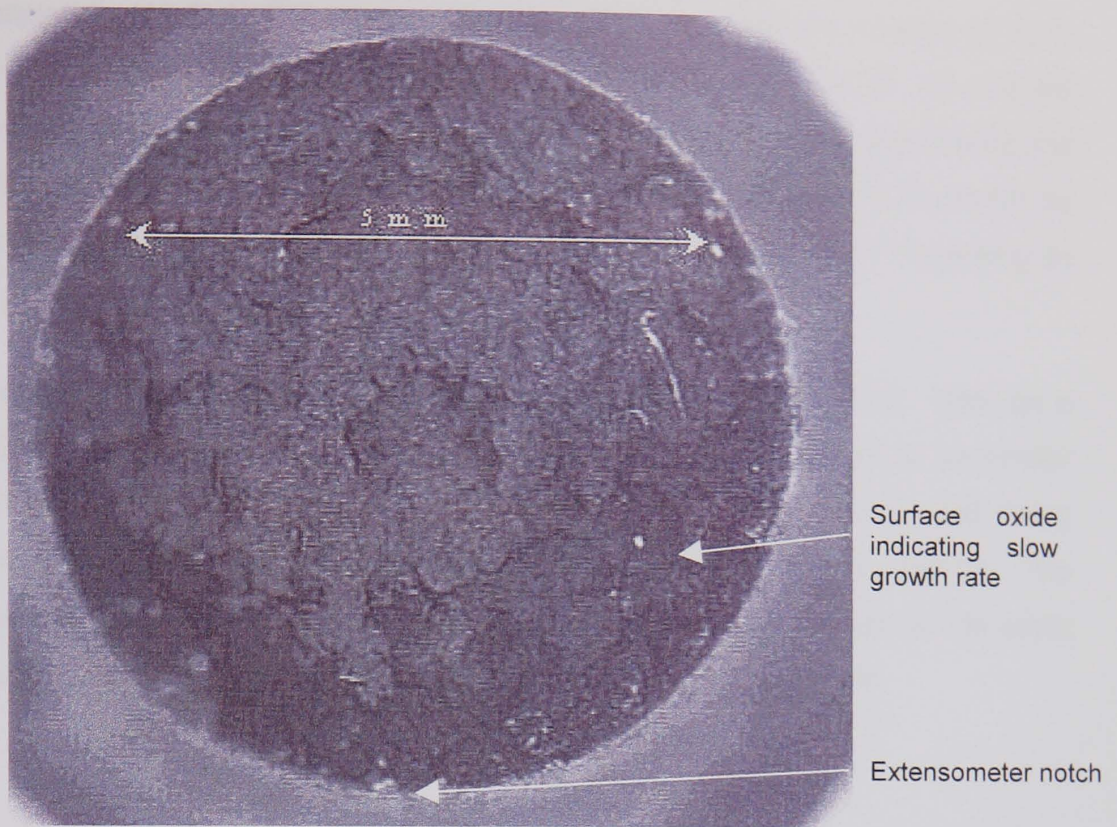
Figure 13.14a Fracture surface of 650°C dip test failure. Fracture oxide covering indicates crack growth path

Extensometer notch

100μm
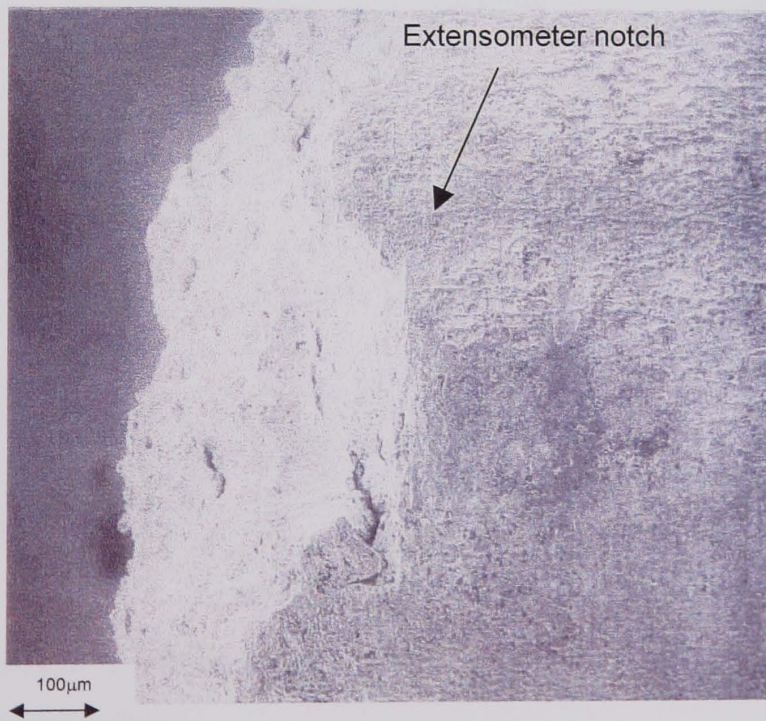
Figure 13.14 b Initiation at extensometry landing notch (within gauge length)

184

Applying equation (13.8) to the dip test data at 700°C revealed an n value of 12.1. The plot of log stress against log strain rate is shown in Figure 13.15. As can be observed in this figure the data correlates relatively poorly with the straight trend line (correlation factor 0.97). The data correlates better with a polynomial fit shown by the dashed line (correlation factor 0.99). This is due to the n exponent increasing as the stress is decreased.

The n exponent values of most metals are normally in the range of 2-5. With an n value of 12.1 the response of the Alloy C6B material at 700°C appears to be similar to ODS alloys where stress exponent values are often well above 20 and many exceed 100 (Lund & Nix (1976), Oliver & Nix (1982), Biselli & Morris (1991)). The high temperature creep behaviour of ODS alloys is generally explained on the basis that, below a threshold stress value, the creep rate becomes negligible.
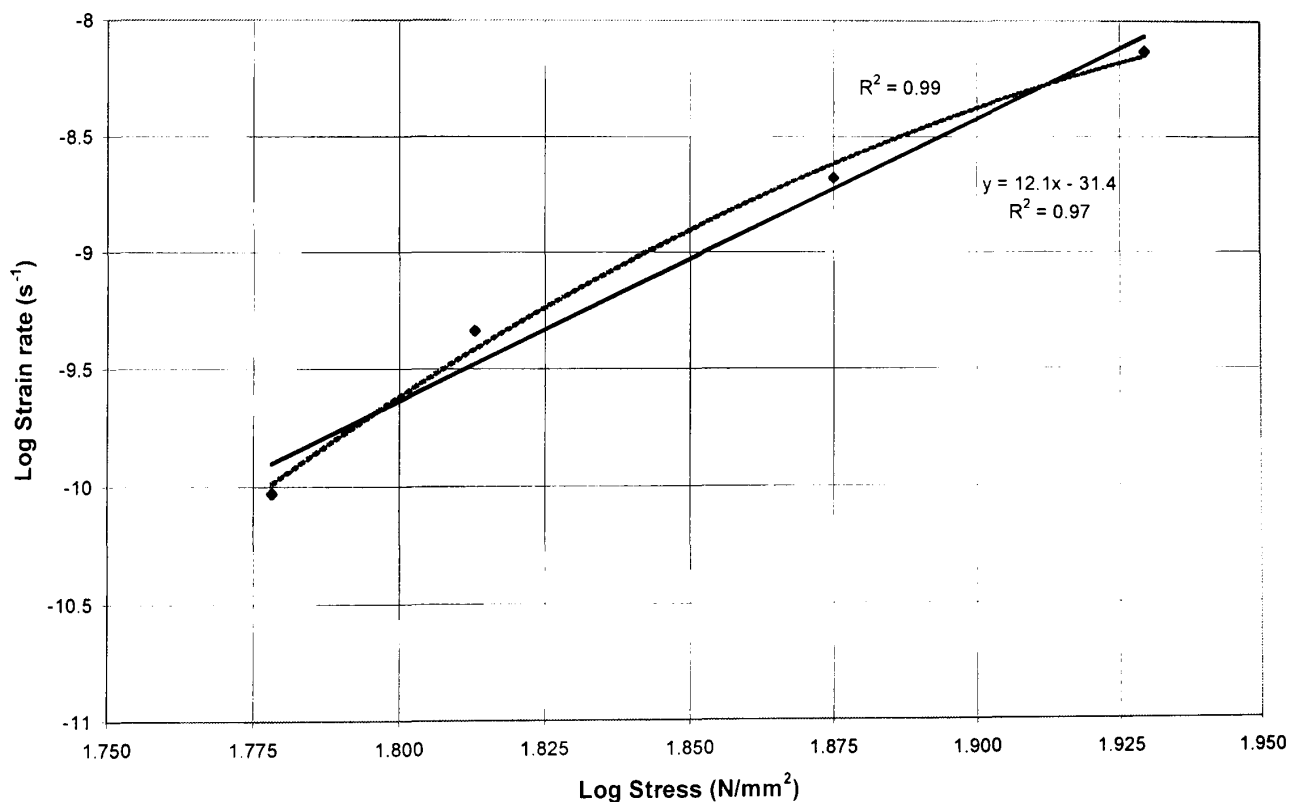
Figure 13.15 Linear and polynomial fit of the Alloy C6B 700°C dip test data on log strain rate, log stress graph

13.5 THRESHOLD STRESS FOR DISLOCATION CREEP

The threshold stress is defined as the stress below which the creep rate is negligible. The existence of a threshold stress has been attributed to a number of mechanisms:

(i)   Repulsive dislocation – particle interactions.

(ii)   Dislocation particle interactions involving localised climb.

(iii)   Attractive dislocation particle interactions.

Taking each of these dislocation particle interactions in turn:

13.5.1 Repulsive Dislocation – Particle Interaction

The repulsive dislocation – particle interaction mechanism involves dislocations either looping the particles as in the Orowan mechanism or by dislocation climb. In each case, the threshold stress has been quoted as stress required for dislocation by-pass.

Lund & Nix (1976) testing Ni-20Cr-2ThO$_2$ showed that the diffusion compensated minimum creep rate as a function of modulus compensated applied stress asymptotically approached the calculated Orowan stress, indicating that the measurable creep rate does not take place below this value. However, other data from Hausselt & Nix (1976) and Petkovic, Srolovitz & Luton (1982) revealed that the threshold stress is only about half the calculated Orowan stress. This feature was also reported by Clauer & Wilcox (1967).

13.5.2 Dislocation Particle Interactions Involving Localised Climb

At high temperatures, dislocations can circumvent hard particles by climb. In the models that have been proposed to account for the threshold stress, the length over which the dislocation climbs is a critical parameter. One such process proposed by Brown & Ham (1971) assumed that climb is local, i.e. the dislocation profiles the particle closely. This segment undergoes climb while the remaining dislocation line stays in the glide plane. By this mechanism of "local climb" by-pass of dispersoid particles leads to an overall increase in dislocation line length. The increase in line length necessary to surmount the particle needs an increase in energy and this is provided by the applied stress. A threshold stress must be exceeded before the

energy requirements are achieved and localised climb occurs. This mechanism leads to sharp corners in the dislocation path at the points where it meets the particle. Arzt & Ashby (1982) have proposed that this sharp dislocation curvature cannot be sustained at the point of the dislocation particle contact and the dislocation would "unravel", i.e. the dislocation would rapidly release by diffusion reducing the high curvature at these bends leading to more general climb. A threshold stress still exists from general climb of dislocations, however this has been estimated by Arzt and Ashby (1982) to be less than 10% of the Orowan stress. A similar value was estimated by Shewfelt & Brown (1977).

13.5.3 Dislocation Particle Attraction

This was first considered by Nardone & Tien (1983) who observed that dislocations were attached to incoherent particles on the departure side. It appeared as if a stress was required to pull the dislocations off the particles. This seemed surprising, as it was the general view that stable precipitate and dispersoids are strongly bonded and have high elastic constants that repel dislocations. It has, however, now been shown by many authors, including Srolovitz et al (1984), Arzt, Rosler & Schroder (1987) and Zakine, Prioul & Francois (1996), that attractive dislocation particle interaction exist.

An attractive interaction between particle and dislocations climbing around them has shown to have two separate effects on the climb and by-pass process:

(i)   It introduces an athermal threshold stress for dislocation detachment from the particles after climb is completed.

(ii)   It stabilises local climb at sufficiently high stresses.

These effects have been postulated to explain the highly stress sensitive dislocation velocity observed for the ODS type alloys.

Cooper, Nardone & Tien (1984) studying MA754 alloy also found particle matrix attraction. It was found that the dislocation maintained contact with the dispersoid throughout the range of tilt angles used on the TEM. The authors suggested that the attractive dislocation particle interactions stem from a change in the line and core energy of the dislocation due to elastic modulus differences and micro chemistry effects at the oxide interface. It was proposed that the elastic modulus of

187

the yttria dispersoid at high temperatures was less than the matrix allowing the dislocation to approach the particle. Cooper quotes values of modulus for the yttria and matrix at 760°C as 145 and 154 GPa respectively. The author continues to propose that the main source of dislocation particle pinning will occur if the oxide matrix interface separates to form a localised void. It has long been established that there is an attractive interaction between a dislocation and a void, (Ashby (1970)), since the encounter results in the elimination of a segment of dislocation line (and thus core and elastic energy) equal to the diameter of the void. Such an interaction would lead to a threshold stress below which dislocations would be unable to detach themselves from the voids.

Arzt, Rosler & Schroder (1987) and Rosler & Arzt (1988) thoroughly analysed the phenomenon. The authors proposed that at high temperatures diffusion relaxes both shear and hydrostatic stresses imposed on the particle by the approaching dislocation and that a phase boundary is considered as "slipping" at high temperatures. The dislocation can thus lower its energy because of the interaction with the particle, which after complete relaxation behaves elastically like a void. The attractive interaction was modelled by deriving a relaxation factor k where

$$T' = kT \hspace{4cm} (13.9)$$

T' is the line energy at the particle and T is the dislocation line energy remote from the particle when k = 1. The particle does not interact; i.e. it does not attract or repel the dislocation. When k = 0, this approximates the case where the particle has become detached from the matrix and behaves as a void. When Arzt, Rosler & Schroder fitted the derived equation to a range of dispersion strengthened materials, it was found that the strengthening observed is significantly less than the maximum achievable by considering void dislocation particle interaction, i.e. k = 0. The authors found that the dispersoid particles do not quite behave as voids and the relaxation of the dislocation is far from complete. The experimental threshold values observed would require k = 0.8-0.9. As such it was proposed that a minor relaxation would be invisible to conventional TEM techniques.

13.5.4 Threshold Stress Evaluation

The threshold stress, although complicated by the complexity of the theories, when viewed in a "mechanical metallurgy" concept it is simplified as it is analogous to the factors contributing to the yield stress, as described in Section 13.3.

$$\sigma_o = \sigma_m + \sigma_d + \sigma_p + \sigma_{ss} + Kyd^{-\frac{1}{2}}$$

The fundamental difference is that these parameters are not constant during long term exposure at the operating or test temperature.

σ_{ss} The solid solution elements can be removed by precipitation reactions; e.g., the removal of the strong solid solution strengthener molybdenum from solution during the precipitation of Laves phase in 9Cr tungsten containing martensitic steels such as E911 and NF616.

σ_p The strength from precipitates alters by coarsening due to Ostwald ripening and new precipitates forming, e.g. Laves phase precipitate described above.

σ_d The strength factor from dislocation interaction is largely controlled by the initial density (determined by the initial heat treatment and any subsequent deformation) and the ability to retain this dislocation density by means of pinning by the fine precipitates.

Grain Size   The extreme effect of grain size is apparent from the work carried out within this thesis. Above the equicohesive temperature, grain boundary sliding contributes more to the creep rate as the grain boundary area increases and thus grain size decreases. At higher temperatures a fine grain size is equally detrimental as the rate of diffusional creep increases rapidly with decreasing grain size.

Thus, there are at least two régimes during creep tests depending on the alloy:

(1) The initial régime where solid solution elements are still in solution and the precipitate particle size is small and commensurate dislocation density is high.

(2) Removal of solid solution elements by precipitation. Coarsening of particles which essentially means that the effective stress continues to increase and

189

thus so does the creep rate.

The change in the material properties as a result of creep exposure is shown in the creep strength versus duration diagram shown in Figure 13.16. This Figure describes the relationship between the stress (σ - σ_o) that controls the creep rate (where σ is the applied stress and σ_o is the sum of the strengthening mechanism, i.e. the threshold stress) and the particle size. The particle size was chosen as the X2-axis domain as in most ferritic creep resistant alloys precipitation strengthening is the main creep resistance mechanism. The actual form of the graph would not change if the other time dependant strengthening mechanisms, i.e. dislocation density, solid solution content etc. were chosen. At time zero, the initial structure has a large threshold stress and hence low effective stress giving low creep rates. As the service exposure time increases to t_3 the particles coarsen, decreasing the threshold stress and increasing the creep rate. The limit condition is that for iron with a threshold stress of zero.
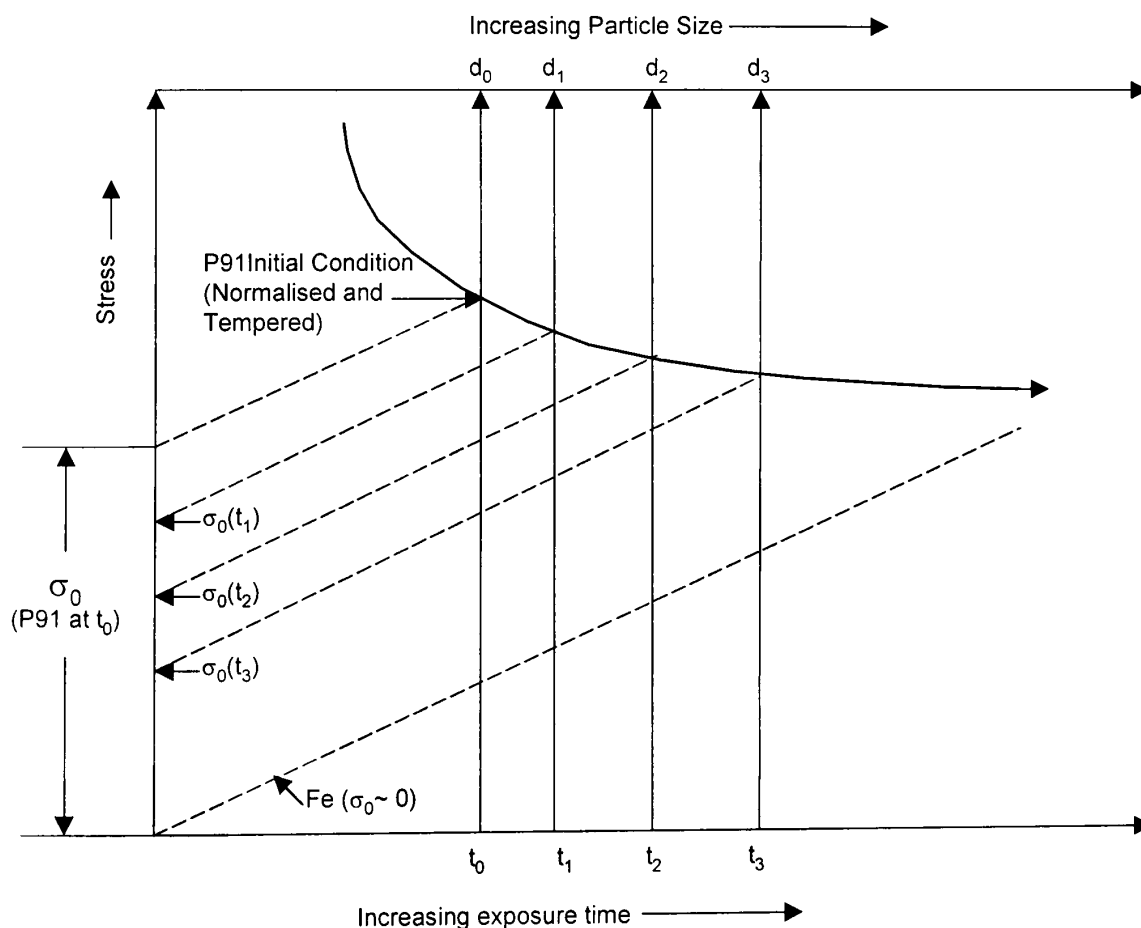
Figure 13.16 Schematic creep strength exposure diagram showing the reduction in threshold stress with increasing particle diameter for a conventional creep resistant alloy

This situation, however, changes with the advent of alloys containing oxide dispersions and titanium nitride precipitates. The initial fine particle size effectively does not coarsen during the service life of the components, e.g. boiler design life 150K hours. Therefore, their pinning effect upon the three-dimensional dislocation mesh does not effectively decrease with time giving a time independent strengthening parameter, i.e. a threshold stress below which creep does not occur.

Determining the threshold stress for the titanium nitride strengthened alloys will depend on the particle dispersion and the dislocation density. The principal method, which has been developed to measure σ_0 under a given set of creep conditions, was proposed by Williams & Wilshire (1973) and Davies et al (1973). This involves utilising the dip test technique (as performed in Section 13.4.2). The reduction in the applied stress by a small amount $\Delta\sigma_1$ results in an elastic contraction of the specimen which is followed by an incubation period of zero creep rate before creep recommences at a reduced stress level, as shown schematically in Figure 13.13 and for the actual 700°C 10 N/mm^2 reduction in stress from 75 to 65 N/mm^2 in Figure 13.17.
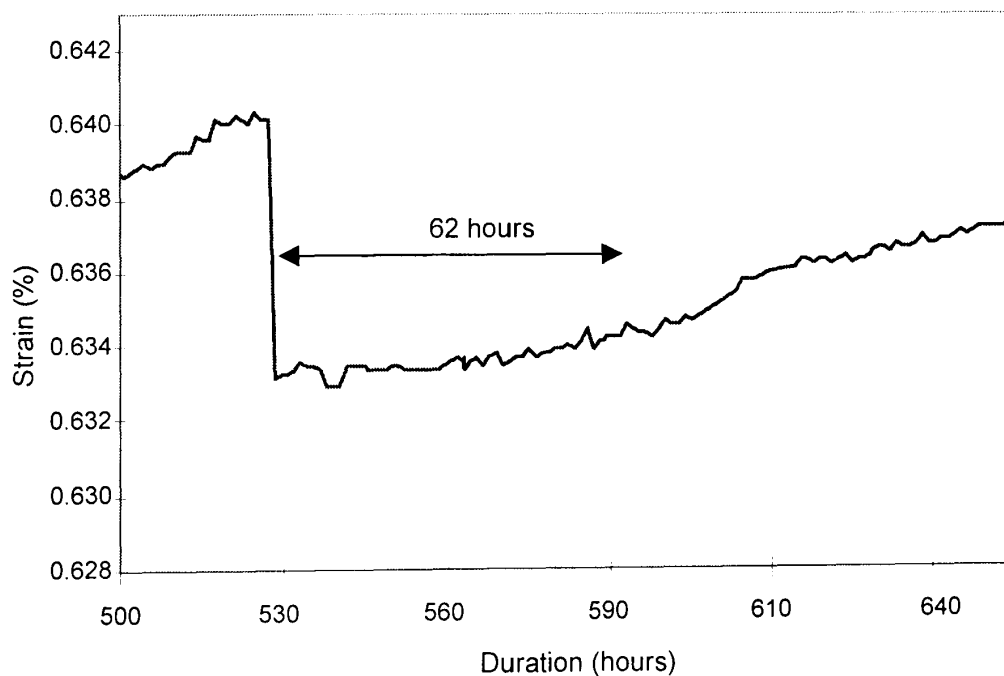
Figure 13.17   Strain duration plot following the reduction in stress from 75 to 65Nmm^{-2}

The duration of successive incubation periods (ΔT_1, ΔT_2, ΔT_3 etc) is recorded for each consecutive small stress reduction ($\Delta\sigma_1$, $\Delta\sigma_2$. $\Delta\sigma_3$ etc). This procedure allows the value of $\Delta\sigma_o$ to be determined as:

$$\sigma_o = \sigma - \Sigma\Delta\sigma_o \qquad (13.10)$$

Where $\Sigma\Delta\sigma_o$ is the sum of the consecutive small stress reductions which must be made until the cumulative incubation period $\Sigma\Delta T$ appears to approach infinity. This was developed by Zakine, Prioul and Francois (1996):

$$\sigma = \sigma_o + a\,(\Sigma\Delta T_I)^{-m} \qquad (13.11)$$

Where a and m are two adjustable parameters. The threshold stress was deduced by plotting the experimental data of σ as a function of $\Sigma\Delta T_I$ and extrapolating the curve following the power law to infinite incubation time.

For the "Dip tests" carried out on the Alloy C6B material at 700°C, the results are shown on Table 13.5. Due to the rapid increase in incubation time and reduction in the secondary creep rate as the stress was reduced from 65 N/mm^2 to 60 N/mm^2 the end of the incubation period could not be determined. Thus, only two incubation periods were recorded, 15 hours and 62 hours for the reductions to 75 N/mm^2 and 65 N/mm^2 respectively. A similar rapid increase in incubation time was reported by Parker & Wilshire (1978) due to the applied stress approaching the σ_o value. To obtain more data regarding $\Delta\sigma$ and ΔT_I, smaller stress reduction increments should have been performed as the applied stress approached the threshold stress.

The inevitable problem with this technique is differentiating between the end of the incubation time and the re-initiation of creep when the creep rate is low. Although this problem is not addressed specifically, Zakine, Prioul & Francois state that the tests were performed until the new steady state strain rate was negligible where negligible was defined as $10^{-9}s^{-1}$. The applied stress to achieve this strain rate was assumed to be close to the threshold stress.

Material	Temperature °C	Stress Reduction N/mm²	Incubation Time Δt_i (hrs)
C6B	700	85 – 75	15
		75 – 65	62
		65 – 60	∞

Table 13.5 Incubation times following stress reductions

By extrapolation to infinite incubation time the threshold stress value obtained by Zakine, Prioul and Francois, for the ferritic titanium oxide dispersion strengthened Alloy DT2906 at 700°C was 60 N/mm². Although with only two Δt_i data points for the Alloy C6B material at 700°C a similar extrapolation cannot be carried out. It is, however, apparent that with an $\dot{\varepsilon}$ of $10^{-11}s^{-1}$ the threshold stress for the titanium nitride strengthened alloy is also close to 60 N/mm².

The threshold stress has been incorporated into the Norton equation by Threadgill & Wilshire (1974) and Parker & Wilshire (1975).

$$\dot{\varepsilon}_s = A(\sigma - \sigma_o)^p \left(-\frac{Q}{RT} \right)$$

(13.12)

With this approach n = p where σ_o = 0

Thus, the equation considers that a part of the applied stress serves to overcome the relatively constant internal resistance stress due to the stable particles and the remaining effective stress produces dislocation creep as for particle free materials. The threshold stress concept was applied to the data previously presented in Figure 13.15 resulting in a log strain rate versus log effective stress rather than the log stress utilised earlier. Through an iterative process the value of 50 N/mm² threshold stress was found to give the best linear correlation of the data (0.99) as shown on Figure 13.18. Additionally, the stress exponent, which was 12.2 without the threshold stress being considered, is reduced to 3.2.
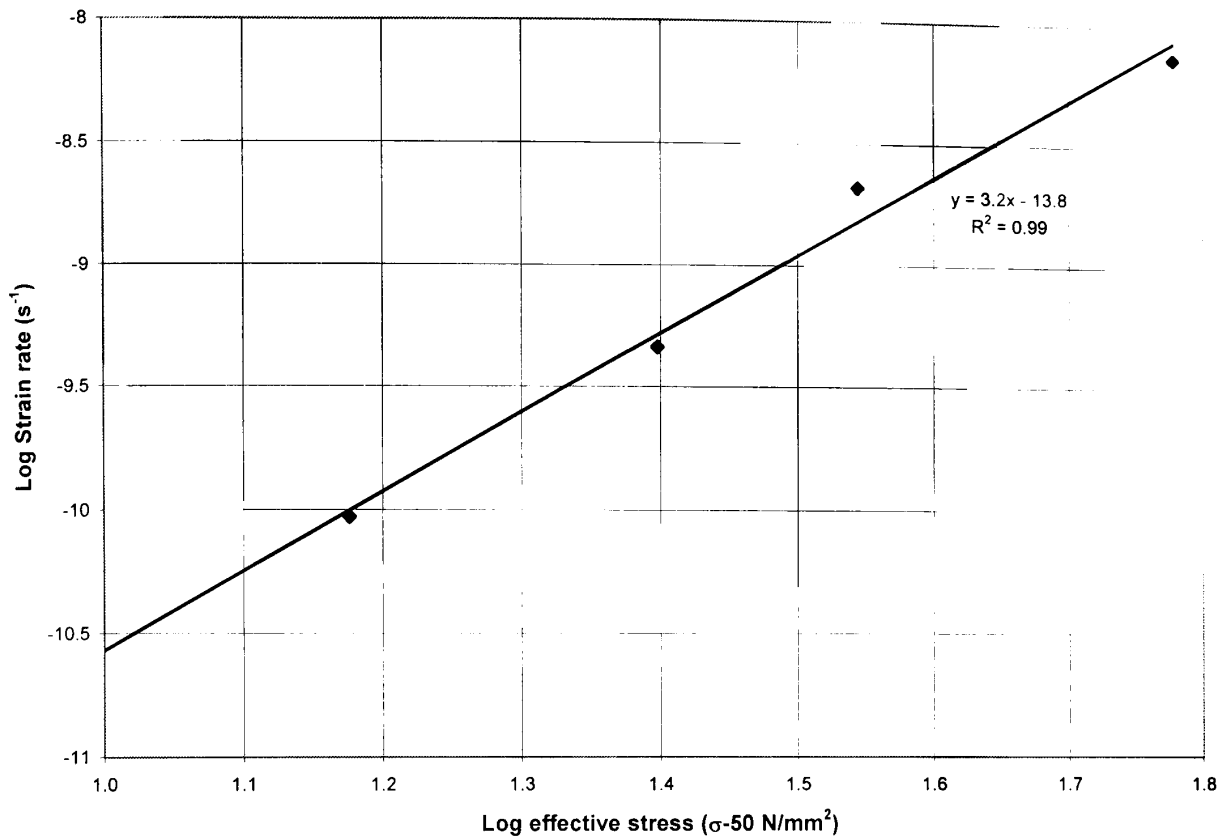
Figure 13.18 Improved linear correlation of the Alloy C6B 700°C dip test data for a threshold stress of 50N/mm²

13.6 SUMMARY

The additional heat treatment step has been successful in precipitating the fine relatively homogeneous distribution of titanium nitride particles. The decreased titanium nitride particle diameters with concomitant decreased interparticle spacing have resulted in the hardness, tensile and creep properties being dramatically improved. The most significant improvement lies with the creep properties where the material now exhibits a threshold stress of around 50 N/mm^2 at 700°C. This effectively results in a component operating at 700°C with a stress <50 N/mm^2 suffering no degradation in properties throughout its life. A relatively small increase in stress above this value does, however, result in significant reduction in creep life.

Chapter 14

Discussion

Precipitate strengthening is one of the most effective ways of retaining the dislocation density and thus retaining the strength of ferritic steels for boiler and turbine components that experience extended service at elevated temperatures. The most successful martensitic steels currently in use, utilise precipitates which are relatively stable and have achieved properties which safely allow application of up to 600°C, 120 N/mm^2 and 100K hrs operation. Extensive development of the creep resistant martensitic steels are currently being conducted in pan European projects co-ordinated by the Thermie and COST organisations and in Japan by the Electric Power Development Corporation. Their aim is to develop a high creep strength 12%Cr steel to overcome the 600°C upper temperature limit on heat transfer components that has been imposed on 9%Cr steels due to their steam side oxidation rate. The target properties of these new martensitic steels is to allow 650°C, 100 N/mm^2 and 100K hrs operation.

Conventional martensitic creep resistant materials appear to be reaching their limit of development both in terms of creep strength and oxidation resistance. Thus, the objective of this work was to develop an entirely new family of ferritic creep resistant alloys. The novel aspect of the materials being developed was to replace the various precipitates utilised in the conventional martensitic alloys with a fine dispersion of highly stable titanium nitride particles.

14.1   TITANIUM NITRIDE STABILITY

Thermally activated processes, i.e. diffusion can help dislocations to move and grain boundaries to slide; they can also give rise to time dependent instabilities of the particles themselves.   These instabilities include precipitate coarsening, dissolution and nucleation and growth of larger and thus less effective strengthening particles. With conventional advanced ferritic steels, the situation is complex.   Hofer & Cerjak (1998) on studying 9-12%Cr martensitic steels produced Figure 14.1.   Here the growth of $M_{23}C_6$ carbides is moderate, whereas the growth of Laves phase and Z-phase is relatively fast.   The growth of MX phase is very slow; however, the volume fraction is decreased by dissolution of this phase to form Z-phase.   With regard to Laves phase, there is no unified opinion whether the removal of tungsten and molybdenum from solid solution to form Laves phase has a positive or negative effect on the creep strength.

Figure 14.1 Precipitation sequence and observed particle size in 12% Cr steel, after Hofer & Cerjak (1998)

These constant changes in grain boundary, as well as dislocation pinning particles, result in significant changes in properties during service.   The property changes are generally a decrease in strength and a decrease in ductility.   These changes also restrict the application of the Ashby deformation characterisation maps and restrict the accuracy of the Larson Miller type creep life extrapolations.

The solution adopted by the work described in this thesis to the problem of lack of stability in multicomponent alloys is to make the alloy with fewer components and depend on very stable particles.   Titanium nitride particles have the lowest solubility of all the conventional "micro alloying" elements, and thus, they are the most resistant to particle coarsening.   By the use of the powder metallurgy techniques, solubility limits that restricted the solid state precipitation of fine titanium nitride particles to minimal levels have been removed allowing the solid state precipitation of high volume fractions of titanium nitride.

14.2 TITANIUM NITRIDE PRECIPITATION

As the material derives the majority of its strength from a fine dispersion of titanium nitride precipitates, it is critical that the precipitation reaction be given priority over any other processing consideration. This is due to the fact that titanium nitride particles cannot be taken back into solution and re-precipitated as in standard normalising and tempering operations on conventional precipitation strengthened steels such as P91, as titanium nitride is stable even in the melt (melting point 1330°C), therefore this would only result in coarser particles. Initial trials to incorporate the precipitation process into the Osprey spraying or Extrusion processes did not prove to be entirely successful in producing fine particles. This was especially the case as the titanium nitride content was increased. The reason for this is that although titanium nitride coarsens very slowly, it can grow relatively quickly. The driving forces controlling precipitate growth in the early stage of precipitation are much larger than the driving forces controlling coarsening. Thus, precipitate growth would have to be almost complete before coarsening can take over as the particle size controlling mechanism. In order to achieve a fine particle distribution a high nucleation rate and slow growth is required. To achieve this requires the sites for nucleation to be maximised and the growth rate minimised. Both these factors are in effect controlled by temperature. The effect temperature has on the diffusion rate and thus the growth rate is straight forward, but with regard to nucleation sites, it is more involved. Reducing the temperature decreases the critical nucleus size, however the main influence is on the heterogeneous nucleation sites. High dislocation density provides ample heterogeneous nucleation sites for fine titanium nitride precipitates, however, the high dislocation density produced by the Mechanofusion Process will have been removed by primary recrystallisation before any titanium nitride is precipitated at the 1000°C extrusion temperature. This results in the majority of precipitates being present at the grain boundaries, as observed in Alloys C5 and C6.

By reducing the temperature to the optimum level, the precipitation reaction can occur before recrystallisation, resulting in a homogeneous distribution of fine titanium nitride precipitate on the dislocations. This was achieved in Alloy C6B by performing a precipitation heat treatment immediately after the Mechanofusion Process i.e. before any other process induced heating. The heat treatment parameter was 600°C x 17 hours. This intermediate step is at present not possible

with the Osprey Process as the titanium nitride precipitates are largely formed during the spraying process. As this occurs at high temperature, it was found that the titanium nitride precipitates formed were significantly coarser than with the optimised Mechanofusion Process. As the Osprey Process however, offers lower production costs than utilising the Mechanofusion apparatus, recommendations for future development work to achieve required fine titanium nitride precipitates are discussed in Chapter 16.

With both processes, an additional consideration in achieving a homogeneous distribution of the fine titanium nitride particles is to minimise counter diffusion. In counter diffusion, the classical internal nitriding process breaks down such that the substitutional titanium is not immobile with respect to the interstitial nitrogen. Thus, it was found with relatively large diffusion distances that titanium began to diffuse to the nitrogen leading to macroscopic inhomogeneities in the product. Counter diffusion was subsequently minimised by restricting the titanium containing powder size to less than 45μm.

The conditions necessary to obtain a fine dispersion of titanium nitride particles are therefore:

- High dislocation density during precipitation process.

- Low precipitation temperature to retain the above and minimise growth rate.

- Utilising the Mechanofusion Process rather than the Osprey Process.

- Minimising counter-diffusion by restricting the titanium containing steel powder size to <45μm.

14.3 TITANIUM NITRIDE PARTICLES AND CREEP DEFORMATION

Generally, a particular microstructural feature will affect predominantly one of the creep mechanisms. A particular strengthening mechanism is only useful therefore if it slows the dominant mechanism. In designing creep resistant steels it is therefore necessary to know the dominant deformation mechanism which operates under the specific service or testing conditions in order to employ the correct strengthening mechanism. Dislocation creep is the dominant deformation mechanism for high temperature power plant components from service experience and is shown on the

Ashby deformation map in Figure 2.2. The most effective method of avoiding dislocation movement and therefore maintain the initial dislocation density, is to pin the dislocations by fine particles. Thus, the effect of particles on creep rupture properties was an important consideration in the alloy design of the new titanium nitride strengthened ferritic steels.

This research work has clearly shown that care has to be taken when applying one strengthening mechanism to counteract a particular creep deformation process as this can then cause the material to deform by another mechanism. In the case of the titanium nitride strengthened alloys the result of the introduction of the highly stable particles was to limit the grain size, causing grain boundary sliding to become the dominant mechanism. Thus, the work performed within this thesis demonstrated that in designing an alloy, all mechanisms of plastic flow must be considered and the appropriate strengthening mechanisms applied.

The critical factors controlling the time to rupture are the steady state creep rate $\dot{\varepsilon}_c$, and the final stress rupture ductility $\dot{\varepsilon}_f$. In order to assess the steady state creep rate of the alloy for design purposes, the overall steady state creep rate must be assessed. Thus, for the alloy design process, a superposition of three major flow mechanisms, grain boundary sliding creep, dislocation creep and diffusional creep must be assessed. That is:

$$\dot{\varepsilon}_c = \dot{\varepsilon}_{gbs} + \dot{\varepsilon}_{disl} + \dot{\varepsilon}_{diff}$$
(14.1)

14.3.1 Grain boundary Sliding

In the initial alloys produced, both the martensitic variant and the fully ferritic variant suffered from grain boundary sliding dominated strain rate. This was due to the very fine grain size (and prior austenite grain size) present in these alloys. Grain boundary sliding is the result of the accommodation of high shear strain gradients across grain boundaries through sliding of adjacent grains along the grain boundary. The creep rate, due to grain boundary sliding, has been derived by Raj & Ashby (1971) and Langdon (1970).

$$\dot{\varepsilon}_{gbs} = \frac{\beta b^3 D_B \sigma^2}{KTGd}$$
(14.2)

199

It is clear from equation 14.2 that the strain rate due to the grain boundary sliding process can be reduced, if not eliminated, by minimising the grain boundary area per unit volume. As a result of the creep strength being limited by the high degree of grain boundary sliding experienced by the fine grained titanium nitride strengthened steels, the development of coarser grains became critical in developing the performance of the material. This was achieved by secondary recrystallising the material as discussed in section 14.4.

14.3.2 Dislocation Creep

Dislocation creep is the dominant creep mechanism for conventional creep resistant ferritic steels. As such, the titanium nitride strengthened ferritic steels were specifically designed to suppress the movement of dislocations at high temperatures (>650°C and at long lives >100K hours). Thus, the highly stable titanium nitride precipitates would offer a step increase in creep properties over the conventional steels which utilise less stable $M_{23}C_6$, MX, M_2X etc. precipitates. This, however, only became possible after the development of a coarse grained microstructure. Prior to this the grain boundary sliding dominated the total strain rate and, therefore, masked the dislocation strengthening.

Dislocation creep, as the name implies, is the result of the thermally activated motion of dislocations within the grains. To effectively impede the dislocation movement requires fine distribution of the precipitates to minimise the interparticle spacing. On the basis of the current analysis of the phenomenological as well as the analytical aspect of the dislocation creep process the steady state creep rate derived from the Norton type equation does not adequately describe the strain rate relationship of the material to stress due to the existence of a threshold stress. The effect of a threshold stress has been incorporated into the Norton equation by Threadgill & Wilshire (1974) and Parker & Wilshire (1971), equation (13.12). The high stability titanium nitride precipitates give the Alloy C6B material the characteristic high threshold stress apparent in the most advanced creep resistant alloys such as ODS alloys. Concentrated work by other authors has gone into developing particle strengthening mechanisms to account for high threshold stresses and exhaustive and often elegant reviews are now available. The threshold stress is effectively a time independent stress value below which creep deformation does not occur. In actual fact, only totally inert particles could contribute to a threshold stress. In real terms, the threshold stress is taken as the

stress value below which the creep rate approaches zero, as even oxide dispersion particles and titanium nitride particles coarsen slightly during service.

Although the creep resistance factor for the Alloy C6B is positive with a high threshold stress, there is a very sharp stress dependence. This is demonstrated in the Dip Tests and also the comparison of the 58 Nmm^{-2} ongoing tests with the additional test conducted at 80 Nmm^{-2} and 700°C. This relatively small increase in stress (58 Nmm^{-2} to 80 Nmm^{-2}) at 700°C resulted in a decrease in the rupture life from virtually infinity to 1K hours. This sharp stress dependence is not entirely desirable in boiler design because, to ensure safe operation through minor excursions in temperature and pressure would require design safety factors to be extremely high.

14.3.3 Diffusional Creep

Diffusional creep is a result of the biased diffusional flux of atoms in the direction of the tensile stress resulting in time dependent elongation of the specimens in this direction. From the review by Ashby (1973) the expressions for creep rate due to such a diffusional flow have been derived by Nabarro & Herring and later by Coble and can be written in the general form:

$$\dot{\varepsilon}_{diff} = \frac{CD_{BG}b^3\sigma}{KTd^n}$$

(14.3)

where C is a geometric constant of the alloy, n is the exponent, which is dependent on the diffusion path, being two for bulk diffusion and three for diffusion along grain boundaries. This mode of creep is usually only significant at high temperatures (>0.8T_m), however, it too is reduced by the large grain size.

From the above work carried out, the creep properties of the material are only improved by combating all the relevant creep flow processes, not just concentrating on the limiting factor of the present alloys, e.g. stability of the precipitates. Accordingly, it is concluded that the creep resistance of the material is only improved in the titanium nitride strengthened alloys if:

- The system is coarse grained.

- The volume fraction of titanium nitride precipitates is high

- The titanium nitride particles are fine and have a homogeneous distribution

- The initial structure possesses a high dislocation density.

14.4 GRAIN GROWTH

Due to the grain boundary sliding which led to superplastic type behaviour of the fine grained titanium nitride strengthened alloys, grain coarsening was required in order to increase the creep strength. Heat treatment to induce normal grain growth was not possible due to the high grain boundary pinning force exerted by the titanium nitride particles. Grain growth was, however, achieved by secondary recrystallisation. Secondary recrystallisation is applied to the most advanced dispersion strengthened creep resistant alloys such as PM2000 and MA956. Its process is characterised by the anisotropic coarse columnar grain structure and the very high recrystallisation temperature, typically 0.7 to 0.9 Tm. This very high recrystallisation temperature and the fact that only a few grains nucleate and grow is indicative of a very high activation energy for the nucleation process.

There is considerable discussion within the literature as to the main driving force for secondary recrystallisation. The two main driving forces available within the as-extruded material for the process of nucleation and growth of an existing grain are:

- A reduction in the strain energy associated with the dislocation structure. This is the driving force for primary recrystallisation.

- A reduction in the surface energy associated with the overall area of the grain and subgrain boundaries: This is the driving force for normal grain growth.

This work has shown that with a relatively low vol% of titanium nitride pinning (Alloy C3) it is possible to secondary recrystallise the fine grains after primary recrystallisation is complete. Therefore, it is only the reduction in grain boundary energy that promotes secondary recrystallisation. As the vol% titanium nitride particles, and thus the degree of grain boundary pinning was increased, it was found not to be possible to secondary recrystallise the material (Alloys C4, C5 and C6) in the primary recrystallised state. With these materials, additional plastic deformation was required before secondary recrystallisation could be initiated. The exception to this was Alloy C6B. This material, due to the fine titanium nitride particles suppressed dynamic recrystallisation during the consolidation process and therefore

possessed a highly dislocated, hot deformed structure prior to the secondary recrystallisation treatment. Secondary recrystallisation was achieved without further plastic deformation.

It is thus demonstrated that the nucleation and growth of secondary recrystallisation grains can be influenced by variations in the level of fine titanium nitride particles and the degree of prior plastic deformation. There are two main theories as to why plastic deformation increases the susceptibility to secondary recrystallisation, these are:

- Increase the driving force due to the dislocation energy

- Decrease the resistance by modifying the crystallographic texture.

It is likely that both aspects contribute to increasing the susceptibility to secondary recrystallisation. The difficulty lies in determining the dominant factor as in most experiments, including those performed within this thesis, the cold deformation is performed in the same direction as the dominant texture due to the forming process. The definitive experiment has, however, been performed by Regle & Alamo (1993). In this work swaging and drawing were used to achieve the same degree of cold reduction, therefore similar levels of dislocations were generated. The two processes did, however, lead to quite different crystallographic textures. The results of the secondary recrystallisation study were that in all cases the reduction process decreased the recrystallisation temperature. However, the reduction due to cold drawing was 31% greater than for swaging in the MA956 material. This demonstrates that the susceptibility to secondary recrystallisation depends far more on the crystallographic texture than the level of cold work and thus dislocation density. Although no explanation was proposed by by Regle & Alamo, it is possible that this finding supports the Sha & Bhadeshia model for grain boundary pinning as the texture likely leads to the clustering of adjacent grains into similar orientations, effectively increasing the grain size and thereby making the nucleation of secondary recrystallisation easier.

There is little doubt that the grain growth is affected by the fibre texture in that the grain growth is orientated in the deformation direction. Once nucleation has occurred, the rate at which the grain growth occurs in secondary recrystallisation is very fast. In this work, the minimum time between inspections was 15 minutes and

in that time grains had grown from the original 4 μm to the secondary recrystallised grain size of approximately 10mm. Even allowing the maximum 15 minutes for the process to occur, this is still very fast when the degree of crystallographic re-orientation is considered. This too would support the influence of crystallographic texture, as the grain growth rate would be more rapid in samples where the original fine grains are already orientated.

Texture considerations would also account for the fact that it was found not to be possible to secondary recrystallise the martensitic variants. When these alloys are heated to the typical recrystallisation temperature (1200-1300°C) the martensite has transformed to austenite. This phase transformation alters the texture and for the reasons outlined above retards recrystallisation. The phase transformation also removes the dislocation density from the martensitic structure, and this too could influence the susceptibility to secondary recrystallisation.

It is thus apparent that secondary recrystallisation is a complicated phenomenon in titanium nitride strengthened alloys and depends on a range of finely balanced variables. To move to an industrial application further work is required to determine the relative effects that the fine grain size and particles have on pinning the grain boundaries, the relative recrystallisation energy from the reduction in grain boundary energy and the reduction in dislocation energy, and the effect of texture. Texture appears to have a significant influence on the secondary recrystallisation properties, however, the mechanism remains speculative. It is apparent that even in the commercially available ODS alloys secondary recrystallisation is not fully controlled as creep failures have been experienced due to the presence of fine grains in experimental applications, Starr (1998). This implies that even with alloys, that have been under development for the last decade, all the variables are not accurately quantified.

From this work the main features of secondary recrystallisation in addition to those presented by Cahn (1966) in Chapter 7 are:

- For low vol% pinning particles the reduction in grain boundary energy is sufficient to trigger secondary recrystallisation

- For high vol% of fine titanium nitride particles, the onset of secondary recrystallisation is dependent on the level of plastic deformation.

- Phase transformations retard secondary recrystallisation.

- Secondary recrystallisation can occur without prior primary recrystallisation.

14.5 PROPERTIES ACHIEVED

14.5.1 Positive Attributes: Creep Strength

As a result of developing the material to minimise grain boundary sliding by secondary recrystallising the grain structure, the creep properties were increased by precipitating a high volume fraction of titanium nitride particles with a small interparticle spacing in order to pin the dislocations. A high dislocation density was introduced to the specimen after secondary recrystallisation but before testing by cold straining. The development of the creep properties is shown in Figure 13.12. In this Figure it can be observed that the ongoing tests in Alloy C6B have exceeded the properties of 316 stainless steel (mean data from PD 6525) at 700°C. This is a significant increase in the properties of a ferritic material at this temperature, as austenitic steels with their FCC structure exhibit creep rates at temperatures above $0.6T_m$ which are 200 to 1000 times slower than the creep rates of typical BCC steels. This is due to the atom mobility in the close packed austenitic steels being lower than the more open ferritic steels by a factor of around 200.

The creep life of the coarse grained Alloy C6B is approaching four orders of magnitude greater than the creep lives of the early secondary recrystallised Alloy C3(1) or the base 430 type ferritic stainless steel. The secondary strain rate is also lower than the most advanced martensitic alloys such as P92 as shown in Figure 14.2.
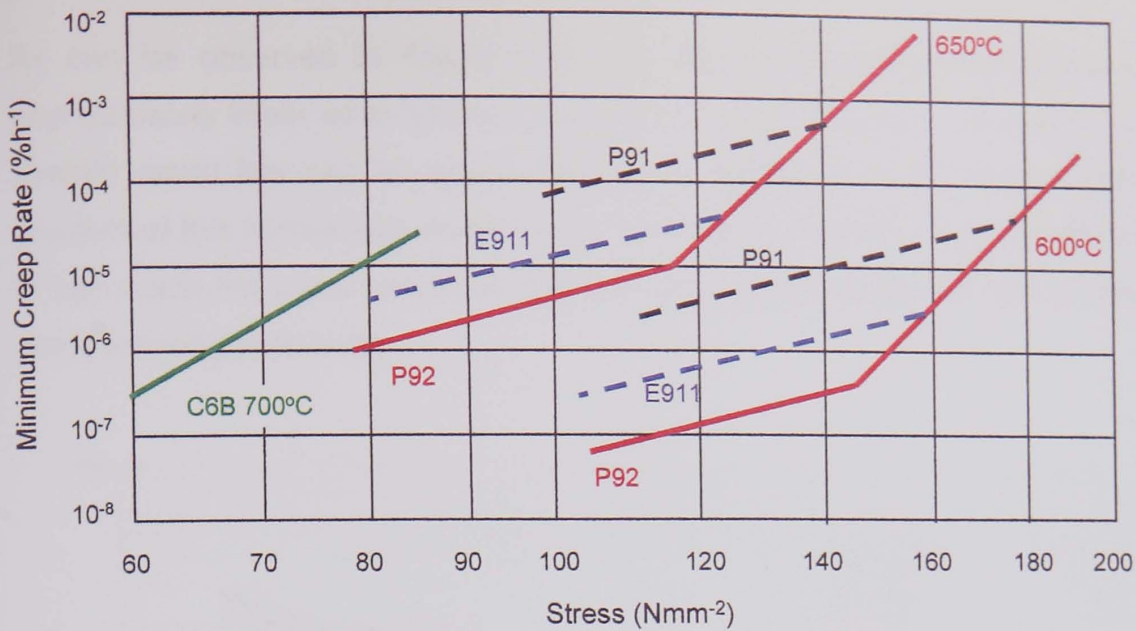
Figure 14.2   Minimum creep rate of Alloy C6B (700°C) in comparison with P91, E911 and P92 (600 & 650°C)

A further assessment of the creep performance of the alloy C6B material was conducted by performing a comparison with a range of ferritic boiler materials from C-steel to P91.   The stress temperature relationships are shown for 15K hours rupture strength on Figure 14.3.   The Alloy C6B test points are annotated by an arrow, as these are not failure points as the tests are continuing.   Duration at 31/1/00 is 17720K hours.
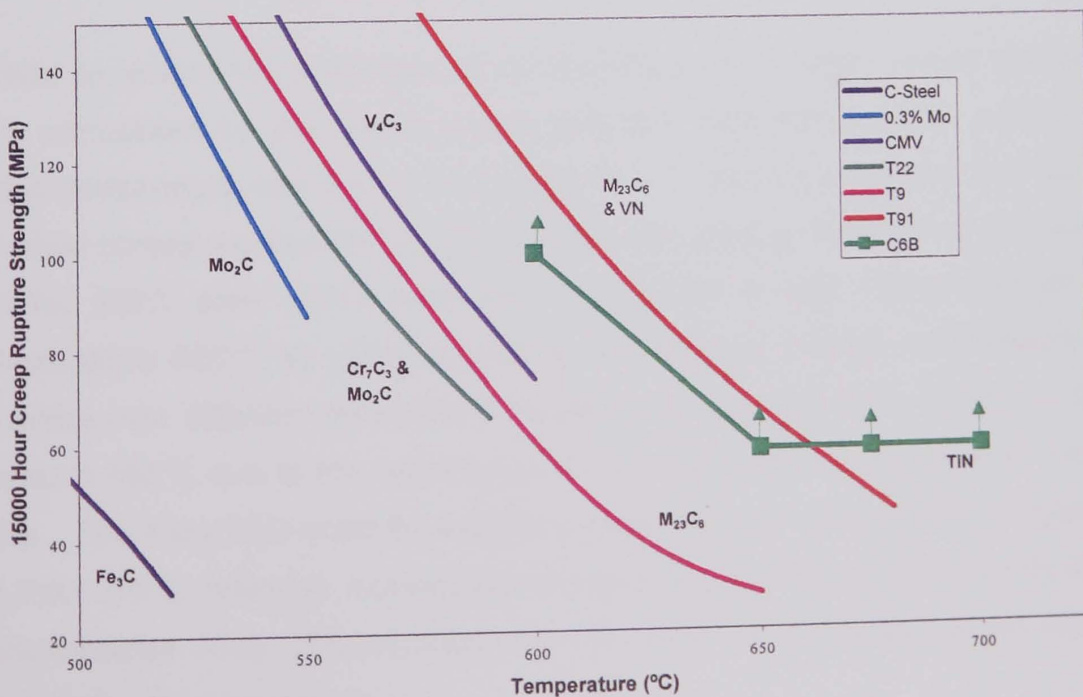
Figure 14.3   15,000 hour stress rupture versus temperature

As can be observed in Figure 14.4, the fall off in stress with temperature is approximately linear when plotted on a logarithmic stress axis. As a result of this, a straight mean line can be drawn though this family of ferritic alloy curves. The gradient of this normalised stress line is controlled primarily by the self-diffusion rate of iron within the creep range, as it is this factor that controls the rate of dislocation climb around precipitates.
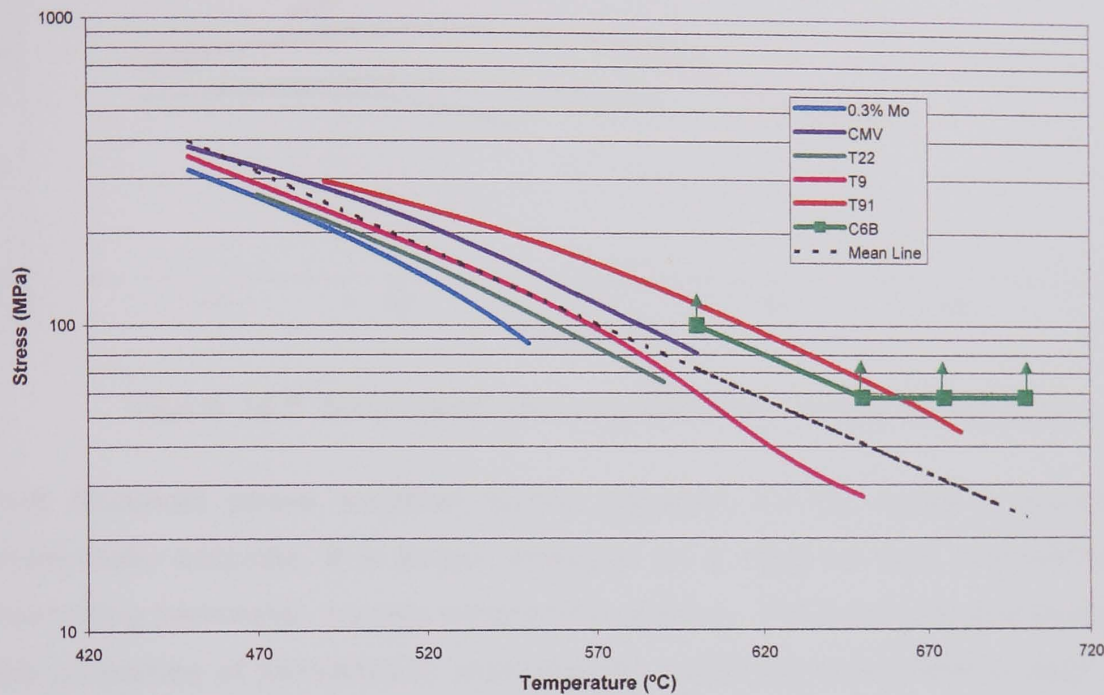
Figure 14.4 15,000 hour stress rupture strength (log stress) versus temperature.

In order to assess the properties of the individual alloys, their rupture strength has been normalised by this mean line to give the normalised stress rupture value versus temperature plot shown on Figure 14.5. The movement up and down the individual curves represents the precipitation and ageing of individual phases. The modified 9%Cr steel (T91) does well to maintain a high creep strength up to approximately 650°C by using numerous precipitation locking mechanisms which are active over different temperature ranges. The strength does, however, drop off at around 650°C due to the coarsening of its highest stability precipitate, vanadium nitride. The Alloy C6B material exhibits a lower strength than P91 at temperatures less than 670°C, however, beyond this temperature, due to the high stability titanium nitride particles, Alloy C6B achieves over 2.5 times the normalised stress which is a very significant improvement.
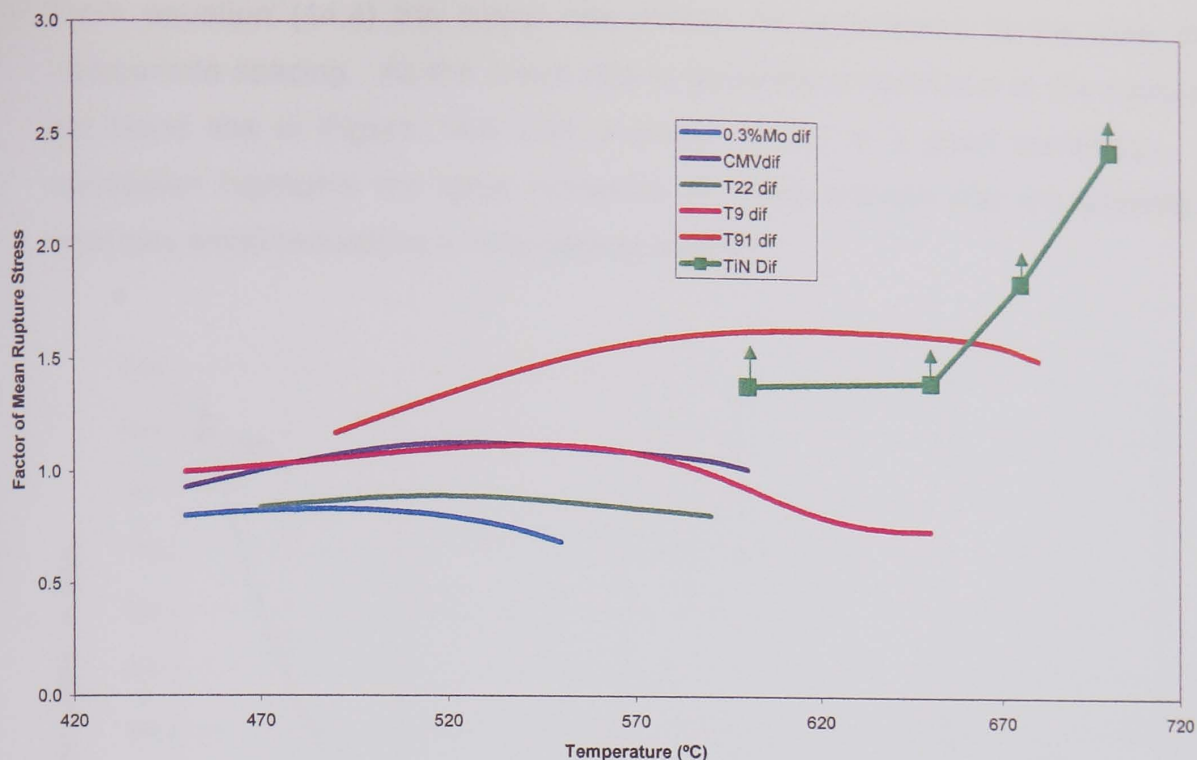
Figure 14.5 Normalised stress rupture value versus temperature.

The threshold stress modified Norton equation (13.12), whilst it proves to be numerically accurate, it is largely empirical as it does not take cognisance of the controlling parameter, namely interparticle spacing. Phenomenological evaluation of the properties of precipitation strengthened materials have primarily been derived from room temperature properties as evaluated in Chapter 13 with equation (13.7). This is most probably due to the fact that with conventional creep resistant ferritic alloys, the interparticle spacing can significantly change during the lifetime of the alloy at elevated temperature. With the titanium nitride strengthened alloys however, it is apparent (Figure 14.6) that there is a clear relationship between the measured average interparticle spacing and the creep rupture life. The equation of the trend line is $Y=2\times10^{11}x^{-3.2}$. This agrees well with the work of Sherby, Klundt & Miller (1977) and Walser & Sherby (1982), who developed equation (14.4) mainly from precipitation strengthened aluminium data:

$$\frac{d\varepsilon}{dt}=K\left(\frac{\lambda}{b}\right)^{3}\frac{D_{eff}}{b^{2}}\left(\frac{\sigma}{E}\right)^{2} \tag{14.4}$$

where λ is the interparticle spacing, D_{eff} is the effective diffusion coefficient, E is the Young's Modulus, b is the Burgers vector and K is a material constant.

From equation (14.4) the creep rate should be proportional to the cube of the interparticle spacing. As the creep rate is generally proportional to the rupture life, the trend line in Figure 14.6 with a power of 3.2 is a good correlation. This correlation highlights the large increases in creep strength that are possible with relatively small reductions in interparticle spacing.
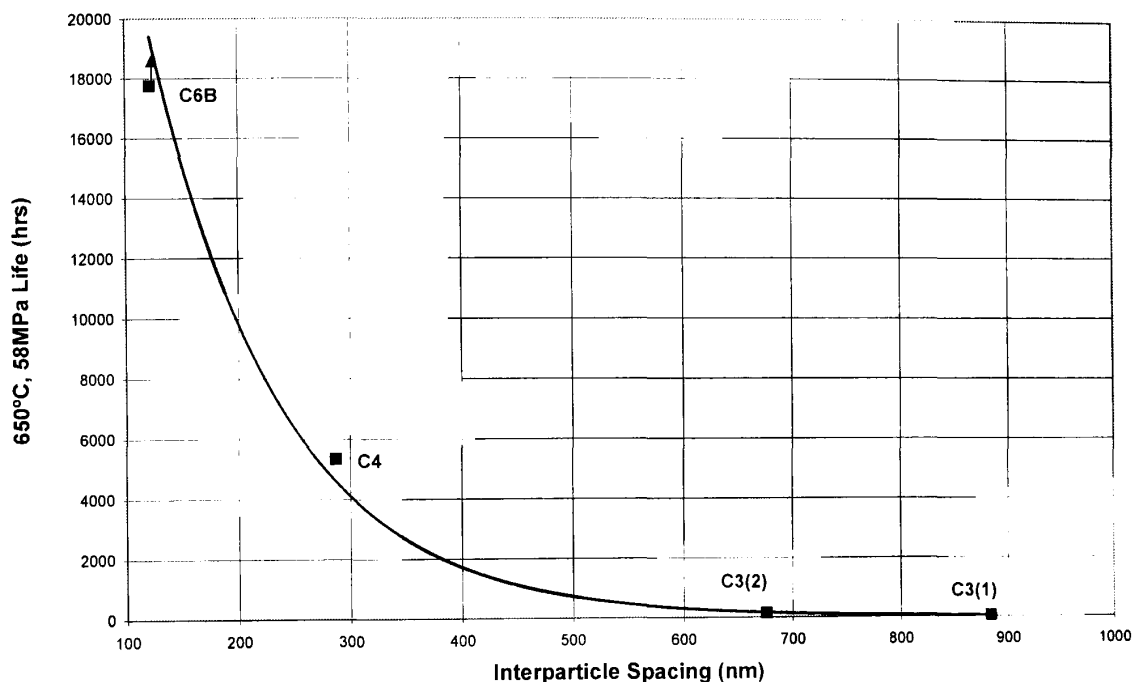
Figure 14.6   Variation of the creep rupture life (650°C/58MPa) of the secondary recrystallised alloy C materials with their average measured interparticle spacing.

14.5.2   Negative Attributes

14.5.2.1   Ductility

While strengthening factors associated with titanium nitride precipitates are positive, the ductility factor is not. The ductility factor between the conventional advanced martensitic materials i.e. P91 material and the Alloy C4 material is of the order of -0.8. It appears that negative ductility factor is an unavoidable consequence of particle strengthening.

Particles deform less than the softer matrix, therefore, dislocations are produced near particles during the early stages of deformation. This produces a high density of dislocations that are pinned by the same particles which initially suppresses mechanical instabilities. However, as the deformation progresses this strengthening can become a detriment since it prevents further accommodation between the

209

precipitate and the matrix. As a result the particles now act as centres of void initiation, and the subsequent coalescence of these voids can cause low ductility premature fracture of the system.

The titanium nitride particles increase the creep resistance of the alloy, i.e. they decrease $\dot{\varepsilon}_c$, and as a result, they increase the time to rupture. However, they also decrease the stress rupture ductility. A phenomenological theory for combining stress rupture life and ductility does not appear to have been developed. However, empirically there appears to be an inverse correlation between the minimum strain rate and the time to rupture, Monkman & Grant (1956):

$$(\dot{\varepsilon}_c)^{\beta} \; x \; t_{rup} = \text{constant} \qquad\qquad (14.4)$$

The exponent β is a function of the alloy system and microstructure. This value is found to be 1 in many cases.

Although tensile ductility is a good indicator of the reliability of an alloy under initial loading conditions, most components operate under more complex states of stress. A typical example, and relatively common situation, is the state of plane strain loading encountered in regions of stress concentrations in headers or pipework such as in the vicinity of small cracks, flaws, oxide intrusions etc. Plane strain ductility of materials is generally less than their uniaxial ductilities. With regard to particle strengthened alloys, Argon, Im & Needleman (1975) have shown that triaxial stresses add to local stresses around particles and enhance the particle-matrix interfacial stresses. Under such circumstances, the interfacial stress σ_{int} is given by:

$$\sigma_{int} = \sigma_T + \sigma_y(\bar{\varepsilon}_p) \qquad\qquad (14.5)$$

where σ_T is the local triaxial stress and $\sigma_y(\bar{\varepsilon}_p)$ is the flow stress of the particle free matrix corresponding to the local plastic strain around the particle. This parameter is dependent on the matrix yield strength and work hardening. The local triaxial stress σ_T depends on the state of stress in the vicinity of the particle and will be higher in plane-strain situations than plane stress situations. As a result, the higher interfacial stresses at the particle-matrix interface under plane-strain conditions would result in poorer ductility.

The above equation thus explains the situation, but does not provide any information regarding the effect of particle size or volume fraction etc.

14.5.2.2 Creep Crack Growth

An important aspect with high strength alloys is their susceptibility to creep crack growth (CCG). A simple definition of CCG is that high local stresses ahead of a stress concentrator in a component operating under creep loading can create a process zone in which creep damage accumulates and, with time, manifests itself as a crack. This crack will also create a highly stressed volume of material in front of it; therefore, a further process zone and crack length will occur. By this mechanism, the crack moves forward with time. As the creation of voids is diffusion controlled, the timescales for nucleation and growth can extend over many thousands of hours. This can be divided into two sub-sections, namely creep crack initiation and creep crack growth.

14.5.2.2.1 Initiation

Creep crack initiation is not considered presently in the design of components. However, it is addressed in the defect assessment procedure such as R5 (1998). The time to crack initiation is related to crack opening displacement δ_i and the creep characterising parameter C^* by:

$$t_i = \frac{1}{2}\left[\frac{\delta_i}{C^*}\right]^{\frac{n}{n+1}} D^{\frac{-1}{n+1}}$$

(14.6)

D and n are constants and for secondary creep C^* is constant, so the crack initiation time t_i is approximately proportional to crack opening displacement δ_i for high values of n. The crack opening displacement is a direct measure of creep ductility in the multiaxial stress field of a crack tip. Values of δ_i generally increase with ductility, however, there is considerable scatter due to the difficulties involved in determining the point of crack initiation (e.g. using DC potential drop equipment).

The creep crack initiation parameter is critical as this determines whether or not the material under the given circumstances is susceptible to CCG. The susceptibility of the titanium nitride strengthened materials to CCG is demonstrated by the initiation and growth of cracks from the root of the extensometer landing notch in the 650°C test. The higher temperature (and thus implied higher ductility) test did not suffer

from this cracking mechanism. The author believes that the importance of creep crack initiation will increase with the move to higher strength and thus lower ductility creep materials.

14.5.2.2.2   Growth

In the same way that crack initiation is related to creep ductility via the crack opening displacement, creep crack growth is also strongly dependent upon creep ductility. R5 (1998) states that in general terms the creep crack growth rates can be described by:

$$\dot{a} = AC^{*q} \tag{14.6}$$

Nikbin, Smith and Webster (1986) have demonstrated that for a broad range of materials the data can be approximated by the empirical equation

$$\dot{a} = \frac{3C^{*0.85}}{\varepsilon_f^*} \tag{14.7}$$

where a is the CCG rate and ε_f^* is the rupture ductility at the crack tip. Nikbin, Smith & Webster also proposed that for plane strain conditions ε_f^* could be as low as 1/50th of the uniaxial ductility on the basis of models of void growth.

In this present work the positive attributes of increased tensile and creep strength of the titanium nitride strengthened alloys have been assessed and models to predict their performance have been found to be relatively accurate. In contrast, however, the potentially negative attributes of these alloys, specifically their poor ductility when in the high volume fraction titanium nitride secondary recrystallised condition, giving rise to such problems as creep crack growth has not been investigated within this research work and generally these aspects are not well understood. The reduced ductility has important implications on the use of the titanium nitride creep resistant material and important properties such as the plane-strain ductility and creep crack initiation conditions will have to be assessed before implementation of this new material can be considered.

To increase ductility and thus avoid brittle fracture modes such as creep crack growth, the volume fraction of particles must be kept to a minimum. This is obviously contrary to the parameters required for high creep strength steels. Therefore, incorporation of high creep strength materials such as the titanium nitride strengthened ferritic steel into boilers will have to be accompanied by a re-design to minimise, for example, component fillet radii or grooves at which creep strain may preferentially accumulate during service.

14.6 GENERATION CYCLE EFFICIENCY

Assuming that the design and manufacturing quality can be advanced to take advantage of the titanium nitride strengthened steels, then the benefit gained from utilising this material is demonstrated by an increase in cycle efficiency. The idealised efficiency of a power cycle η can be calculated using equation (1.1). Thus, a power plant that operates at a steam temperature of 700°C and condenses the steam at 30°C while extracting the energy to make electricity cannot operate at an efficiency greater than 68.9%. In practice, however, the efficiency realised is far less as power plants do not operate under the idealised Carnot (1962) cycle but operate the Rankine cycle.

Calculations of the achievable power plant efficiencies of actual plant, i.e. the efficiency using the supercritical Rankine cycle required the use of the Thermo Flex 3.0 (1998) programme. This programme is based on actual component performance (e.g. feedpumps, boiler, steam turbine and condenser) but allows the input parameters to be varied and calculates the output performance. The cycle components are shown on Figure 14.7 and the assumptions used in the model are as follows:

- supercritical Rankine cycle

- superheat but no reheat

- no feedwater heating

- perfect components (no mechanical losses)

- boiler efficiency of 100%

- Condenser pressure of 40 millibars

The results of such calculations over the temperature range 500°C to 780°C and steam pressures from 250 barg to 375 barg are given in Table 14.1.
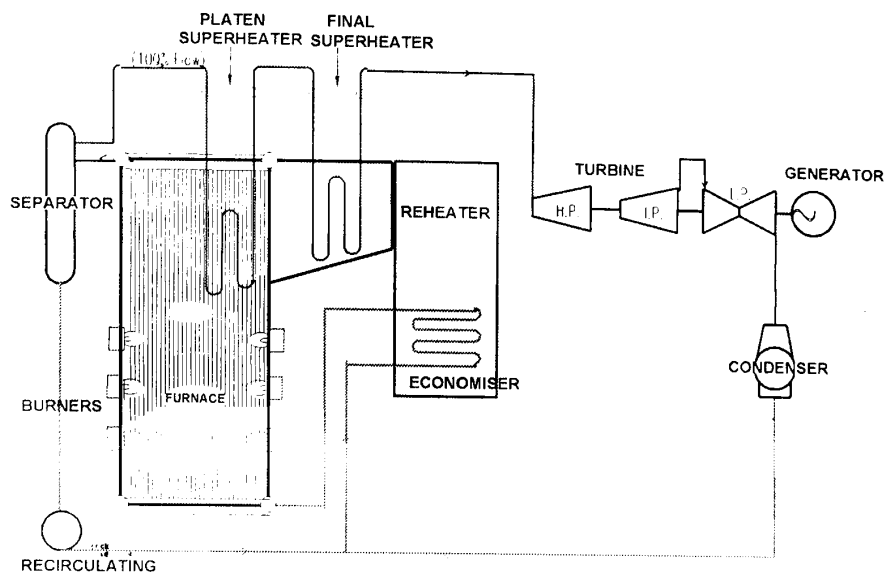
Figure 14.7 Schematic of modelled steam thermal cycle

Steam Pressure (barg)	Cycle Efficiency at Temperature (°C)						
	500	550	600	650	700	750	780
250	44.50	45.44	46.31	47.14	47.94	48.73	49.19
275	44.56	45.58	46.47	47.32	48.15	48.94	49.40
300	44.58	45.67	46.61	47.48	48.32	49.12	49.60
325	44.56	45.74	46.71	47.61	48.46	49.29	49.77
350	44.51	45.77	46.8	47.73	48.60	49.44	49.91
375	44.42	45.78	46.85	47.82	48.70	49.55	50.05

Table 14.1 – Supercritical power plant efficiency % variation with maximum steam temperature and pressure

As can be observed, efficiency rises more rapidly with an increase in temperature than with an increase in pressure. At 500°C increasing the pressure to 375 barg has a net loss of efficiency of 0.08% due to additional auxiliary power requirements being greater than the resultant increase in efficiency. At the upper end of the temperature range increasing the pressure has a more positive effect, but is still significantly less than the effect of increasing the temperature.

The relation of pressure, temperature and efficiency is shown graphically in Figure 14.8 where efficiency is given as a function of steam temperature with a separate plot for each steam pressure. From this graph, combinations of steam temperature and pressure can be obtained for any efficiency levels bounded by the data. Consequently, constant efficiency lines can be plotted on axes of temperature and pressure. In order to relate the material properties to achievable efficiencies, the pressure is converted to hoop stress in the component for thick walled components such as headers and thin walled components such as tubes and is given by BS1113 (1998). For the purposes of this comparison, thin walled tube conversion is utilised. The tube dimensions were taken from the Mitsui Babcock advanced boiler design.
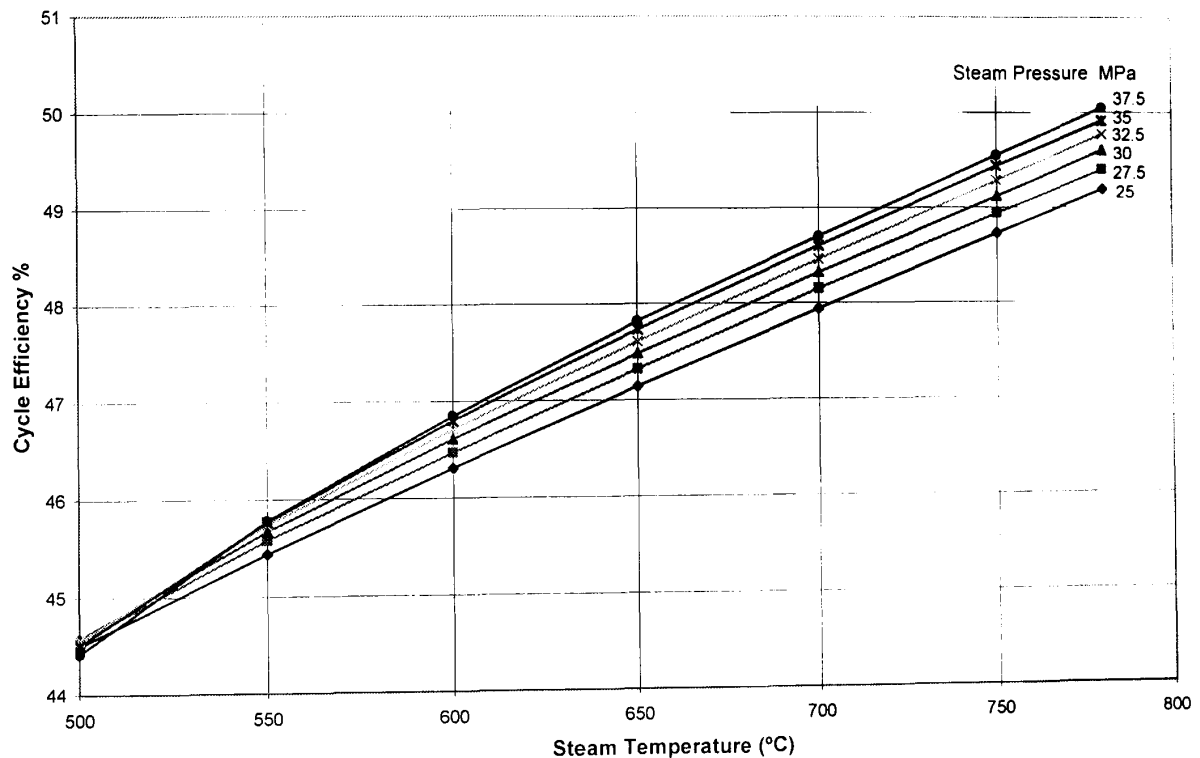
Figure 14.8 Plant efficiency as a function of steam temperature and steam pressure.

The material data can now be compared to the iso-efficiency lines. The material data plotted on Figure 14.9 is for 100K hours life which is typical of the design life utilised in calculations.

215
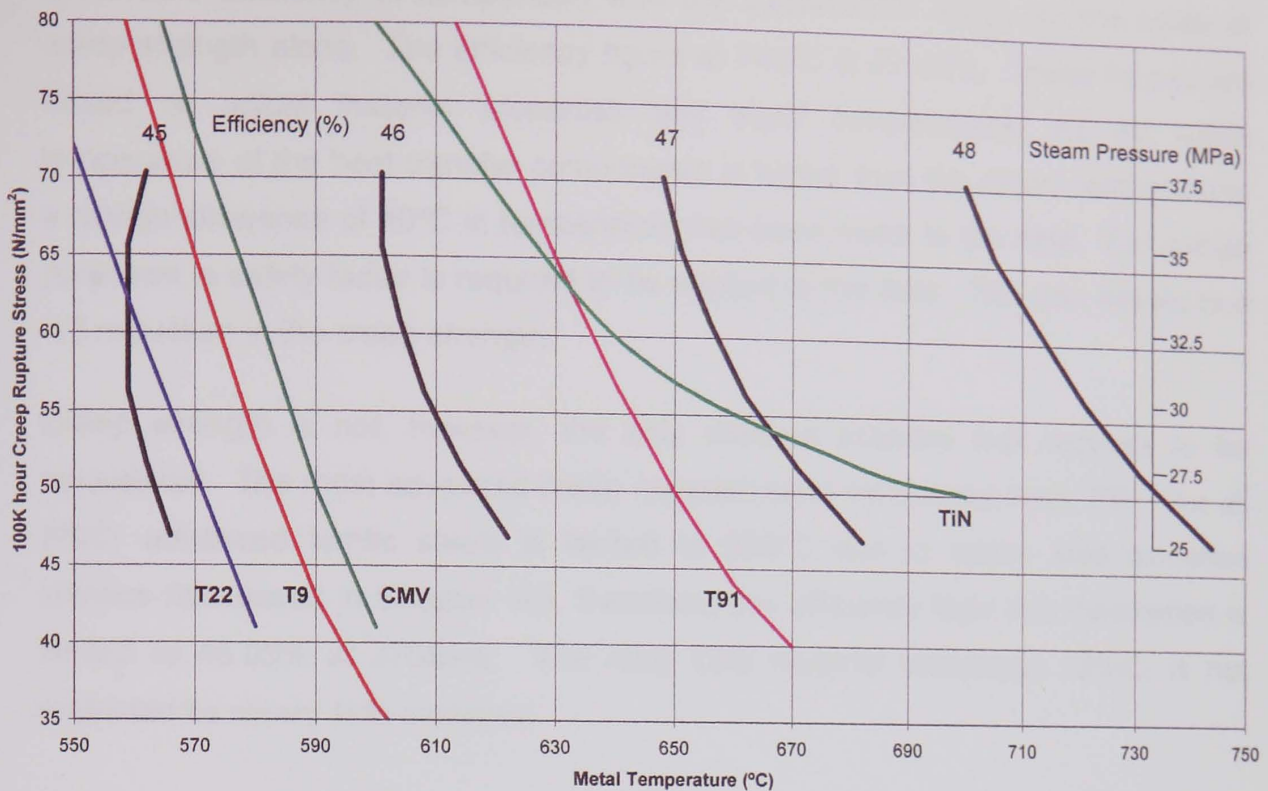
Figure 14.9 Creep data compared to calculated iso efficiency lines

In order to plot the Alloy C6B material on a similar timescale involves extrapolating the creep data well beyond that which is conventionally acceptable. However, it can be argued that the use of the estimated threshold stress for the range of temperatures in the Alloy C6B material provides a greater degree of confidence than extrapolating the data by, for example, using the Larson Miller (1952) parameter in materials that demonstrate sigmoidal behaviour. In addition to the Alloy C6B material, the conventional ferritic alloys previously discussed are added for comparison. Using this graph which illustrates the creep characteristics of the alloys with the iso-efficiency lines, the optimum combination of operating stress and temperature can be determined to maximise the cycle efficiency that could be achieved if the power plant was manufactured using that material for the highest temperature components.

The creep behaviour curves for most of the alloys cross the efficiency lines as the stress is reduced and the temperature is increased, demonstrating that the efficiency increase is greater than the decrease in creep performance. The characteristic creep performance of the Alloy C6B material where, due to the stability of the fine titanium nitride particles, the creep strength is largely retained at high temperature results in the Alloy C6B material achieving the highest level of

achievable efficiency in comparison with the conventional alloys on the basis of creep strength alone. The efficiency figure at 700°C is 47.45%. These figures are based on actual material properties and metal temperatures. As the metal temperature of the heat transfer components is higher than the steam temperature, a design allowance of 40°C in temperature has been made to the data. For design purposes, a safety factor is required to be applied to the data. This can equate to a 1/3 reduction in the creep strength.

Creep strength is not, however, the only material property that requires to be considered. The most advanced creep resistant steel considered here, P91, like all 9%Cr advanced ferritic steels is limited to 600°C due to steam side oxidation kinetics (discussed in Chapter 10), therefore, the efficiency from this calculation is limited to 46.05% at 375barg. The Alloy C6B material containing 18%Cr is not restricted by steam side oxidation.

14.7 ECONOMIC BENEFIT

In order to quantify the economic and environmental benefits that the increase in efficiency would bring, the efficiency data generated above was applied to a 660 MW reference power plant. Table 14.2 details the simulation based on a linear extrapolation of the baseline data. The temperature efficiency values quoted are the calculated values from section 14.6 at 275 barg pressure. This Figure demonstrates the fuel savings and thus the reduction in fuel costs that can be achieved by introducing new material that can operate at higher temperatures and thus achieve higher efficiencies. However, more advanced materials such as the titanium nitride strengthened Alloy C6B are more expensive to produce than conventional alloys. The cost of the new material must be more than reimbursed by the savings due to increased efficiency. To determine the admissible additional investment in moving from P91 (600°C metal temperature/ 275barg: efficiency 45.77%) to titanium nitride strengthened steels (700°C metal temperature/ 275barg: efficiency 47.44%) the assessment of the manufacture construction and operation of a 660MW supercritical power plant was assessed and is shown in Table 14.3.

217

Steam Temp. °C	Efficiency %	Coal Consumption (ton/hr)	Fuel Costs* (USD/MWh)	Lifetime** Coal Consumption (M ton)	Lifetime** Coal Cost (MUSD)
500	44.56	143.49	13.18	31.42	1728.6
550	45.58	140.28	12.87	30.72	1689.7
600	46.47	137.59	12.59	30.13	1657.3
650	47.32	135.12	12.40	29.60	1627.5
700	48.15	132.79	12.21	29.08	1599.5
750	48.94	130.65	11.93	28.61	1573.7
780	49.40	129.43	11.91	28.35	1559.0

*   Coal cost of 55 USD/ton and LCV of 27 GJ/ton)

**   25 years based on 20% down time resulting in 175.2 Khours operation

Coal prices have not been inflated.

Table 14.2 Extrapolation of 660MW (supercritical) fuel costs to higher efficiency plant

ITEM	
Power plant investment (MUSD)	918
Specific investment (USD/kW)	1391
Pressure parts budget – boiler walls, tube banks headers and piping (MUSD)	183.6
Coal cost saving by efficiency increase (available for material improvements (MUSD))	62.2
Coal savings/coal cost during power plant lifetime (%)	3.8
Coal cost saving/pressure parts budget (%)	33.9
Coal cost savings/investment (%)	6.8
Admissible investment with efficiency improvements (MUSD)	980.2
Specific investment with efficiency improved (USD/kW)	1485
Admissible increase in specific investment (USD/kW)	94

Table 14.3 Estimation of admissible specific additional investment

Thus, it can be observed that there is significant available investment for new high temperature materials due to the fuel cost saving. There is also the intangible benefit of reducing the harmful emissions with higher efficiency plant i.e. with a decrease in coal used per MW of electricity produced, there is also a CO_2 reduction as shown in Figure 14.10.
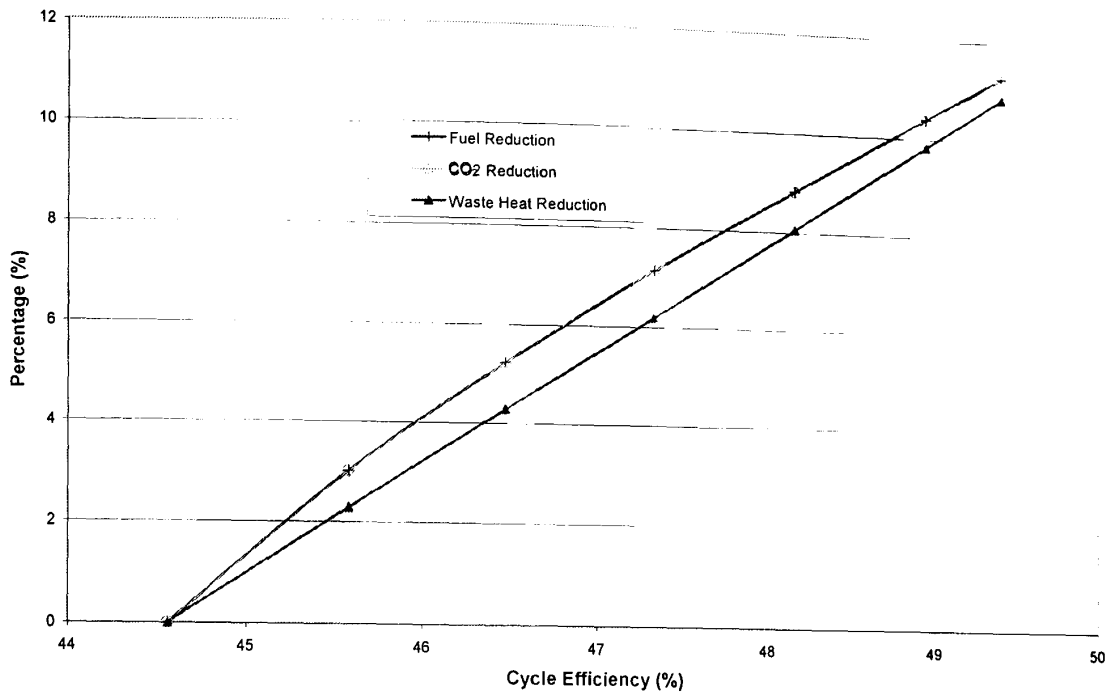
Figure 14.10 CO_2 emission reduction with increasing efficiency

This is becoming increasingly important. There have been several international debates on the subject of CO_2 reduction. The first international meeting took place in 1972 and it was followed by other meetings at which calls for reductions in the emission of "greenhouse" gases were made, Heinloth (1998). However, the first international agreement was only reached at the Environment Conference in Rio de Janeiro in 1992. It was decided at that time that the emission of such gases should be reduced by the year 2000, to the level current in 1990. The current status was laid down at the Kyoto Conference in December 1997, where the industrialised countries agreed to binding targets on emission levels.

It is widely regarded that amongst the greenhouse gases CO_2 contributes to around 50% of the effect on global warming. Power generation is one of the contributors to the production of CO_2; electric power generation is responsible for over 20% of the CO_2 generation by human activities. Since this centralised generation can be more easily targeted than, for example transportation, it is expected that this is where the major reductions will be sought. As the amount of CO_2 produced per MW/h in a PF station depends directly on the efficiency, the introduction of high temperature creep resistance materials allowing higher efficiency is the key to making these stations environmentally as well as commercially favourable.

14.8 COMMERCIAL EXPLOITATION

This development work has been successful in demonstrating the creep strength increase and thus the increase in thermal efficiency of the generating thermal cycle that is possible due to the use of fine stable titanium nitride particles. At present, however, it is unlikely that titanium nitride strengthened ferritic steels will enter commercial service within the power industry. The reason for this is that the estimated cost of the alloy is only slightly less than the iron based ODS alloys and the creep properties of the titanium nitride strengthened ferritic steels are at present significantly inferior to the ferritic ODS alloys such as PM2000 as shown in Figure 14.11. Additionally, the ferritic ODS with high aluminium contents potentially possess superior corrosion/oxidation resistance. Even with its excellent performance, ODS alloys have only been commercially exploited in specific applications such as injector nozzles etc, presumably due to the high cost.
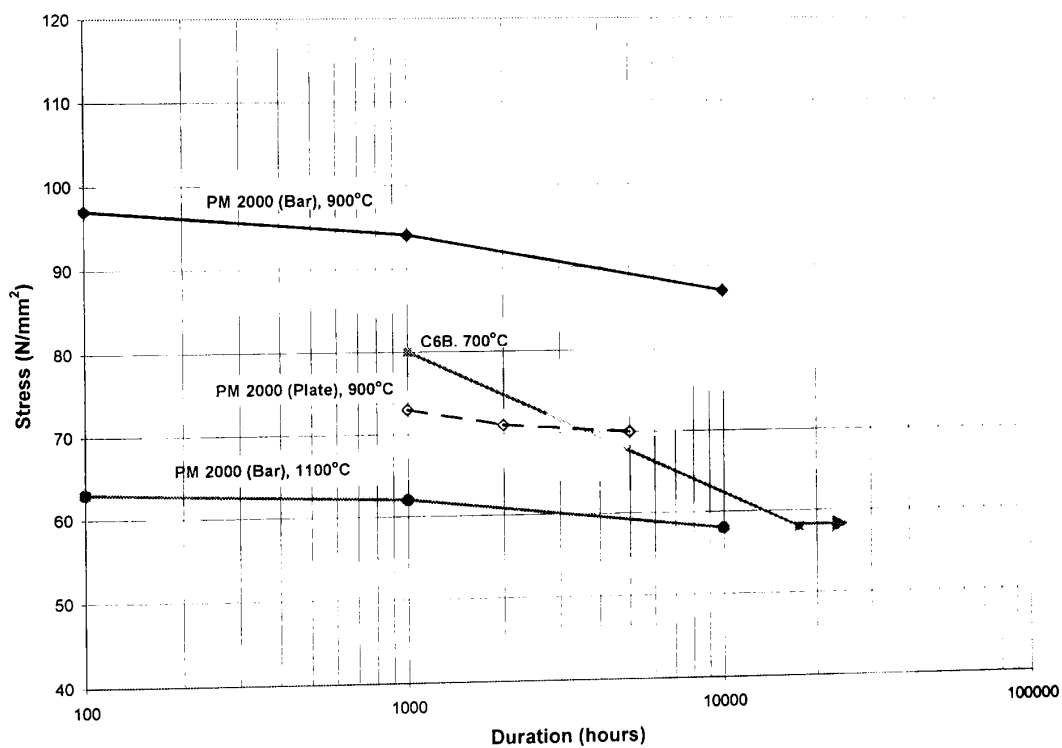
Figure 14.11 Comparison of the creep properties of Alloy C6B and PM 2000

The cost of advanced conventional ferritic steels; e.g., new 12%Cr steels to match or slightly exceed the properties of NF616 or E911 are, however, increasing significantly. This is due to the addition of up to 4 wt% cobalt to allow the 9%Cr strength to be achieved or surpassed, but increase the chromium content to 12wt% for steam side oxidation resistance. Even more expensive experimental alloys have been developed with rhenium, Masuyama & Komai (1998). Rhenium costs around

57 times the cost of nickel, resulting in these new ferritic steels being significantly more expensive than the advanced austenitic alloys that are historically of greater expense due to nickel costs. This development of ferritic alloys which are more expensive, but have significantly inferior creep properties to even conventional austenitic steels, demonstrates the advantage that ferritic components possess in being able to produce flexible plant to meet the energy demands of the client due to their higher heat transfer coefficient and lower thermal expansion coefficient.

For titanium nitride strengthened ferritic steels to be successful, they will have to have a cost advantage over the ferritic ODS alloys. A significant proportion of the production cost is attributed to producing an intimate homogeneous mixture of the titanium containing steel powder and the chromium nitride powder. At present both the ODS and the Alloy C6B materials are produced by the cold mixing of the powders in similar apparatus. The cost penalty arises as the time taken to achieve a suitable mixture is measured in days.

The Osprey Process offers the potential of significantly reduced costs as the process is rapid (minutes rather than days) and would not only replace the Mechanofusion operation to achieve the homogeneous mixture, but could also incorporate the VIM melting (carried out at Special Melted Products to produce the titanium containing steel matrix), and the powder production presently performed at Osprey. The trials with the Osprey Process performed in this work with titanium nitride strengthened steels proved unsatisfactory due to irregular injection rates resulting in inhomogeneous mixtures and also relatively coarse titanium nitride particles due to the high precipitation temperature. Thus, significant improvements would have to be achieved if the Osprey Process is to become a viable lower cost production technique. The upgrades required to produce a fine uniform distribution of titanium nitride particles are discussed in Chapter 16.

If the production costs of the titanium nitride strengthened creep resistant ferritic steel can be reduced, then, in addition to being a fascinating alloy to develop it could also be a commercially successful material.

Chapter 15

Conclusions

There is a worldwide drive to increase the efficiency of fossil-fired power plant in order to reduce both fuel consumption and the level of emissions. Boiler designs able to achieve significant efficiency increases already exist; the limiting factor is the performance of materials. The requirement that such materials should possess good thermal fatigue performance in addition to adequate creep performance dictates the selection of ferritic/martensitic steels for many components.

The most advanced conventional ferritic steels such as P92 – P122 are 9-12% Cr martensitic steels which gain their creep strength from the tempered martensite structure and the precipitated carbides and nitrides which stabilise the high dislocation density. The long term creep performance of these materials is ultimately limited by the rate at which these precipitates coarsen or otherwise transform over time at elevated temperatures.

The alternative approach taken here is to develop an alloy with increased high temperature long term creep performance by replacing the relatively low stability carbide and nitride precipitates with a thermodynamically more stable dispersion of titanium nitride precipitates in the steel.

The microstructures at each stage of the materials production development and at each stage of the material composition development, were examined by a combination of optical, scanning electron and transmission electron microscopy.

The testing was mainly performed on extruded bars from either the Osprey or Mechanofusion route. Comparative tests were performed by tensile and stress rupture testing. The stress rupture programme included tests in excess of 17,000 hours and at temperatures between 600 and 700°C.

The research reported in this thesis has established a number of features which contribute to the successful production of titanium nitride strengthened alloys, the understanding of the evolution of the microstructure and the correlation between the microstructure and the material properties, specifically the high temperature creep strength.

The important findings are summarised in the following sections.

15.1 DEVELOPMENT OF PRODUCTION ROUTE TO ACHIEVE FINE TITANIUM NITRIDE PRECIPITATES

Several production processes and routes were considered as part of the development process. The key issue in considering the applicability of the various production routes is the resultant size and distribution of the titanium nitride precipitates.

- Advanced reactive powder processing has been used to develop the high volume fractions of fine titanium nitride precipitates.

- The reactive powder processing technique of internal nitriding is analogous to internal oxidation. The controlling factors are also applicable to both processes.

- The stability of the titanium nitride precipitates have been assessed by the Wagner theory. The coarsening rate of titanium nitride precipitates were calculated and compared with vanadium nitride precipitates (currently the most stable precipitate utilised for strengthening conventional martensitic creep resistant steels). This revealed that although the diffusion rate of titanium was greater than vanadium, due to the lower solubility of titanium nitride, the coarsening rate of titanium nitride was significantly less than vanadium nitride.

- The Hertz design model has been shown to give a good relationship between the interparticle spacing, particle size and volume fraction titanium nitride.

223

- The phase structure of the titanium nitride strengthened alloys can be predicted from the Schneider modified Shaeffer diagram using the 25 x interstitial nitrogen wt% component of the nickel equivalent calculation and the chromium equivalent after removing the titanium precipitated as titanium nitride.

- The chromium nitride supply requires to have the maximum nitrogen content and the minimum powder size to minimise the chromium inhomogeneity.

- The Osprey processing route proved to be inconsistent due to the difficulty in matching the chromium nitride injection rate with the atomisation rate of the titanium containing steel. The source of the problem was due to the fine chromium nitride size required to achieve a relatively homogeneous distribution of chromium.

- The Mechanofusion process proved to be very controllable which resulted in a product superior to that produced by the Osprey Process.

- The achievement of a fine homogeneous distribution of titanium nitride particles depends on:

I. **Penetration Depth**: Low penetration depth is required to minimise counter diffusion. Counter diffusion of titanium leading to reduced volume fraction of titanium nitride precipitation in the prior powder particle centre occurs if the effective nitrogen diffusion distance is too great. To minimise counter diffusion the maximum titanium containing powder size was limited to 45 μm diameter.

II. **Precipitation Temperature**: Although the reduction in temperature reduces the activation energy barrier for nucleation thus the critical stable particle size is reduced, the major temperature effect observed here is in controlling the number of heterogeneous nucleation sites available. This controls the particle size by determining the length of time a nucleated particle has to grow before the next nucleation event depletes the supply of available titanium.

- **High Precipitation Temperature**: For Alloys C3-C6 the titanium nitride precipitation process was incorporated with the consolidation process

(extrusion or spray) thus the high temperature was required to achieve a dense product. The high temperature resulted in primary recrystallisation before precipitation leaving grain boundaries as the main heterogeneous precipitation site. As the grain boundary sites are limited, increasing the titanium content above 1.1wt% resulted in increased titanium nitride particle diameters.

- **Low temperature precipitation**: Fine homogeneous distribution of titanium nitride particles was achieved by completing the precipitation reaction before primary recrystallisation. By retaining the dislocation density this dramatically increased the number of heterogeneous nucleation sites. This was achieved by separating the precipitation reaction from the consolidation process, which allowed the precipitation temperature to be reduced to the optimum level. This modification to the production reduced the particle diameter from 211nm to 61nm and the interparticle spacing from 259nm to 122nm.

- Experience gained in the manufacture and processing of titanium nitride strengthened steels has shown that, provided the difficulties in production are recognised and appropriate manufacturing procedures formulated, titanium nitride precipitation strengthened ferritic steels can be produced with a fine homogeneous distribution of titanium nitride particles.

- The use of powder metallurgy opens up very interesting alternative manufacturing routes for a number of components such as complex headers which are required for advanced steam cycles.

15.2 DEVELOPMENT OF MICROSTRUCTURE

15.2.1 As-Extruded Material

The as-extruded microstructure is determined by the titanium nitride size and distribution.

- The Alloy C6B material consisted of fine micron sized grain structure, heavily worked and deformed in the extrusion direction. The level of deformation retained demonstrates the strong inhibiting effect that the fine homogeneous

distribution of titanium nitride precipitates has in preventing extensive recovery and any primary recrystallisation during the extrusion process.

- The earlier ferritic alloys (C3 – C6) with either low volume fraction titanium nitride or higher volume fraction titanium nitride, but coarser particles, did not retard primary recrystallisation during extrusion and thus had a equiaxed fully recrystallised grain structure.

- The recrystallised grain structure was micron sized due to the strong grain boundary pinning effect of the titanium nitride particles.

- The martensitic materials possessed titanium nitride pinned, micron sized prior austenite grain size and highly dislocated structure due to the transformation to martensite.

15.2.2 Normal Grain Growth

- Normal grain growth to any significant extent was not possible due to the high degree of gain boundary pinning from the titanium nitride particles. Any marginal increase in grain size at higher temperatures and extended durations was due to particle coarsening in accordance with the Zener model.

15.2.3 Secondary Recrystallisation

The development of a coarse grain structure by secondary recrystallisation is crucial to the performance under creep conditions. It has been found from this work that secondary recrystallisation is extremely sensitive to a number of parameters including the heat treatment time, temperature, volume fraction and distribution of titanium nitride particles and the level of prior deformation.

- The transformation from high stored energy, fine grain size structure to the lower energy coarse grain structure has a large activation energy. This is characterised by the high transformation temperature and rapid subsequent transformation.

- The large activation energy is due to the grain boundary pining by the titanium nitride and from the grain junctions of the ultra fine grains.

226

- It is not possible to form the required grain structure whilst the titanium nitride is in solution due to the high stability of the titanium nitride precipitates.

15.2.3.1   Fully Ferritic Alloys

- When the volume fraction of titanium nitride particles is low (Alloys C3(1) and C3(2)), it is possible for the fully recrystallised, as-extruded microstructure to overcome the activation energy and induce secondary recrystallisation by thermal means only.

- The transformation to the coarse elongated interlocking grains has a threshold temperature below which no secondary recrystallisation occurs.

- Secondary recrystallisation of the titanium nitride strengthened alloys is a highly anisotropic process, the grains being elongated in the extrusion direction.

- The grain boundaries have a serrated nature resulting in the interlocking of adjacent grains.

- For higher volume fractions of titanium nitride (Alloys C4, C5 and C6) it was found not to be possible to secondary recrystallise the material from the as-extruded, fully recrystallised condition.

- Secondary recrystallisation was only possible in Alloys C4, C5 and C6, after cold plastic deformation of the materials prior to heat treatment. The various levels of prior straining produced three distinct structures after the secondary recrystallisation heat treatment.

  - Less than 6% plastic deformation - no secondary recrystallisation.

  - 6-8% strain - Preferential nucleation of secondary recrystallisation in the vicinity of the outer surface of the bar.

  - 10-12% strain - Full secondary recrystallisation of the bar cross section.

- No upper limit of the pre-strain to induce secondary recrystallisation was detected with the Alloy C materials. From the literature there is an upper limit on the nickel ODS alloys. This is most probably due to the high dislocation

energy encouraging primary recrystallisation prior to secondary recrystallisation, thus, destroying the necessary structure for secondary recrystallisation. The upper limit on strain to induce secondary recrystallisation is likely to be less limiting in BCC ferritic alloys that can readily recover prior to recrystallisation rather than lower stacking fault energy FCC γ or Ni alloys where recovery is limited, therefore primary recrystallisation takes place more readily.

- The available literature indicates that the inducing effect of cold straining on secondary recrystallisation is more the result of lowering the activation energy by creating a favourable texture rather than increasing the driving force by increasing the dislocation density. The mechanism, however, is still not well understood.

- In the Alloy C6B material where the titanium nitride particles retarded dynamic primary recrystallisation during the extrusion process, no further mechanical processing was required to be added to the thermal treatment to induce secondary recrystallisation.

15.2.3.2   Martensitic Materials

- It was not possible to induce secondary recrystallisation in the martensitic material in the as-extruded condition or at various levels of cold deformation. This is a result of the phase change to austenite prior to reaching the recrystallisation temperature.

15.2.4 Summary

It is apparent that secondary recrystallisation is a complex phenomena and depends on a range of finely balanced variables. It cannot be guaranteed that a particular thermo-mechanical process designed to produce secondary recrystallisation in one alloy will do so in another. The entire production route must be considered in optimising the materials ability to secondary recrystallise as only a slight change in one aspect of the whole thermo-mechanical process may result in the development of a non-optimised structure or the complete loss of the materials ability to undergo secondary recrystallisation.

15.3 MECHANICAL PROPERTIES

Significant improvement in the mechanical properties of high chromium ferritic steels can be achieved through the precipitation strengthening by solid state internal nitriding.

15.3.1 Tensile Properties

- There is a good correlation between the calculated room temperature yield stress using the latest modification of the Orowan equation and the measured values. This indicates that the titanium nitride interparticle spacings determine the changes in the mechanical properties.

- The titanium nitride strengthened secondary recrystallised material indicated a strong tendency of localisation of the plastic deformation at temperatures above 600°C. This led to the early onset of necking.

- Tensile and creep failure modes vary with strain rate and temperature. At a given temperature, the titanium strengthened secondary recrystallised material can exhibit increasing then decreasing ductility as the strain rate is decreased.

15.3.2 Creep Properties

- Creep strain is the superposition of several distinct mechanisms, the one that is dominant depends on the microstructure and the stress and temperature applied to the material.

- Precipitation strengthening should be regarded as attacking a particular flow mechanism but does not slow all mechanisms effectively. Effective materials require many mechanisms.

- Creep testing highlighted the fact that the initial properties were strongly influenced by grain boundary sliding rather than dislocation creep. This was due to the fine micron size grain structure, which in turn is dependent on the thermo-mechanical processing history and titanium nitride particle size and distribution.

- The ultra fine grained material exhibited superplastic type behaviour during the 600°C creep tests.

- The creep properties have been improved from the initial poor results to properties exceeding those of conventional martensitic steels at high temperature. This has been achieved by controlling the critical factors of grain size, particle size and interparticle spacing.

- An improvement in creep resistance and rupture life is obtained when the secondary recrystallised material is pre-strained. Pre-straining results in a decrease in the extent of primary creep and a decrease in the secondary creep rate by introducing a high dislocation density to the secondary recrystallised structure.

- The final Alloy C6B material gives a lower creep rate and longer rupture life than all other conventional martensitic materials (P91, E911, P92 etc) at 700°C. The creep strength of Alloy C6B is also greater than 316SS where the self diffusion of iron is approximately 200 times slower.

- The high creep strength was achieved at the expense of ductility.

- Creep fracture occurs in a brittle transgranular and intergranular manner due to the nucleation, growth and coalescence of cavities with very little strain to failure. The creep cavities observed were very localised to the fracture surface.

- The high strength and low ductility of the material increase the risk of CCG failures.

- It was found that the highest creep strength material (Alloy C6B) exhibits a high stress sensitivity to creep deformation.

- The high stress dependence of creep deformation has been rationalised by describing the stress dependence of the creep rate in terms of an effective stress rather than a simple applied stress. The effective stress is the applied stress minus a threshold stress.

- The threshold stress, below which the strain rate is negligible, was estimated for Alloy C6B by the creep dip test technique. The estimated value at 700°C was 50 N/mm^2.

230

- The modified Norton equation to account for a threshold stress was shown to give a good correlation with the Alloy C6B dip test strain rate data.

- The creep life of the secondary recrystallised materials was found to be proportional to the cube of the measured interparticle spacing. This is in agreement with the phenomenological equation developed by Sherby et al.

15.4 OPTIMISED PRODUCTION ROUTE TO MAXIMISE CREEP PROPERTIES

This work has illustrated that to obtain the best possible properties of the titanium nitride strengthened ferritic steels it is critical to control all the processing steps from the powder size to the pre strain in order to obtain the optimum microstructure for creep retardation. The dependence of the creep properties on the total production process is illustrated in Figure 15.1. In this figure the optimisation of each level in the process is dependent on the level below. This is detailed as follows:

- The creep strength is dependent on the dislocation density and the coarse interlocking grains.

    - The titanium nitride precipitates obstruct the movement of dislocations and thereby stabilise the dislocation density, which controls the creep strain as a function of time. The effectiveness of the titanium nitride dispersion in stabilising the dislocation substructure is inversely proportional to the titanium nitride particle size for a given volume fraction.

    - The coarse interlocking grains produced by secondary recrystallisation minimise grain boundary sliding. The creep strength of the grain boundaries is inversely proportional to the grain boundary area.

- The secondary recrystallised grain structure is dependent on the alloy chemistry (to avoid phase changes), the titanium nitride particle size and distribution, and the deformed structure which in turn is dependent on the titanium nitride particle size and distribution.

- The titanium nitride particle size and distribution is dependent on the powder mixture to create a high dislocation density within the powder particle, the

231

chromium nitride distribution and the precipitation temperature. These conditions are critical in order to complete the heterogeneous precipitation mainly on the dislocations before primary recrystallisation occurs.

- The powder mixture is dependent on the titanium bearing steel powder diameter to minimise counter diffusion and the chromium nitride powder size and chemistry to minimise chromium inhomogeneity.

15.5 APPLICATION TO POWER PLANT

The design of fossil fired steam power plant starts with the qualitative assessment of the sequential process of working fluids as a function of temperature, pressure, enthalpy and entropy. The design of modern power plant represents, however, more than the application of thermodynamic data. It is a synthesis of economic considerations with thermal performance criteria that govern the selection of materials for power plants. Thus, the design of power plant represents the optimisation of thermodynamic and economic considerations, the latter including initial, manufacturing and fuel costs.

- The complex interactions between the additional costs which may be required for materials to operate at higher temperatures and the resultant savings from efficiency gains, together with other benefits such as reduced CO_2 emissions have been assessed in a techno-economic feasibility study.

- This work has shown that the advancement of high temperature creep properties of the titanium nitride strengthened steel over conventional ferritic/martensitic steels offers substantial lifecycle cost savings due to the higher achieved efficiencies.

- Oxide dispersion strengthened ferritic steels, however, offer greater high temperature creep strength. Even with their superior properties oxide dispersion strengthened steels have not, as yet, been adopted by the power industry due to their high cost and earlier failures as a result of the inferior properties of non fully secondary recrystallised tubes.

- It is likely that using the material processing route developed during this work that the production costs of the titanium nitride strengthened steel would only be marginally less expensive than the ODS alloys, thus, it is likely that this would

result in the selection of the ODS alloys over the titanium nitride strengthened alloys.

- The cost of the titanium nitride strengthened alloys, could, however. be reduced by utilising the Osprey Process in the production route. Although trials in this project did not prove to be successful, the required parameters are now known and thus it is only the control mechanisms that have to be developed in order to contribute to the material production process.
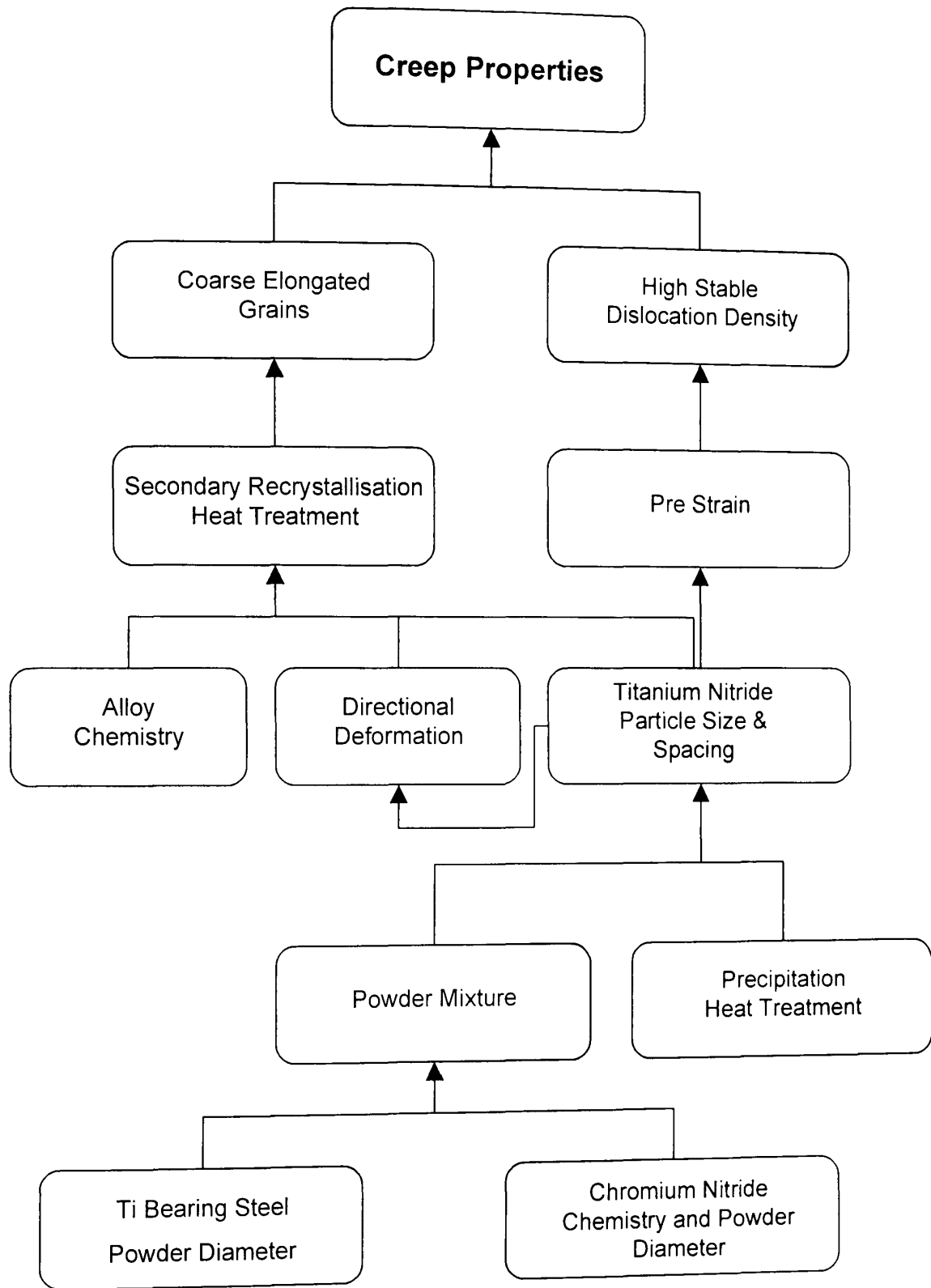
Figure 15.1 Schematic diagram depicting the processing steps necessary in achieving the excellent creep properties.

234

Chapter 16

Recommendations for further work

This research work to develop the concept of titanium nitride strengthened creep resistant ferritic steel produced by solid state internal nitriding has concentrated on achieving the main aim of enhanced creep properties. To this end it has been successful in achieving high temperature creep strength superior to all conventional ferritic/martensitic creep resisting steels. During the course of this development work, many areas for further work were highlighted. The main areas are as follows:

- Negative performance attributes

- Creep/fatigue interaction

- Secondary recrystallisation understanding

- Grain orientation

- Osprey Process development

- Welding development

Brief reviews of these areas for further work follow.

16.1 NEGATIVE ATTRIBUTES

This work has shown that the conflicting design requirements of the ideal alloy to posses high creep strength and high ductility have not been achieved with the titanium nitride strengthened ferritic steels. This study has concentrated on the positive attribute of high creep strength, but, for the material to be adopted by the power industry the potential negative attributes such as ductility, toughness and CCG resistance require to be studied. Additionally, this work has concentrated on uniaxial material properties, however, the actual components will experience multiaxial loading, thus, the further work should incorporate notched sample and model component tests.

16.2 CREEP / FATIGUE INTERACTION

For power plant components, deformation at elevated temperature cannot be considered to arise from pure creep or pure fatigue but from an interaction between the two damage mechanisms. At typical boiler operating parameters, creep/fatigue fracture is due to the nucleation, growth and eventual linking up of the creep cavities as in pure creep. The difference in creep/fatigue damage is that the interlinking of the creep cavities is due to fatigue crack growth. Consequently, the interaction of the two mechanisms gives shorter lives than the two mechanisms operating independently. There are several interaction diagrams such as the AEA fast reactor design code or the diagram derived from ASME code case N-47. The ASME line is the most widely used and is largely based on failure data from conventional ferritic creep resistant materials. The typical boiler design envelope is superimposed on the creep fatigue interaction diagram in Figure 16.1.

With the high creep strength titanium nitride steels developed here, the creep/fatigue interaction properties may be significantly improved. This is possible because the high precipitate strengthening and coarse interlocking grains result in the titanium nitride steel being very resistant to cavity formation. As the cavities in the titanium nitride strengthened steel most probably only nucleate and grow very near the final fracture event, there will be far less interaction between the creep and fatigue mechanisms. Thus, not all of the properties not investigated by this study are potentially negative. The synergistic effect of creep and fatigue damage currently places severe restrictions on the operating parameters of advanced power plant. If further work could demonstrate that the combined creep and fatigue effect on the

236

titanium nitride strengthened ferritic steel was less than for conventional power plant ferritic steels then this would be a major benefit.
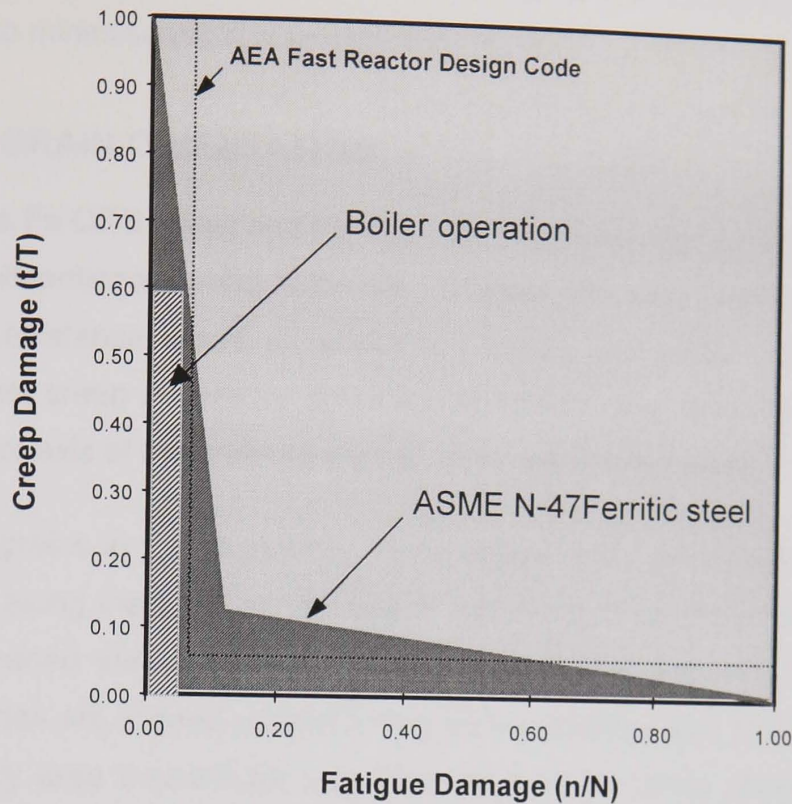
Figure 16.1 Creep fatigue interaction diagrams

16.3   SECONDARY RECRYSTALLISATION UNDERSTANDING

In the present work, evaluation of the conditions necessary to induce secondary recrystallisation were largely the result of trial and error. Whilst the grain pinning of the grain boundaries due to particles is well understood the relative effects of grain corner pinning and the effect of the stored energy due to dislocations and the texture effect on secondary recrystallisation are less well understood.

There is conclusive evidence in the literature that the secondary recrystallisation temperature can be sensitive to the initial texture. It has been postulated that the texture leads to the clustering of adjacent grains into similar orientations. This would lead to an increase in the effective grain size, thereby making the nucleation of recrystallisation easier. However, at present this explanation remains speculative. With regard to dislocations, it is conceivable that the removal of the stored energy would aid secondary recrystallisation in a similar fashion to primary recrystallisation. The work by Chou (1997), however, found that there was no increase in stored energy with deformation, in fact it was found that the deformation led to a reduction

in the stored energy. There was no clear explanation for this phenomenon. It is thus apparent that further work is required to determine the relative effects of the variables and therefore reliably form the coarse interlocking secondary recrystallised grains to minimise grain boundary sliding.

16.4 GRAIN ORIENTATION

Both the Fe ODS alloys and the Alloy C6B material offer considerable creep benefits over conventional ferritic materials, however, the high GAR structures induced for creep resistance result in anisotropic creep properties. The materials exhibit maximum creep resistance when the principal creep stress is aligned parallel with the major axis of the grain structures, Timmins & Arzt (1988).

As the grains in the secondary recrystallised material studied within this work are aligned along the bars, all the tensile and creep tests performed on titanium nitride strengthened steels have necessarily been orientated such that the longitudinal boundaries are aligned parallel to the principal stress axis, thus minimising the grain boundary area that will be favourably aligned for cavity growth and, in doing so, maximising the properties.

16.4.1 Tubes

For tubular boiler components produced by extrusion, the principal stress (hoop) is aligned normal to the longitudinal direction and hence the longitudinal grain boundaries. This will result in reduced properties. In the case of Fe ODS alloys; the creep life of pressurised tubes is no better than 20% of the longitudinal properties, Jones (1997).

Work is underway within the BRITE EuRAM co-ordinated project BE97 4994 to specifically address this limitation in the Fe based ODS alloys. The method being investigated to minimise the weakness is to alter the deformation texture. Initial trials have been successful in inducing torsional flow into the material, which on subsequent secondary recrystallisation resulted in coarse torsionally wound grain structures. Tubes produced in this manner will be tested to determine the resultant increase in creep life under pressure testing. This technology could be readily transferred to the production of titanium nitride strengthened tubing, however, from the review carried out within this work it may not be possible to obtain a similar spiral grain structure in the nickel base alloys.

16.4.2 Headers

For header components, a preferential grain alignment could be developed using a two-stage formation process. The first stage would involve hot isostatic pressing the powder to produce a consolidated preform. The second stage would take advantage of the high temperature low strength and high elongation properties of the fine grain size material by expanding the preform via internal pressurisation into a die with the header components (eg. the main penetrations and tube stubs, as shown in Figure 16.2), expanded into place. This expansion process would create a deformation texture in the component that would be aligned parallel to the resolved major stress axis. Thus, upon heat treatment to induce secondary recrystallisation the grains would also be aligned parallel to the major stress axis. This would apply to simple geometries, e.g. the header body where the grains would be orientated circumferentially around the header and also complex geometries, such as the crotch and saddle positions of the main penetrations. As a result of this orientated grain structure, the strength will be maximised in the direction of maximum stress in a way that is impossible in conventional equiaxed material. The actual process could be likened to fibre reinforced composites where the direction of the fibres is positioned to strengthen specific areas. The advantage that the method described above has, is that the expansion of the preform determines the orientation rather than relying on finite element type simulations.

Final Superheater Outlet Header

Figure 16.2 Typical header geometry

In summary, there are potential methods for transforming the excellent uniaxial properties demonstrated by the titanium nitride particles and high GAR into excellent properties in multiaxial simple components such as tubes and complex multiaxial components such as headers.

16.5 OSPREY PROCESS DEVELOPMENT

At present the commercial exploitation of the titanium nitride strengthened ferric steel is not thought to be feasible as its creep properties are inferior to the ferritic ODS alloy PM 2000 and both alloys would have similar high production costs. The Osprey Process, however, offers the potential of significantly reduced costs as the process would not only replace the time consuming and thus costly Mechanofusion operation to achieve the homogeneous mixture, but could also incorporate the VIM melting (carried out at Special Melted Products) to produce the titanium containing steel matrix), and the powder production presently performed at Osprey. The trials with the Osprey Process performed within this work with titanium nitride strengthened steels proved unsatisfactory due to irregular injection rates resulting in inhomogeneous mixtures and also relatively coarse titanium nitride particles due to the high precipitation temperature. Thus, significant further development work is required if the Osprey process is to become a viable lower cost production technique. The list of further developments required to produce a homogeneous mixture would include the following:

- Vacuum induction melting furnace.

- Injector system specifically designed for sub 10 μm chromium nitride powders.

- Metal spray size reduced to produce sub 45 μm droplets.

In order to avoid high temperature precipitation of titanium nitride during cooling of the combined powders, the mixing of the powders would have to be reduced to below approximately 600°C. This could be achieved by increasing the flight time of the atomised metal spray and injecting the chromium nitride at the lowest possible point prior to collection.

As the temperature would be reduced, collection would be by means of a hopper rather than the preform. This does not result in an additional stage as the preforms produced required additional consolidation by means of extrusion of HIPping due to the porosity present.

An additional stage would, however, have to be incorporated in order to produce a high dislocation network within the metal powder particles to achieve a fine heterogeneous precipitate distribution. This could be achieved by cold compacting

240

the canned powder to a greater extent. A comparison of the industrial ODS alloy production, the experimental Alloy C6B production and the possible industrial production of titanium strengthened ferritic alloys is shown in Figure 16.3.

Ferritic ODS Alloy	Experimental C6B Alloy	Proposed Industrial TiN Manufacturing Route
Mechanical blending for approx. 6 days under vacuum	Steel powder production and classified to <45μm	Improved Osprey Process
Canned	Milling of chromium nitride to <10μm diameter	Canned
Cold compacted	Mechanofusion for approx. 3 days under vacuum	Cold Compacted
Sintered (1100°C/1hr)	Canned	Precipitation heat treatment 600°C x 17 hours
Hot compacted (1100°C, 1900 bar 3 sec)	Cold Compacted	Hot extrude 1000°C 17 1 extrusion ratio
De-Can	Precipitation heat treatment 600°C x 17 hours	De-Can
Hot extrude 1150°C, 9:1 extrusion ratio	Hot extrude 1000°C 17:1 extrusion ratio	Heat treat 1200°C x 1.5 hrs to produce secondary recrystallisation
Grind	De-Can	
Cold draw	Heat treat 1200°C x 1.5 hrs to produce secondary recrystallisation	
Heat treat approx. 1200x1 hr to produce secondary recrystallisation		
Heat treat to produce alumina scale		

Figure 16.3 Production route comparison of a typical ferritic ODS alloy, the experimental Alloy C6B and proposed industrial route for titanium nitride strengthened ferritic steels.

16.6 WELDING DEVELOPMENT

Joining of materials is a critical aspect of power plant fabrication, particularly for boiler applications. For a material to be successful it must be able to be joined economically and the degradation in parent material properties must not be excessive. Further work is required; however, the author has conducted a limited number of trials with interesting results. This work has demonstrated that the titanium nitride strengthened ferritic steels can be joined economically under industrial conditions without significantly coarsening the titanium nitride particles using amorphous metal diffusion bonding techniques.

Chapter 17

Bibliography

Ahlborn H., Hornbogen E.& Koster U. (1969), J Mat. Sci, **4**, 944.

Alamo A., Regle H. & Bechade J.L. (1992), Novel Powder Processing, Advances in Powder Metallurgy and Particulare Materials, **7**, 169.

Ahlquist C.N. & Nix W.D. (1971), Acta Metall., **19**, 373.

Anderson W.A. & Mehl R.F. (1945), Trans. Met. Soc. AIME **161**, 140.

Argon A.S., Im J. & Needleman A. (1975), Met. Trans., **6A**, 815.

Arzt E. & Ashby M.F. (1982), Scripta Met., **16**, 128

Arzt E. (1984) Superalloys '84' TMS AIME, p189.

Arzt E., Rosler J. & Schroder J.H. (1987), Creep and Fracture of Engineering Materials and Structures (ed. Wilshire & Evans), 217.

Ashby M.F. (1970), Proc. 2nd Int. Conf. Strength of Metals and Alloys, **2**, 507.

Ashby M. F. (1973), The Microstructure and Design of Alloys, Proc. Of the 3rd International Conference on the Strength of Metals and Alloys, The Institute of Metals, **1**, 8.

Avrami M. (1941), J. Chem. Phys., **9**, 177.

Beck P.A. & Sperry P.R. (1950), J App. Phys. **21**, 150.

Benjamin J.S. & Bomford M.J. (1974), Met. Trans. **5**, 615.

Birks N. & Meier G. H. (1983), Introduction to High Temperature Oxidation of Metals, Edward Arnold.

Bilsby C.F. (1974) Diffusion and Precipitation Processes During the Nitriding of a 20/25Ti Stabilised Steel and Some Practical Implications. TRG Memorandum 6442(s).

Biselli C. & Morris D.G. (1991), Mat. Sci & Eng., **A148**, 163.

Brown L.M. & Ham R.K. (1971), Strengthening Methods in Crystals (ed. Kelly A. & Nicholson R.B.) Elsvier Amsterdam, p9.

BS 1113 (1998) Design and Manufacture of Water Tube Steam Generating Plant (Including Superheaters, Reheaters and Steel Tube Economisers) Prepared by Technical Committee PVE/2.

Burgers W.G. & Basart J.C.M. (1929), Z Phys., 54.

Burke J.E. & Turnbull D. (1952), Progr. Metal Phys., **3**, 220.

Cahn R.W.(1966), Recrystallisation Grain Growth and Texture, ASM, 99.

Carnot S.N.L., Clapeyron E. & Clausius R. (1962) Reflections in the Motive of Fire, Gloucester, Peter Smith.

Cocks A.C.F. & Ashby M.F.(1982) Mat. Sci., **27**, 189.

Cooper A.H., Nardone V.C. & Tien J.K. (1984), Superalloys '84, Proc. of 5th Int. Conf. TMS-AIM.

Chou T.S. (1997), Mat. Sci.Eng., **A223**, 78.

Christian J.W. (1975), The Theory of Transformations in Metals and Alloys: Equilibrium and General Kinetic Theory, 2nd Edition, Pergamon, Oxford.

Corti C.W., Cotterill P. & Fitzpatrick G.A. (1974), Int. Met. Rev., Review 182, **19**, 77.

COST 522 (1998), Co-Operation in Science and Technology Project 522, European Commision.

Cotterill P & Mould P.R. (1976), Recrystallisation and Grain Growth in Metals. Surrey University Press.

Clauer A.H. & Wilcox B.A. (1967), Metal Sci. J., **1**, 86.

Davies P.W., Nelmes G., Williams K.R. & Wilshire B. (1973), Matal Sci. J., **7**, 87.

Doherty R.D. & Martin J.W. (1963), J. Inst. Metals, **91**, 332.

Dyson B.F. (1976), Mat. Sci., **10**, 349.

Dyson B.F. (1983), Scr. Met., **17**, 31.

Fawley R.W. (1972), The Superalloys, Sims C.T. &Hagel W.C. (Eds), New York. John Wiley and Sons, p3.

Fleck R.G., Taplin D.M.R.& Beevers C.J. (1975), Acta Met., **23**, 414.

Fleischer R.L. (1963), Acta Metall., **11**, 203.

Foreman A.J.E., Hirsch P.B. & Humphreys F.J. (1970), Fundamental Aspects of Dislocation Theory, vol 2, N.B.S. Publ. No. 317, p1083.

Fukuyo H., Tsai H.C., Oyama T. & Sherby O.D. (1991), ISIJ international **31**, 76.

Gladman T. (1966), Proc. Royal Soc. A, 294.

Gladman T & Pickering (1967),JISI June 1967, p653.

Gladman T. (1997), The Physical Metallurgy of Microalloyed Steeld. The Institute of Materials Book 615.

Goods S.H. & Brown L.M. (1979), Acta Metall., **27**, 1.

Hald J (1995), New Steels for Advanced Plant up to 620°C. The EPRI/National Power Conference, The Society of Chemical Industry, London p152.

Hall E.O. (1951), Proc. Phys. Soc. London, **643**, 747.

Hamerton R.G., Jaeger D.M. & Jones A.R. (1994a), Materials for Advanced Power Engineering, Kluwer Academic Publishers, **1**, 477.

Hamerton R.G., Jaeger D.M. & Jones A.R. (1994b), Proc. Powder Metallurgy, World Congress 1994, Les Editions de Physique, Les Ulis, p2085.

Hamerton R.G. , Jaeger D.M. & Jones A.R. (1995), 4th International Conference on High Nitrogen Steels, Koyoto Sept. 1995.

Harris J.E. (1965), Trans. Met. Soc. Am. Inst. Min. Metall. Engns., **233**, 1509.

Hart E.W. (1967), Acta Metall., **15**, 1545.

Hatherley M. & Hutchieson W.B. (1979), An introduction to Textures in Metals. The Institute of Metallurgists Monograph No. 5.

Hazzledine P.M. & Newbury D.E. (1973), Proc. of the 3rd International Conference on the Strength of Metals and Alloys, Cambridge, **1**, 41, p202.

Hausselt J.H. & Nix W.D. (1977), Acta Metall., 25, 1491.

Heinloth K. (1998), Materials for Advanced Power Engineering. Proc of the 6" Liege Conf. p19.

Hofer P. & Cerjak (1998), Materials for Advanced Power Engineering. Proc of the 6" Liege Conf. p549.

Hollomon J.H. & Jafee L.D. (1945), Trans AIME 162, 223.

Honeycombe R. W. K (1981), Steels, Microstructure and Properties, Edward Arnold London.

Hotzler R.K. & Glasgow T.K. (1980), Proc. Superalloys 1980, p455.

Hu H. (1963), Recovery and Recrystallisation in Metals, Hunnel L. (ed), Interscience, New York, p311.

Humphreys F.J (1977), Acta Metall., 25, 1323.

Humphreys F.J. & Stewart A.T. (1972), Surf. Sci. 31, 389.

Hunter A.N.R.H. (1999), ACCT Final Report, MBEL reference M/99/09.

Jack K. H. (1973), Heat Treatment '73, The Metals Sociey p39.

Jaeger & Jones (1994), Materials for Advanced Power Engineering, Part II, p1515, Kluwer Academic Publishers.

Jesser W.A. (1969), J. Phil. Mag. 19, 993.

Johnson W.A. & Mehl R.F. (1939), Trans. Met Soc. AIME, 135, 416.

Jones A.R. (1997), Proposal for Project No. BE97-4949, Contract No.BRPR-CT98-0755, p3.

Juul-Jensen D., Hansen N. & Humphreys F.J. (1985), Acta Metall., 33, 2155.

Juul Jenson D. & Kjems J.K. (1983), Textures Microstruct., 5, 239.

Kaltenhauser R.H. (1971), Met Eng Quarterly 11, 4, 41.

Kimmel E.R. & Inman M.C. (1969), Trans, ASM, 62, 390.

Kindlimann L. E. (1984), Dispersion Strengthened Ferritic Stainless Steel. United States Patent 4,464,207.

Kindlimann L. E. & Ansell G. S. (1970), Met Trans, 1, 163.

Korb G. & Sporer D. (1990), Proc. Conf. High Temperature Materials for Power Engineering, Liege.

Koster U. & Hornbogen E. (1968), Z. Metallkde, Bd. **59**, 792.

Koster U. (1974), Metal Science, **8**, 151.

Krautwasser P., Czyrska-Filemonowic A., Widera M & Carsughi F. (1994) Mat Sci Eng, **A177**, 199.

Kreye H.& Hornbogen E.(1970), J Mat. Sci. **5**, 89.

Lai G. Y. (1990), High Temperature Corrosion of Engineering alloys, ASM International, p73.

Laing K. C. (1989), PhD Thesis, Gaseous Nitriding of 9%Cr Steels Containing Ti or V. University of Strathclyde.

Langdon T.G. (1970), Phil. Mag., **22**, 689.

Larson F.R. & Miller J. (1952), Trans ASME, **74**, 765.

Leatham A. (1996), Materials World, **4**, 6, 317.

Lee D. (1969), Acta Metall., **17**, 1057.

Lee D. (1970), Met Trans **1**, 309.

Lee S.L. (1998), PhD Thesis, High Nitrogen Austenitic Stainless Steels by Powder Metallurgy, University of Strathclyde.

Leslie W.C, Michalak J.T. & Aul F.W. (1963), Iron and its Dilute Solid Solutions ed. Spencer C.W. & Werner F.E., p119.

Li J.C.M. (1962), J App Phys., **33**, 2958.

Lui W.J. & Jonas J.J. (1980), Met Trans A, **19A**, 1403.

Lui W.J. & Jonas J.J. (1988), Processing, Microstructure and Properties of HSLA Steels (Ed A.J. DeArdo, The Minerals, Metals & Materials Society, 1988, p39.

Lund R.W. & Nix W.D. (1976), Acta Metall., **24**, 469.

Luton M.J. (1986), Strength and Fractures of Materials and Structures, Oxford. p859.

McLean D. (1957), Inst. Metals., 181.

McLean D (1970), Met Sci Journal, **4**, 144.

Machlin E.S. (1956), Trans. Met. Soc. **206**, 106

Masuyama F. & Komai N. (1998),), Materials for Advanced Power Engineering. Proc of the 6th Liege Conf. Part 1, p269.

Maurickx T. & Taillard R. (1988) Proc. HNS 88, p327.

Melton K.N., Edington J.W., Kalland J.S. & Cutler C.P. (1974), Acta. Metall. **22** 165

Metals Handbook (1990), 10th Edition, American Society for Metals.

Mino K., Nakagawa Y.G. & Ohtomo A. (1987), Met. Trans. A, **18A**, 777.

Monkman F.C., Grant N.J. (1956), Proc. ASTM, **56**, 593.

Murakami K., Mino K., Harada H. & Bhadeshia H.K.D.H., (1993), Metall. Trans A, **24**, 1049.

Nardone V.C. & Tien J.K. (1983), Scripta Met., **17**, 467.

Narita K. (1975). Trans Iron & Steel Inst. Of Japan, **15**, 145.

Nikbin K.M., Smith D.J. & Webster G.A. (1986), Trans ASME, **108**, 186.

Nix W.D. (1988), Mat. Sci. Eng., A103, 103.

Norton F.H. (1929), The Creep of Steel at High Temperatures, McGraw-Hill, New York.

Novikov (1997), Scripta Met., **37**, 4, 463.

Oliver W.C. & Nix W.D. (1982), Acta Metall., **30**, 1335.

Orowan E. (1947), Symposium on Internal Stress, Institute of Metals, London, p451.

Parker J.D. & Wilshire B. (1975), Metal Science, **9**, 248.

Parker J.D. & Wilshire B. (1978), Metal science, **12**, 453.

PD6525 (1990), Elevated Temperature Properties for Pressure Purposes Part 1. Stress Rupture properties, BSI Iron and Steel Standards policy Committee ISM ¯3 - /1.

Pearson J. & Ursula J.C.E. (1953), JISI No III, **175**, 52.

Petch N.J. (1953), JISI, London, **173**, 25.

Petkovic-Luton R., Srolovitz D.J. & Luton M.J. (1982), Scr. Met., **16**, 1401

Pickering F.B. (1978), Physical Metallurgy and the Design of Steels. Materials Science Series.

Porter D.A. & Easterling K.E. (1988), Phase Transformations in Metals and Alloys Van Nostrand Reinhold Int.

Powell G.W. (1986), Metals Handbook, 9th Edition, **11**, 263.

Quadakkers W.J. & Ennis P.J. (1998), Materials for Advanced Power Engineering Proc of the 6th Liege Conf. Part 1, p123.

R5 (1998), Assessment Procedure for the High Temperature Response of Structures, British Energy.

Raj R. & Ashby M.F. (1971), Met. Trans., **2**, 1113.

Raj R. & Gosh A.K. (1981), Met. Trans. A, **12A**, 1291.

Rankine WJM (1908) A Manual of the Steam Engine and Other Prime Movers – Revised by W J Miller, Griffin & Co.

Reed-Hill R.E. (1973), Physical Metallurgy Principals, 2nd Edition, D. Van Nostrand Co., p399.

Regle H. & Alamo A., (1993), J Phys IV, **3**, C7, 727.

Rickerby D.S. & Hendry A. (1986), Acta Metall., **34**, p1911.

Rickerby D. S., Hendry A. & Jack K. H., (1981), Heat Treatment 81, Proc. of an International Conference Organised by the Metals Society, p130.

Rickerby D.S., Hendry A. & Jack K.H. (1986), Acta Metall., **34**, p1925.

Roberts A.C. & Evans H.E. (1992), Effects of Titanium and Silicon Additions on Creep Behaviour of TiN Dispersion strengthened 20Cr25Ni Stainless Steel. AEAT Internal Report.

Rogers G. F. C. & Mayhew Y. R. (1980), Engineering Thermodynamics Work and Heat Transfer, Third Edition, Longman Scientific and Technical.

Rosler J. & Arzt E. (1988), Acta Metall., **36**, 1043.

Rukwied A (1973), Metall. Trans., **3**, 3009.

Schey J.A. (1977), Introduction to Manufacturing Processes. Edward arnold. London.

Schneider H (1960), Foundary Trade Journal **108**. 562.

Singer R.F. & Gessinger G.H. (1982), Met. Trans A, **13A**, 1463.

Speich G.R. (1972) Met Trans, **3**, 1045.

Sporer D. & Lang O. (1994), Materials for advanced Power Engineering Part II, p1469, Kluwer Academic Publishers.

Sha W. & Bhadeshia H.K.D.H. (1997), Mat. Sci. & Eng. **A223**, 91.

Shaw R.B., Shepherd L.A., Starr C.D., Dorn J.E. (1953), Trans. Amer. Soc. Metals. **45**, 429.

Sherby O.D., Walser B., Young C.M. & Cady E.M. (1975), Scripta Met., **9**, 569.

Sherby O.D., Klundt R.H. & Miller A.K. (1977), Met. Trans., **8A**, 843.

Shewfelt R.S.W. & Brown L.M. (1973), The Microstructure and Design of Alloys, Paper 63, p311.

Smallman R.E. (1990) Modern Physical Metallurgy, 4th Edition.

Smithells (1998), Metal Reference Book, Ed Brandes E. A. & Brook G. B. 7th Edition. Reed Educational and Professional Publishing.

Srolovitz D.J., Luton M.J., Petkovic-Luton R., Barnett D.M. & Nix W.D. (1984), Acta Metall., **32**, 1079.

Starr F. (1998), Materials for Advanced Power Engineering, Proc of the 6th Liege Conf. p695.

Staubli M., Bendick W., Orr J., Deshayes F. & Henry Ch (1998), Materials for Advanced Power Engineering, Proc of the 6th Liege Conf, **I**, p87.

Stephens J.J. & Nix W.D. (1985), Met. Trans, **16A**, 1307.

The World Energy Council Report (1993), Energy for Tomorrow's World – The Realities, Real Options and the Agenda for Achievement, European Commision Report.

Thermie 700 (1998), A Strategy for the Development of Advanced Pulverised Coal Fired Power Plants (700°C), European Commision DGXVII.

Threadgill P.L. & Wilshire B. (1974), Metal Science, **8**, 117.

Timmins R & Arzt E (1988), Scripta Met. **22**, 1353.

Torronen K. (1976), Proc. 4th International Conf. On the Strength of Metals and Alloys, vol. 1 (ed Laboratoire de Phsique du Solide), p239.

Ubhi S.H. (1988), PhD Thesis, Development of Microstructure in MA956 Leeds University.

Uenishi N. & Takeda Y (1990), Structural Applications of Mechanical Alloying Conference Proc.

Wagner C. (1959), Z Elekrochemie, **63**, 772.

Wagner C. (1961), Z Elekrochemie, **65**, 581.

Walser B. & Sherby O.D. (1982), Scripta Met., **16**, 213.

Wilcox B.A. & Clauer A.H. (1966), Trans AIME, **236**, 570.

Wilcox B.A. & Clauer A.H. (1972), Acta Met., **20/743**, 87.

Williams K.R. & Wilshire B. (1973), Metal Science, **7**, 176.

Wilson A. M. (1989a), High Nitrogen Steels 88 Conference Proceedings, The Institute of Metals p392.

Wilson A. M (1989b), The Development of TiN Strengthened Ferritic Stainless Steels, AEA Internal Research note.

Wilson A. M. & Laing K. C. (1990), Interim Progess Report on the Development of TiN Stremgthened Ferritic Stainless Steel, PFR Clad Panel Note 1054.

Wilson E.G. & Wilson A.M. (1980), AEA Internal Report ND-M-987(s).

Zabelt K., Wachter O. & Melzer B, (1996), VGB Kraftwerkstechnik 76, **12**. 936.

Zakine C., Prioul C. & Francois D. (1996), Mat. Sci. & Eng. **A219**, 102.

Zener C. (1948), Referenced to by Smith C.S. Trans AIME **175**, 15.

Zener C. (1949), Journal of App. Phys., **20**, 950.